Study of microscopic dynamics of complex fluids containing charged hydrophobic species by neutron scattering coupled with molecular dynamics simulations

Debsindhu Bhowmik

THESE de DOCTORAT de l'UNIVERSITE PARIS VI
PIERRE ET MARIE CURIE

Spécialité :

Matière Condensée, Chimie et Organisation

présentée par

M. Debsindhu BHOWMIK

pour obtenir le grade de

DOCTEUR de l'UNIVERSITE PARIS 6

Sujet de la thèse :

Etude de la dynamique d'ions hydrophobes en solutions aqueuses par diffusion de neutrons et par simulation numérique

soutenue le *30 Septembre 2011*

devant le jury composé de :

M. KUNZ Werner .... *Rapporteur*

M. DUFRECHE Jean-François .... *Rapporteur*

M. TURQ Pierre .... *Directeur de thèse*

Mme. DUBOIS Emmanuelle .... *Examinateur*

Mme. LYONNARD Sandrine .... *Examinateur*

Mme. MALIKOVA Natalie .... *Examinateur*

M. TEIXEIRA José .... *Invité*

1

Remerciements, Acknowledgement

This PhD thesis was carried out in LLB (Laboratoire Léon Brillouin) of CNRS (Centre National de La Recherche Scientifique) and CEA (Commissariat á l'énergie atomique et aux énergies alternatives), Saclay in collaboration with PECSA (Physicochimie des Electrolytes, Colloïdes et Sciences Analytiques) of UPMC (Université Pierre et Marie Curie), Paris. First I would like to thank Philippe Mangin and Christiane Alba-Simionesco, the successive directors of LLB and their deputy directors Susana Gota-Goldmann and Jean-Paul Visticot for welcoming and accepting me to the laboratory. I also want to thank Alain Menelle, Chantal Marais, Aurore Verdier, Claude Rousse, Catherine Doira and Bernard Mailleret for their regular valuable administrative assistance with much efficiency and kindness.

I express my deepest gratitude to Jean-Franç̧ois Dufrêche and Werner Kunz for accepting to be the rapporteurs of my thesis, Emmanuelle Dubois and Sandrine Lyonnard to serve as the jury members. At the same time I thank them for having taken a great interest in my work and making constructive comments.

My sincere thanks to Pierre Turq, my thesis director. Day after day, he supported my work and poured the much needed confidence into me by his valuable comments, effective advices with incomparable experience and pushed me hard to defend it in French (which I truly appreciate). My heartiest regards to my responsible of thesis, Natalie Malikova for all the valuable scientific and technical discussions, help, teaching me the proper way of 'presentation' and also the thorough learning procedure of new subjects with interrelating them. I also thank you for being patient enough to me for all the three years. At the same time I would like to pay my highest degree of gratefulness and appreciation to José Teixeira (who spent countless hours with me teaching all possible kinds of subjects in the world from his vast knowledge), Guillaume Merriguet and Olivier Bernard who relentlessly helped me to grasp the subject from its core and never hesitated to provide me the time whenever and wherever it was needed.

I also thank the researchers of third floor of LLB who always encouraged me (right from the beginning even though with my zero knowledge in French at my arrival to the laboratory): Jacques, Sophie, François, Annie, Marie Claire, Geraldine, Lay-Theng, Julia and of course Didier, Stéphane, Jean-Marc. My special regards for Fabrice Cousin for encouraging me endlessly (though people see you as Fabrice 'Michael' Cousin but for me you always remain as 'James Bond'). Also in PECSA, I thank Mathieu, Marie, Christian, Virginie, Vincent, Benjamin, Guillaume, Sami, John and Alexandro.

But this acknowledgement would be incomplete if I do not mention some of my wonderful friends (from LLB). First to my elder sister Clémence, thanks a lot for the clarifications and answers of all those 'out of the world' questions

that I always had (fortunately we had the same office). And yes, I now know that you can not run a helicopter. Then comes Chloé and Nicolas. Chloé, we spoke quite less and discretely in the beginning but that is because I was (and still am but less of course) always very afraid of you. But over the years I learned that there is nothing to fear. And Nicolas (Hail Nicolas, Hu! Hu!) once a KING is always a KING. Next comes my best buddy with numerous talents, Christophe Tasserit. Thank you for being my French professor and for having all those discussions that we had. Probably you are the sole person in the whole world who understands my dream of life (even though it is still not very clear to me). So Thank you again and also to François, the 'strongest man in the world' (only because you defeated me in 'wrist fight' but I have not forgotten it and will have my revenge :-)). Next comes the other PhD students who were pursuing their thesis at the same time. For you Anso, I can not and will not write anything because whatever I say, would not be enough; whatever I write, would not be 'exactly the words I am trying to search for'. So I'm just saying thank you very much for always supporting me and encouraging me, the rest you know. To 'ma petite mère' (Anne-laure), I promise that I will always try to eat vegetables (legumes) as much as I can. And Cynthia, I wish you a very prosperous future. To Zineb, soon I will visit Marocco, you must guide me; by the way the sweets that you brought, has no comparisons and Caroline thanks for all the mental boost that I needed. In short, guys, I could never have done this thesis (and also defend it in French) without you all. You all are probably one of the best gifts I have ever had, I could not ask for more. So thank you once again for everything. I equally thank Alexandros, Vincent, Émilie, Claire, les deux Adrien, Cédric, Isabelle for their support.

Before I finish, I want to thank my parents and my younger brother for always motivating me, keep supporting and giving me the freedom for whatever I wanted to do and of course for being present at the most important day in my life. I do not know how much my efforts can make up for what you have done over the years for me but still... I know that I always have problems of expressing my feelings in a proper way, so just to say this thesis is for you...

Merci beaucoup

Thank you very much

শুক্রিয়া

ধন্যবাদ

Sindhu (সিন্ধু)

Contents

List of Figures

List of Tables

2

Introduction (version française)

Le plus souvent, les molécules non polaires s'agrégent via des interactions hydrophobes de maniére à minimiser le contact direct avec les molécules d'eau voisines. La notion d'hydrophobicité est couramment utilisée pour expliquer de nombreux phénomènes - repliement de protéines, association d'un substrat avec une enzyme, changements de conformation des membranes biologiques. Aussi, des molécules non polaires chargées interviennent dans de nombreux processus biologiques et qui concernent l'environnement, justifiant l'intérêt pour les ions et polyions hydrophobes. Leur comportement en solution aqueuse est déterminé par une combinaison des interactions hydrophobique et électrostatique. Par ailleurs, l'abondance naturelle et les nombreuses applications des ions hydrophobes dans les domaines de la biologie, de la chimie ou de la technologie, font de leur étude un sujet de recherche extrêmement actif depuis de nombreuses années. Cependant, même si la notion d'hydrophobicité est couramment utilisée, sa description au niveau moléculaire n'est pas satisfaisante. En particulier, les conditions de sa coexistence avec des charges électriques restent relativement peu connues. En général, il est admis que l'arrangement des molécules de l'eau autour de solutés hydrophobes dépend de leur taille [Franks 1975] [Chandler 2005]. Pourtant, la coexistence d'hydrophobicité et de charges change nécessairement cette description des ions hydrophobes. En outre, ce n'est pas seulement le modèle structural (statique) qui doit être révisé, puisqu'il convient de tenir compte aussi de la dynamique de ces ions hydrophobes, ainsi que de celles de leurs contre-ions et des molécules d'eau.

Les cations de tetraalkylammonium (TAA) $[N^+(C_nH_{2n+1})_4]$ constituent un exemple typique d'ions hydrophobes à cause de leur structure très simple où quatre chaînes hydrocarbonées sont reliées à un atome central d'azote, chargé positivement. Ils ont été étudiés en tant que membres de sels halogénures et comparés aux halogénures alcalins (NaBr, KBr etc.), supposés être leurs homologues électrostatiques. La nature hydrophobe des ions TAA provient de la présence des chaînes alcanes non chargées et de longueur variable, qui

nécessairement augmente la complexité structurale par rapport aux solutions d'ions alcalins et joue aussi sur les interactions ion-ion et ion-eau.

Dans ce mémoire, nous prèsentons l'étude des propriétés structurales et dynamiques de solutions aqueuses de TAABr à l'èchelle microscopique via des simulations numériques et la diffusion de neutrons. Les deux méthodes analysent la dynamique des atomes ou des molécules à des échelles de temps entre la ps et la ns, et des échelles spatiales s'étendant de l'angström au nm, ce qui permet de comparer directement leurs résultats. Leur combinaison constitue donc un outil puissant pour l'étude de nos systèmes.

2.1   Bref aperçu

Ce mémoire est divisé en dix chapitres. Après l'introduction (en anglais et en français) dans les chapitres 1 et 2, les résultats d'études précédentes sur les solutions aqueuses TAA en rapport avec nos travaux sont discutés dans le chapitre 3. Les deux chapitres suivants résument les principes des deux méthodes principales utilisées au cours de ce travail. Le chapitre 4 introduit les bases de la diffusion de neutrons utilisée au cours des études structurales et de la dynamiques, ainsi que la modélisation et interprétation des résultats qui en sont issus. Les détails expérimentaux sont également expliqués ici. Dans le chapitre 5 nous parlons des concepts de base de la technique de simulation de dynamique moléculaire en détaillant les paramètres du champ potentiel utilisés au cours des simulations de la dynamique moléculaire. Nous présentons nos résultats au cours des trois chapitres suivants. La caractérisation structurale des solutés TAABr est discutée en détail dans le chapitre 6, tandis que l'analyse de la dynamique est l'objet du chapitre 7. Le chapitre 8 discute la structure et la dynamique de solvant. Pour conclure, nous résumons nos résultats dans les chapitres 9 et 10 (en anglais et français).

3

Introduction

Generally, non-polar molecules cluster via so-called hydrophobic nteractions to avoid direct contact with neighbouring water molecules. The idea of hydrophobicity is used to explain many phenomena - protein folding, association of a substrate with an enzyme, conformational changes in biopolymers and biological membranes. Moreover, in many biological and environmental processes, non-polar molecules also carry charge and we deal thus with hydrophobic ions or polyions. Their behaviour in aqueous solution is then governed by a combination of hydrophobic and electrostatic interactions. The high natural abundance and numerous applications of hydrophobic ions makes them an active field of study for decades. Though hydrophobicity is a widely used concept, its molecular basis still unclear. It has been suggested that the molecular arrangement of solvent water around neutral hydrophobic solutes depends on their size which also control the solvent dynamics [Franks 1975] [Chandler 2005]. Combining hydrophobicity with charge necessarily changes this picture for hydrophobic ions. However it is not only the structural (static) picture that deserves attention, it is also the dynamics of the hydrophobic ions, their counterions and the water solvent molecules.

Symmetric tetraalkylammonium (TAA) cations $[N^+(C_nH_{2n+1})_4]$ are considered as typical examples of hydrophobic ions because of their simple structure, where four hydrocarbon chains (or arms) are attached to a positively charged central nitrogen atom. They have been mostly strudied as part of TAA halide salts and compared to alkali halides (NaBr, KBr, etc.), considered as their purely electrostatic homologues. The hydrophobic nature of TAA ions comes from the presence of the uncharged hydrocarbon arms, of varying length. This necessarily increases the structural complexity of TAA cations in comparison to alkali cations and, in turn, has influence on the ion-ion and ion-water interactions in solution.

In this manuscript, we study the structural and dynamic properties of aqueous TAABr solutions on the microscopic scale using both microscopic simulation and neutron scattering. Both of these two techniques deal with

the dynamics of atoms or molecules present in the system on the timescale of picosecond to nanosecond and distances which range from Angstrom up to a nanometer. A direct comparison between them is thus possible and their combination is a powerful tool.

3.1   A Brief Outlook

This manuscript is divided into ten chapters. After the Introduction (in English and in French) in Chapter 1 and 2, a review of the relevant results from previous studies on aqueous TAA solutions is presented in Chapter 3. The next two chapters focus on two principal techniques employed in this work. Chapter 4 introduces the basics of neutron scattering for both structural and dynamic studies, along with the modelling and analysis of neutron data. The experimental details of our studies on TAABr solutions are also explained here. In Chapter 5 I highlight the basic concepts of molecular dynamics simulations with the details of force field parameters used here for the molecular dynamics simulations of TAABr solutions. I further present our main findings in three separate Chapters. The structural characterisation of TAABr solutions, with emphasis on the ions, is discussed in Chapter 6. The TAA cation dynamics is presented in Chapter 7. Chapter 8 discusses the solvent structure and dynamics in various TAABr solutions. We summarize our results, conclude and present further perspectives thereafter in Chapter 9 and Chapter 10 (in English and in French).

4

Review on Aqueous Solutions of Tetraalkylammonium Salts

Contents

4.1 Introduction

The study of hydrophobic ions in aqueous solution remains a dynamic field because of its numerous biological, chemical and technical applications. Hydrophobicity is the main source of bio-molecular interaction and protein stability as suggested by Kauzmann [Kauzmann 1959]. The term hydrophobicity originates from two Greek words - 'hydro' and 'phobos' which mean water and fear respectively. We usually define those substances hydrophobic that do not mix with water. Though it is tempting to conclude that hydrophobicity occurs because of the repulsion of oil like solutes from water, in reality this happens because of the modification of H-bonds between solutes and solvent water molecules. Theory coupled with thermodynamic measurements concludes that the change in entropy for the solvation of apolar hydrocarbon solutes is negative while enthalpy is positive. This indicates that water structure around the solutes could be more structured than in bulk and depending on the solute size, the surrounding solvent water network is reformed (H-bonds can be broken or modified) [Franks 1975] [Chandler 2005].

In our study, the hydrophobic solutes in aqueous solution are also charged. Thus in a solution of hydrophobic ions, the interactions among different particles are influenced by both charge and hydrophobicity. It can be taken as the fundamental difference with simple ions where coulombic interaction is the sole dominating factor.

4.2 Hydrophobic Interaction

Hydrophobic substances are easily soluble in non-polar solvents while other solutes (non-hydrophobic) are not soluble as they become solid due to their intermolecular attachment. The idea of hydrophobic interaction is often used to describe many bio-chemical processes such as denaturation of proteins, association of a substrate with an enzyme, conformational changes in biopolymer, phase-transfer catalysis, aggregation, formation of micro-emulsions or biological membranes (such as in case of living cell membrane) and many others. Historically hydrophobicity is measured by distribution coefficient (ratio of solute concentrations between two solvents at equilibrium) which is analogous to calculate the free energy transfer. The technique permits to measure the affinity of the solute towards each of the solvents. In case one of the solvent is water, it is called hydrophobic hydration and when there are more than one solute it is termed as hydrophobic interaction [Ben-Naim 1980]. Two of the most important aspects to study hydrophobicity are what is its solubility mechanism and how we can study this hydrophobic interaction.

When a solute is immersed in water, there can be two situations - the solute is either 1) non-polar or 2) polar or ionic. In case of non-polar molecules (containing for example hydrocarbon chains), the water-water attraction is the deciding factor. To incorporate the solutes inside its network, water structure is deformed or distorted. This leads to decrease in free energy but not bond energy because the hydrogen bonds in water molecules are there, even in distorted or deformed structure. The hydrogen bond still remains strong and is the principal deciding parameter to control the equilibration process. Ionic or polar solutes are more easily soluble because they form H-bonds with water molecules in the solvent and this makes up for the loss that is caused due to the bond disruption for the presence of the solute [Tanford 1979].

Hydrophobic interaction is often accompanied by various other forces like long range electrostatic forces between charges, short range Van der waal forces due to attraction or repulsion, strong repulsion because of hard sphere effect (impenetrable volume), hydrogen-bonds. To know the individual effect of each force, it may be tempting to follow the idea of studying all these different forces independently. But obviously that cannot be the right solution because there is no prior knowledge about how these forces combine among themselves and with what weightage. Thus it is a popular idea to study various model processes and model systems such as free energy transfer measurement in case of aggregation. Here is one simple example [Ben-Naim 1980]. Imagine that n number of hydrophobic solutes are dissolved in an aqueous medium which in turn form an aggregate. Obviously the molecules at the surface (n_{sur}) and the inside of the aggregate (n_{int}), are in different environment (i.e. water and non-polar respectively). Thus it paves the way to study the effect of different factors separately (but not isolating them) in a model system.

In this work, we will study the structure and the dynamics of symmetric Tetraalkylammonium (TAA) $(C_nH_{2n+1})_4N^+$ cations (with Bromide anion) which is one of the most investigated hydrophobic charged systems. At the same time, we will also present how the solvent structure and dynamics is changed due to the effect of these TAA ions. The remainder of this chapter will include a brief review of the previous works which were performed on TAA halide salts in aqueous solution and are relevant to this study.

4.3   Tetraalkylammonium Salts

The advantage of using TAA salts are - i) being a model system TAA halide solution go beyond the simple 1:1 electrolytes (like alkali salts) and so one can study the competing forces among electrostatic (long range) and hydrophobic interactions (short range) present in the system ii) by changing the length

of the hydrocarbon chains of TAA cations, the effect of the hydrophobicity can be modified. Based on the capabilities of making or breaking the hexagonal hydration water structure, some ions are called 'structure makers' (that destroy the free movement of water molecules) and some are termed as 'structure breakers' (increase the free movement of water molecules). As for example in TAA family, for long, Tetramethylammonium (TMA$^+$) (CH$_3$)$_4$N$^+$ is considered as a 'structure breaker' because it decreases water hexamer structure and Tetrapropylammonium (TPA$^+$) (C$_3$H$_7$)$_4$N$^+$ or Tetrabutylammonium (TBA$^+$) (C$_4$H$_9$)$_4$N$^+$ (figure 4.1) are considered as structure maker while Tetraethylammonium (TEA$^+$) (C$_3$H$_7$)$_4$N$^+$ is neutral in this point of view [Kay 1966a] [Kay 1966b] [Lee 1988] [Bradl 1993] (this will be discussed later in this chapter).
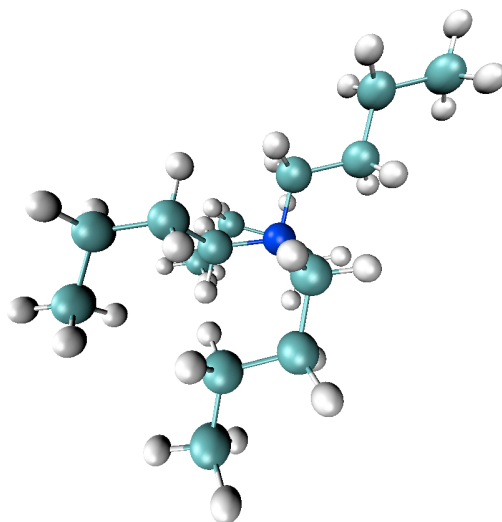
Figure 4.1: TBA$^+$ (C$_4$H$_9$)$_4$N$^+$ cation (blue - nitrogen, green - carbon and white - hydrogen atom). The hydrophobicity can be modified by changing the length of the hydrocarbon chains. This is one fundamental difference with simple inorganic ions where electrostatic interaction is the sole deciding factor.

4.3.1 Structure

4.3.1.1 Ion-Ion Correlation

The measurement of vapor pressure, osmotic pressure and activity coefficient are useful ways to study the solute or solvent behavior. The Chemical model and Pitzer equations[1] [Pitzer 1974b] [Pitzer 1974a] [Pitzer 1973b] [Pitzer 1977] [Pitzer 1973a] are used to compare with the experimental data (such as osmotic coefficients). The results conclude weaker dependence of vapor pressure, osmotic pressure and activity coefficient on the length of the alkyl chain of a cation for a particular halide anion series (ex: Bromide) compared to different anion effect in a particular cation series (ex: TBA). Though chemical model predicts good agreement with experiment, the technique is found to be suitable for dilute solution[2]. Therefore a more sophisticated way is proposed by Friedman and Rasaiah [Rasaiah 1969] [Rasaiah 1968] which could be used for the concentration range 0.4M-1.0M depending on the system. This method, called hypernetted chain (HNC) theory[3] works at McMillan-Mayer level (solvent-averaged potentials) and can calculate ion-ion pair correlation functions. The HNC calculation depends on the chosen pair-potential. Small angle neutron scattering (SANS) derived results can be useful to compare with the HNC result. As an example earlier SANS result on 0.15M and 0.30M TBABr in D_2O [Calmettes 1992] is well reproduced by this HNC approximation using the potentials [Ramanathan 1972] where three different types of potentials are taken which are coulombic, repulsive and so called Gurney potential. The main conclusions of this work is 1) the alkyl chains are fully stretched, 2) cation-cation correlation shows no hydrophobic bonding, 3) water molecules, anions or alkyl chains of different TBA cations could interpenetrate. This model is shown to be working in small Q or large distances (up to 0.5 Å^{-1}).

4.3.1.2 Charge-Charge Structure Factor

The charge density fluctuation in solution can be described by the charge-charge structure factor S_{ZZ} (Z = + or -) which helps to understand ion-ion correlation as a function of distance. In an ionic solution, the three possible kinds of structure factors are [Hansen 1986] [Nallet 1983]

---

[1]see A.1 for brief explanation
[2]see A.1 for brief explanation
[3]see A.2 for brief explanation

$$S_{NN}(Q) \quad = \quad \frac{1}{N}\langle\rho^N(Q)\rho^N(-Q)\rangle = \sum_i\sum_j S'_{ij}(Q) \tag{4.1}$$

$$S_{NZ}(Q) \quad = \quad \frac{1}{N}\langle\rho^N(Q)\rho^Z(-Q)\rangle = \sum_i\sum_j Z_j S'_{ij}(Q) \tag{4.2}$$

$$S_{ZZ}(Q) \quad = \quad \frac{1}{N}\langle\rho^Z(Q)\rho^Z(-Q)\rangle = \sum_i\sum_j Z_i Z_j S'_{ij}(Q) \tag{4.3}$$

$$\tag{4.4}$$

where Q is the reciprocal wave vector (discussed in detail in section 5.3.1), ρ is the number (N) or charge (Z) density. In the last equation, S_{ZZ} is called the total charge-charge structure factor which is the sum of different partial charge-charge structure factors. The S_{ZZ} can be useful to determine the ionic effect on structure function. The $S'_{ij}(Q)$ is related to the pair correlation function $[g_{ij}(r)]$ by

$$S'_{ij}(Q) = (\delta_{ij} + \frac{4\pi}{Q}\sqrt{\rho_i\rho_j}\int_0^\infty sin(Qr)[g_{ij}(r)-1]rdr) \tag{4.5}$$
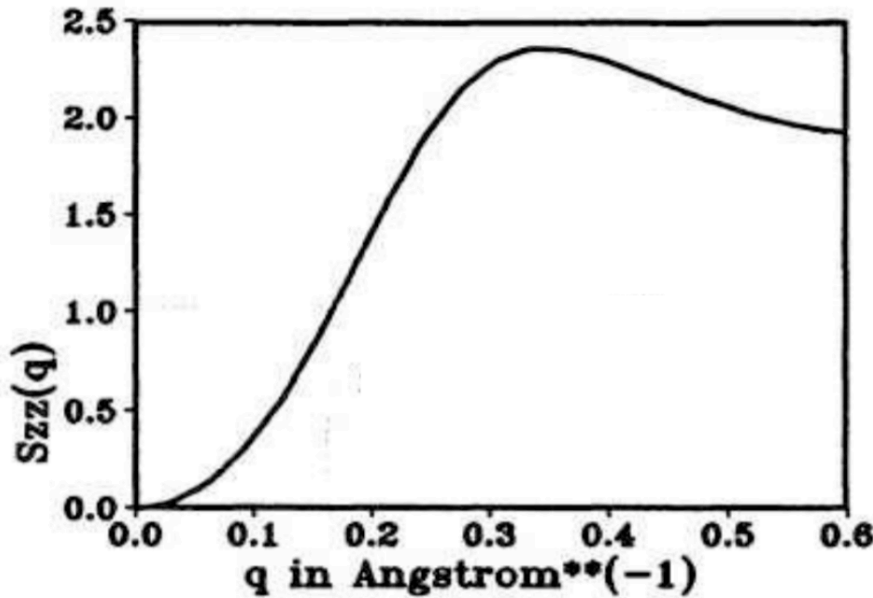
Figure 4.2: Charge-Charge structure factor $[S_{ZZ}(Q)]$ as a function of Q for 0.25M $Et_3PhN^+Ph_4B^-$ in DMF [Kunz 1992a].

For a spherical ion (form factor becomes unity at small Q) total S_{ZZ} can be decomposed as below

$$S_{ZZ}(Q) = S_{++}(Q) - 2S_{+-}(Q) + S_{--}(Q) \qquad (4.6)$$

It follows Stillinger and Lovett condition. At Q=0, $S_{ZZ}(Q) = 0$ and at a finite Q value (Q $< \kappa$, where κ^{-1} is Debye screening length), $S_{ZZ}(Q) \simeq \frac{2Q^2}{\kappa^2}$. The first condition means that at Q=0 or infinite distance, the charge of an ion is completely screened by other ions while the second condition indicates that the screening of a charge is partial at a finite distance. An example of charge-charge structure factor calculation of $Et_3PhN^+Ph_4B^-$ is shown in figure 4.2 [Kunz 1992a].

4.3.1.3   Ion-Pair Formation And Penetration

The formation of ion-pair (cation-anion) is an important aspect. This was studied by several ways such as measurement of vapor pressure, activity co-efficients, partial molar volume or conductivity. Lindenbaum and Boyd [Lindenbaum 1964] reported that activity coefficients for TAA chloride increases with cation size which is opposite to bromides and iodides. In order to explain different kinds of counterion association with TAA, they have used different explanations for chlorine and for bromine and iodine. This was first proposed by Diamond [Diamond 1963]. The association for bromide and iodide is due to 'water structure-enforced ion pairing' and for chloride the phenomenon can be explained by modified arrangement of water structure around the hydrocarbon portions of the cations. According to that when two large hydrophobic ions try to dissolve, they form one single cavity instead of two for each ion by forming an ion-pair, which can be stabilized considering mainly the water structure and not by electrostatic effect. In case of chloride, they prohibit this tendency of ion-pair formation. This idea is further supported by the result for partial molal volumes of aqueous TAABr solutions (0.1-10m concentration) [Wen 1964] where clathrate-like cages of water produce cavities to accommodate both cation and anion. In order to check these ideas by conductivity measurement, most of the studies have been carried out in dilute solution where the theory is expected to be more applicable. By Evans et al. [Evans 1966] [Lee 1988] precise measurements were carried out for all of TAA Chloride, bromide and iodide salts. A comparison of the Walden 'conductance-viscosity' product for TAA ions in H_2O shows that for TMA^+, the value is higher than for TBA^+. This is because as the carbon chain length increases, water structure enforcement decreases. As from the result the decrease in conductance of iodides over bromides is because of the greater

association (cation-anion) in iodides which probably comes from higher po-
larizability of iodide ion (but it should be noted that this is not the case for
KI and KBr, where KI has higher conductivity). It is not clear whether this
ion-pair association is electrostatic or solvent-stucture stabilized [Wen 1964]
or something else.
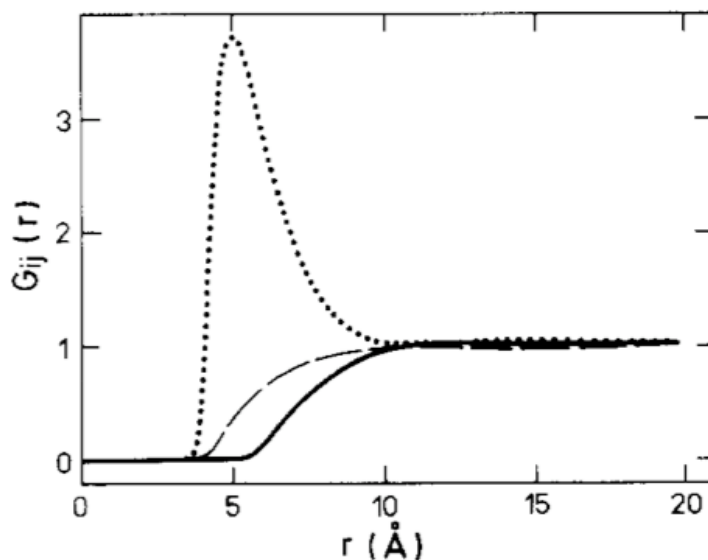
**Figure 4.3: Pair correlation between cation-cation (solid
line), cation-anion (dots) and anion-anion (dashed line)
in 0.15M and 0.30M aqueous TBABr calculated by HNC
method [Calmettes 1992].**

The cation-cation, cation-anion and anion-anion correlation func-
tions, $g_{ij}(r)$ (by HNC) show usual characteristics of TAA solu-
tions in different solvents: water [Calmettes 1992] (figure 4.3),
acetonitrile [Kunz 1991] [Kunz 1990], methanol [Barthel 1994] or 2-
propanol [Kunz 1992b]. As the main interest of our work is to study solute
behavior in aqueous medium so we will not further discuss about other sol-
vents. The basic conclusions are that the counterion could penetrate between
the cation alkyl chains and also cation could penetrate into other cations
(this is called 'shoulder in armpit model' [Friedman 1988]). However HNC
calculations can not successfully reproduce scattering data at concentration
higher than a certain level (0.3 M for n-Pe$_4$NBr solution). By molecular dy-
namics (MD) simulation one can study in more detail. Recently one such
study [Heyda 2010] is performed by using an all atom explicit model of am-
monium (NH$_4^+$) ion as well as Tetraalkylammonium cations (TMA$^+$, TEA+

and TPA^+) in water at three different concentrations (0.25, 0.5 and 1M). The authors show that for TAA cations, cation-anion ion pairing follows the order $I^->Br^->Cl^->F^-$, indicating that large TAA cations tend to form ion pair with large anions which is opposite to the case of NH_4^+.

Aggregation of TAA cations and Effect on Water Structure It is natural that as the salt concentration increases, the possibility of forming 'aggregation' also increases which may be originated from the possible intersection of surrounding water structure around the solute ions. These aggregations can be driven electrostatically or by hydrophobic interaction. Various kinds of ions pairs can possibly occur within these aggregations such as 1) solvent separated (ions pairs are more than one water molecule apart) 2) solvent shared (exactly one water molecule apart) 3) contact ions pairs (absence of covalent bond). Conductance and viscosity results as a function of concentration and temperature can provide handful of information [Marcus 2008].

Conductivity and Viscosity Measurement From figure 4.4, we see that TBABr conductance is sharply decreasing with respect to infinite dilution [Eagland 1972] [Buchner 2002] [Surdo 1979]. Comparing with other TAABr members, we find that as the size of cation increases the rate of change of conductance as a function of both concentration and temperature becomes slower. A rough estimate of the degree of dissociation indicates that it increases as the temperature increases and/ or concentration decreases.
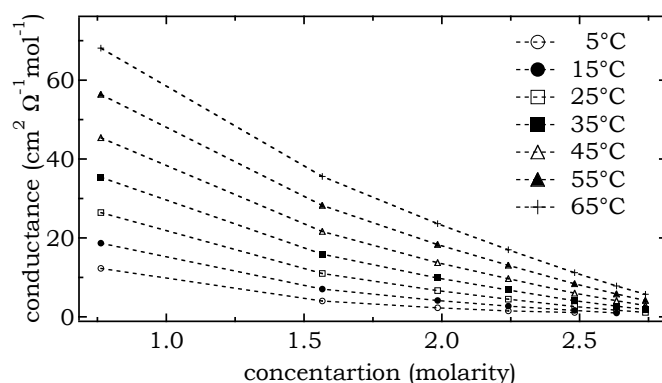
Figure 4.4: Conductance of aqueous TBABr as a function of concentration and temperature. Conductance is sharply decreasing from infinite dilution value [Eagland 1972] [Buchner 2002] [Surdo 1979].
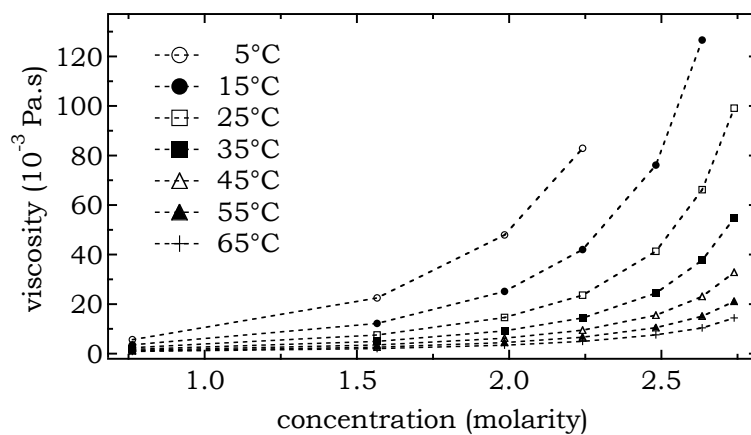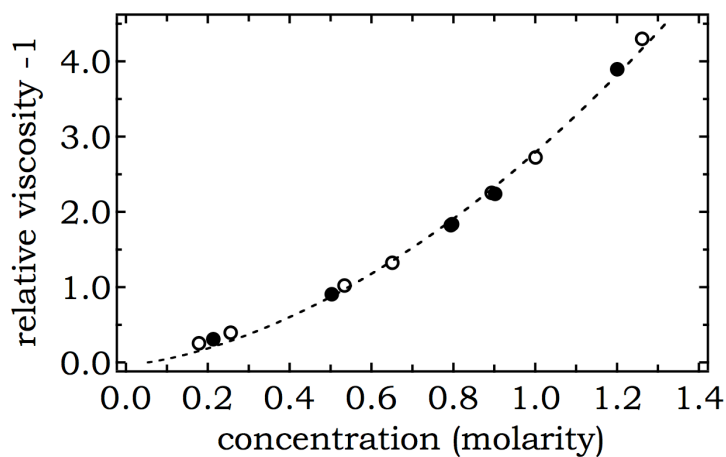
Figure 4.5: Viscosity of aqueous TBABr solution as a function of concentration and temperature [Kay 1966a] [Surdo 1979].

The modification of water structure due to solutes can be probed by viscosity measurements. From the fitting of experimental data with extended Jones-Dole equation one can determine the B coefficient.

$$\eta_{rel} - 1 = Ac^{\frac{1}{2}} + Bc + Dc^2 \tag{4.7}$$

where η_{rel} is the ratio of viscosity of solution and water and A, B and D are the coefficients which depend on the solute, solvent and on temperature (figure 4.5). At high concentration B coefficient becomes important because of the ion-ion interaction. The value of B is accountable for ion solvent interaction and depends on the ion volume. The B values of TBABr and TPABr in water and methanol suggest that at low temperature, it is always higher in aqueous solvent than in methanol and in methanol solvent it is constant as a function of temperature (figure 4.6). The effect due to anion is very small, the decrease of B for TPA or TBA in water is mostly due to the cations. For TMABr (in water) the situation is different where little increase can be seen with temperature and the B value in methanol solvent is higher than aqueous solvent. In case of TEABr, B value in methanol is higher than TMABr in water but then the B value decreases with increase of temperature as TPABr or TBABr in water. All these data support the conductance measurement [Kay 1966a] [Surdo 1979] and concludes that for larger TAA ions (TBA$^+$ or TPA$^+$), the water molecules are rearranged by increasing hexamer structure around TAA hydrocarbon chains and thus increases the viscosity by forming a bigger diffusive particle. This is not the case for TMABr in water. The TEABr in water shows an intermediate behavior. This proves that (in water) TBABr or TPABr are structure makers while TMABr is structure breakers while these two effects cancel each other for TEABr.

Volume Shrinkage   The measurements of partial molar volume in aqueous and non-aqueous solutions show that from TPA to bigger TAA ions the volume expands while there is a shrinkage for lower TAA members [Marcus 2008] from aqueous to non-aqueous solvent. At first sight this does not agree with the concept of ice like cage structure that forms in aqueous but not in non-aqueous medium. It could be explained by imagining the relaxation of hydrocarbon chains in non-aqueous solvent than aqueous one.

4.3.2   Dynamics

Macroscopic thermodynamical or microscopic structural information or ion-ion correlation are not enough to make a full picture of the systems under con-
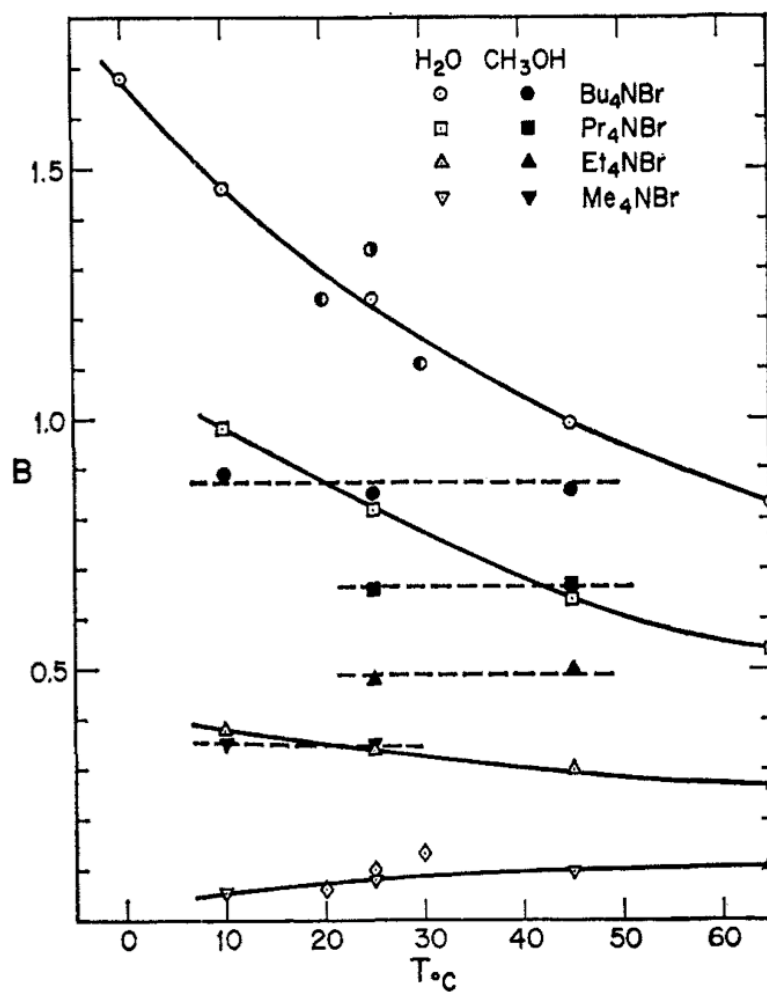
Figure 4.6: B coefficient of Jones-Dole equation for TAABr in water and methanol as a function of temperature. A clear difference can be observed for TBABr and for TPABr compared to TMABr with TEABr as neutral, after [Kay 1966b].

sideration. A detailed side by side study on diffusion mobility and rotational-vibration movements is necessary.

4.3.2.1   at Infinite Dilution

Table 4.1 summarizes diffusion coefficients at infinite dilution in water (extracted by conductivity and NMR measurementss) for TAA cations in comparison to Stokes-Einstein relation (Diffusion coefficient D $= \frac{k_B T}{6 \pi \eta R}$ where k_B is Boltzmann's constant, T is absolute temperature, η is viscosity and R is the radius of the spherical particle.). The result (figure 4.7) shows that as the cation radius increases, the Stokes-Einstein relation estimates the diffusion coefficient (translational) better. The conductivity data [Robinson 2002] for TBA$^+$ can be found in table 4.2. On increasing the temperature the activation energy can also be calculated from conductivity data [Eagland 1972] [Buchner 2002] [Surdo 1979]. For TBABr in H$_2$O, it is ~ 23kJ mol^{-1} (figure 4.8).

ion	radius (Å)	D$_0$ (at infinite dilution) $10^{-9} m^2 s^{-1}$		
	by Experiment	by Model	by Experiment	
	density measurement	Stokes-Einstein relation	conductivity measurement	NMR
TMA	3.6	0.55	0.97	1.1
TEA	4.1	0.48	0.70	0.73
TPA	4.6	0.43	0.50	0.52
TBA	4.9	0.40	0.40	0.39

Table 4.1: Comparison of radius and translational diffusion coefficient of TAA cations in D$_2$O between experiment and Stokes-Einstein relation at infinite dilution. The infinite dilution translational diffusion coefficient is extrapolated from NMR [Hertz 1969] and conductivity experiment [Kay 1965] and then compared with Stokes-Einstein prediction using the radius from density measurement [Wen 1964].

4.3.2.2   at Concentrated Solution

Apart from conductivity and NMR measurements, quasi-elastic neutron scattering (QENS) experiment is an effective tool proved over the years to study molecular/ atomic dynamics. QENS Time of Flight (TOF) study was performed on aqueous solution of TMA$^+$ and TBA$^+$ chloride [Novikov 1996a]
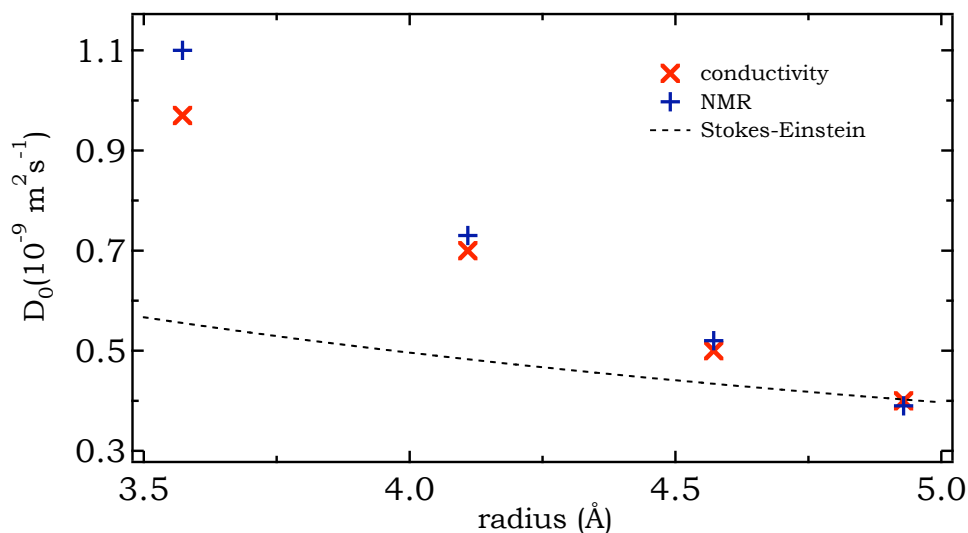
Figure 4.7: Comparison of TAA cation translational diffusion coefficient at infinite dilution extracted from experiment (NMR and conductivity) and Stokes-Einstein relation. As the cation size increases the agreement between Stokes-Einstein and experiment becomes better.

temperature ($°C$)	λ_0 ($\frac{cm^2 Int.}{\Omega equiv}$)	temperature ($°C$)	λ_0 ($\frac{cm^2 Int.}{\Omega equiv}$)
0	9.6	0	24.1
10	12.59	10	30.94
25	19.4	18	40.0
		25	44.9

Table 4.2: TBA$^+$ and TMA$^+$ limiting equivalent conductivity data in water.

[Novikov 1999]. The authors concluded that TBA$^+$ diffuses like a big particle [$(0.32\pm0.02)\times10^{-9}$m^{2}s^{-1} at 0.75M] following the law of continuous diffusion with a diffusion coefficient close to NMR prediction [Hertz 1969] with no evidence of other types of motions seen in their data [$(0.74\pm0.03)\times10^{-9}$m^{2}s^{-1} for TMA$^+$ at 2M].

It should be noted that there is a clear difference of the mobility of TBA$^+$ in the aqueous solution with different anions. A comparison of mutual diffusion coefficient of TBA$^+$ for various halide anions can be found from the work of Kim et al [Kim 1973] (measured by optical diffusiometer). A brief
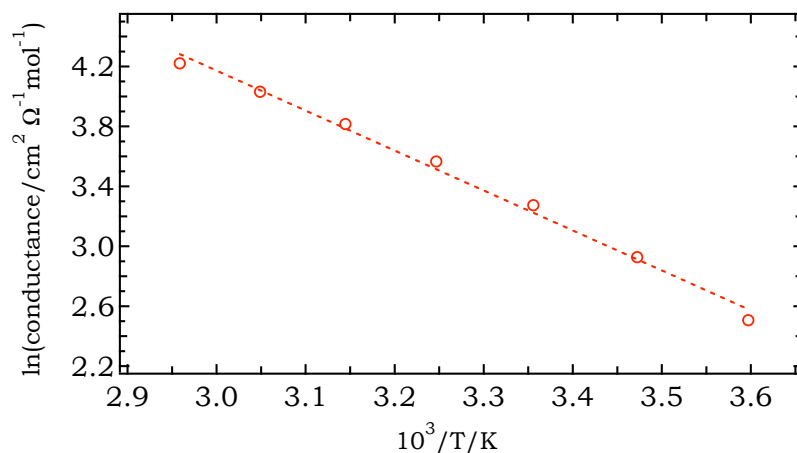
Figure 4.8: Estimation of activation energy $\sim$ 23kJ mol^{-1} of TBA^{+} mobility in aqueous TBABr solutions from conductivity measurement (data taken from [Eagland 1972] [Buchner 2002] [Surdo 1979]).

summary of the self and mutual diffusion coefficient (for TBA with different anions) measured by different techniques can be found in figure 4.9. Note that due to low solubility of TBAI, measurement of diffusion coefficient at higher concentration is not possible.

4.4 Hydration Shell

The first ion-water interaction model by Frank and Wen [Frank 1957] is based on structure-making and structure-breaking effects. The water hydration shell involves mainly three kinds of zones. The first zone consists of those water molecules which are mostly affected by the central ion. Usually these molecules stuck to the central ion for a longer time compared to the bulk. But only a well defined structure around a dissolved ion is not sufficient to be called as the first zone. The condition requires the water molecules of this zone (also called as primary hydration shell) stay for a longer time comparable to the ion itself. Normally this zone [either hydration of first kind (electrostriction) or hydration of second kind (clathrate like cages)] have more immobilized water molecules. The second region contains the water molecules which are less structured and feels the combined effect of central ion and the normal water (third region) [Kay 1965]. But measuring second shell water dynamics
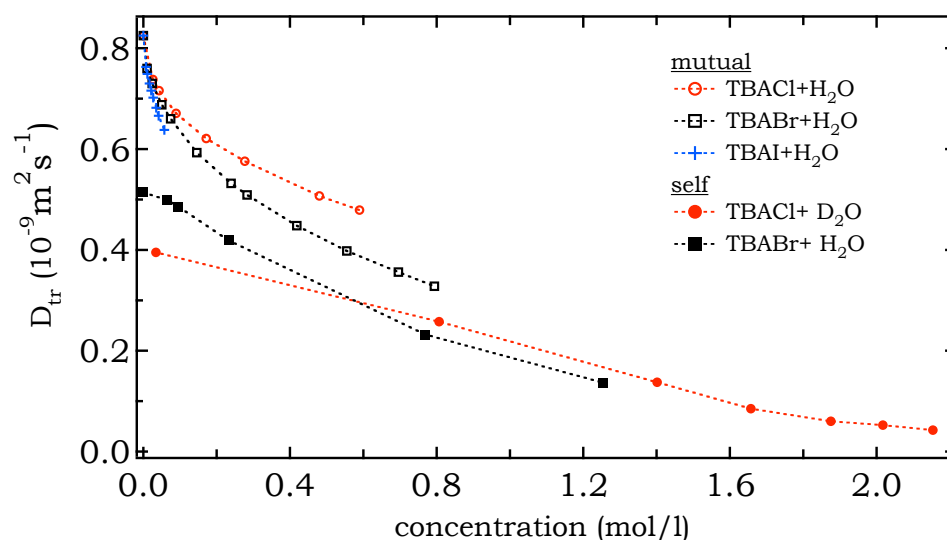
Figure 4.9: Self and mutual diffusion coefficient of aqueous TAA halide solution, estimated by different experimental techniques. The mutual diffusion coefficients are measured by optical diffusiometer. The self-dynamics of TBA cation is measured by NMR (Br anion) [Hertz 1969] and Tracer (Cl anion) [Woolf 1982] and mutual-dynamics by optical diffusion technique [Kim 1973].

is not easy [Hewish 1983]. By QENS technique they indeed proved the idea that first hydration zone is influenced by the ion itself. From their results it is also evident that distinction of hydration shell based on 'free' and 'bound' water around ion is not sufficient, the hydration water contains a range of dynamic properties at different distances from the ion. In the third segment, one can see a normal or bulk water behavior. The idea was further supported by [Buchner 2002] [Slusher 1997]. They find the 'slow' water is more probable to be found around large TAA cations (like TPA and TBA than TMA cations).

4.4.1   Structure

Partial Pair Correlation Function   The structural study based on partial pair correlation function coupled with isotope substitution on aqueous TAA solution is done extensively by Turner and Soper [Turner 1990] [Soper 1992] [Turner 1992] [Turner 1994] [Turner 1995]. For the knowledge about hydration, neutron diffraction serves as a useful tool for a long time. Problem is

that from experiment we obtain only total pair correlation function which is the weighted sum of partial pair correlation functions $g_{ij}(r)$. But to analyze the result in light of $g_{ij}(r)$, even for a small number of different atom types, total number of partial pair correlation functions $g_{ij}(r)$ become too much to handle. For this purpose the technique which uses the isotope substitution (developed by Enderby and Neilson [Enderby 1979]) is someway useful.
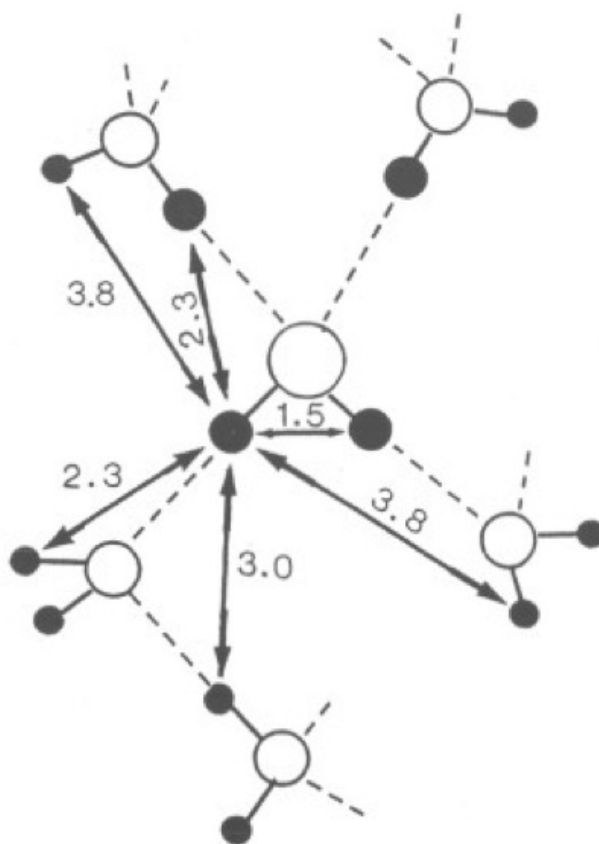
Figure 4.10: Structural geometry of hydrogen bonding in water molecules and its nearest neighbors (distance in Å). white - oxygen atom, black - hydrogen atom [Turner 1990].

For aqueous TMACl solutions (0.5M - 2.0M) Turner et al tried to look at the clathrate crystal structure where 20 to 28 water molecules forming the vertices of polyhedron cage with average radius of 3.9 to 4.7 Å. In this

kind of cage structures, two-third of the H-bonds correspond to the O...H bonds forming the polyhedron edges, and the rest remain as pointing outwards. The results indicates the Nitrogen atom could be placed at the center of the cage and both the oxygen and deuterium (or hydrogen) of water are equidistantly (equal to the radius) placed. This is more like 'edge-on' arrangement (tangential orientation) of water molecule that helps to make H-bond as in bulk (figure 4.11). It points to the fact that electrostatic interaction between TMA ion and water is not capable enough to decrease the average TMA-water distance and thus creating 'apolar' behavior in TMA cation in water. More detailed analysis predicts that both HOH plane and bisector are tangential to the TMA cation surface. This also allows the water molecule to form four bonds to other water molecules (figure 4.10). However existence of non tangential orientations is also not improbable which is responsible to disrupt water H-bond and subsequently the cage structure. There could be second layer of water molecules at 8 Å from nitrogen atom. On increase of concentration there is no indication of change in hydration structure [Turner 1990] [Turner 1992] [Turner 1994] [Turner 1995].
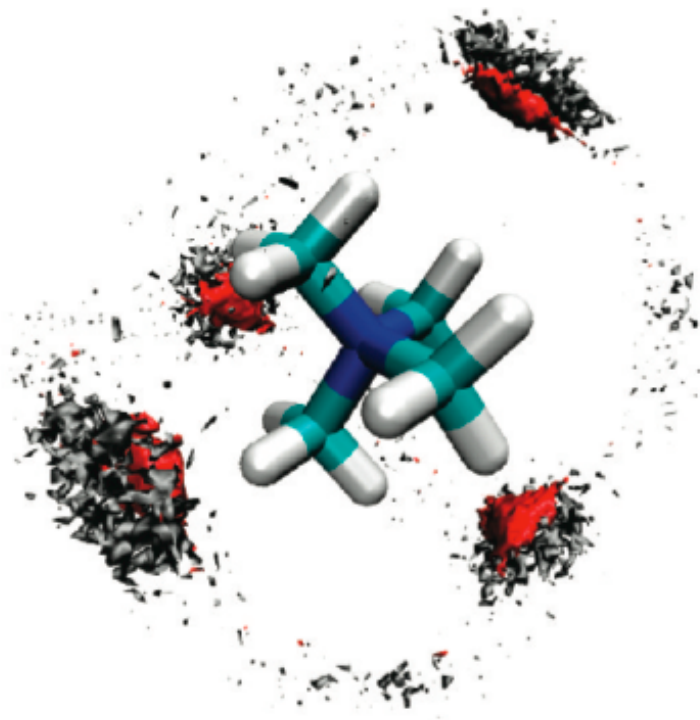
Figure 4.11: Water around TMA$^+$. (grey- hydrogen atom, red-oxygen atom) [Heyda 2010].

In order to force water molecules to share with TMA ions, a higher concentration (4.0M) is used. The center-center correlation function $g_{center}(r)$ indicates that first neighbor TMA ions are often in contact (no conclusion is drawn for cation-anion pair formation) which agrees with their previous result [Turner 1990] that TMA is more like a apolar species in water than a ionic solute. Having said that TMA cation is more like apolar in aqueous solution it also true that it does not coordinate the neighboring water molecules and thus agreeing the fact that water structure surrounding TMA ion is not more ordered than bulk water [Soper 1992].

At a higher concentration (8.0M), the peak position and width of H-H correlation function still do not change compared to bulk water even though there is not enough water to make all H-bonds. The decrease of coordination number of first neighbor hydrogen atoms with increase in concentration is most probably because of the fact that the broken water-water H-bonds are replaced by water-chloride ion hydration bonds where number of coordinated water molecules is weakly dependent on concentration. The fact that there is no change in H-H correlation with increasing solute concentration, contradicts other experiments on aqueous solution of apolar solutes where a prominent change in ordering effect on the water hydration is found (as an example, in hydrogen sulphide, with a very similar H-H correlation to water, showing total absence of H-bonds [Andreani 1991]). In other example, in dimethylsulphoxide, peak movements and other changes in H-H correlation are observed with increase of concentration. In case of aqueous TMA solution, a hydrophobic hydration effect is observed though it is delicate to analyze and also it remains unclear when and how the effect of charge balances the effect of apolar groups in aqueous solution.

Moving to larger member of the same tetraalkylammonium ion family with the number of water molecules required to constitute one hydration sphere per cation (56 water molecules for TBA^+ and 40 for TPA^+), a small difference in average water structure is found (although this trend is not observed in alcohol, while going from ethanol to t-butanol). Though it is possible that the average water structure around ethanol to t-butanol does seem to be changing and any small change is hindered by $OH_{alcohol}$-water interaction [Turner 1994]. The small though significant increase in water structure for the mentioned TAABr solution, could imply that water is slightly stabilized for this solution and eventually the 'hydrophobicity' is also changed very little (first suggested by Feakins et al [Feakins 1989]).

4.4.2 Dynamics

The mobility of water molecules around TAA cations is significantly suppressed (by a factor of 1.5 to 2) compared to bulk though we previously found a little (for TBA$^+$) or no change (for TMA$^+$) in neighboring water hydration structure. QENS experiments shows that (as predicted before) the diffusion mobility of water reduced in the vicinity of solute TAA cation and the characteristics is similar to the simple cationic hydration [Novikov 2001] [Novikov 1996b] [Novikov 1997]. But the hydrophobicity does not affect much the vibrational-rotational motion just as it does not modify the hydrating water structure. Thus it could be stated that the hydrophobic hydration is a weak parameter to alter the structural configuration or vibrational-rotational dynamics, contrary to the expectation. Though that does not answer the primary question of the source of decrease in entropy. Again same kind of experiment on dilute TBAOH (0.02M) points that the solvent water is more structured [Calandrini 2006]. The result supports the Stillinger's hypothesis which states that cavities exist in pure water and fluctuate about their mean. Introduction of any apolar molecule stabilize the configuration which provides enough cavities to accommodate them. These cavities are connected to the unstrained H-bond similarly formed spontaneously in water on reducing the temperature in sub-zero region [Calandrini 2006].

Up to now all the discussion covered TAA ion solution at room temperature but a handful of information can be drawn from the undercooled aqueous (R$_4$N$^+$) solution. Because it possess reduced thermal excitation, the surrounding hydrophobic hydration structure of solvent would be more stable with a longer lifetime which could slow down the translational and orientational movement. Here we discuss some of the results which measures deuterium (^{2}H) relaxation time in undercooled aqueous solution of TMA$^+$, TPA$^+$ and TBA$^+$ (with bromide anion) solution by NMR [Bradl 1993] [Bradl 1994] [Lang 1990] [Lang 1991]. The essential information is that the solvent dynamics is slowed down at room temperature due to the interaction between water and dissolved apolar TAA$^+$ surface. At low temperature the H-bond around the TAA$^+$ is nicely formed and rotational water dynamics is increased even close to apolar surface of the solute cation [Bradl 1993]. Larger TAA$^+$ cation than TMA$^+$ strongly enhance average rotational dynamics of solvent water dynamics which does not agree with clathrate cage formation. But things are not same when there is just enough water molecules around the solute. The relaxation time is strongly enhanced due to the interaction between hydration water and apolar surface. The dynamics is even more reduced at higher concentration due to H-bond bridging.

To relate these dynamic data with structural information, neutron diffraction with isotopic substitution (NDIS) experiment [Slusher 1997] was performed. In brief because of the mutual effect of coulombic, hydrophobic and H-bond interactions, the dynamics (rotational and translational) of solvent is changed according to the state of H-bond network of the hydration water molecules. It turns out that even in undercooled state a short lived and highly transient hydration cage exist and its overall tumbling motion is faster than expected from theory of hydrodynamics. The fast reorientation of methyl group agrees with the simulation result that TMA^+ ions trapped in a cavity formed by water molecules. The strong cross-relaxation of fast methyl group with almost similar proton relaxation time of solute and solvent at low temperatures cause a relaxation sink as a whole. Thus it requires a structural confirmation. By previously mentioned NDIS experiment, H/ D isotope substitution technique in solvent provides water-water correlation for aqueous solution of TMA^+ ions. A distinct difference is found in the position and sharpness of $g_{HH}(r)$ which indicates a more structured H-bond network compared to room temperature hydration. Although within hydration shell positional and rotational correlations do not differ much even though NMR predicts difference in corresponding dynamics. But before concluding anything a clear comparison of corresponding partial structure factor [Cartailler 1991] is necessary [Bradl 1993] [Bradl 1994].

4.5   Normal Water and Heavy Water
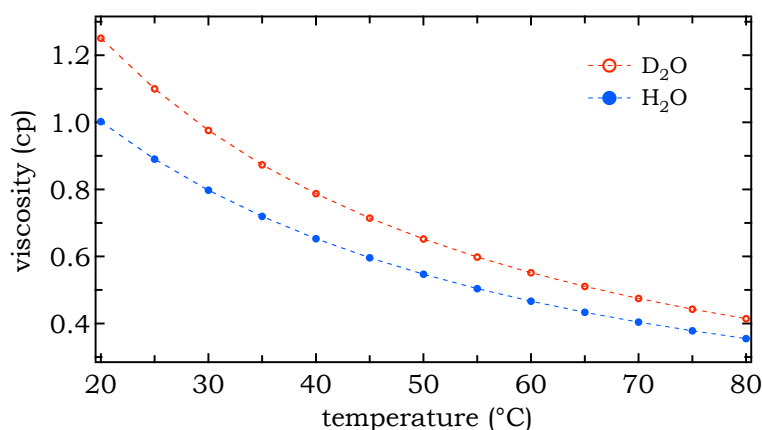
Figure 4.12: Viscosity of H_2O and D_2O as a function of temperature.

The principal objective of this work is to study the TAA solute and solvent dynamics. To study the solute dynamics, previously and also in this work, often D_2O is used as a solvent. Thus it is necessary to know the H_2O and D_2O properties. H_2O and D_2O are identical in view of their chemical properties but there exists some important differences. Having larger mass, D_2O shows stronger and more stable 'deuterium bond' than 'hydrogen bond' due to lower zero-point energy. Thus heavy water is comparably more ordered than normal water. Inevitably this more structured D_2O makes different hydration structure (H or D bond) around solutes through direct or indirect hydrophobic interaction [Lopez 1998] [Hummer 2000].

Hydrophobic effects differ from heavy water to light water. From experiments it is known that hydrocarbons are soluble more in D_2O than H_2O. This decreases as the solute size or temperature increases. It means that H_2O shows more hydrophobic effect than D_2O which is unexpected considering the stronger D-bond that D_2O have compared to H_2O. It is not explainable also from the surface tension because both of H_2O and D_2O have same surface tension. This apparent paradox can be solved by invoking the difference between D_2O and H_2O compressibility. As the temperature increases, the difference becomes less [Hummer 2000]. [Masakatsu 1996]

In case of dynamics the Hubbard-Onsager dielectric friction is larger in D_2O than in H_2O. This happens mainly due to the difference in viscosity. Thus solute dynamics (diffusion coefficients) is also decreased by 24% (figure 4.12).

A short summary of water and heavy water properties can be found in table 4.3[4,5,6]

Property	Data
Surface area ($\mathring{A}^2$)	8.84
Bond energy $(\frac{kJ}{mol\ bond})$	H_2O, 458.9 D_2O, 466.4
Boiling point ($^{\circ}C$)	H_2O, 100.00 D_2O, 101.42
Isothermal elasticity (GPa)	H_2O, 2.174 D_2O, 2.100
Adiabatic compressibility (GPa^{-1})	H_2O, 0.4477 D_2O, 0.4625
Isothermal compressibility (GPa^{-1})	H_2O, 0.4599 D_2O, 0.4763

---

[4]http://www.iapws.org/
[5]http://www.lsbu.ac.uk/water/data.html
[6]http://www.iwra.org/

Thermal conductivity $\left(\frac{W}{mK}\right)$	H_2O, 0.686
	D_2O, 0.636
Density $\left(\frac{kg}{m^3}\right)$	H_2O, 997.05
	D_2O, 1104.36
Dielectric constant $(25°C)$	H_2O, 78.4
	D_2O, 78.06
Enthalpy of formation	H_2O, -285.85 $\frac{kJ}{mol}$
	D_2O, -294.6 $\frac{kJ}{mol}$
Expansion coefficient $\left(\frac{1}{°C}\right)$	H_2O, 0.000253
	D_2O, 0.000172
Gibbs energy of formation $\left(\frac{kJ}{mol}\right)$	H_2O, -237.18
	D_2O, -243.44
Ionic dissociation constant $\left(\frac{mol}{l}\right)$	H_2O, 1.821×10^{-16}
	D_2O, 3.54×10^{-17}
Molar mass $\left(\frac{g}{mol}\right)$	H_2O, 18.015268
	D_2O, 20.027508
Molecular dimension	H_2O, O-H bond length 0.991 Å
	H_2O, H-O-H bond angle 105.5°
	D_2O, O-D bond length 0.970 Å
	D_2O, D-O-D bond angle 106°
pH/ pD	H_2O, 6.9996
	D_2O, 7.43
Shear modulus	H_2O, 2.44 GPa
Refractive index (real n and imaginary k)	H_2O, n 1.306169; k 0.300352153
	D_2O, n 1.342528; k 0.279696327
Shear modulus (adiabatic elasticity) (GPa)	H_2O, 2.44
	D_2O, 2.50
Specific heat capacity (C_p) $\left(\frac{J}{molK}\right)$	H_2O, 75.338
	D_2O, 84.67
Specific heat capacity (C_v) $\left(\frac{J}{molK}\right)$	H_2O, 74.539 $\frac{J}{molK}$
	D_2O, 84.42 $\frac{J}{molK}$
Speed of sound $\left(\frac{m}{s}\right)$	H_2O, 1496.7
	D_2O, 1399.2
Surface tension $\left(\frac{J}{m^2}\right)$	H_2O, 0.07198
	D_2O, 0.07187
Vapor pressure (kPa)	H_2O, 3.165
	D_2O, 2.734
Viscosity (dynamic) (mPa s)	H_2O, 0.8909
	D_2O, 1.095

Molar volume (cm^3)	H$_2$O, 18.0685
	D$_2$O, 18.1331
Zero point energy $(\frac{kJ}{mol})$	H$_2$O, 55.44
	D$_2$O, 40.54

Table 4.3: Different properties of H$_2$O and D$_2$O.

4.6   Conclusion

We can now make a brief summary of the previous result which are related to this work.

Based on the ability of modifying the solvent water structure, TBA$^+$ and TPA$^+$ are called 'structure maker' and TMA$^+$ as 'structure breaker' while for TEA$^+$ the two effects cancel each other. The results show that a weaker dependence of osmotic pressure, vapor pressure and activity coefficient on the length of the TAA$^+$ hydrocarbon chain for a particular halide anion series (ex: Bromide) compared to different anion effect in a particular cation series (ex: TBA$^+$). There is also a possibility of formation of ion-pair. From viscosity and conductivity measurement it is revealed that the water structure is differet for smaller and larger TAA cations which is further supported by neutron Diffraction data but no definitive conclusion is not drawn.

For TAA$^+$ dynamics at infinite dilution, the Stokes-Einstein relation (using calculated solute radius from density measurement) predicts better agreement with cation self translational diffusion coefficient D_{tr} (by NMR or conductivity measurements). There are also results for self and mutual D_{tr} at higher concentration by NMR, Tracer and optical diffusion technique. All these measurements show no other dynamics except the translations (even for large TAA cations like TBA$^+$). Some of the QENS studies suggest that the solvent water dynamics is slowed down a factor of 1.5-2 depending on the TAA cation and concentration of the solution.

5

Neutron Scattering Techniques

Contents

5.1   Introduction

This chapter deals with the basic neutron scattering theory and techniques which are used in this work. For details one can consult the following references [Squires 1988] [Bée 1988] [Mezei 1980] [Lovesey 1984]. It is important to note that the technical specification varies from spectrometer to spectrometer and here I present only the fundamental concept for them. All of the specified neutron scattering experiments mentioned here, are carried out in Laboratoire Léon Brillouin (LLB), CEA-CNRS, Saclay, France and Forschungsneutronenquelle Heinz Maier Leibnitz (FRM II), Garching, Germany. The details of the spectrometers can be found be on respective websites[1,2]

5.2   Neutrons

5.2.1   Properties

For decades neutrons (charge 0 and spin $\frac{1}{2}$) have been considered to be an useful probe for studying the condensed matter. Irrespective of the origin (whether from fission of a heavy nucleus in reactor or colliding high energy proton on heavy target in spallation source), neutrons are produced with very high velocity which is slowed down by repetitive collisions with a moderator at a certain temperature. The neutron velocity $\mathbf{v}$ follows the Maxwell distribution which can be written as

$$f(v) = 4\pi(\frac{m}{2\pi k_B T})^{\frac{3}{2}} v^2 e^{-\frac{mv^2}{2k_B T}}$$ (5.1)

with an energy (normally in units of meV)

$$E = \frac{1}{2}mv^2 = \frac{p^2}{2m} = \frac{\hbar^2 k^2}{2m}$$ (5.2)

where m is the neutron mass (1.66×10^{-24}g), $\mathbf{k}$ is neutron wave vector, $\mathbf{p}=\hbar\mathbf{k}$, k_B is Boltzmann constant and T is the temperature (in K). Like light, electrons or protons, the neutrons also show wave-particle duality. The wave length associated with the neutron can be written according to de Broglie relation

$$\lambda = \frac{2\pi\hbar}{mv}$$ (5.3)

---

[1]LLB: www-llb.cea.fr
[2]FRM II: http://www.frm2.tum.de
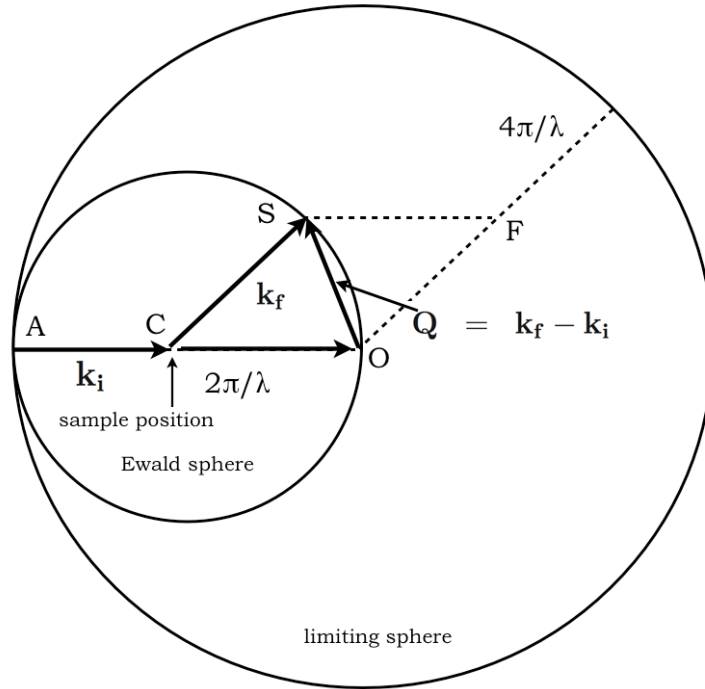
Figure 5.1: Ewald sphere construction.
Concept of reciprocal space: As sample orientation and detector position changes, the Ewald sphere also moves but always touches the limiting sphere.

Depending on the wavelength λ or energy E, neutrons can be classified into three different types: Cold ($\sim$6.16 Å, $\sim$2.16 meV, $\sim$25K), thermal ($\sim$1.69 Å, $\sim$28.4 meV, $\sim$330K) and hot neutrons ($\sim$0.689 Å, $\sim$172 meV, $\sim$2000K) [James 2000].

5.3 Basic Theory

5.3.1 Reciprocal Space

In scattering experiments it is common to work with the notation of reciprocal space. Thus it is important to properly understand how this concept works and what is its connection with real space phenomenon. Following is a brief description of figure 5.1 which explains it visually.

First consider the incident beam with wavelength λ is directed along **AO** ($\mathbf{k_i}$), fall on the sample under consideration which is at C and scatters in the direction **CS** ($\mathbf{k_f}$). In that case $\mathbf{Q}=\mathbf{k_f}-\mathbf{k_i}$ will be the direction of wave vector

transfer. Now if the scattered wave vector changes its direction i.e. if **CS** direction changes, **Q** also changes its direction and simultaneously changes its touching point on the surface of the sphere with radius $\frac{2\pi}{\lambda}$ centered at C. This sphere is called 'Ewald sphere'. In an experiment depending on the orientation of the sample (C) and detector (in the direction of **CS**), the Ewald sphere can move but always passes through the centre O, touching the 'limiting sphere' with radius $\frac{4\pi}{\lambda}$. The vector **Q** (in units $\frac{1}{length}$) is the reciprocal wave vector.

5.3.2 Scattering

In any neutron scattering experiments where incoming neutron beam interacts with a sample, it can be shown that during interaction with a nucleus the neutrons scatter isotropically and the whole interaction process of neutrons with sample nucleus can be characterized by a single parameter which is called scattering length. This is normally a complex number which has a real and an imaginary part. The imaginary part represents the absorption. For the rest of the discussion only the real part will be dealt and will be denoted by b. The value of b depends on the element nuclear spin state and on the nature of the nucleus of specific neutron-nucleus system. The scattering length b can be of two types, coherent scattering length (b_{coh}) and incoherent scattering length (b_{inc}). In case of b_{coh} the isotope and spin fluctuation are averaged while b_{inc} is calculated exactly from these fluctuations. For an element j, mathematically they are expressed as

$$
\begin{aligned}
b_{coh} &= \bar{b}_j \\
b_{inc} &= \sqrt{\bar{b_j^2} - \bar{b}_j^{\,2}}
\end{aligned}
\tag{5.4}
$$

In all neutron scattering experiment the scattered intensities are measured either as a function of transfer of wave-vector **Q** (difference between scattered and incident wave-vector) and in dynamics measurements as transfer of energy ω (difference in scattered and incident neutron energy, E_f and E_0 respectively) i.e.

$$
\begin{aligned}
\mathbf{Q} &= \mathbf{k_f} - \mathbf{k_i} \\
\Delta E &= \hbar\omega = E_f - E_0 = \frac{\hbar^2}{2m}(k_f^2 - k_i^2)
\end{aligned}
\tag{5.5}
$$

where k_f and k_i are the modulus of $\mathbf{k_f}$ and $\mathbf{k_i}$. Depending on the value of E_f there can be two distinct possibilities. The interaction can be either inelastic (when scattered neutron energy is not equal to incident neutron energy i.e. E_f

$\neq E_i$) or elastic (when scattered neutron energy is equal to incident neutron energy i.e. $E_f = E_i$) (figure 5.2). In case where $E_f \simeq E_i$ it is called quasi-elastic. All the dynamical studies which are going to be presented here, are performed in this condition.
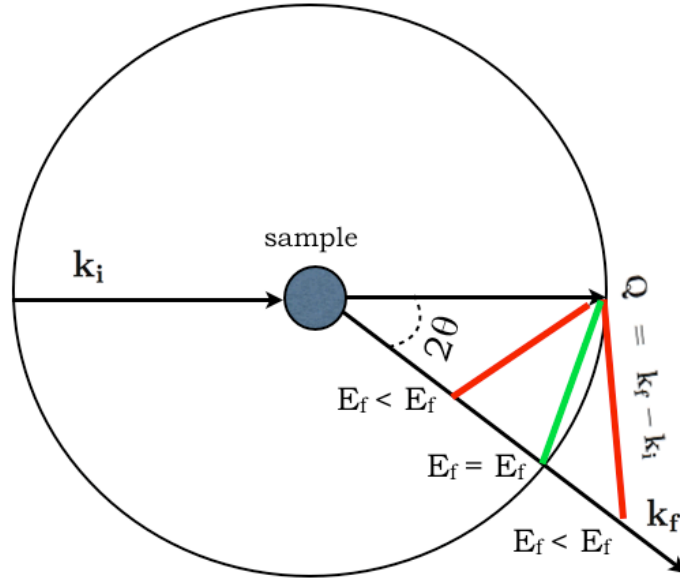
Figure 5.2: Elastic and inelastic scattering as incident wave vector scatters through an angle 2θ.
Different kinds of neutron scattering: After the collision with sample, the incident beam k_i scattered (denoted by k_f) and based on the final energy the scattering can be called elastic (green scattering wave vector Q) or inelastic (red scattering wave vector Q).

The measured quantity is the number of neutrons per unit time through a solid angle $d\Omega$ (in a given direction) with energy exchange $\hbar\omega = E_f - E_i$. This is called 'double differential cross-section' ($\frac{\partial^2\sigma}{\partial\Omega\partial\omega}$), where σ represents the scattering cross-section of the sample (in units of barn, 1 barn= 10^{-24}cm^2). In terms of coherent or incoherent scattering length, the scattering cross section can be defined as

$$\begin{aligned}\sigma_{coh} &= 4\pi\bar{b}^2 = 4\pi b_{coh}^2 \\ \sigma_{inc} &= 4\pi(\bar{b^2} - \bar{b}^2) = 4\pi b_{inc}^2\end{aligned} \qquad (5.6)$$

Now based on the assumption that there is no coupling between scattering

length and position of each nucleus, we take the thermal average of the positions $\mathbf{R_j}$ of all the sample nuclei (and also the spin states) and can write the double differential scattering cross-section as

$$
\begin{aligned}
\frac{\partial^2 \sigma}{\partial \mathbf{\Omega} \partial \omega} &= \frac{1}{2\pi N} \frac{k_f}{k_i} \sum_j \sum_{j'} b_j \bar{b}_{j'} \int_{-\infty}^{\infty} \langle e^{i\mathbf{Q}\cdot\mathbf{R_j}(t)} e^{-i\mathbf{Q}\cdot\mathbf{R_{j'}}(0)} \rangle e^{-i\omega t} dt \\
&= \frac{1}{2\pi N} \frac{k_f}{k_i} \Big(\sum_j \sum_{j'} b_{coh,j} b_{coh,j'} \int_{-\infty}^{\infty} \langle e^{i\mathbf{Q}\cdot\mathbf{R_j}(t)} e^{-i\mathbf{Q}\cdot\mathbf{R_{j'}}(0)} \rangle e^{-i\omega t} dt \\
&\quad + \sum_{j=j'} (b_{inc,j})^2 \int_{-\infty}^{\infty} \langle e^{i\mathbf{Q}\cdot\mathbf{R_j}(t)} e^{-i\mathbf{Q}\cdot\mathbf{R_j}(0)} \rangle e^{-i\omega t} dt \Big) \qquad (5.7)
\end{aligned}
$$

where N is the total number of atoms and using equation 5.6. Thus the total partial differential cross-section can be written as

$$
\frac{d^2 \sigma}{\partial \mathbf{\Omega} \partial \omega} = \left(\frac{d^2 \sigma}{\partial \mathbf{\Omega} \partial \omega} \right)_{coh} + \left(\frac{d^2 \sigma}{\partial \mathbf{\Omega} \partial \omega} \right)_{inc}
$$

If we now define $S_{coh}(\mathbf{Q}, \omega)$ and $S_{inc}(\mathbf{Q}, \omega)$ as the coherent and incoherent scattering function, in terms of atomic correlation, the scattering functions can be written as

$$
\begin{aligned}
S_{coh}(\mathbf{Q}, \omega) &= \frac{1}{2\pi} \int_{-\infty}^{\infty} \sum_j \sum_{j'} \langle e^{i\mathbf{Q}\cdot\mathbf{R_j}(t)} e^{-i\mathbf{Q}\cdot\mathbf{R_{j'}}(0)} \rangle e^{-i\omega t} dt \\
S_{inc}(\mathbf{Q}, \omega) &= \frac{1}{2\pi} \int_{-\infty}^{\infty} \sum_j \langle e^{i\mathbf{Q}\cdot\mathbf{R_j}(t)} e^{-i\mathbf{Q}\cdot\mathbf{R_j}(0)} \rangle e^{-i\omega t} dt \qquad (5.8)
\end{aligned}
$$

By taking the inverse Fourier transformation, we arrive at the respective intermediate scattering function in time domain

$$
\begin{aligned}
I_{coh}(\mathbf{Q}, t) &= \frac{1}{N} \sum_j \sum_{j'} \langle e^{i\mathbf{Q}\cdot\cdot\mathbf{R_j}(t)} e^{-i\mathbf{Q}\cdot\mathbf{R_{j'}}(0)} \rangle \\
I_{inc}(\mathbf{Q}, t) &= \frac{1}{N} \sum_j \langle e^{i\mathbf{Q}\cdot\mathbf{R_j}(t)} e^{-i\mathbf{Q}\cdot\mathbf{R_j}(0)} \rangle \qquad (5.9)
\end{aligned}
$$

From the above equations it is clear that coherent scattering originates due to the correlation between the positions of the nucleus j at time 0 and a different nucleus (that includes nucleus j) at time t while for incoherent scattering the correlation is calculated from the positions of same atom at different times.

Essentially because of this correlation among same and different nucleus, coherent scattering contains structural information as a function of time. On the other hand incoherent scattering comes from the same nucleus and normally is not able to provide any structural knowledge (figure 5.3).
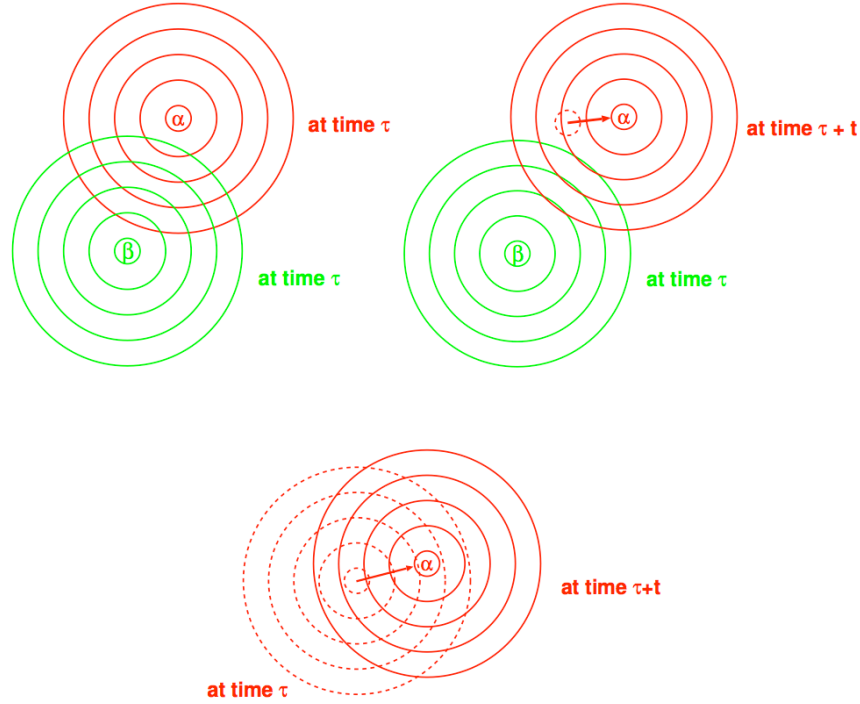
Figure 5.3: Origin of coherent and incoherent scattering. Pictorial representation of coherent and incoherent scattering: 1) upper left: coherent elastic scattering-interference of neutron waves from different atoms at same time; 2) upper right: coherent inelastic scattering-interference of neutron waves from different atoms at different times; 3) bottom: incoherent inelastic scattering-interference of neutron waves from the same atom at different time (after Gerald R. Kneller, Lecture B9, Hercules 2004).

Continuing from equation 5.9 if another fourier transformation is carried out in reciprocal space domain, one can eliminate the Q dependence and come to the real space by obtaining pair correlation and self correlation function

$$
\begin{aligned}
G(\mathbf{r}, t) &= \frac{1}{(2\pi)^3} \int_{-\infty}^{\infty} I_{coh}(\mathbf{Q}, t) e^{-i\mathbf{Q}\cdot\mathbf{r}} d\mathbf{Q} \\
G_{inc}(\mathbf{r}, t) &= \frac{1}{(2\pi)^3} \int_{-\infty}^{\infty} I_{inc}(\mathbf{Q}, t) e^{-i\mathbf{Q}\cdot\mathbf{r}} d\mathbf{Q}
\end{aligned}
\tag{5.10}
$$

The physical significance is as follows. Considering a particle at the origin at t=0, the probability for finding any particle in a volume $d\mathbf{r}$ around position $\mathbf{r}$ at time t is $G(\mathbf{r}, t)$ while $G_{inc}(\mathbf{r}, t)$ denotes the probability for the same particle to be in volume $d\mathbf{r}$ around position $\mathbf{r}$ at time t. Taking the integral over all the space, while $G(\mathbf{r}, t)$ gives the total number of particles in the system, $G_{inc}(\mathbf{r}, t)$ results in unity ($\int G(\mathbf{r}, t)d\mathbf{r} = N$ and $\int G_{inc}(\mathbf{r}, t)d\mathbf{r} = 1$).

Thus the different quantities $S(\mathbf{Q},\omega)$, $I(\mathbf{Q},t)$ and $G(\mathbf{r},t)$ provide the same information. The difference is that while $S(\mathbf{Q},\omega)$ and $I(\mathbf{Q},t)$ work in reciprocal space and either in energy or in time domain; $G(\mathbf{r},t)$ is a common tool for real space investigation. All of these three functions are connected by Fourier (or inverse) transformation.

5.4   Techniques

In this section the basics of the neutron scattering techniques (for structural and dynamic studies) will be presented.

5.4.1   Structural Study

5.4.1.1   Small-Angle Scattering

For static structural study, one of the widely used technique is Small Angle Neutron Scattering (SANS) (other is diffraction). The size of the investigated objects can vary from micrometer to the order of angstrom. During 1930s, the idea of SANS first came to Guinier while performing X-ray diffraction study. About 30 years later, the first SANS instrument was begun to be developed. The beauty of SANS lies in the deuteration method when compared to the other small angle techniques (x-ray or light scattering). This can be achieved by contrast variation technique where parts of the system are deuterated with an added advantage of measuring density fluctuation.

Principle   The SANS spectrometer is comprised of four basic parts i) monochromatization of incoming neutrons (using velocity selector), ii) collimating by two slots placed near to source and sample position, iii) scattering as interacts with the sample and iv) detection at the detector at a range of scattering angle (see figure 5.4). The collimation is decided prior to the experiment keeping the balance between size of the incident neutron beam and the flux. In order to prevent the observed intensity dominated by the transmitted intensity, a beam stop is placed in front of the detector in the direction of direct beam. Depending on the collimation, sample to detector distance and neutron wavelength the beam-stop position vary.
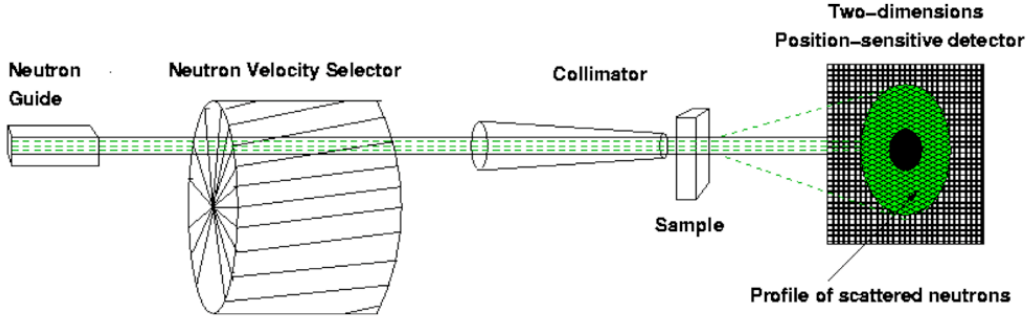
Figure 5.4: Schematic diagram of Small Angle Neutron Scattering spectrometer.
In Small angle neutron scattering spectrometer, after the collimation the incident neutron beam is scattered by the sample and intensity is recorded at the detector at various scattering angles (after IAEA research report 2006).

Data Treatment The SANS data treatment consists of several steps and the resultant intensity is in units of cm^{-1}. Let us suppose that the sample under consideration, is interacted by a incident neutron flux of Φ_i to produce a scattered flux Φ_{scat} in $\mathbf{Q}$ direction for a time t. Assuming the sample volume as V, thickness as d and Tr as Transmission, the intensity per unit volume $\mathcal{I}$ can be written in terms of double differential cross section as

$$\mathcal{I} = \frac{1}{V}\frac{d\sigma}{d\Omega} = \frac{\Phi_{scat}}{\Phi_i.\Delta\Omega Tr.d.t} \tag{5.11}$$

Thus normally for a sample which is under the beam, the scattering cross section in unit volume can be expressed according to

$$(\frac{d\sigma}{d\Omega})_{sample} = \frac{1}{d_{sample}\Phi_i}[\frac{\mathcal{I}_{sample}}{\Delta\Omega.Tr.t_{sample}} - \frac{\mathcal{I}_{EC}}{\Delta\Omega.Tr.t_{EC}}] \tag{5.12}$$

where subscript EC refers to the case when there no solution and the measurement is solely with empty can. Of course this is not in absolute units (cm^{-1}). To get in absolute units this needs to be corrected by a standard (equation 5.13). Usually bulk water (or vanadium) is used because water scattering intensity does not depend on the value of $\mathbf{Q}$.

$$(\frac{d\sigma}{d\Omega})_{sample} = \frac{\mathcal{I}_{sample}}{\mathcal{I}_{standard}}(\frac{d\sigma}{d\Omega})_{standard} \tag{5.13}$$

One other important quantity is the normalization factor which comes because of the effect of attenuator. The renormalization is expressed by the following equation

$$\mathcal{F}_{norm} = \frac{\frac{\mathcal{I}_{H_2O}}{Mon} - \frac{T_{H_2O+EC}}{T_{EC}} \frac{\mathcal{I}_{EC}}{Mon}}{\frac{I_{EB}}{Att.Mon}.Tr.d\frac{d_{H_2O}}{d_{EB}}} \tag{5.14}$$

where EB refers empty beam, Att is the attenuator factor measured by a highly scattering sample (like graphite) in presence or absence of a attenuator, and Mon refers to the Monitor count. Thus considering all these effects into account, the final expression becomes

$$\begin{aligned}\mathcal{I}_{sample}(cm^{-1}) &= \mathcal{F}_{norm}\mathcal{I}_{sample} \\ &= \frac{\frac{1}{d_{sample}\Phi_i}\left[\frac{\mathcal{I}_{sample}}{\Delta\Omega.Tr.t_{sample}} - \frac{\mathcal{I}_{EC}}{\Delta\Omega.Tr.t_{EC}}\right]}{\frac{1}{d_{H_2O}\Phi_i}\left[\frac{\mathcal{I}_{H_2O}}{\Delta\Omega.Tr.t_{H_2O}} - \frac{\mathcal{I}_{EC}}{\Delta\Omega.Tr.t_{EC}}\right]}\end{aligned} \tag{5.15}$$

5.4.1.2 Diffraction

The other technique used in this work to study the structures is the Neutron Diffraction (ND). The diffraction experiments are performed on G 4-1 spectrometer (figure 5.5) of Laboratoire Léon Brillouin (LLB), CEA-CNRS, Saclay, France. Here is a very brief description of the spectrometer. G 4-1 is a two axis powder diffractometer with a graphite monochromator. The incoming neutron beam wavelength can be varied between 2.43 Å to 5.5 Å covering a diffusion angle (2θ) from 3° to 105° with an angular resolution of 0.02°. One multi-detector with 800 cells (of BF_3) distributed over 80°, detects the diffracted neutrons and measures the total scattered intensity S(Q) [S(Q)=$\int_{-\infty}^{\infty} S(Q,\omega)d\omega$, S(Q) is the sum of coherent and incoherent contribution [Squires 1988] [Bée 1988]].

5.4.2 Dynamics Study

5.4.2.1 Time of Flight

The most known quasi-elastic neutron scattering technique for dynamics measurement is the Time of Flight (TOF) technique. By this technique, the scattering function is measured as function of energy transfered due to the interaction of the neutrons with sample [Bée 1988].
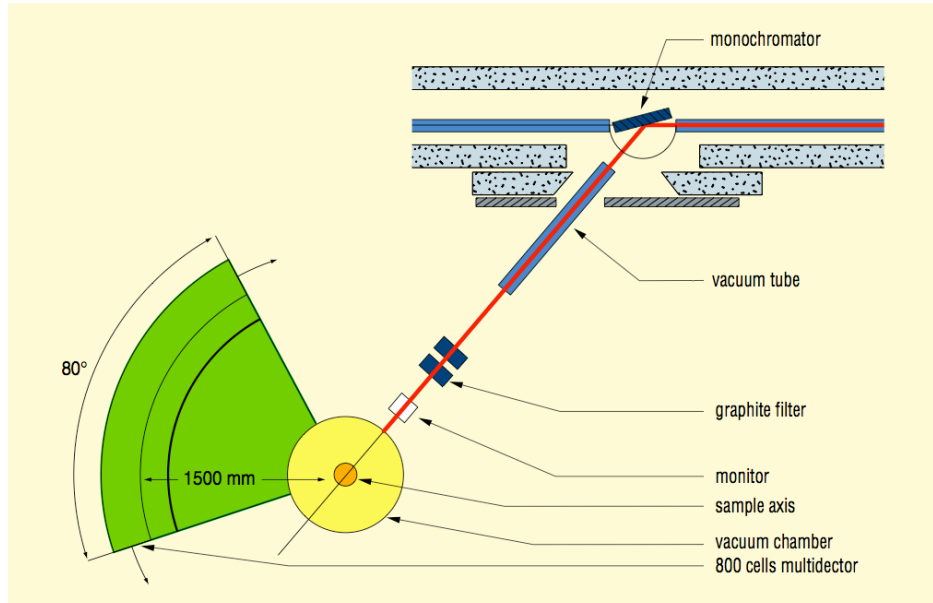
Figure 5.5: Schematic diagram of Neutron Diffractometer. Incident neutron beam is scattered by the sample and intensity is recorded at the detector at various scattering angles (www-llb.cea.fr)

Principle First I will present the basic geometry of TOF spectromter. A schematic diagram can be found in figure 5.6.

The basic idea for TOF is to record the energy transfer which is characterized by the velocity of scattered neutrons. This is calculated from the flight time over a known distance. First the incident neutron beam is passed through a set of choppers where they are monochromatized (keeping different neutron pulses apart and selecting a particular wavelength following the relation $\lambda = \frac{h}{mv} = \frac{h}{m\frac{L_{chop}}{\tau_{chop}}}$, where v is neutron velocity, L_{chop} the length of the choppers and τ_{chop} is the flight time between choppers). It is important to note that as the incoming neutron wavelength is increased, the spectrometer resolution also increases but at the cost of intensity (figure 5.7). This is easy to understand from the Maxwellian distribution of velocity (or in other words by wavelength). As we move further from the peak of this distribution (equation 5.1) to a lower velocity, the number of neutrons with the desired wavelength quickly diminish.

Monochromatic neutron pulses fall on the sample under consideration. Then they are detected at an angle 2θ with a final energy equal (elastic) or not equal (inelastic or quasi-elastic) to the initial. In case of quasi-elastic ($E_f \simeq E_i$) or inelastic case ($E_f \neq E_i$), the energy transfer ω depends on the flight
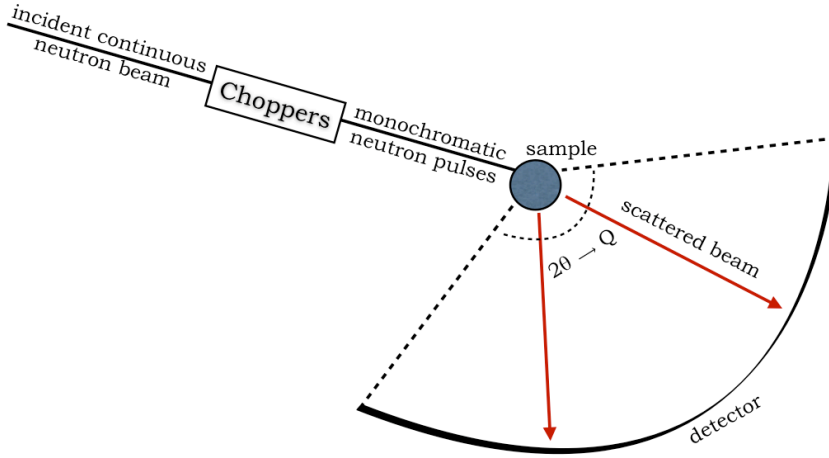
Figure 5.6: Time of Flight spectrometer.
Basic diagram of Time of Flight (TOF) technique. Monochromatic neutron pulses are generated from continuous incident neutron beam. After interaction with the sample, the neutrons are scattered through an angle 2θ. The detector records the neutrons coming with different wavelength as a function of time.

time between sample position and detector. This can be expressed as

$$
\begin{aligned}
\Delta E &= \hbar\Delta\omega = \frac{m(\Delta v)^2}{2} = \frac{mL_{TOF}^2}{2}\left(\frac{1}{t_{els}} - \frac{1}{t_{inels}}\right)^2 \\
&= \frac{mL_{TOF}^2}{2}\left(\frac{\Delta\tau_{TOF}}{t_{els}^2 + t_{els}\Delta\tau_{TOF}}\right)^2
\end{aligned}
\tag{5.16}
$$

where L_{TOF} is distance between sample and detector and τ_{TOF} is the difference between inelastic/ quasi-elastic (t_{inels}) and elastic (t_{els}) neutron flight time. The scattering angle 2θ can be converted to reciprocal wave-vector **Q**. Thus the detector signal is recorded as a function of **Q** (reciprocal space) and ω (energy space).
Now recalling equation 5.5 (figure 5.2), it follows that

$$
\frac{Q}{K_i} = \sqrt{2 - \frac{\hbar\omega}{E_i} - 2cos(2\theta)\sqrt{2 - \frac{\hbar\omega}{E_i}}}
\tag{5.17}
$$

where the transfer of momentum Q (due to interaction) is a function of both ω and 2θ (figure 5.8). The maximum value of $\Delta\omega$ can be $\frac{E_i}{\hbar\omega}$ because it can not go beyond the energy of the incoming neutrons. Figure 5.8 shows the span
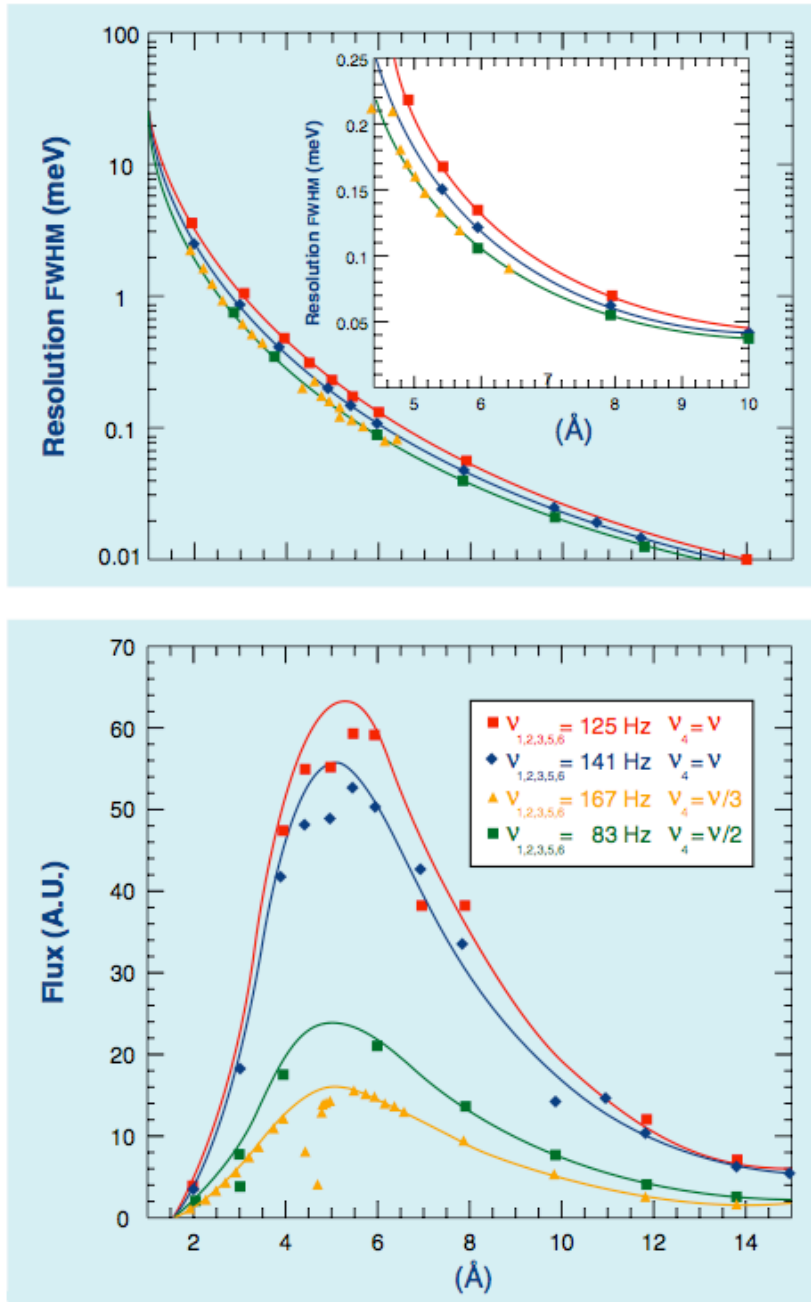
Figure 5.7: Plot of Resolution and Flux as a function of incident neutron wavelength of Mibemol TOF spectrometer. The resolution is a slowly varying function while the flux depends strongly on the wavelength. Here is an example for four frequencies of the 6 choppers. Except 4 (this is anti-over lap chopper), the frequencies of all other choppers are indicated in the figure (www.llb-cea.fr).
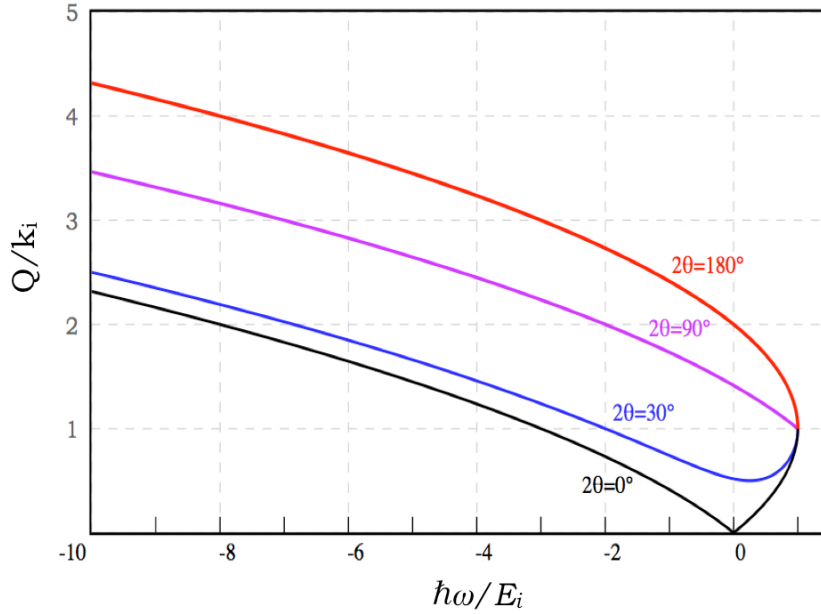
Figure 5.8: Span of (Q, ω) as a function of initial energy E_i for different scattering angle (2θ).

of (Q, ω) domain for a particular initial energy E_i for a scattering angle (2θ) ranging from 0 to π. For TOF data analysis, the S (Q, ω) as a function of different Q values and varying energy transfer (ω) is of interest. It is obvious that since the energy loss of the neutrons during interaction with a nucleus can not exceed the initial energy (which is E_i), the upper bound (limit) of ω is $\frac{E_i}{\hbar}$ (figure 5.8).

As the energy transfer $\Delta\omega$ increases, different domains (modes) are observable in the scattered signal (figure 5.9). The strong elastic (ideally a delta function) peak can be seen at ΔE=0. At the region $E_f \simeq E_i$ different kinds of motion (translational or rotational) can be detected. Much far from elastic/ quasi-elastic domain, the inelastic zone exist. The vibrational motion energy can be analyzed in this zone.

Data Treatment   TOF data treatment consists of several steps. The basics is presented here. Before any data treatment the bad detectors are removed from the raw data. During this time the neutrons counts per time channel are transformed to neutron counts per unit energy. The spectra is then regrouped according to the choice that determines the value Q. Then the energy-binning is carried out to have equidistant energy bins for the spectra. This is important for the last part of the data analysis where a proposed model is convoluted with
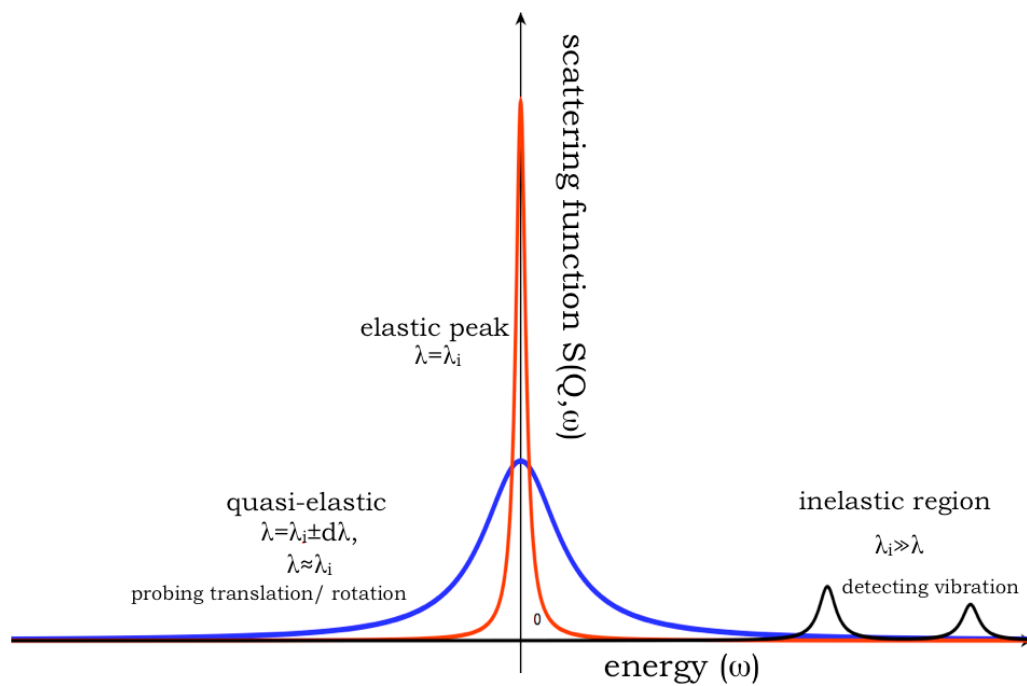
Figure 5.9: Different energy regimes in TOF spectra.
Different energy regions are probed in TOF measurement. The elastic peak (red) is a delta function which is broadened by experimental resolution. The dynamical studies are carried out in quasi-elastic part (blue) and in inelastic domain (black) where vibration motion can be seen. the λ is the recorded wavelength of the neutron at the detector.

the resolution function for comparing with sample spectra. The resolution is normally measured by vanadium which is also used to correct the detector efficiencies.

5.4.2.2 Spin Echo

The neutron spin echo (NSE) technique allows to measure the intermediate scattering function $I(Q,t)$ and thus the dynamics is measured directly as a function of time. The idea was first introduced by Ferenc Mezei in 1972 and subsequently the first NSE spectrometer was started to be built in Institut Laue-Langevin, Grenoble in January 1973.

The basics of NSE (with resonance option) will be demonstrated here. Details can be found in [Mezei 1980] [Lechner 2006] [Bée 1988].

Larmor Frequency As stated before, neutrons have spin $1/2$. It is well known that when a particle travels through magnetic field inclined with a certain angle θ, it starts to precess around the direction of magnetic field. The dynamics of this spin can be explained as

$$\frac{d\mathbf{J}}{dt} = \gamma \mathbf{J} \times \mathbf{B} \tag{5.18}$$

where $\mathbf{J}$ is the angular momentum vector of the spin which precesses around the magnetic field $\mathbf{B}$ with a frequency (called Larmor frequency) $\omega = |\gamma|$ B. γ is the gyromagnetic ratio. In NSE experiment if we imagine, when a polarized neutron passes through its arm (with magnetic field B), the total angular displacement it covers is ϕ; then $\phi = \omega t = |\gamma|$ Bt $= |\gamma| B \frac{L}{v}$ (L is the total linear displacement and v is velocity of neutron, figure 5.10).

Principle We start by considering the basic geometry of the Spin Echo spectrometer which is briefly illustrated in figure 5.11. Let us suppose that the incident neutrons comes with a distribution of wavelength $f(\lambda_i)$ having peak at λ_0 and enters in the first arm. Now because of the magnetic field B_0 in the first arm, the spins start to precess about the direction of B_0. The precession of the neutrons over a fixed path length, depends on its linear velocity. For example a faster neutron will have less precession than a slower neutron for a definite path length common to both of them. Next assuming that after a elastic collision between neutrons and samples, the neutrons enters into second arm where the applied magnetic field B_1 is in opposite direction keeping its wavelength $f(\lambda_i)$ unchanged. Thus again the neutron spins precess around B_1 but in opposite direction and come back to its initial state.
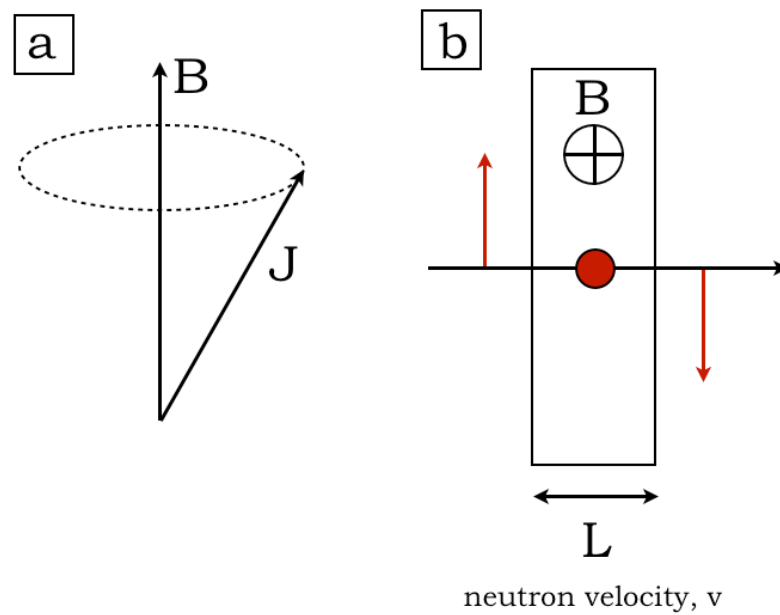
Figure 5.10: Larmor frequency.
(a) Angular momentum vector of the spin **J** precesses around the magnetic field **B** with a frequency called Larmor frequency ω. (b) the total angular displacement it covers is $\phi=\omega t=|\gamma|B\frac{L}{v}$ (section 5.4.2.2).
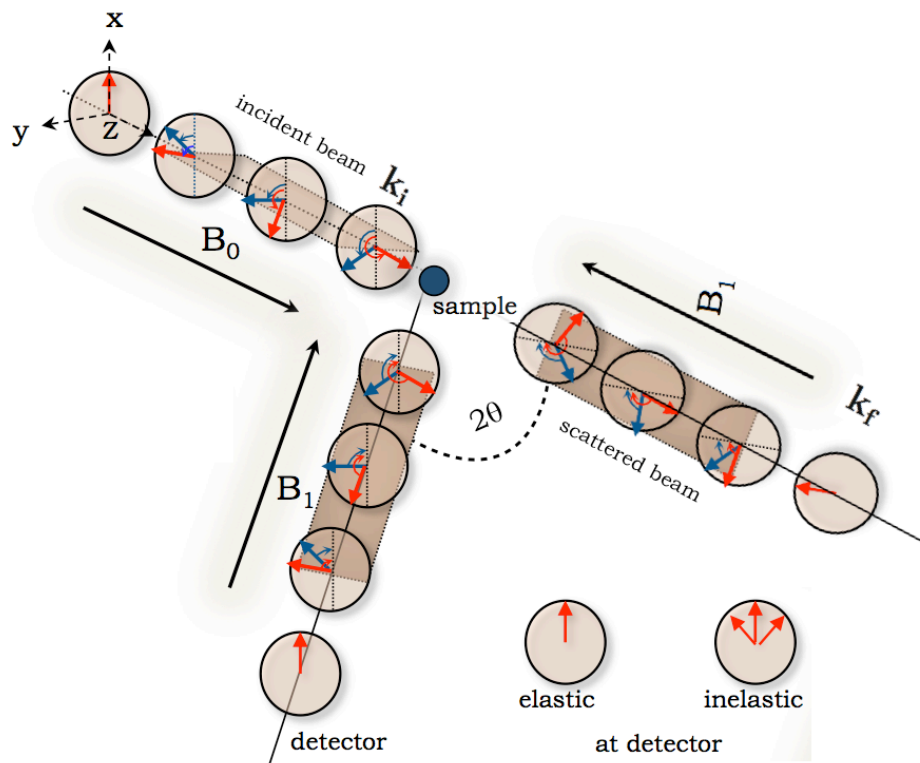
Figure 5.11: Classical Neutron Spin Echo technique.
The classical neutron spin echo spectrometer: Two opposite direction magnetic field are applied in two spectrometer arms. In elastic collisions the neutron spin precession in two arms are exactly equal but in opposite direction. Thus no deflection in spin direction is observed at the detector. In inelastic collision spin direction deflects due to the energy transfer between neutrons with sample nucleus (modified figure from the presentation by S. Longeville).

Now let us assume the total precession angles covered in the first and second arm are ϕ_1 and ϕ_2. Recalling the concept of Larmor precession, they can be expressed as

$$
\begin{aligned}
\phi_1(\lambda_i) &= \frac{\gamma m \lambda_i}{h} \int B_0 dz = 2\pi N_{+,\lambda_0} \frac{\lambda_i}{\lambda_0} \\
\phi_2(\lambda_i) &= \frac{\gamma m \lambda_i}{h} \int B_1 dz = -2\pi N_{-,\lambda_0} \frac{\lambda_i}{\lambda_0}
\end{aligned}
\tag{5.19}
$$

where the integration is over the length of the each spectrometer arm and N_{+,λ_0} and N_{-,λ_0} are the number of positive and negative (clockwise or anti-clockwise) spin precision in first and second arm due to change in magnetic field direction. Thus total change in precession angle of neutron spin is

$$
\begin{aligned}
\phi_1(\lambda_i) + \phi_2(\lambda_i) &= (2\pi N_{+,\lambda_0} \frac{\lambda_i}{\lambda_0}) + (-2\pi N_{-,\lambda_0} \frac{\lambda_i}{\lambda_0}) \\
&= 2\pi \frac{\lambda_i}{\lambda_0} (N_{+,\lambda_0} - N_{-,\lambda_0})
\end{aligned}
\tag{5.20}
$$

The echo point is achieved when $\phi_1(\lambda_i) + \phi_2(\lambda_i)$ is zero. This implies that at this condition the total magnetic field path integral in one arm is equal to the other arm of the spectrometer (i.e. $\int B_0 dz = \int B_1 dz$) and there is no dependence on the wavelength of the incident neutron. Let us suppose the incident neutron with wavelength λ_i changes its wavelength of an amount $d\lambda$ due to the interaction. Obviously wavelength λ_i has a distribution (denoted by $f(\lambda_i)$ and we suppose the probability that λ_i is changed by an amount $d\lambda$ is p($\lambda_i, d\lambda$). It can be shown that to note that p($\lambda_i, d\lambda$) in energy domain is equal to the scattering function S($\mathbf{Q}, \omega$) [Lechner 2006]. In case of neutron beam, the average beam polarization can be written as

$$
\bar{P} = \int_0^\infty f(\lambda_i) \int_{\lambda_i}^\infty p(\lambda_i, d\lambda) cos(\phi(\lambda_i, d\lambda)) d\lambda_i d(d\lambda))
\tag{5.21}
$$

Here $\phi(\lambda_i, d\lambda)$ is the total change in precession angle (change in first and second arm, $\phi_1(\lambda_i) + \phi_2(\lambda_i)$). In this case where the incident wavelength is also changed due to quasi-elastic interaction the total change in precession angle can be written as

$$
\begin{aligned}
\phi(\lambda_i, d\lambda) &= (2\pi N_{+,\lambda_0} \frac{\lambda_i}{\lambda_0}) + (-2\pi N_{-,\lambda_0} \frac{\lambda_i + d\lambda}{\lambda_0}) \\
&= 2\pi \frac{\lambda_i}{\lambda_0} (N_{+,\lambda_0} - N_{-,\lambda_0}) - 2\pi N_{-,\lambda_0} \frac{d\lambda}{\lambda_0}
\end{aligned}
\tag{5.22}
$$

If equation 5.22 and 5.20 are compared side by side, it is clear that the first part of the last expression becomes 0 at echo point condition i.e. when path integral of the magnetic field of first and second arm becomes equal. In that case

$$\phi(\lambda_i, d\lambda) = -2\pi N_{-,\lambda_0} \frac{d\lambda}{\lambda_0} = \frac{\gamma m d\lambda}{h} \int B_0 dz \qquad (5.23)$$

Taking all of these factors into account along with the condition of quasi-elastic interaction where change in wavelength ($d\lambda$) is much smaller than the incident (λ_i), we can rewrite [Lechner 2006] equation 5.21 as

$$\bar{P} \approx \int_0^\infty f(\lambda_i) \int_{-\infty}^\infty S(\mathbf{Q}, \omega) cos(\omega \tau_{NSE})) d\lambda d(d\omega)) \qquad (5.24)$$

where τ_{NSE} is the spin-echo time which is proportional to the third power of the wavelength λ_i ($\tau_{NSE} = \frac{m^2 \gamma \int B dz}{2\pi h^2} \lambda_i^3$) and estimates the real time t. In equation 5.24 taking the ratio of polarization at time t and t=0, we get the expression of normalized I(Q,t). so finally the expression of polarization becomes

$$I(Q, t) = \frac{\bar{P}(Q, t)}{\bar{P}(Q, t = 0)} = \frac{\int_{-\infty}^\infty S(\mathbf{Q}, \omega) cos(\omega, \tau_{NSE}) d(d\omega)}{\int_{-\infty}^\infty S(\mathbf{Q}, \omega) d(d\omega)} \qquad (5.25)$$

Data Treatment Let us suppose the total scattered intensity is N(Q). This N(Q) is the sum of coherent $A_{coh}(Q)$ and incoherent contribution A_{inc}. Note that the coherent contribution $A_{coh}(Q)$ depends on Q while ideally the incoherent contribution A_{inc} is independent of the value Q. The speciality of NSE is that taking the advantage of polarization analysis, it is possible to decouple the coherent and incoherent signal. From the principle of NSE technique [Mezei 1980]

$$\begin{aligned} \bar{P}(Q, t = 0) &= \frac{A_{coh}(Q) - \frac{1}{3} A_{inc}}{N(Q)} \\ N(Q) &= A_{coh}(Q) + A_{inc} \end{aligned} \qquad (5.26)$$

where $P(Q, t = 0)$ is overall polarisation of the scattered beam. The '$-\frac{1}{3}$' factor in the incoherent contribution comes because neutron spin changes its direction after colliding with the sample. The treatment is relatively straight forward to carry out. Thus the incoherent signal which is recorded in NSE is

a factor of 3 less than the actual incoherent signal (this is actually measured by TOF).

The data treatment for NSE is relatively simpler than TOF. The $I(Q,t)$ (normalized by definition) is corrected by the spectrometer resolution in the following way

$$I(Q,t) = \frac{\bar{P}(Q,t)}{\bar{P}(Q,t=0)} \frac{\bar{P}_{res}(Q,t=0)}{\bar{P}_{res}(Q,t)} \tag{5.27}$$

where subscript 'res' refers to resolution.

Now as discussed earlier in this section (equation 5.26) the $I(Q,t)$ (normalized by definition) is calculated by taking the ratio of the average polarization at time t and t=0 ($\frac{\bar{P}(Q,t)}{\bar{P}(Q,t=0)}$).

$$I(Q,t) = \frac{\bar{P}(Q,t)}{\bar{P}(Q,t=0)} = \frac{A_{coh}(Q)I'_{coh}(Q,t) - \frac{1}{3}A_{inc}I'_{inc}(Q,t)}{A_{coh}(Q) - \frac{1}{3}A_{inc}} \tag{5.28}$$

where, by construction, $I(Q,t)$ is a normalised function in the time domain, as are $I'_{coh}(Q,t)$ and $I'_{inc}(Q,t)$.

5.5 Analysis of Structure and Dynamics

5.5.1 Structure

For static structure analysis small angle neutron scattering (SANS) is considered to be an important tool. Before going into the detailed technical discussion in the next segment, here is the basics of SANS data analysis [Grillo 2008]. The SANS concept works with the idea of scattering length density (SLD) ρ which averages the atomic coherent lengths of the scatterers according to $\rho(r) = \sum_j \rho_j(r)b_{coh,j}$ (ρ_j is the SLD for an atom j).

5.5.1.1 Without Interaction Among Scatterers

Let us assume that when a neutron collides with an element in a system, the scattering process is not a function of other scatterer. Then the total scattering amplitude will be a sum of all of them. Proceeding with this, the measured total intensity I($\mathbf{Q}$) per unit volume of the sample is then

$$\begin{aligned}
\mathcal{I}(Q) &= \frac{1}{V}\langle \int_{V,V} \rho(\mathbf{r})\rho(\mathbf{r}')e^{-i\mathbf{Q}\cdot(\mathbf{r}-\mathbf{r}')}d\mathbf{r}d\mathbf{r}'\rangle \\
&= \frac{1}{V}\int_{V,V} \delta\rho(\mathbf{r})\delta\rho(\mathbf{r}')e^{-i\mathbf{Q}\cdot(\mathbf{r}-\mathbf{r}')}d\mathbf{r}d\mathbf{r}' \tag{5.29}
\end{aligned}$$

Here $\delta\rho(\mathbf{r})$ is the fluctuation of $\rho(\mathbf{r})$ about a median value $\bar{\rho}$ (The median value $\bar{\rho}$ contributes zero at $\mathbf{Q} > 0$. Now considering a two component system where the system consists of solute and solvent, let us suppose the respective SLDs are $\rho_{solute}(\mathrm{r})$ and $\rho_{solvent}(\mathrm{r})$. Equation 5.29 then can be further simplified as

$$
\begin{aligned}
\mathcal{I}(Q) &= \frac{(\rho_{solute} - \rho_{solvent})^2}{V} \int_{V,V} e^{-i\mathbf{Q}\cdot(\mathbf{r}-\mathbf{r}')} d\mathbf{r} d\mathbf{r}' \\
&= \frac{(\Delta\rho)^2}{V} \int_{V,V} e^{-i\mathbf{Q}\cdot(\mathbf{r}-\mathbf{r}')} d\mathbf{r} d\mathbf{r}'
\end{aligned}
\tag{5.30}
$$

where $\Delta\rho$ is the difference in SLD between solute and solvent matrix. Extrapolating the above condition for a N number of solutes of volume V_{solute}, one arrives

$$
\mathcal{I}(Q) = \frac{V_{solute}^2}{V} N \Delta\rho^2 P(\mathbf{Q})
\tag{5.31}
$$

$P(\mathbf{Q})$ $(= \frac{1}{V_{solute}^2}(\int_{V_{solute}} e^{-i\mathbf{Q}\cdot\mathbf{r}} d\mathbf{r})^2)$ is generally called the particle form factor (as it describes the geometry of the particle) and becomes 1 as Q tends to 0.

5.5.1.2   With Interaction Among Scatterers

In case, where the particle is itself a complex entity and shows correlation among its constituent scatters; the individual position vector of each scatterer becomes important. Let us take the particle centre of mass (CoM) is at $\mathbf{r}_j$ and thus for each of its constituent scatterer we can write $\mathbf{r} = \mathbf{r}_j + \mathbf{u}$ (where $\mathbf{u}$ is the distance from CoM for individual scatterer). Using this condition, the measured intensity per unit volume becomes

$$
\begin{aligned}
\mathcal{I}(Q) &= \frac{1}{V}\langle \int_{V,V} \rho(\mathbf{r})\rho(\mathbf{r}')e^{-i\mathbf{Q}\cdot(\mathbf{r}-\mathbf{r}')} d\mathbf{r} d\mathbf{r}'\rangle \\
&= \frac{1}{V}\langle [\int_{V_{solute}} \sum_r \rho(\mathbf{r})e^{-i\mathbf{Q}\cdot\mathbf{r}} d\mathbf{r}][\int_{V_{solute}} \sum_{r'} \rho(\mathbf{r}')e^{i\mathbf{Q}\cdot\mathbf{r}'} d\mathbf{r}']\rangle \\
&= \frac{1}{V}\langle [\int_{V_{solute}} \sum_r \rho(\mathbf{r})e^{-i\mathbf{Q}\cdot\mathbf{r}_j}e^{-i\mathbf{Q}\cdot\mathbf{u}} d\mathbf{r}][\int_{V_{solute}} \sum_{r'} \rho(\mathbf{r}')e^{i\mathbf{Q}\cdot\mathbf{r}'_j}e^{i\mathbf{Q}\cdot\mathbf{v}} d\mathbf{r}']\rangle
\end{aligned}
\tag{5.32}
$$

In case where interactions are identical, the product of the statistical average is equal to the statistical average of the product. Finally we can write

$$\mathcal{I}(Q) = \frac{N}{V}\langle[\frac{\sum_j \sum_{j'} e^{-i\mathbf{Q}\cdot(\mathbf{r}_j-\mathbf{r}_{j'})}}{N}][\int_{V_{solute}}\int_{V_{solute}}\rho(\mathbf{r})\rho(\mathbf{r}')e^{-i\mathbf{Q}\cdot(\mathbf{u}-\mathbf{v})}d\mathbf{r}d\mathbf{r}']\rangle$$

Obviously as per the assumption the first part is about the particle CoM correlation. It describes the correlation between particle CoM. Technically it is termed as structure factor S($\mathbf{Q}$). The exponential in the second term can be identified as the particle form factor which talks about the geometry as explained before. Thus the final expression is written as

$$\mathcal{I}(Q) = \frac{V_{solute}}{V}N(\Delta\rho)^2 S(\mathbf{Q})P(\mathbf{Q}) \qquad (5.33)$$

where $\frac{N}{V}$ is the solution concentration.

5.5.2 Dynamics

5.5.2.1 Atomic Motion

The dynamics is hidden in energy dispersion. In case of analysis of dynamics usually we decompose total intensity into various motions assuming each of the motions do not affect other. This is based on two assumptions where the first one says that intramolecular vibration is not affected by rotational motion or lattice vibration. Usually the intramolecular vibration is much higher in energy ($\sim$100 meV) and falls in the inelastic domain while our main interest is in quasi elastic which is in order of meV. Thus the first assumption is a feasible approximation to consider. The second assumption is less legitimate. Here we assume there is no coupling between different kinds of motions - translational, rotational and vibrational. Based on these two assumptions [Bée 1988], the decomposing of total intensity is done. It must be mentioned that these decoupling of motion is possible if energy and momentum transfer follow the classical approximations - that is i) $\hbar\omega << \frac{k_B T}{2}$ and ii) $\frac{\hbar^2 Q^2}{2m} << \frac{k_B T}{2}$. In these approximations, the scattering function is symmetrical over Q and ω i.e. $S(Q,\omega) = S(-Q,-\omega)$. Obviously at low temperature regime this approximation is no more valid and to satisfy detailed balanced condition, the scattering function is multiplied by the Boltzmann factor ($e^{-\frac{\hbar\omega}{2k_B T}}$) [Squires 1988] [Bée 1988]. The detailed analysis and its application in real system will be carried in the result section. Only the basic idea will be introduced here. To make the task simpler, only one type of atom will be considered and the incoherent scattering function will be discussed.

If we start from the time domain, the intermediate scattering function $I_{inc}(Q,t)$ comes into play. Based on the previous discussion the total $I_{inc}(Q,t)$ can be written as

$$I_{inc}(\mathbf{Q},t) = \frac{1}{N}\sum_j \langle e^{i\mathbf{Q}\cdot\mathbf{R_j^{tr}}(t)}e^{-i\mathbf{Q}\cdot\mathbf{R_j^{tr}}(0)}\rangle\langle e^{i\mathbf{Q}\cdot\mathbf{R_j^{rot}}(t)}e^{-i\mathbf{Q}\cdot\mathbf{R_j^{rot}}(0)}\rangle$$

$$\langle e^{i\mathbf{Q}\cdot\mathbf{R_j^{vib}}(t)}e^{-i\mathbf{Q}\cdot\mathbf{R_j^{vib}}(0)}\rangle$$

$$= I_{inc}^{tr}(\mathbf{Q},t)I_{inc}^{rot}(\mathbf{Q},t)I_{inc}^{vib}(\mathbf{Q},t) \tag{5.34}$$

In energy domain, we can have the same information from the $S_{inc}(\mathbf{Q},t)$. Taking the Fourier transformation of equation 5.9, we arrive

$$S_{inc}(Q,\omega) = S_{inc}^{tr}(Q,\omega)\otimes S_{inc}^{rot}(Q,\omega)\otimes S_{inc}^{vib}(Q,\omega) \tag{5.35}$$

Note that the expression of $S_{inc}(\mathbf{Q},\omega)$ are not a simple product of different motions (translational, rotational or vibrational) like $I_{inc}(Q,t)$ but convoluted with each other. Recalling again the fact that the vibrational energy is much higher and can be found in inelastic domain while we are interested in the quasi elastic zone, the equation 5.34 and 5.35 are written as

$$I_{inc,j}(\mathbf{Q},t) = I_{inc,j}^{tr}(\mathbf{Q},t)I_{inc,j}^{rot}(\mathbf{Q},t)e^{-\frac{1}{3}\langle u^2\rangle Q^2} \tag{5.36}$$

$$S_{inc}(\mathbf{Q},\omega) = [S_{inc}^{tr}(\mathbf{Q},\omega)\otimes S_{inc}^{rot}(\mathbf{Q},\omega)]e^{-\frac{1}{3}\langle u^2\rangle Q^2} \tag{5.37}$$

where $\langle u^2\rangle$ is the mean square vibrational displacement of atoms. The appearance of the exponential ($e^{-\frac{1}{3}\langle u^2\rangle Q^2}$) term is due to the fact that vibrational energy takes a shape of Gaussian distribution in quasi elastic domain and this is called Debye-Waller factor. In Time of flight measurement the slope of the logarithm of scattered intensity ($\ln\int_{d\omega} S(Q,\omega)d\omega$) (in quasi-elastic region) at a particular Q, is equal to $-\frac{\langle u^2\rangle}{3}$.

5.5.2.2 Modeling of Atomic motion

In the previous section the decoupling of different motions is shown. Here I show how the basic modeling of various motions (translational, rotational etc) is done. Because in the quasi-elastic domain, the vibrational motion is absent and takes a Gaussian shape; only translational and rotational motions are needed to be modeled. Here the main formalism of continuous diffusion

model (for translational motion) and isotropic rotational diffusion model (for rotational motion) will be shown [Squires 1988] [Bée 1988].

Let us call the concentration fluctuation of any liquid as G. Due to this fluctuation, the atoms in the liquid move to nullify this fluctuation. The change in concentration fluctuation as a function of position is proportional to the change in time (known as diffusion equation) and the proportionality constant denotes the diffusion constant.

Let us start by the case of translational motion. In this case, the diffusion equation can be written as

$$D_{tr}\nabla^2 G_{tr}(\mathbf{r}, t) = \frac{\partial G_{tr}(\mathbf{r}, t)}{\partial t} \tag{5.38}$$

where D_{tr} is the translational diffusion coefficient. The $G_{tr}(\mathbf{r}, t)$ can be imagined as self correlation function (see equation 5.10). It is the probability for finding an atom at position $\mathbf{r}$ at time t which denotes that at the starting point (t=0) the particle is at origin and at any time t, on integrating over all the space, the probability is 1. Based on these, the solution of equation 5.38 is

$$G_{tr}(\mathbf{r}, t) = (4\pi D_{tr}t)^{-\frac{3}{2}} e^{-\frac{\mathbf{r}^2}{4D_{tr}t}} \tag{5.39}$$

Performing Fourier transformation of this function in space and time (Q,t) or energy (Q,ω) domain gives the scattering functions I(Q,t) and S(Q,ω) which can be written as

$$
\begin{aligned}
I^{tr}(\mathbf{Q}, t) &= \int G_{tr}(\mathbf{r}, t) e^{-i\mathbf{Q}\cdot\mathbf{r}} d\mathbf{r} \\
&= e^{-D_{tr}\mathbf{Q}^2 t}
\end{aligned}
\tag{5.40}
$$

and

$$S^{tr}(\mathbf{Q}, \omega) = \frac{1}{\pi} \frac{D_{tr}\mathbf{Q}^2}{(\omega^2 + D_{tr}\mathbf{Q}^2)^2} \tag{5.41}$$

Here $D_{tr}\mathbf{Q}^2$ is the half-width at half-maximum of the function expressed by equation 5.41. This can also be written by a Lorentzian $L(\omega, D_{tr}\mathbf{Q}^2)$.

Next comes rotational motion. The model of free isotropic rotation is first derived by Sears [Sears 1966a][Sears 1966b]. Starting again from the basic diffusion equation one can write

$$D_{rot}\nabla_{sph}^2 G_{rot}(\mathbf{\Omega}, \mathbf{\Omega_0}, t) = \frac{\delta G_{rot}(\mathbf{\Omega}, \mathbf{\Omega_0}, t)}{\delta t} \tag{5.42}$$

where $G(\mathbf{\Omega}, \mathbf{\Omega_0}, t)d\mathbf{\Omega}d\mathbf{\Omega_0}$ is the probability of finding the particle when the position vector $\mathbf{r}$ in $\mathbf{\Omega}$ orientation at time t and in $\mathbf{\Omega_0}$ at starting point t=0. Δ_{sph}^2 is the double differential operator which in spherical coordinates are

$$\nabla_{sph}^2 = \frac{1}{sin\theta}\frac{\delta}{\delta\theta}(sin\theta\frac{\delta}{\delta\theta}) + \frac{1}{sin^2\theta}\frac{\delta^2}{\delta\phi^2} \tag{5.43}$$

with θ and ϕ are polar and azimuthal coordinate angles. Proceeding again like before, the next task is to write the intermediate scattering function I(Q,t). Using this probability $G(\mathbf{\Omega}, \mathbf{\Omega_0}, t)d\mathbf{\Omega}d\mathbf{\Omega_0}$, the I(Q,t) for rotational dynamics becomes

$$I^{rot}(\mathbf{Q}, t) = \sum_{\mathbf{\Omega}}\sum_{\mathbf{\Omega_0}} e^{-i\mathbf{Q}\cdot[\mathbf{R}(\mathbf{\Omega})-\mathbf{R}(\mathbf{\Omega_0})]}G_{rot}(\mathbf{\Omega}, \mathbf{\Omega_0}, t)G_{rot}(\mathbf{\Omega_0}) \tag{5.44}$$

Now using again the two assumptions (similar to translation dynamics) i.e. at starting point t=0, $G_{rot}(\mathbf{\Omega}, \mathbf{\Omega_0}, t) = \delta(\mathbf{\Omega} - \mathbf{\Omega_0})$ and integrating at any time over all the angles gives 1, one has the solution as

$$I^{rot}(\mathbf{Q}, t) = \sum_{l=0}^{\infty}(2l + 1)j_l^2(\mathbf{Q}a)F_{l,rot}(t) \tag{5.45}$$

where $j_l(\mathbf{Q}a)$ is the Bessel function of order l and depends on the radius of the rotation (denoted by a) of the particle under consideration and the value of reciprocal wave vector Q. $F_{l,rot}(t)$ is the rotational relaxation function written as

$$F_{l,rot}(t) = e^{-l(l+1)D_{rot}t} \tag{5.46}$$

Substituting the expression of $F_{l,rot}(t)$ in equation 5.45, the full I(Q,t) for isotropic rotational motion becomes

$$I^{rot}(\mathbf{Q}, t) = \sum_{l=0}^{\infty}(2l + 1)j_l^2(\mathbf{Q}, a)e^{-l(l+1)D_{rot}t} \tag{5.47}$$

This clearly says that each term in the rotational dynamics depends on the appropriate order of Bessel function with the sum of all the prefactors is equal to 1 according to

$$\sum_{l=0}^{\infty}(2l+1)j_l^2(x) = 1 \tag{5.48}$$

Now depending on the radius and the value of Q, in real experimental data treatment one needs to consider the order (value of the subscript l) of the Bessel function.

Normally most of the QENS experiment are performed for Q smaller than $\sim 2\text{Å}^{-1}$ and thus higher order ($l>1$) Bessel functions do not contribute much in the sum (depending on the values of a). In figure 5.12, $j_l(Qa)$ is shown as a function of Qa. We see that $j_0(Qa)$ and $j_1(Qa)$ contributes more than other higher order and the sum of the total is mostly determined by $j_0(Qa)$ and $j_1(Qa)$. Based on that, the infinite Bessel series can be reduced up to $l=1$ without introducing much error. But then to satisfy equation 5.48, the I(Q,t) and S(Q,ω) are written as

$$I^{rot}(\mathbf{Q},t) = j_0^2(\mathbf{Q},a) + [1 - j_0^2(\mathbf{Q},a)]e^{-2D_{rot}t} \tag{5.49}$$

$$S^{rot}(\mathbf{Q},\omega) = j_0^2(\mathbf{Q}a)\delta(\omega) + [1 - j_0^2(\mathbf{Q}a)]L(\omega, 2D_{rot}) \tag{5.50}$$

Thus combing the rotation and translation motion we have the total intermediate scattering function as

$$I(\mathbf{Q},t) = [\left(C + Bj_0{}^2(\mathbf{Q}a)\right)e^{-D_{tr}Q^2t} + B\left(1 - j_0{}^2(\mathbf{Q}a)\right)$$
$$e^{-(D_{tr}Q^2+2D_{rot})t}]e^{-\frac{1}{3}\overline{u^2}Q^2} \tag{5.51}$$

and the corresponding scattering function in energy domain is

$$S(\mathbf{Q},\omega) = [\left(C + Bj_0{}^2(\mathbf{Q}a)\right)L(\omega, D_{tr}Q^2) + B\left(1 - j_0{}^2(\mathbf{Q}a)\right)$$
$$L(\omega, D_{tr}Q^2) \otimes L(\omega, 2D_{rot})]e^{-\frac{1}{3}\overline{u^2}Q^2} \tag{5.52}$$

where B and C are the number of non-rotating and rotating hydrogen atoms in our system.
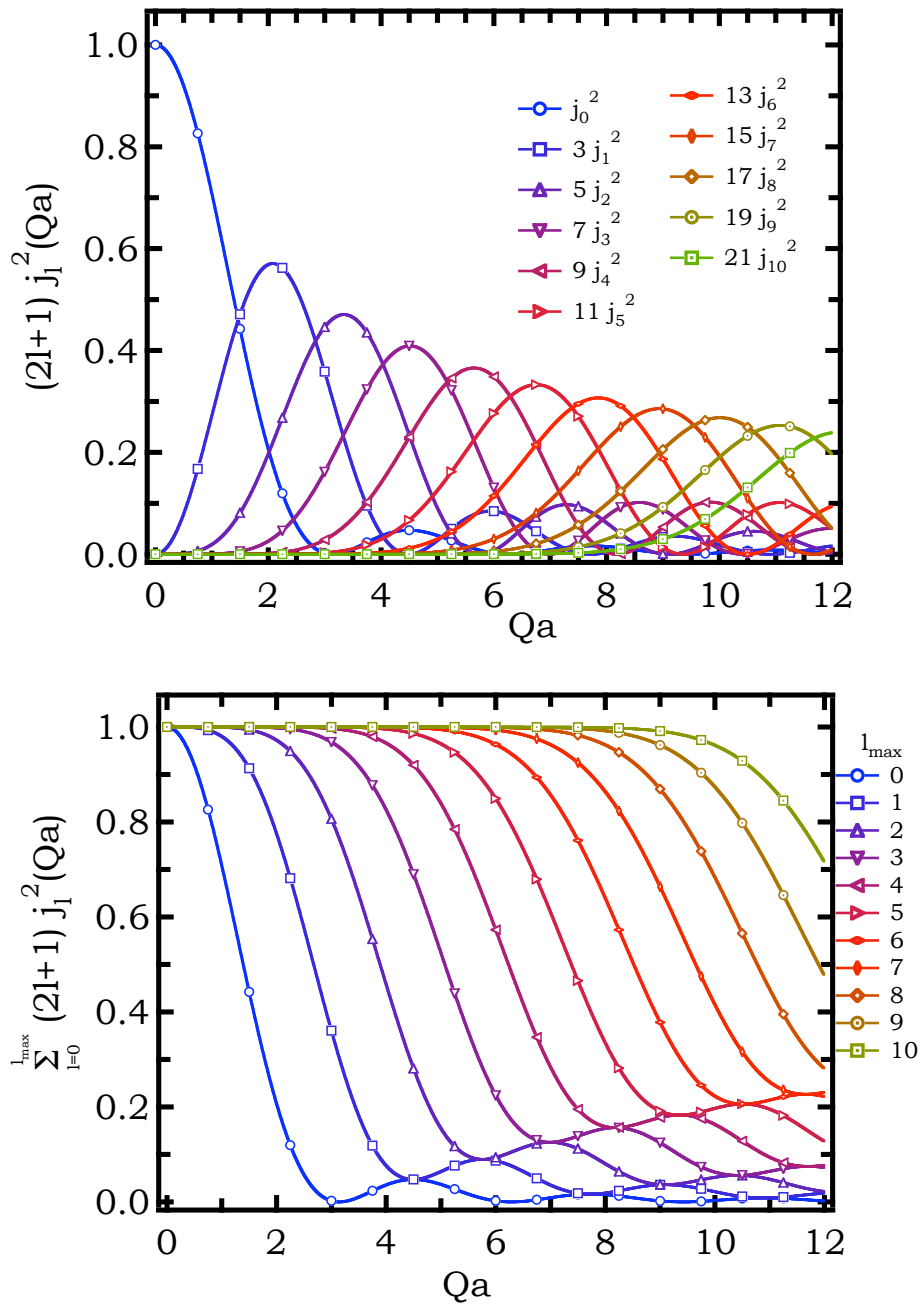
Figure 5.12: Change in the value of Bessel function is shown as a function of the product of **Q** (reciprocal wave vector) and a (radius). Top: each of the Bessel function (for $l=0$ to 10) is shown separately. Bottom: The sum of the Bessel functions are shown. The curves show that the first two orders j_0 and j_1 dominates over the higher terms at low value of **Qa**.

5.6 Experimental Details

The experimental set-up for the neutron experiment is as follows.

5.6.1 Sample Preparation

The hydrogenated TAABr (TMABr to TBABr), CholineBr, NaBr and KBr is bought from Fluka (purity >99%) and preserved at a dry place far from direct sunlight. Prior to each experiment, the salts are dried under vacuum for several hours. Then they are dissolved into liquid D_2O (Euriso-top, 99.9%D) or H_2O (distilled) with desired solute and solvent ratio. After the preparation of each sample, the salts are stored in presence of nitrogen gas. The deuteration of the solvent is important for the incoherent QENS experiment (this will be explained later). The absence of exchangeable Hydrogen atoms in the TAA cation is advantageous which guarantees to keep the solute and solvent character unchangeable inside the solution.

5.6.2 Experimental Setup

The Small Angle Neutron scattering (SANS) and Neutron Diffractometer (ND) is used for structural study of aqueous TAABr at different concentrations. The SANS measurement is performed on the PAXE spectrometer (LLB-Orphee, Saclay, France). The technical details are as follows: incident neutron beam wave-length is 4.5 Å with sample to detector distance 1.5 m which covers Q range of 0.03 to 0.3 Å^{-1}. Each sample is kept under the beam for 1.5 hours in a 2mm quartz cell.

For dynamic measurements, the Neutron Spin Echo (NSE) and Time of flight (TOF) techniques are used. The NSE experiments are performed on MUSES (LLB-Orphee, Saclay, France) and Reseda (FRM-II, Munich, Germany) spectrometers at different temperatures (298K, 316K, 336K and 348K) under controlled Helium pressure (1 atm) varying the Q vectors from 0.2 Å^{-1} to 1.6 Å^{-1}. Each of the I(Q,t) is measured for 1 day. The sample holder is 1 mm thick flat quartz cell. Aluminum cells are not used because of the deformation of the sample holder while aqueous TAABr solutions are under the neutron beam for long. Carbon-glass and quartz are used for experimental resolution at low Q (<0.8 Å^{-1}) and high Q (>1.3 Å^{-1}) domain respectively. The correlation time is measured up to 1100 ps. TOF measurements are carried out on MIBEMOL spectrometer in LLB-Orphee with 0.2 mm thick flat quartz cell. Like NSE, all the experiments are performed under controlled temperature and pressure. Our TOF resolution is 50 μeV (HWHM) with an incident neutron beam wavelength of 6 Å. The experimental resolution is mea-

sured by a vanadium sample. The covered Q range is from 0.49 Å^{-1} to 1.97 Å^{-1}.

For each of the above mentioned measurements, we confirm no loss of sample by comparing the sample weight at the beginning and the end of experiments.

6
Simulation Techniques

Contents

6.1   Introduction

Following the heavy-use in the 'Manhattan Project' during World War II, computer simulation becomes an important tool in scientific work and is rapidly proven to be useful for pure mathematical, analytical treatment or modeling. Today computer simulations are being employed in almost every field - from basic science, engineering, technology to information, business or economics. Molecular Dynamics (MD) simulation is one special variant of computer simulation to study the structural and transport properties of atoms and molecules in the domain of material science. It is a way of tracing the individual particle motion at the atomic scale with timescale ranging from picosecond to nanosecond (even up to microsecond). At this scale therefore, MD simulation becomes useful tool to understand the system behavior or to validate any analytical model for the interpretation of experimental data. For many-body interacting systems an analytical solution for explaining their properties is not only cumbersome and often impossible to execute. MD simulation uses the combined approach of statistical mechanics and ergodic theory. Ergodic theory [Evans 1990] [Hansen 1986] equates the time average of particle trajectories to the space average (where the system is running for a sufficiently long time to generate sufficient statistics). Needless to say that as the system becomes complex, large and is allowed to run for a very long time, it also demands heavier computation support which is made possible with rapid development in new and high end computers. The core of the MD simulation is the numerical integration of Newton's equation of motion for which we need an expression for the potential that generates the forces among interacting particles in system. Technically these potentials are called 'force fields'. Based on force fields, the outcome of the simulation can vary for a given system and thus great care needs to be taken when developing and choosing from available force fields..

6.2   Thermodynamics and MD simulation

The part of the physical science which studies the relation among different types of energy is called Thermodynamics. It deals with the macroscopic observables like temperature (T), volume (V) and pressure (P) to explain the physical properties of a system. The 'equation of state' provides the relationship between P, V and T. MD simulation deals with the microscopic details of the concerned system at atomic level such as particle position, velocity and the interacting force. The link between macroscopic observables and microscopic simulation study is the statistical mechanics. This provides the necessary

mathematical expressions to study the thermodynamic properties by relating the macroscopic properties to the distribution and the atomic motion for a large number of particles. The equation of motion of the particles are studied by MD simulation and thus one can study the thermodynamic and the dynamics of of the system by MD simulation [Frenkel 2002][Hansen 1986].

The idea of ensembles comes when one considers infinite (ideally) number of identical copies of a system that consists of a large number of particles, all at a time and where each of the copy represents a possible state for the system. In other way if one particular experiment is carried out different times in exactly same external condition the final result will be within a certain range. Both of the two representation talks about ensemble which is a collection of statistically large number elements shows definite macroscopic character although the microscopic details are constantly changing with the time.

There can be four different ensembles -

Microcanonical (NVE)   The number of atoms (N), system volume (V) are fixed and the total system energy (E) is conserved through out the experiment and the system is isolated.

Isovolumic-isothermal (NVT)   The number of atoms (N), system volume (V) and the temperature (T) are fixed for the system through out the experiment. The system is coupled with a thermostat.

Isobaric-isothermal (NPT)   The number of atoms (N), system pressure (P) and the temperature (T) are fixed for this ensemble. In NPT the system exchanges energy with thermostat and barostat.

Grand Canonical   Here the particle and the energy are exchanged keeping the system temperature unchanged and keeping the chemical potential μ, volume (V) and temperature (T) fixed.

6.3   MD Simulation Theory

6.3.1   Interaction Potential

In principle the total energy (E_{tot}) can be decomposed into kinetic (E_{KE}) and potential energy (U_{pot}). The potential energy or system configurational energy is taken as a sum of intra-molecular and inter-molecular potential energy. The intra-molecular energy can be bonded and non-bonded while the inter-molecular energy is originated from the non-bonded energy. In our study the

bonded energy is the sum of bond, angle and dihedral energy while the non-bonded energy denotes the Lennard-Jones (L-J) and electrostatic (Coulomb) potential. Mathematically they can be expressed as

$$
\begin{aligned}
E_{tot}(r_i) &= E_{KE}(r_i) + U_{pot}(r_i), \text{ where} \\
U_{pot} &= U_{bonded}(r_i) + U_{non-bonded}(r_i)
\end{aligned}
\tag{6.1}
$$

and

$$
U_{bonded}(r_i) = \sum_i^{N_{bond}} U_{bond}(r_a, r_b, i_{bond}) + \sum_i^{N_{ang}} U_{ang}(r_a, r_b, r_c, i_{ang})
$$

$$
+ \sum_i^{N_{dih}} U_{dih}(r_a, r_b, r_c, r_d, i_{dih})
\tag{6.2}
$$

$$
U_{non-bonded}(r_i) = \sum_i^{N_{L-J}} U_{L-J}(r_i, r_i', i_{L-J}) + \sum_i^{N_{elec}} U_{elec}(r_i, r_i', i_{elec})
\tag{6.3}
$$

where the position are denoted by r_i for a particular atom i, subscript $_a$, $_b$, $_c$, $_d$ represent the atoms in certain bond formation in a molecule with N referring to the different numbers of interactions in the system. The first three different terms in equation 6.2 expresses the total energy generated due to bond potential, angle potential and dihedral angle potential.

6.3.1.1 Bonded Potential

Before proceeding any further, different kinds of bonded potential functions (intra-molecular in nature as said earlier) which are relevant to this works, are going to be discussed. The first of which is the bond potential (U_{bond}) which is controlled by the distance of the bond that is formed between a pair of atoms. Different forms can be used such as Harmonic (simple or restrained), Morse, Lennard-Jones, Quartric and others, depending on the particular force field used in the simulation. The angle potentials (U_{ang}) depends on the angle between the bonds which are specified by three participating atoms. Like Bond potential, angle potentials also can be of several types. The next is the dihedral angle potential (U_{dih}). The geometry shows that four atoms are necessary to define two planes which are separated by a certain angle. The interaction is produced due to the torsional forces among these atoms placed in different planes. In this work we use the simple Harmonic function for bond

potential (U_{bond}) and angle potential (U_{ang}) and cosine function for dihedral angle potential (U_{dih}). The mathematical expression of the above mentioned bond potential are as follows

$$U_{bond} = k_{bond}(r - r_0)^2 \qquad (6.4)$$

$$U_{ang} = k_{ang}(\theta - \theta_0)^2 \qquad (6.5)$$

$$U_{dih} = \frac{A}{2}[1 + cos(m\phi - \delta)] \qquad (6.6)$$

where variable k_{bond}, r_0, k_{ang}, θ_0, A, m and δ depend on the particular type of bond or angle in a molecule.

6.3.1.2   Non-bonded Potential

The non-bonded potentials lead to two kinds of intra or inter-molecular pair interaction potentials. They are long range electrostatic coulomb and short range 6-12 Lennard-Jones (L-J) and thus each atom in the system experiences a resultant potential which can be written as

$$V_{ij} = \frac{q_i q_j}{4\varepsilon_0 r_{ij}} + 4\varepsilon_{ij}[(\frac{\sigma_{ij}}{r_{ij}})^{12} - (\frac{\sigma_{ij}}{r_{ij}})^6] \qquad (6.7)$$

where the first part is electrostatic and the second is due to L-J. σ_i, ε_i are L-J parameters and charges are represented by q_i. Lorentz-Berthelot rule is applied for calculating the pair parameters (energy and size) between unlike atoms (for $i \neq j$) i.e.

$$\varepsilon_{ij} = (\varepsilon_i \varepsilon_j)^{\frac{1}{2}}$$

$$\sigma_{ij} = \frac{(\sigma_i + \sigma_j)}{2} \qquad (6.8)$$

Ewald Sum and Cut-off Radius   The Long ranged potentials usually refers the electrostatic (Coulomb) potential where different methods can be used to calculate the sum; such as direct sum, Ewald sum, truncated and shifted sum, damped shifted, distance dependent dielectric and charge group implementation etc. Among these Ewald sum is the most accurate and efficient method in a system with periodic boundary condition. The Ewald sum technique decouples the total electrostatic sum into real space and reciprocal space with correction for self energy [Smith 2007] [Frenkel 2002]. One of the important quantity for calculating the non-bonded interactions is the cut-off radius. This is basically done by Verlet neighbor list algorithm. Due to the

regenerated neighbor list, the simulation requires to carry out the calculation for all the molecules but up to a certain sphere which is defined by the cut-off radius r_{cut}. The list consists of all the atom (called 'secondary' atoms) which are inside this sphere centered around a 'primary' atom. Use of Δr_{cut} provides the option to use the same list without updating for consecutive time steps till the radius is within the value $r_{cut} + \Delta r_{cut}$. There can be two different approaches - Brode-Ahlrichs (when r_{cut} is higher than simulation cell) and link-cell algorithm (when r_{cut} is smaller) [Frenkel 2002] [Smith 2007].

6.3.2 Integration Algorithm

Newton second law's of motion is the base of the MD simulation. According to Newton's equation of motion $\mathbf{F}=m\mathbf{a}$ with $\mathbf{F}$ is applied force, m is the mass and $\mathbf{a}$ is the acceleration due to the applied force on mass m. Thus once we have the knowledge of the correct expression of force on the particle, by doing consecutive integration one can have the particle velocity and position as a function of time. This can be mathematically formulated as follows

$$\mathbf{F_i}(t) = m\frac{d^2\mathbf{r_i}(t)}{dt^2} \tag{6.9}$$

for a particle i. Based on this position or velocity (as a function of time) various properties (both dynamic and structural) at a definite time, can be calculated. Thus the first important quantity is to correctly calculate the force which can be determined from the interacting force field between the atoms according to

$$\mathbf{F_i}(t) = -\sum_j \nabla \mathbf{U_{ij}} \tag{6.10}$$

In simulation the potential energy is a function of positions (in three dimension) of all the atoms and it is difficult to find analytical solution of equation 6.9 and 6.10. Also the time steps are taken discretely. There are several algorithms for carrying out the numerical integration of equation of motion. One of most used is Verlet algorithm. We use the Taylor expansion to express the position after a time interval δt.

$$\mathbf{r_i}(t + \delta t) = \mathbf{r_i}(t) + \frac{d\mathbf{r_i}(t)}{dt}\delta t + \frac{1}{2}\frac{d^2\mathbf{r_i}(t)}{dt^2}\delta t^2 + ... \tag{6.11}$$

In the same way, we can write

$$\mathbf{r_i}(t - \delta t) = \mathbf{r_i}(t) - \frac{d\mathbf{r_i}(t)}{dt}\delta t + \frac{1}{2}\frac{d^2\mathbf{r_i}(t)}{dt^2}\delta t^2 + ... \tag{6.12}$$

Now by adding up equation 6.11 and 6.12, we have

$$\mathbf{r_i}(t + \delta t) \simeq 2\mathbf{r_i}(t) - \mathbf{r_i}(t - \delta t) + \frac{d^2\mathbf{r_i}(t)}{dt^2}\delta t^2 \tag{6.13}$$

Thus in Verlet algorithm, the atom position r_i at time $(t + \delta t)$ is determined solely from $\mathbf{r_i}(t)$ and $\mathbf{r_i}(t - \delta t)$ according to equation 6.13.

In addition to Verlet, the Leapfrog algorithm is coupled. The name Leapfrog comes as here first the velocities *leap* over position and vice versa. During this algorithm first the velocities are determined at time $(t+\frac{\delta t}{2})$ and using that the position of the atoms are determined

$$\begin{aligned} \mathbf{v_i}(t + \frac{\delta t}{2}) &= \mathbf{v_i}(t - \frac{\delta t}{2}) + \frac{d^2\mathbf{r_i}(t)}{dt^2}\delta t \\ \mathbf{r_i}(t + \delta t) &= \mathbf{r_i}(t) + \mathbf{v_i}(t + \frac{\delta t}{2})\delta t \end{aligned} \tag{6.14}$$

At any time t the velocities are approximated by

$$\mathbf{v_i}(t) = \frac{\mathbf{v_i}(t - \frac{\delta t}{2}) + \mathbf{v_i}(t + \frac{\delta t}{2})}{2} \tag{6.15}$$

Now in case of rigid bodies, each bonded atoms are driven by SHAKE algorithm (which works on the foundation of Verlet Leapfrog) and the equation of motions are calculated slightly differently. First the position of atoms are modified according to Verlet algorithm as defined before without considering the bond constraints. Next based on the specified bond constraints, the correction are made for each bonded atoms and also for neighboring atoms. This is an iterative process and it continues till all the bond constraints are converged.

6.3.3   Thermostats and Barostats

6.3.3.1   Thermostats

The Thermostats are usually used in NPT and NVT ensemble to keep the temperature of the system constant throughout the whole simulation. The most straight forward option is to change the temperature in every few timesteps

by scaling the velocity of the partiles. This is done by multiplying the veloci-
ties by a factor which is square root of the ratio of temperature at any time t
and the desired temperature. Though it is obvious that this simple rescaling
does not correctly reproduce the canonical temperature where temperature
fluctuation is always present. The effect of velocity scaling can be seen in the
energy at each timestep where the scaling is done. This is an ad-hoc method
for bringing the system to desired temperature which must be switched off
after an initial crude equilibrium stage.

Berendsen Thermostat   One modified version of the velocity scaling is the
Berendsen thermostat where the system is connected to an external heat reser-
voir with a constant temperature (T_{ext}). The particle velocities are changed
following the change in temperature according to

$$\frac{dT(t)}{dt} = \frac{T_{ext} - T(t)}{\tau_T} \tag{6.16}$$

where τ_T is the time-constant for the thermostat. This rescaling brings down
the system temperature $[T(t)]$ exponentially to desired value. The final rescal-
ing variable $[\kappa(t)]$ is expressed as

$$\kappa(t) = \sqrt{1 + \frac{\delta t}{\tau_T}(\frac{T_{ext}}{T(t)} - 1)} \tag{6.17}$$

In Berendsen thermostat total momentum remains constant. The value of τ_T
is important to alter the system behavior. In case it tends to infinity, the
thermostat is turned off and system evolves in NVE ensemble while $\tau_T =$
timestep of the simulation causes the simple velocity scaling. If τ_T value is
very small then system shows low temperature fluctuation. Normally $\sim$ 0.5-2
ps is chosen for τ_T.

Nosé Hoover Thermostat   The most efficient thermostat to study canon-
ical ensemble is Nosé Hoover thermostat. Berendsen is good to achieve the
desired temperature but after being equilibrated it is more realistic to use
Nosé Hoover. The algorithm is first developed by Nosé and then modified by
Hoover. In this algorithm an external heat reservoir is completely considered
as an integral part of the system. The complete equation of motion can be
written as

$$\frac{d\chi(t)}{dt} = \frac{fk_B[T_{ext} - T(t)]}{Q_{ext}} \tag{6.18}$$

where $\chi(t)$ is can be thought as a friction coefficient causing damping of the particle motion and thus controlling the temperature. Q_{ext} ($=fk_BT_{ext}\tau_T^2$) is the effective mass associated with the heat reservoir, with f being the number of degrees of freedom [Smith 2007]. Although it must be noted that the total system energy is not conserved and the sampling is carried out in canonical ensemble. The resultant equation (equation 6.18) is time-reversal and heat is exchange between the real sample and the heat bath is carried out in a periodic way which generates an oscillatory temperature fluctuation. The right choice of Q_{ext} is important for the simulation which largely depends again on the time-constant (τ_T) specified for the simulation. Having a high Q_{ext} makes the simulation longer whereas a value too small causes rapid and high amplitude temperature oscillation. The conserved energy is the total Gibbs free energy of the integrated system, which can be written as

$$\mathcal{H}_{NVT} = KE_{real} + U_{real} + \frac{Q_{ext}\chi(t)^2}{2} + \frac{Q_{ext}}{\tau_T^2}\int_0^t \chi(s)ds \qquad (6.19)$$

with KE_{real} and U_{real} are the real system (with out external heat reservoir) kinetic and total internal energy and the last two describe heat reservoir kinetic and potential energy.

6.3.3.2 Barostats

To achieve a desired volume of simulation box, the barostat is used in NPT ensemble. It couples the system with an external barostat to have a average pressure (P_{ext}). Here only the Hoover barostat will be discussed where the equation of motions are solved by coupling simultaneously the Nosé Hoover thermostat and barostat. Based on the same idea as in 6.3.3.1 (but this time coupling both the Nosé Hoover thermostat and Hoover barostat), the equation of motions can be written as

$$\frac{d\chi(t)}{dt} = \frac{fk_B[T_{ext} - T(t)]}{Q_{ext}} + \frac{1}{Q}(W_{ext}\zeta(t)^2 - k_BT_{ext}) \qquad (6.20)$$

$$\frac{d\zeta(t)}{dt} = \frac{3}{W_{ext}}V(t)[P(t) - P_{ext}] - \chi(t)\zeta(t) \qquad (6.21)$$

$$\frac{dV(t)}{dt} = [3\zeta(t)]V(t) \qquad (6.22)$$

with W_{ext} ($=fk_BT_{ext}\tau_P^2$) is the barostat effective mass, τ_T the specified time constant for pressure fluctuation, $\zeta(t)$ is barostat friction constant and $P(t)$, $V(t)$ are the instantaneous system pressure and volume.

The conserved quantity is the total Gibbs free energy that can be written as

$$\mathcal{H}_{NPT} = KE_{real} + U_{real} + \frac{Q_{ext}\chi(t)^2}{2} + \frac{W_{ext}\zeta(t)^2}{2} + \int_0^t (\frac{Q_{ext}}{\tau_T^2}\chi(s) + k_B T_{ext})ds \quad (6.23)$$

Both the Nosé Hoover thermostat and Hoover barostat needs a number of iterations to achieve the equilibrium condition.

6.4   Transport Properties

We have chosen to incorporate the Molecular dynamics (MD) simulation in our study because different contributions (coherent and incoherent) are mixed in the neutron scattering experiments and at times it is hard to separate them. To decouple these different contribution, the MD simulation is important. Apart from that many of the neutron scattering results (such as structure factor, intermediate scattering function) are also possible to compute by MD. At the same time, using the trajectory of the atoms as a function of time, we can study the structure and dynamics at the atomic level.

This section briefly combines how we can relate two different techniques (neutron experiments and MD simulation). MD simulation provides the trajectory which is the atomic positions as a function of time. Based on that the transport properties (such as the diffusion coefficients) are measured either in real or in reciprocal space. In real space, the calculation is direct. Here we determine the mean square displacement (described before) for a particular atom and based on that diffusion coefficients are deduced. But the neutron measurement are carried out in reciprocal space and scattering functions are either in time [I($\mathbf{Q}$,t)] or in energy [S($\mathbf{Q}$,ω)] domain. From there based on the model if the relaxation time shows dependence on Q, the diffusion coefficients are estimated. The same (as experiments) can also be carried out by inverse Fourier transformation in MD simulation where the atomic trajectories are converted from real space to reciprocal space and/ or units of time can be changed to units of energy. Thus we arrive at the same scattering function [I($\mathbf{Q}$,t) and S($\mathbf{Q}$,ω)] and can compare the diffusion coefficient like same as in experiment. A schematic diagram for all the levels described above is presented in figure 6.1.

The most direct way to study the transport phenomenon is to calculate the diffusion coefficient (can be either translational or rotational). The phenomenon is exactly same what we have discussed in section 5.5.2.2. Due to
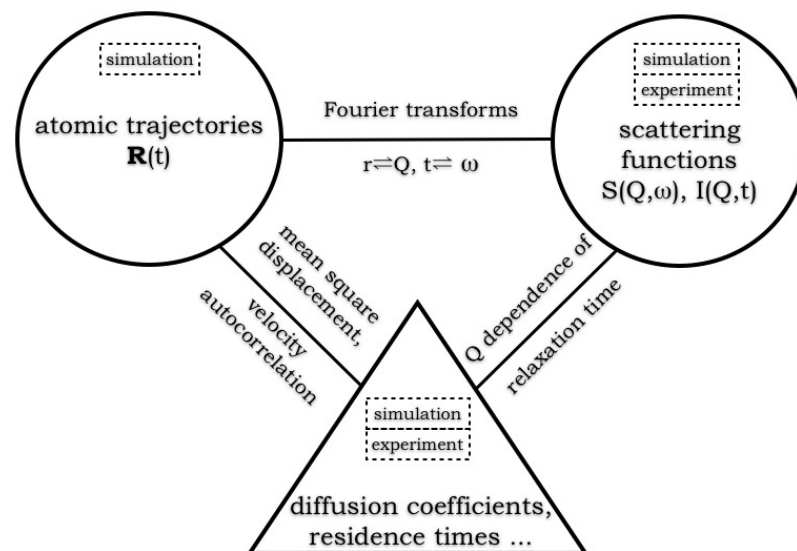
Figure 6.1: **Calculation of diffusion coefficient from neutron experiment and MD simulation.**
Mutual relation between neutron experiment and MD simulation to estimate diffusion coefficient. The neutron data are available in reciprocal space and either in time or in energy domain while the simulated data can be both in real space or in reciprocal space. Fourier transformation can produce scattering function from simulated atom trajectory.

concentration fluctuation in any liquid atoms start to move to bring the system to equilibrium state. This generates the transportation of the particles and the whole situation can be generalized (irrespective of translational or rotational movement) as

$$D\nabla^2 \rho(\mathbf{r}, t) = \frac{\partial \rho(\mathbf{r}, t)}{\partial t} \tag{6.24}$$

with D being the diffusion coefficient and ρ is the concentration gradient whose change with time equates with the change in time generating diffusive motion. Based on the condition that probability of finding an atom at any position $\mathbf{r}$ at time t (integrating over all the space) is 1 and at the starting point (t=0) the atom is at origin, we have the solution of equation 6.24 as

$$\rho(\mathbf{r}, t) = (4\pi D t)^{-\frac{f}{2}} e^{-\frac{r^2}{4Dt}} \tag{6.25}$$

where f is the dimension of the system [Frenkel 2002] [Hansen 1986]. This diffusion coefficient can be calculated via different ways. In the following sections we will mention the method of calculating the mean square displacement (MSD) and intermediate incoherent scattering function (individual atom motion and collective motion)

6.4.1   Mean Square Displacement

In MSD we calculate the change $\mathbf{d}_i(t)$ in a particular atomic position $\mathbf{R}_i(t)$ from its starting point $\mathbf{R}_i(t = 0)$ and determine the diffusion coefficient D_i according to Einstein-diffusion equation in the long time limit. The mathematical formulation is following

$$
\begin{aligned}
\mathbf{d}_i(t) &= \mathbf{R}_i(t) - \mathbf{R}_i(0) \\
D_i &= \lim_{t\to\infty} \frac{\langle \mathbf{d}_i^2(t) \rangle}{ft}
\end{aligned}
\tag{6.26}
$$

with f is the dimension.

6.4.2   Intermediate scattering function

Time correlation functions are an alternative way to represent atomic motion. These are experimentally available and can be calculated from the simulated

trajectories. Like explained before in section 5.3.2, the incoherent and coherent intermediate scattering function can also be possible to derive mathematically in reciprocal space as follows

$$I_{coh}(\mathbf{Q}, t) = \frac{1}{N} \sum_{i,j} b_{i,coh}\, b_{j,coh} \langle e^{[-i\mathbf{Q}\cdot\mathbf{R_i}(0)]} e^{[i\mathbf{Q}\cdot\mathbf{R_j}(t)]} \rangle, \qquad (6.27)$$

$$I_{inc}(\mathbf{Q}, t) = \frac{1}{N} \sum_{i} b_{i,inc}^2 \langle e^{[-i\mathbf{Q}\cdot\mathbf{R_i}(0)]} e^{[i\mathbf{Q}\cdot\mathbf{R_i}(t)]} \rangle \qquad (6.28)$$

The corresponding dynamic structure factors $[S(\mathbf{Q}, \omega)]$ in energy (ω) domain can be derived by Fourier transformation. Note that the MSD is directly related to the incoherent intermediate scattering function via the cumulant expansion. This can readily calculable from

$$I_{inc}(Q, t) = \frac{1}{N} \sum_{i} b_{i,inc}^2 e^{[-Q^2 \rho_{i,1}(t) + Q^4 \rho_{i,2}(t) \mp \cdots]}. \qquad (6.29)$$

where $\rho_{i,m}(t)$ are called cumulants and are defined as

$$\rho_{i,1}(t) = \frac{1}{2!} \langle d_i^2(t) \rangle$$
$$\rho_{i,2}(t) = \frac{1}{4!} \left[\langle d_i^4(t) \rangle - 3\langle d_i^2(t) \rangle^2 \right] \qquad (6.30)$$
$$\vdots$$

As for Gaussian approximation (continuous diffusion following Einstein law) only the first term in the above equation dominates, the MSD calculated diffusion coefficient is identical to the one from incoherent intermediate scattering function.

Some special treatment are exercised in nMoldyn calculation, namely while calculating time correlation function and defining Q vectors in coherent intermediate scattering function. The time correlation function is probably the most important quantity in the scope of present work. And for system consisting thousands of atoms its calculation for each relevant pair of atoms takes long time. Thus computationally it will be efficient if we can make it faster. In nMoldyn [Kneller 1996], Fast Correlation Algorithm (FCA) is used via Fast Fourier Transformation (FFT) where the total number of multiplication is reduced from N_i^2 to $N_i \log_2(N_i)$ where N_i is the total number of timesteps. Next is how the reciprocal Q vectors are chosen. For incoherent intermediate scattering function, the Q vectors are calculated according to

$$\mathbf{Q} = 2\pi \left(k\mathbf{a}^\dagger + l\mathbf{b}^\dagger + m\mathbf{c}^\dagger \right), \tag{6.31}$$

such that

$$\mathbf{a}\mathbf{a}^\dagger = \mathbf{b}\mathbf{b}^\dagger = \mathbf{c}\mathbf{c}^\dagger = 1. \tag{6.32}$$

with

$$\mathbf{R} = x\mathbf{a} + y\mathbf{b} + z\mathbf{c}, \tag{6.33}$$

where $\mathbf{R}$ is atom position vector, x, y, z are coordinates and $\mathbf{a}$, $\mathbf{b}$ and $\mathbf{c}$ is the basis vectors in real space. While k, l and m are integers and 2π is generated because particle coordinates alter a 2π phase during Fourier transformation keeping the average density as before (unchanged). In case of coherent intermediate scattering function certain grids of Q-shells (user defined) is specified with a tolerance in the value of Q. Next only those Q vectors (calculated according to equation 6.31) are chosen whose moduli falls within the limit of the specified tolerance from the grids. The details can be found in [Kneller 1996]

6.5   Simulation Details

Classical molecular dynamics (MD) simulations (using the code DL POLY 2.18 [Smith 2007]) are performed on aqueous solutions of TAABr and CholineBr. An all atom (explicit N, C, H atoms and also O for Choline), flexible (bond stretch, bond bending, dihedral interaction), non-polarizable model is taken for the TAA$^+$ or Choline$^+$ ion. Individual atomic charges within this ion are determined by the Hartree-Fock method (for nonpolarizable force fields), followed by modification using Antechamber (AMBER routine) [Heyda 2010] and other interaction parameters are taken from the Generalized Amber Force Field (GAFF) [Case 2008]. The cationic atom charges and force field parameters for TBA$^+$, TMA$^+$ and Choline$^+$ are summarized in table 6.1, 6.2, 6.3, 6.4, 6.5 and 6.6. The details of TEA$^+$ and TPA$^+$ can be found in B.1. The sodium, bromide charges or force-field parameters are taken from earlier literatures [Koneshan 1998] [Horinek 2009] [Lee 1996] [Joung 2008] [Markovich 1996]. Rigid SPC/E model (O-H bond 1.0 Å , H-O-H angle 109° with charges for hydrogens and oxygens are respectively +0.424 e and -0.848 e respectively) is used for water [Berendsen 1987]. Choosing one from a large number of existing water models, is a difficult task. We decide to continue with the SPC/E model because it reproduces well both the structural and dynamic properties of bulk water over a broad range of temperatures and pressures [Brodholt 1993]. This is an 'extended' version

of SPC model [Guillot 2002] where additionally an 'self-polarisation' energy correction is imposed. The non-bonding interactions in the system are described via the Coulombic and Lennard-Jones (L-J) potentials, with the use of Lorentz-Berthelot mixing rules for the L-J parameters. Before starting any simulation it is necessary to construct the simulation box consists of all the atoms. This is done like following. First the solute ions (TAA or Choline cations) are constructed with correct geometry (in accordance to the experimentally derived bond length, valence and dihedral angles). Next a cubic simulation box is formed with a volume similar to the combined volume of desired number of solute cations, anions and solvent molecules. This simulation box is then filled by the solvent molecules (randomly oriented), leaving empty space for inserting solutes. At this time one must be careful about the fact that the initial simulation box should not very far from the equilibrium condition. Once these formalisms are completed, the MD simulation is performed in NPT ensemble and is allowed to run until the potential and kinetic energies are stable, temperature and pressure becomes constant and the system density agrees with experimental value i.e until it is equilibrated. Three dimensional periodic boundary conditions are used, a cutoff radius for short-range interactions is half the box-size, long-range part of the electrostatic interaction is evaluated using the 3D Ewald sum, SHAKE algorithm is used for rigid SPC/E water molecules. The initial configuration is equilibrated in NPT and NVT ensembles (P=1atm, T=298K), prior to a production run in the NVE ensemble of 3.4ns with a timestep of 1fs. Individual atomic trajectories are saved every 0.1ps, producing 34×10^3 frames in total. Trajectories are then analysed using nMoldyn [Kneller 1996]. As an initial check of the interaction potentials, solutions of different ion concentrations are simulated and the predicted density reproduces well experimental data (difference is <0.2%). In figure 6.2, 6.3 and 6.4 a comparison between experimental and simulated densities is shown for aqueous TBABr, TMABr and CholineBr solution..

Note that all simulations are done with H_2O as the solvent. The scattering lengths of deuterium are used for the solvent H atoms in the post-simulation analysis of atomic trajectories, to yield the comparison with scattering data (measured in D_2O solvent).
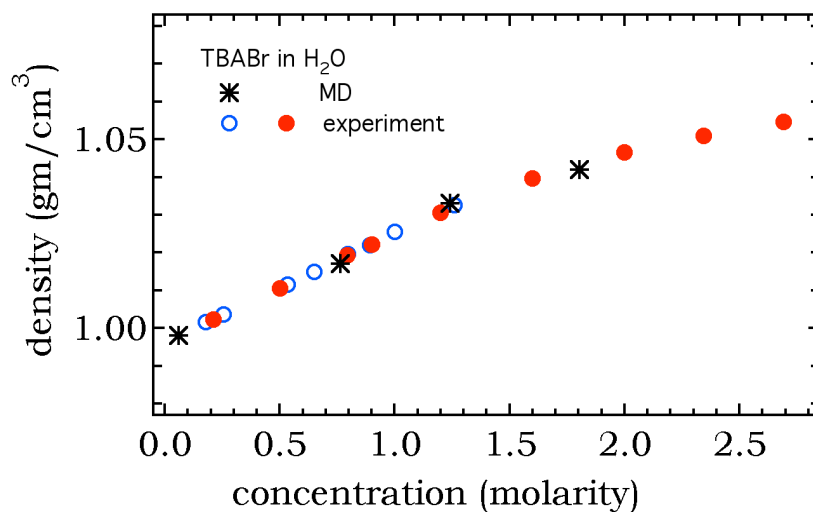
Figure 6.2: Comparison of density of aqueous TBABr solution extracted from MD simulation and experiment [Buchner 2002] [Eagland 1972].
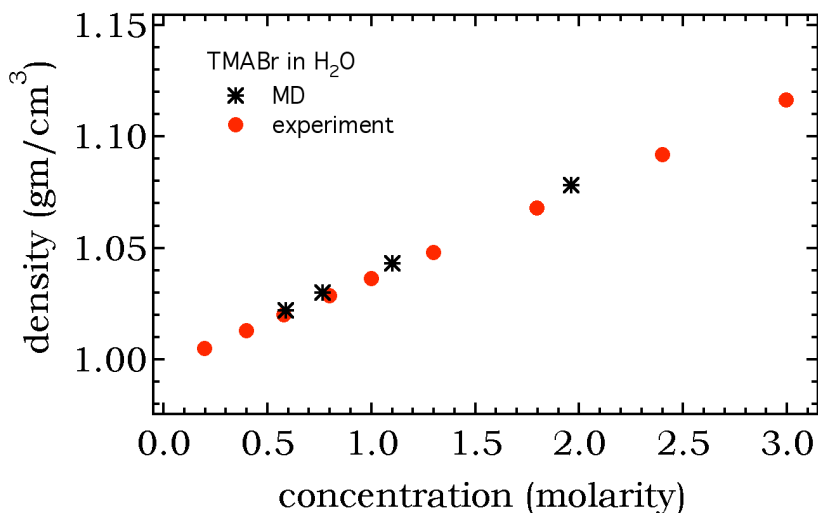
Figure 6.3: Comparison of density of aqueous TMABr solution extracted from MD simulation and experiment [Buchner 2002].
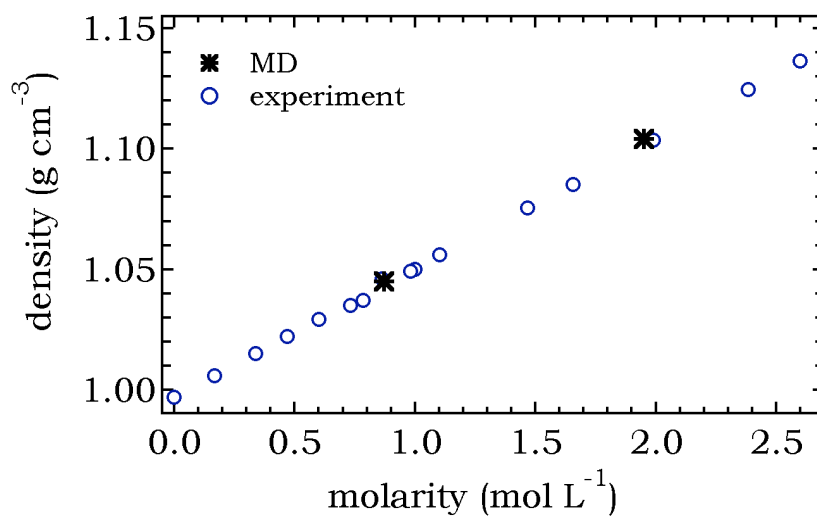
Figure 6.4: Comparison of density of aqueous CholineBr solution extracted from MD simulation and experiment.

atom or part of molecule	atom charge (e) (from bold part)		
	N	C	H
-**N**-	0.056669		
-N-**CH₂**-		0.017461	0.053130
-N-$CH_2 - $**CH₂**-		-0.002556	0.021844
-N-$CH_2 - CH_2 - $**CH₂**-		0.011361	0.020886
-N-$CH_2 - CH_2 - CH_2 - $**CH₃**		-0.086548	0.034799

Table 6.1: TBA$^+$ atomic charge distribution.

atom or part of molecule	atom charge (e) (from bold part)		
	N	C	H
-**N**-	0.096521		
-N-**CH₃**		-0.165381	0.130417

Table 6.2: TMA$^+$ atomic charge distribution.

atom or part of molecule	atom charge (e) (from bold part)			
	N	C	H	O
-**N**-	0.0222			
-N-**CH₃**		-0.142	0.124	
-N-**CH₂**-		-0.050	0.134	
-N-$CH_2 - $**CH₂**-		-0.183	0.043	
-N-$CH_2 - CH_2 - $**OH**-			0.473	-0.669

Table 6.3: Choline$^+$ atomic charge distribution.

bond elongation harmonic parameters	energy (kcal/mol/Å²)	length (Å)
C-H$_C$	340	1.090
C-H$_N$	240	1.090
C-C	310	1.526
C-N	367	1.471

bond bending harmonic parameters	energy (kcal/mol/rad²)	angle (degree)
H$_C$-C-H$_C$	35	109.5
H$_N$-C-H$_N$	35	109.5
C-C-H$_C$	50	109.5
C-C-H$_N$	50	109.5
C-C-C	40	109.5
C-C-N	80	111.2
H$_N$-C-N	50	109.5
C-N-C	50	109.5

dihedral interaction	energy (kcal/mol)	angle (degree)
H$_C$-C-C-H$_C$	0.15	0.0
H$_C$-C-C-C	0.16	0.0
H$_C$-C-C-H$_N$	0.15	0.0
H$_N$-C-C-C	0.16	0.0
C-C-C-C	0.18	0.0
X-C-C-X	0.15	0.0
X-C-N-X	0.15	0.0

L-J parameters	ε kcal/mol	σ Å
H$_C$	0.0157	1.487
H$_N$	0.0157	1.100
C	0.1094	1.900
N	0.1700	1.8240

Table 6.4: TBA$^+$ Force Field.

Force field parameters for TBA$^+$ atoms are shown (H$_N$ represents the hydrogens of the carbon attached to the central N).

bond elongation harmonic parameters	energy (kcal/mol/Å²)	length (Å)
C-H$_N$	240	1.090
C-N	367	1.471

bond bending harmonic parameters	energy (kcal/mol/rad²)	angle (degree)
H$_N$-C-H$_N$	35	109.5
H$_N$-C-N	50	109.5
C-N-C	50	109.5

dihedral interaction	energy (kcal/mol)	angle (degree)
X-C-N-X	0.15	0.0

L-J parameters	ε kcal/mol	σ Å
H$_N$	0.0157	1.100
C	0.1094	1.900
N	0.1700	1.8240

Table 6.5: TMA$^+$ Force Field.
Force field parameters for TMA$^+$ atoms are shown (H$_N$ represents the hydrogens of the carbon attached to the central N).

bond elongation harmonic parameters	energy (kcal/mol/Å²)	length (Å)
C-H$_N$	240	1.090
C-H$_C$	340	1.090
C-C	310	1.526
C-N	367	1.471
C-O$_{OH}$	320	1.410
C-H$_{OH}$	553	0.960
bond bending harmonic parameters	energy (kcal/mol/rad²)	angle (degree)
H$_N$-C-H$_N$	35	109.5
H$_C$-C-H$_C$	35	109.5
C-C-H$_C$	50	109.5
C-C-H$_N$	50	109.5
H$_C$-C-O$_{OH}$	50	109.5
C-C-N	80	111.2
H$_N$-C-N	50	109.5
C-N-C	50	109.5
C-C-O$_{OH}$	50	109.5
C-O$_{OH}$-H$_{OH}$	35	109.5

L-J parameters	ε kcal/mol	σ Å
H$_N$	0.0157	1.387
H$_N$	0.0157	1.100
H$_{OH}$	0.0000	0.0000
O$_{OH}$	0.2104	1.7210
C	0.1094	1.900
N	0.1700	1.8240

dihedral interaction	energy (kcal/mol)	angle (degree)
X-C-N-X	0.15	0.0
X-C-C-X	0.15	0.0
X-C-O$_{OH}$-X	0.15	0.0

Table 6.6: Choline$^+$ Force Field.
Force field parameters for Choline$^+$ atoms are shown (H$_N$ represents the hydrogens of the carbon attached to the central N).

7

Structures of Ions

Contents

7.1   Introduction

After going through a brief review of the aqueous solution of the TAABr, the basics of the neutron scattering and molecular dynamics techniques used in this work; the rest of this thesis will show how a combined approach of experiment and simulation can bring new insights into their solute and solvent behavior (structure and dynamics). While presenting the results, the aqueous TBABr solution will be discussed in detail. At the same time, comparison with aqueous TMABr (the smallest in the TAA family), CholineBr (a close derivative of TMABr with an additional -$CH_2(OH)$ group attached to one arm of TMABr, figure 7.1) and simple salts (like NaBr) solutions will also be carried out.
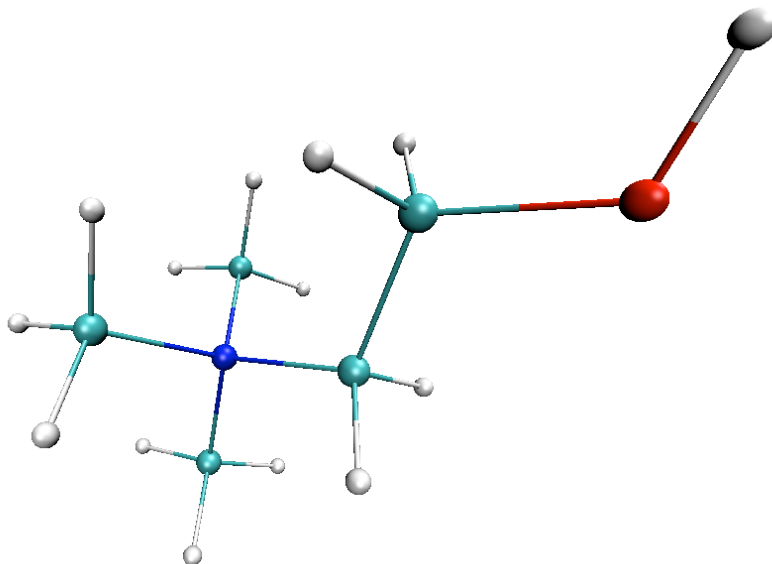
Figure 7.1: Choline$^+$ cation. blue - nitrogen, green - carbon, white - hydrogen and red - oxygen atom.

The current chapter will deal with the solute (ion) structure while its dynamics will be studied in chapter 8 by a combination of TOF, NSE and MD methods. We take advantage of the above mentioned techniques to study separately the coherent and incoherent signal dynamics and will find out if the two approaches (coherent and incoherent signal dynamics) lead to two different results. We will mainly focus on aqueous TBABr solution and then will show the results from other systems (such as TMABr, CholineBr and NaBr). At the end we will determine the change in dynamics as the temperature increases.

The result of solvent structure and dynamics will be presented in chapter 9. Like before (as in solute structure and dynamics) we will concentrate on aqueous TBABr solution and at the end, the results from other systems (such as TMABr, CholineBr, NaBr, KBr and CsBr) will also be shown. Note that in literature there is evidence that at 1m (molar ratio of solute and water = 1:56) concentration, one hydration sphere is formed around TBA cation [Green 1987] [Turner 1994] and at 2.5m (molar ratio of solute and water = 1:22) around TMA cation [Turner 1994].

7.2 Way of Defining Concentrations

Before proceeding any further, we present here a brief discussion on the relation among the different nomenclatures of concentrations which are normally used in literature. To define the concentration, usually the concept of Molarity, Molality or the ratio between solute and solvent are used. Molality (m) and Molarity (M) both are the measurement of molar concentration in a solution. The Molarity (M) is defined as the number of mole of solute divided by the volume of the total solution.

$$\text{Molarity (M)} = \frac{\text{Moles of solute}}{\text{Volume of solution}} \tag{7.1}$$

The SI unit of Molarity is mol/L. 1 mol/L can also be denoted as '1 molar' or '1 M'. But there is a problem in defining the concentration by the notion of Molarity when the volume of the solution changes (such as because of the temperature). Thus to have the concentration to be unchanged irrespective of the change in volume of the solution, the notion of Molality (m) is used. The Molality (m) is defined as follows

$$\text{Molality (m)} = \frac{\text{Moles of solute}}{\text{Mass of solvent}} \tag{7.2}$$

The SI units of Molarity is unit moles/kg. The Molarity (M) and Molality (m) are linked together by the density of the system. It can be briefly explained as follows. Suppose the density of the solution is d (gm/cc). Then we can write the mass of 1 litre of solution = 1000d (in gm). Now considering there are N moles of solutes in the solution and the mass of 1 mol solute as MW, we can express the mass of the solutes in the system is = no of Moles × MW = N × MW. So the mass of the solvent is = (1000d-N×MW). In terms of the definition of the Molality this is written as
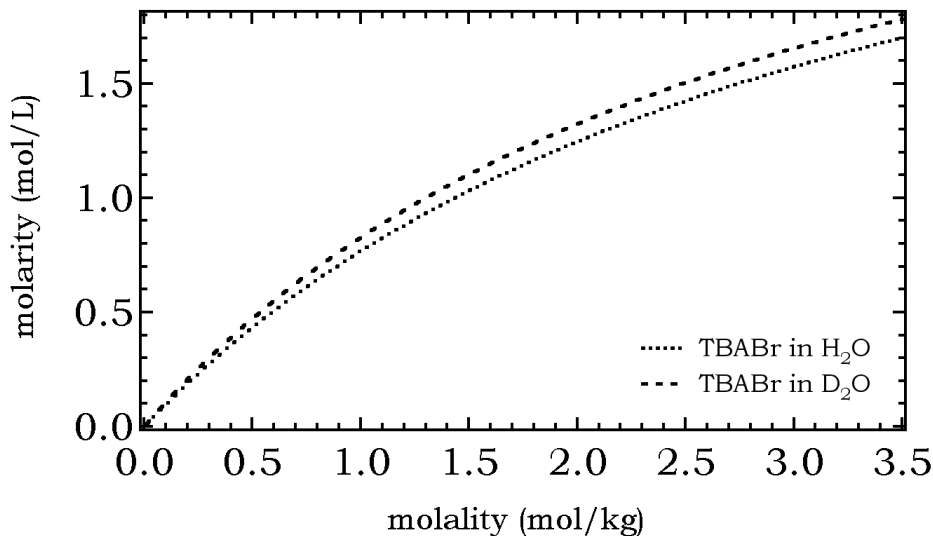
Figure 7.2: The relation between Molarity (M) and Molality (m) for aqueous TBABr solution when the solvent is D_2O and H_2O.

$$
\begin{aligned}
\text{Molality (m)} \quad &= \quad \frac{N}{\frac{1000d - N \times MW}{1000}} \\
&= \quad \frac{1000N}{1000d - N \times MW} \qquad (7.3)
\end{aligned}
$$

This is the relation between Molarity (M) and Molality (m). An example of the conversion between Molarity and Molality for aqueous TBABr in H_2O and in D_2O is shown in figure 7.2. The difference between two systems is because of the difference in mass between H_2O and in D_2O for an equal amount of system volume. To clear the ambiguity, from now on, we will define our systems by the ratio of solute and solvent in this manuscript. For example the concentration of 0.89m (or 0.76M) aqueous solution (in D_2O) of TBABr will be denoted with x_m=1:56 (where x_m=mole of solute:mole of solvent, the molar ratio of solute and solvent).

7.3 Structure

7.3.1 Possibility of Aggregation at High Concentration

As for initial characterization, the SANS is used to verify if there exists any macroscopic aggregation in the aqueous TAABr system in the concentration

range we are interested at. First a series of TBABr solutions in D_2O from x_m (x_m=mole of solute:mole of solvent, the molar ratio of solute and solvent) =1:224 to 1:14 (corresponding to 0.22M to 1.82M) is measured and we see flat curves (or slightly sloped) when solute concentration increases. The measured scattered intensity is analyzed by deducting the incoherent scattering (mainly from hydrogen), the solvent contribution and the empty cell effect from the raw signal. Thus the plotted intensity (as a function of Q) (figure 7.3) is coherent in nature. The final result confirms that there is no aggregation present in solution (figure 7.3) otherwise as Q decreases, a significant increase in the scattered intensity would be observed. The same result is obtained for other TMA, TEA and TPA cations (figure 7.4)) and we see no sign of aggregation.
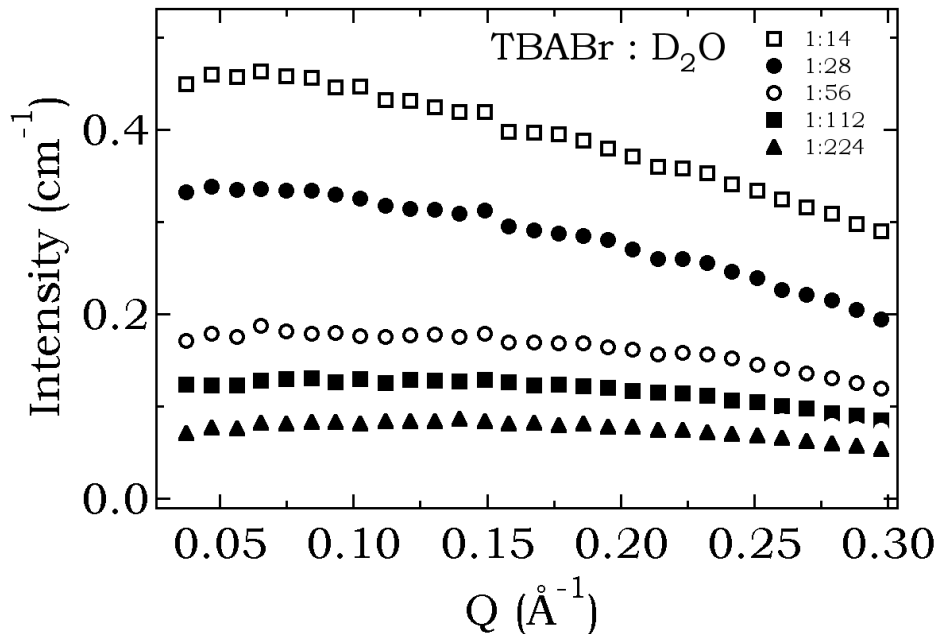
Figure 7.3: SANS coherent intensity (in cm^{-1}) versus the wavevector Q, for a series of aqueous TBABr solutions (with x_m=1:224 to 1:14). Error bars are smaller than symbol size. We do not see any aggregation as the concentration increases.

7.3.2 Origin of Low Q Signal

Looking at figure 7.3, the obvious question is that what is the origin of low Q coherent intensity (the incoherent part is already eliminated)? To interpret,
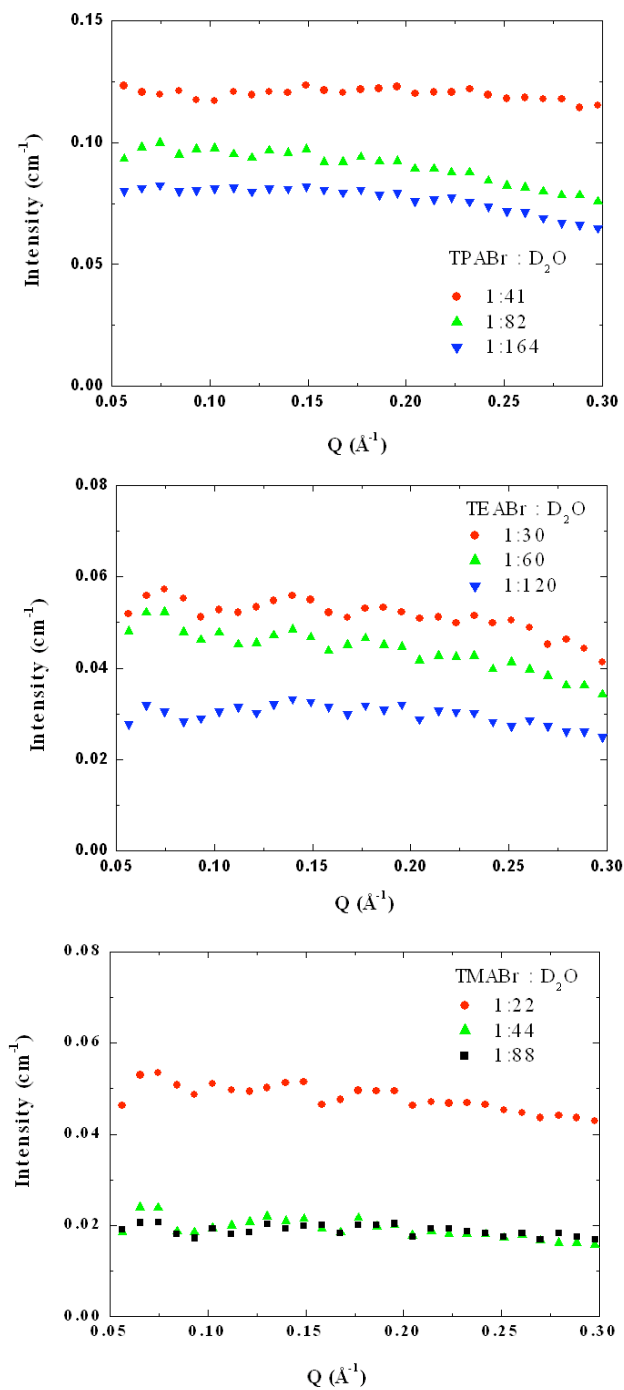
Figure 7.4: SANS coherent intensity (in cm^{-1}) versus the wave-vector Q, for a series of different aqueous TAABr solutions. From top to bottom, TPABr, TEABr and TMABr are in D$_2$O. No sign of aggregation is observed.

we take the coarse-grained model [Kunz 1992b] [Kunz 1992a], where the total system is decoupled into three component - i) cation, ii) anion and iii) solvent. The atomic description of each of the constituent of the ions or D_2O is not taken into account. Thus the coherent intensity is decomposed into the cation-cation, anion-anion and cation-anion correlation functions, according to

$$\mathcal{I}(Q) = \sum_i \sum_j \sqrt{\rho_i \rho_i}(s_i - s_0)v_i(s_j - s_0)v_j P_i(Q)P_j(Q)S_{ij}(Q) \qquad (7.4)$$

where $P_i(Q)$ is form factor of ion i, $S_{ij}(Q)$ is partial structure factor between ions i and j, v_i is partial molar volume (subscript 0 means the solvent), ρ_i is ion number density and the scattering length density of ion i is $s_i = \frac{b_i}{v_i}$ (i can be either $+$ or $-$, b_i is scattering length). For this calculation, volumes are taken from [Wen 1964] [Kim 1973]) and scattering length densities are $4.17 \times 10^9 cm^{-2}$ and $2.15 \times 10^{10} cm^{-2}$ [Dianoux 2003] respectively. Now the condition of electroneutrality requires that all structure factors are equal in the limit of Q=0. So $S_{++}(0) = S_{--}(0) = S_{+-}(0) = S(0)$ and according to the definition of form factor for a sphere $P_n(0) = P_m(0) = 1$. In this limit, we can therefore estimate the relative contributions of the three terms in equation 7.4 to the overall signal. For TBABr in D_2O, we estimate that 92.8% of the overall coherent intensity at Q=0, comes from the cation-cation correlation function, $S_{++}(Q)$ ($S_{--}(Q)$ and $S_{+-}(Q)$ contribute 0.5% and 6.7% respectively).

7.3.3   SANS Data Interpretation

Going back to figure 7.3 and dividing each of the SANS curves by their respective concentration, a single curve can not be obtained (data not shown). This suggests that the interactions between cations exist and the structure factor S(Q) can not be neglected. But having said that, it is also true, within the Q range of SANS measurement the S(Q) is almost a constant and its value depends on the concentration of the system.

Next we take the logarithm of the intensity $[\ln(\mathcal{I})]$ against Q^2 where

$$\mathcal{I} = \mathcal{I}_0 e^{-\frac{R_g^2 Q^2}{3}} \qquad (7.5)$$

Here $\mathcal{I}_0$ is proportional to the structure factor that is dominated by the concentration and the exponential term gives the Q dependence of the form factor (see section 5.5.1 equation 5.33). As TBA is not a spherical cation (with four long hydrocarbon arm) and not sufficiently larger than solvent molecules, it is more logical to calculate the radius of gyration (R_g). In case of a sphere

of radius R, $R_g = \sqrt{\frac{3}{5}}R$. For TBABr, from SANS data, we estimate that R_g is 3.8 Å (figure 7.5). Now considering the TBA hydrocarbon arms as fully stretched, the theoretical calculation of R_g is equal to 4.1 Å. Thus a rough estimate of arms flexibility is $\sim$7%, i.e. (4.1 - 3.8)/4.1. In the later part of dynamical data information, this arms flexibility will be important.
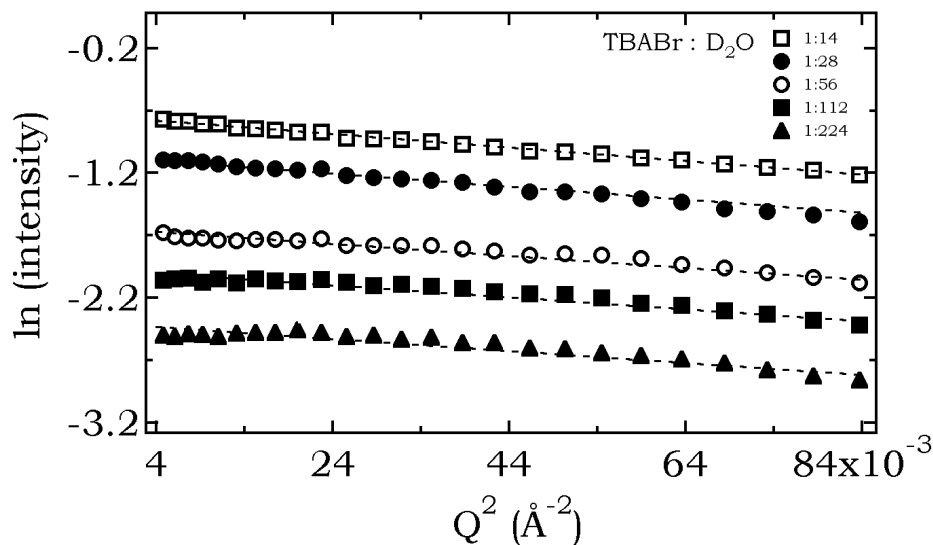
Figure 7.5: Logarithm of the SANS coherent intensity is plotted against the wave-vector Q, for a series of aqueous TBABr solutions (with x_m=1:224 to 1:14) to extract the cation radius of gyration (R_g).

Now we will try if anything can be told about the cation pair correlation. Taking the aqueous TBABr solution with x_m=1:56 and concentrating on it from now on, the average distance between two cation centre of masses can be calculated as 13 Å. Again from the density measurement [Wen 1964], the radius is obtained as 5 Å (which is compatible with radius of gyration calculation, R_g=3.9 Å). This means that little space is left between terminal methyl groups of two adjacent TBA cations. Naturally this conclusion suggests that the electrostatic coulomb repulsive force between two neighboring cations would be very strong, but absence of the repulsive force (as already predicted by SANS data) indicates that it is largely cancelled by the close presence of anions. This supports the cation-anion pair formation in concentrated solution as predicted by other studies [Heyda 2010] [Buchner 2002].

7.3.4   Scattered Coherent Static Signal

In this section we will talk about the structure factor S(Q) of aqueous TBABr solution with x_m=1:56 over a broad Q range combing different techniques. The results are shown in figure 7.6 where the structure factor S(Q) (which is coherent in nature) is extracted from different neutron measurements such as by neutron diffraction (ND) or by already mentioned SANS.

This is also a good opportunity to check whether our simulation field parameters are good enough to produce a S(Q) which would be comparable to the experimental techniques. The details of the MD simulation procedure are discussed in section 6.5. The calculation of S(Q) is performed by taking the positional correlation of the atoms present in the system at time t=0. It is also possible to calculate the S(Q), using the RDFs (Radial Distribution Function) between all the atoms [Kunz 1992b] [Kunz 1991].
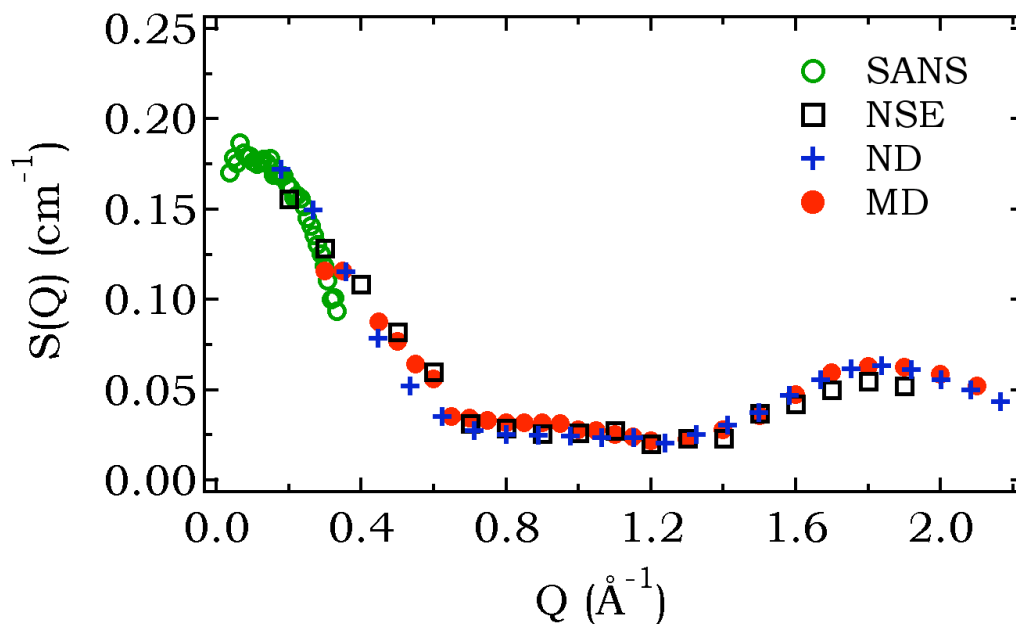
Figure 7.6: Scattered coherent intensity (cm^{-1}) as a function Q of the aqueous TBABr solution with x_m=1:56 by different techniques. The agreement of our MD simulation result with experiments covers a large Q range.

A nice agreement is found among all different techniques, covering a large Q range from Q=0.03 Å^{-1} to 2.2 Å^{-1} (figure 7.6). The increase in intensity of S(Q) at low Q (upto 0.6 Å) is mainly due to the cation-cation (self + different)

correlation which was briefly explained in section 7.3.2. At high Q ($\sim$1.9 Å^{-1}), the slight increase in S(Q) is due to the solvent molecule correlation.

7.3.5   Ion-Ion Correlation

We will first discuss the cation-anion pair distribution function (RDF). Looking into figure 7.7 (a), we find that bromide ions have significantly less pronounced peak for N$^+$ of TBABr but in case Na$^+$ (of NaBr) or N$^+$ of TMABr, distinct correlation peak is observed. This cation-anion RDF also suggests that as the correlation between N$_{TBA+}$ and Br$^-$ goes upto $\sim$4.9 Å, there is probability that bromide can penetrate into cationic hydrocarbon chain of TBA$^+$. Note that The size of the Br ion is 1.96 Å and the distance seen by MD between the central N atom and the TBA$^+$ H atoms of the terminal methyl groups ($\sim$ 4 - 6.2 Å, depending on chain conformation, see figure 7.8). From the figure 7.7 (a), it is also clear that the first N-Br peak has to correspond to a Br ion that stays at least partially inbetween the hydrocarbon arms of the TBA$^+$. The coordination number (CN) calculated from the integral of this first sharp peak yields 0.3 atoms of Br. Considering the second N-Br peak (centred on 8.7 Å), up to 10 Å, we have a CN(Br) of 2, i.e. before the first correlation peak in the N-N g(r) [figure 7.7 (b)]. This proves that there is indeed sufficient negative charge due to Br anions is present between adjacent TBA cations to screen any coulombic repulsion. While confirming the screening of adjacent cations as suggested by structural scattering data, MD clearly shows that the image of TBA$^+$ as spherical impenetrable objects is false on the miscroscopic scale. The penetration can not be seen for TMA$^+$, as the minimum cation-anion distance are larger than the cation size ($\sim$2.2 Å, figure 7.8)). For NaBr, two cation-anion peaks suggest that there are two preferential anion shell around cation or vice-versa.

Moving to the cation-cation pair-distribution function [figure 7.7(b)], we see a small correlation exists around 11 Å for TBA$^+$ while for TMA$^+$ the correlation is higher. The different cation-cation peak for TMA and TBA cation can be explained as follows. The origin of this peak is due to the cationic repulsion. For TBA$^+$, a rough estimate of the distance between two consecutive nitrogen atom (cation Centre of Mass) is $\sim$13 Å. Now the last hydrogen of TBA$^+$ is around 6.2 Å which indicates that two neighboring cations are very closely placed. At the same time recalling the fact that the anion can penetrate up to $\sim$5 Å for TBA cation, the coulombic repulsion between the cations are largely neutralized by the presence of anions (supporting cation-anion pair formation) and leaves a resultant weak repulsive interaction. This fact is further supported by our earlier SANS conclusion and the calculation of structure factor. But is is not the case for TMA$^+$. Although the bromide
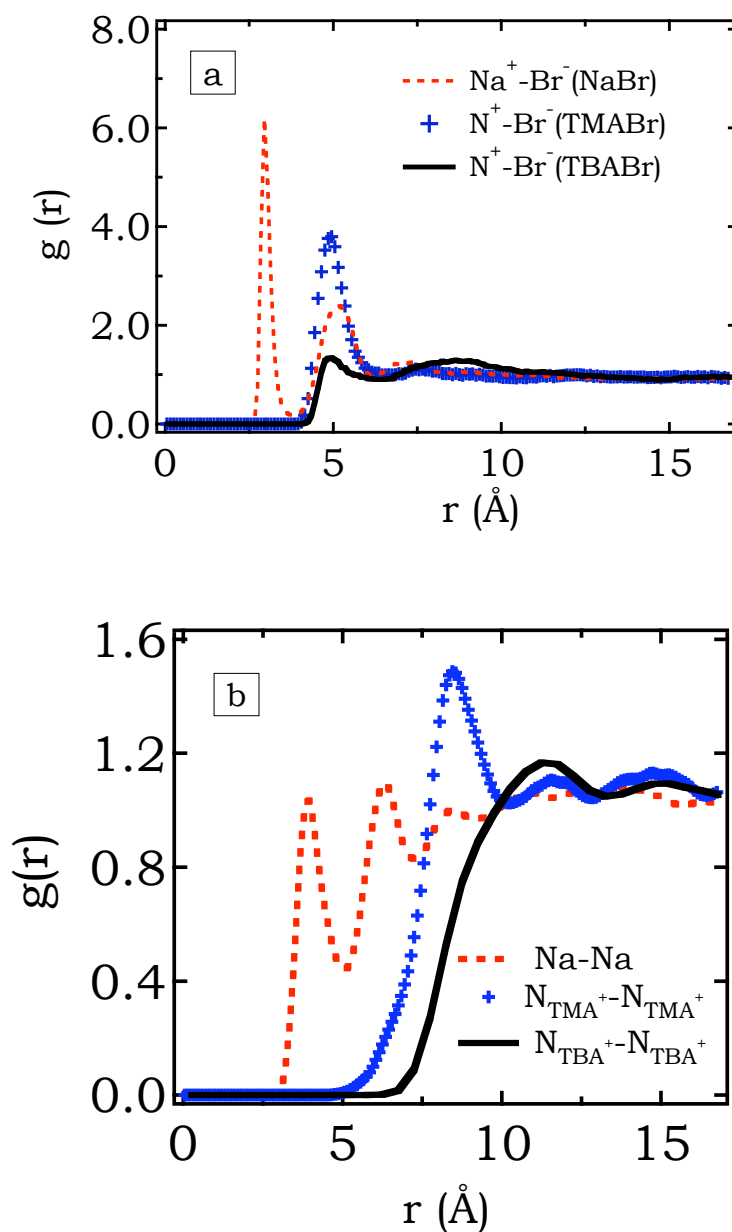
Figure 7.7: Ion-ion radial distribution function of the aqueous TBABr, TMABr and NaBr solution with x_m=1:56. (a) how bromide anion is associated to different cations and penetration in case of TBA$^+$ (b) Some interaction is present around 11 Å for TBA$^+$ cation which is largely nullified by presence of oppositely charged anions.
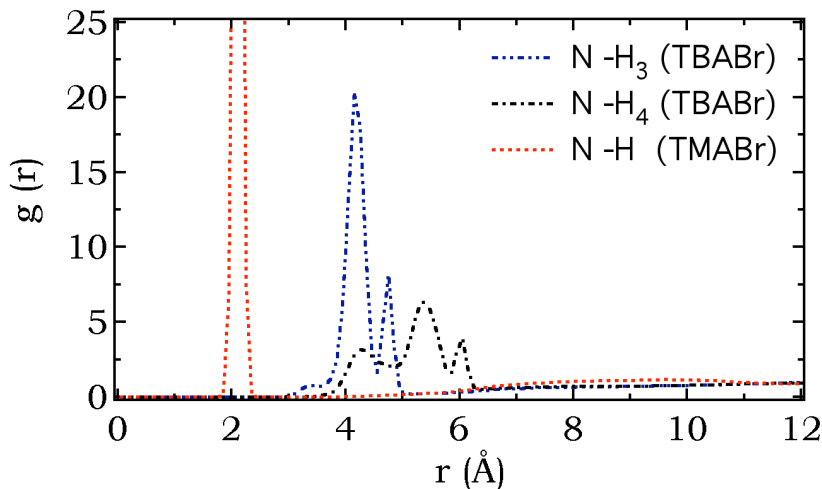
Figure 7.8: The radial distribution function of central Nitrogen and terminal hydrogen atoms of aqueous TBABr and TMABr solution with x_m=1:56. The RDF of hydrogen of third carbon of each alkyl-chain and central nitrogen of TBABr cation is also shown in the figure. It shows that the terminal hydrogen is at ~6.2 Å for TBA$^+$ and ~2.2 Å for TMABr.

ions are present there but they neither go into the cation hydrocarbon chain nor form ion-pair. And thus coulombic repulsion due to cations is not reduced like TBA$^+$. The peak for TMA$^+$ is at shorter distance because of its smaller size. For simple ion (as Na$^+$ presented here), the situation is rather simple. The two cations can not come closer than ~4 Å and their intermediate space is completely filled up by the anions. The dip in Na $^+$ RDF is due to the Br$^-$ ions (i.e. peak in Na$^+$ and Br$^-$ RDF is at the dip of Na$^+$ and Na$^+$ RDF).

If only the RDFs of particle CoM (centre of mass) are taken one can calculate the structure factor S_{CoM}(Q) (figure 7.9). For symmetric TAA$^+$ cation, central nitrogen atom is the cation centre of mass and thus S_{CoM}(Q) is same as S_{NN}(Q). The difference between S(Q) and $S_{CoM}(Q)$ is that while $S_{CoM}(Q)$ determines the positional correlation between particle centre of mass, S(Q) is the product of form factor and $S_{CoM}(Q)$. We continue with the example of aqueous TBABr solution with x_m=1:56. Calculated $S_{CoM}(Q)$ or S_{NN}(Q) for TBA$^+$ cation (figure 7.9), shows a constant value and a small peak around Q=0.65 Å. Then it steadily decreases towards lower Q indicating the presence of some interaction which is also predicted from our earlier SANS experiment. Although it is important to note that the oscillation in the structure factor in figure 7.9 are numerical and non-physical.
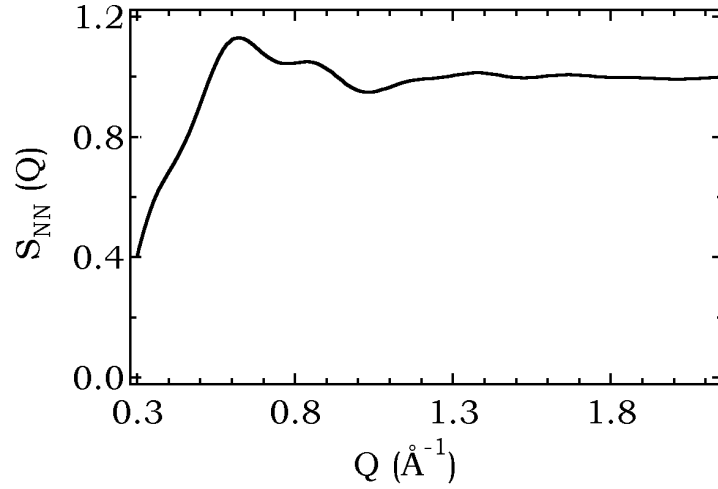
Figure 7.9: Calculated partial structure factor of TBA$^+$ central nitrogen S$_{NN}$(Q) as a function Q, shows constant value and a small peak around Q=0.65 Å and then steadily decreases towards lower Q indicating the presence of some interaction. Nitrogen (N) is the CoM of TBA$^+$.

7.3.6   Effect of Osmotic Coefficient

The asymptotic value of $S(Q)$ at Q=0 indicates the osmotic pressure. The S(0) [Kunz 1992b] can be written as a function of osmotic compressibility

$$
\begin{aligned}
S(Q = 0) &= \frac{1}{4}\rho^2 k_B T \chi_{p,T}^{osm} \\
&= \frac{1}{4}\rho k_B T (\frac{\partial \rho}{\partial \Pi})_{p,T}
\end{aligned}
\tag{7.6}
$$

where ρ is the concentration, T is temperature, $\zeta_{p,T}^{osm}$ and Π are osmotic compressibility and osmotic pressure respectively. Now applying the electroneutrality condition described in section 7.3.2 and recognizing the form factor equals to 1 at Q=0, one can write the total intensity as

$$
\mathcal{I}(Q = 0) = \frac{1}{1000}\frac{c}{2N_A}[(s - s_0)v]^2 \left[\frac{\partial c}{\partial(c\phi^{MM})}\right]
\tag{7.7}
$$

where $s=\frac{s_+ v_+ + s_- v_-}{v_+ + v_-}$ is the scattering length, $\phi^{MM} = \frac{2\beta\Pi}{\rho}$ is the osmotic coefficient at McMillan-Mayer level (molarity scale), c is the concentration of the solute ($c=\frac{N_A \rho}{2}$) in the system with other notations as described as in section 7.3.2. It will be seen that the effect of osmotic pressure becomes more
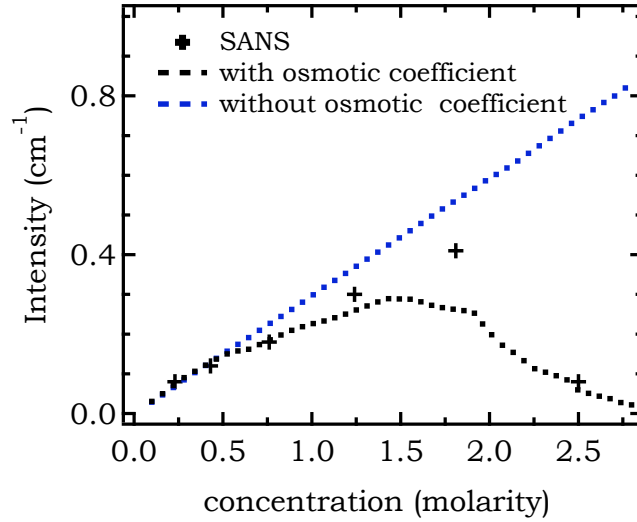
Figure 7.10: Extrapolated SANS intensity at Q=0 as a function of concentration for aqueous TBABr solution with x_m=1:56. The theoretical prediction with and without the effect of osmotic coefficient is shown.

important as we increase the concentration. In figure 7.10 we have compared the extrapolated SANS coherent intensity at Q=0 and recalculated theoretical value with (equation 7.7) and without (equation 7.7 without last part within parentheses i.e. without the dependence of osmotic coefficient as a function of concentration) the osmotic coefficient [Mukherjee 1985] over a large concentration range. The inclusion of osmotic coefficient explains why the intensity decreases as the concentration increases.

7.3.7   Charge-Chrage Structure Factor

Recalling section 4.3.1.2, the partial charge-charge structure factor can be written as

$$S_{ij}(Q) = Z_i Z_j (\delta_{ij} + \frac{4\pi}{Q}\sqrt{\rho_i \rho_j} \int_0^\infty sin(Qr)[g_{ij}(r) - 1]rdr) \qquad (7.8)$$

and the total charge-charge structure factor is expressed as

$$S_{ZZ}(Q) = S_{++}(Q) + 2S_{+-}(Q) + S_{--}(Q) \qquad (7.9)$$

where the symbols have the same meaning as explained before. In figure 7.11, three different partial charge-charge structure factors $S_{++}(Q)$, $S_{+-}(Q)$ and $S_{--}(Q)$ and total charge-charge structure factors $S_{ZZ}(Q)$ are shown for aqueous TBABr and TMABr solution with x_m=1:56 respectively. For a finite Q value ($Q < \kappa$ with κ^{-1} the Debye screening length),

$$S_{ZZ}(Q) \simeq \frac{2Q^2}{\kappa^2} \tag{7.10}$$

where

$$\kappa^2 = 4\pi L_B \sum_i \rho_i Z_i^2 \tag{7.11}$$

Here L_B being the Bjerrum length ($L_B = \frac{\beta e^2}{\varepsilon}$, with ε is the dielectric constant of the solvent). Again we know from the electroneutrality condition that $S_{++}(0) = S_{--}(0) = S_{+-}(0)$=S(0). The result of equation 7.10 is also shown in figure 7.11. The value of S(0) can be evaluated directly from the extrapolation of SANS experimental data at Q=0. The $S_{ZZ}(Q)$ is the result of electrostatic coulomb interaction and has a non-zero value (except at Q=0). This implies that at finite Q, an ion charge can not be totally screened by the other ions. Up to κ the S_{ZZ} is estimated by equation 7.10. $S_{ZZ}(Q)$=0 means that the charge of a particular ion is totally screened by the ions present in the system.

7.4   Conclusion

This chapters describes the structures of TAA ions. We have shown that for aqueous TBABr solution, there is no aggregation up to x_m=1:14 concentration (the same conclusion can be drawn for other smaller TAA cations). The slightly sloped SANS curves helps to estimate the radius of gyration of the cation. From the calculation of radius of gyration and comparing with fully stretched hydrocarbon arms of TBA$^+$ cations, we find that the arms are $\sim$7% flexible. We have shown that there is some cation-cation correlation exists in the TBABr system because a signifiant part of it is neutralized by the close presence of the anion (bromide in this work). From the cation-anion pair correlation function, it is clear that the bromide ions can penetrate inside the alkyl chains of larger TBA$^+$ cation which proves that TBA$^+$ can not be considered as a rigid sphere. We have also shown the variation of coherent intensity as a function of Q over a large Q range by different techniques (both simulation and experiment) with a satisfactory agreement among them where
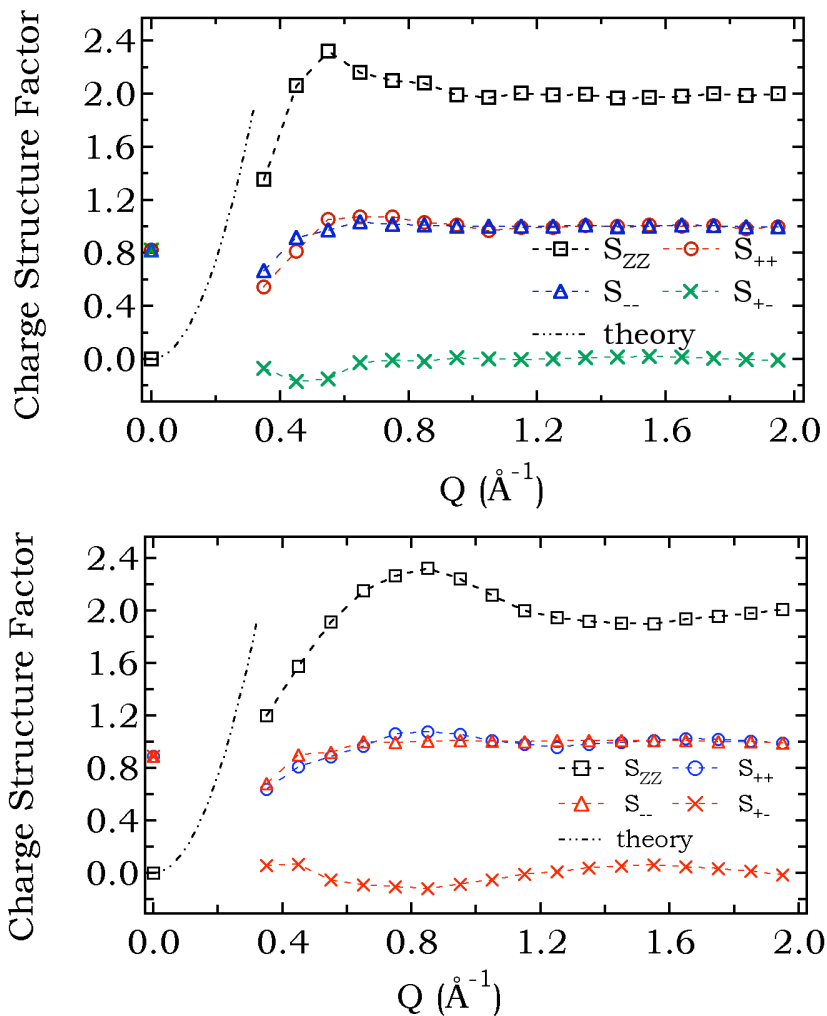
Figure 7.11: Partial ($S_{ij}(Q)$) and total ($S_{ZZ}(Q)$) charge-charge structure factor for TBABr (upper) and TMABr (lower) as a function of Q. At **Q=0**, $S_{ZZ}(0)$=0 and $S_{ij}(0)$= **S(0)**. At finite **Q** value the non-zero value of $S_{ZZ}(Q)$ suggests that an ion charge is not completely screened by other ions. The estimated $S_{ZZ}(Q)$ at $Q < \kappa$ is also plotted in the same graph (denoted by theory).

the low Q coherent intensity mainly comes from cation-cation correlation. From the calculation of charge structure factor, the condition of Stillinger and Lovett is verified which states that the charge of an ion is completely screened by other ions only at Q=0. The effect of osmotic pressure becomes important as the system becomes concentrated.

8

Dynamics of Ions

Contents

8.1 Introduction

After the structure, we present the dynamics of the ions in the current chapter by a combination of TOF, NSE and MD simulation techniques. For studying the micro-dynamics the decoupling of coherent and incoherent signal is necessary. So first we decouple the two different types of signal. The focus will be principally on aqueous TBABr solution and then will show the results from other systems. Along with the results from translational dynamics, global rotation and individual hydrogen dynamics will also be discussed. At the end we will try to find out the temperature dependence of the translational dynamics.

8.2 Decoupling of Coherent and Incoherent Contribution

As said earlier we start by the decoupling of coherent and incoherent contribution. This decoupling is important for studying the dynamics because these two contributions represent two different situations and thus deserve to be treated separately and differently. The coherent scattering represents the correlation between the positions of two nucleus (different and same) at time t=0 and at time t=t′ while the incoherent scattering is originated due to the correlation of the positions of same atom at different times (see section 5.3.2).

8.2.1 Decoupling for Aqueous TBABr Solution

We continue with aqueous TBABr solution of concentration x_m=1:56. Figure 8.1 shows the decomposition of total intensity by NSE polarization analysis into coherent and incoherent contribution (according to equation 5.26) for aqueous TBABr solution with x_m=1:56. The incoherent intensity is featured both without and with a pre-factor of $\frac{1}{3}$ to indicate, respectively, the intensity with which the incoherent dynamic signal is detected in the TOF and NSE techniques. The pre-factor ($\frac{1}{3}$) in equation 5.26 is special in case of NSE incoherent intensity (because of the inherent neutron spin flip during incoherent scattering [Squires 1988]) but not for others (like TOF). This difference is very important for further discussion and the analysis of the dynamic measurements. From figure 8.1, we distinguish three different Q regions. They are i) below 0.65 Å^{-1} where the coherent contribution is predominant, ii) between 0.6 and 1.4 Å^{-1} which is mainly incoherent in nature and iii) above 1.4 Å^{-1} where the coherent contribution is again slightly larger than $\frac{1}{3}$ of incoherent. Among the three regions, the first two are important for the study of ion dynamics. In the first part (below 0.65 Å^{-1}), the NSE measurements are able

to probe the coherent scattering (mainly due to the cation-cation correlation) while in the second part (between 0.6 and 1.4 Å^{-1}) the predominant incoherent signal (originating mainly from hydrogen atoms of the TBA cation) can be measured by TOF. Note that in this region, NSE records a mix of coherent and incoherent signal which are of similar intensities, (both low). Beyond 1.4 Å^{-1}, where again coherent contribution is important over $\frac{1}{3}$ of incoherent background is mainly due to the structural peak of the D$_2$O solvent.
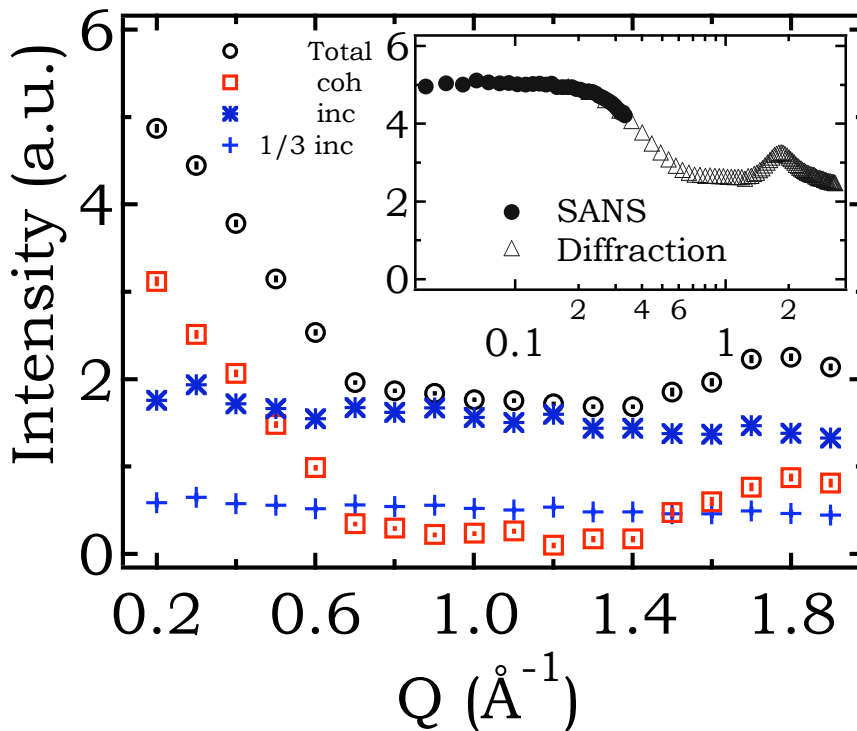
Figure 8.1: **Aqueous solution of TBABr in D$_2$O with x_m=1:56. Total scattered intensity and the decomposition into the coherent and incoherent contribution versus wave-vector Q as measured by NSE (MUSES spectrometer). The diminished incoherent intensity (1/3 inc) reflects the intensity of the incoherent signal contained in the time-dependent NSE measurements. The signal from the quartz sample holder has been subtracted. Insert: For comparison, the total scattered intensity measured by SANS and neutron diffractometer (significantly higher Q-resolution than for NSE).**

Thus in dynamics treatment, our approach will be to use NSE to measure the dynamics related to the coherent signal below 0.6 Å^{-1} and to use TOF to measure the dynamics contained in the incoherent signal in the second region (0.6 to 1.4 Å^{-1}). Here the polarization is low due to almost equal coherent and incoherent contributions. Thus by using the combination of both TOF and NSE techniques in appropriate Q-domains, the self-motion of the constituent H-atoms of the TBA cation or the motion contained in the coherent signal from the solution can be studied.

Other Concentration   After discussing the aqueous TBABr system with x_m=1:56, we have used the same technique of the decoupling of the coherent and incoherent contribution for with x_m=1:112 concentration. As done before, the SANS and simulated result are superimposed one after other in figure 8.2. From simulation we have calculated the $\frac{1}{3}$ of incoherent contribution which can be recorded by the NSE technique. The SANS coherent S(Q) are in agreement with the simulated coherent part. This decoupling of coherent and incoherent contribution is helpful for possible future NSE experiment.
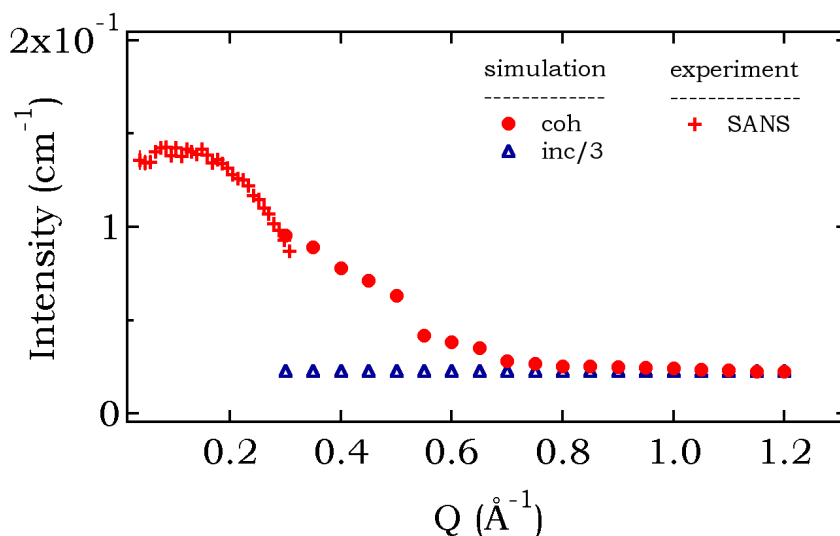
Figure 8.2: Decoupling of coherent and incoherent intensity as a function Q for aqueous TBABr solution with x_m=1:112 (extracted by MD simulation). The coherent SANS signal is in agreement with the predicted simulated result.

8.2.2   Decoupling for Other Systems
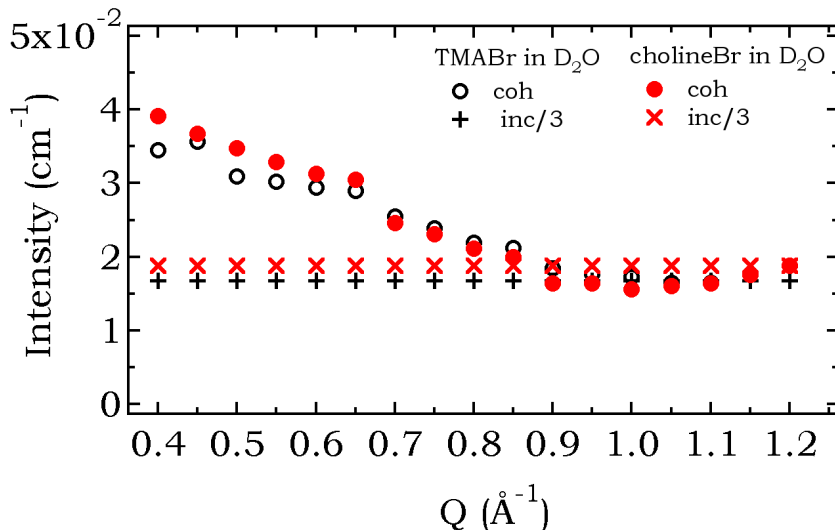
Figure 8.3: **Decoupling of coherent and incoherent intensity as a function Q for aqueous TMABr and CholineBr solution with x_m=1:56 (extracted by MD simulation).**

Similarly we present the application of the previously mentioned simulation method (section 8.2.1) to decouple the coherent and incoherent contribution for aqueous TMABr or CholineBr solution with x_m=1:56. Figure 8.3 shows that both the systems predict almost similar result (with CholineBr solution having slightly larger incoherent contribution because of the more hydrogen atoms than TMABr). But it should be noted that due to smaller size of the cation, the polarization (see 5.4.2.2) is less with large uncertainty in its value and thus experimentally it is difficult to precisely separate the two contributions.

8.3   Dynamics of TBA$^+$: Translation

Now we start analyzing the dynamics of the ions in solution. For the experimental setup see section 5.6 and the simulation details can be found in section 6.5.

8.3.1   Individual Atom Motion

8.3.1.1   Time of Flight Study

We begin by aqueous 1m TBABr solution. As discussed earlier, for hydrogenated TBABr in D_2O with x_m=1:56, incoherent scattering dominates in the region 0.6 to 1.4 Å^{-1}. This is originated from the individual hydrogen atoms of the TBA cation because out of all the elements present in our system, hydrogen has the highest incoherent scattering cross-section [Dianoux 2003]. By the TOF technique, the energy (time) dependence of this incoherent signal will be measured.

The modelling of atomic motion contained in the incoherent signal departs from the hypothesis of decoupling the different kinds of motion on the basis of their different time-scales [Bée 1988]. For the TBA cation in the quasi-elastic region (small energy transfers), we consider according to section 5.37

$$S_{inc}(Q,\omega) = e^{-\frac{1}{3}\langle u^2 \rangle Q^2}\{S^{tr}(Q,\omega) \otimes S^{int}(Q,\omega)\} \tag{8.1}$$

where $\langle u^2 \rangle$ is the mean vibrational displacement and $e^{-\frac{1}{3}\langle u^2 \rangle Q^2}$ is the Debye-Waller factor while superscripts tr and int refer to, respectively, translation (overall ion center-of-mass (CoM) translation) and the internal motion (this encompasses rotational-type motion of H atoms of the individual CH_2 and CH_3 groups within the hydrocarbon arms of the cation). We see that the signature of vibrational motion in the quasi-elastic region is only the energy-(time-) independent Debye-Waller factor. No appreciable Debye-Waller factor was found in our TOF signal, we further concentrate on the tr and int contributions only.

A. First Model Prior to applying the full model in equation 8.1, we attempt at first a rough analysis of the TOF data with a single quasi-elastic (Lorentzian shape) contribution, in addition to an elastic peak and a flat background (the elastic contribution and a flat background is present in all our models and fitting, it corresponds to the signal measured for the empty quartz cell, which was used in our TOF measurements). The broadening of this single contribution was found to be approximately 0.2 meV and it did not show a Q-dependence. This resembles the signal from the rotational motion of CH_3 (methyl) groups [Cabral 2000] [Bée 1988], but viewing the structure of the TBA cation, it is unreasonable to assume that all constituent H atoms, both of the terminal CH_3 groups and of the internal CH_2 groups, carry out a rotational motion as fast as methyl rotation. The latter, referred to as internal hydrogen atoms, are likely to be involved in a significantly more hindered and

slower motion, perhaps as part of the overall arm motion or bending. This is suggested by the low, but non-zero arm flexibility extracted from the SANS data via the radius of gyration.

B. Second Model   After this initial single component analysis, next attempt was to apply the rotational motion only to the terminal methyl groups and treat the "internal" hydrogens as immobile. The data cannot be fitted with such a model, the model predicts an elastic intensity which is 3-4 times higher that the observed value. In conclusion, the internal hydrogens are also seen as mobile on the timescale of the experiment.

C. Third Model   In the next and final model (applied to energy transfers between -0.5 and 0.5 meV), we considered a rotational motion of the terminal methyl groups and allowed an overall ion CoM translation. Thus, starting from Equation 8.1, the expression for $S_{inc}(Q,\omega)$ is

$$S_{inc}(Q,\omega) = B[R^{CH_3}(Q,\omega) \otimes T(Q,\omega)] + C[T(Q,\omega)] \tag{8.2}$$

where the ratio of B and C intensities is fixed to the ratio of the number of hydrogen atoms in the CH_3 and CH_2 families (12 and 24 respectively); $R^{CH_3}(Q,\omega)$ describes the methyl group rotation and $T(Q,\omega)$ the overall ion translation. Taking the models of methyl group rotation (undergoing three fold jumps) and free continuous translation, which both lead to a Lorentzian-type broadening, we arrive at [Chahid 1994] [Cabral 2000] [Bée 1988]

$$\begin{aligned} T(Q,\omega) &= \frac{\Gamma_{tr}}{\pi(\Gamma_{tr}^2 + \omega^2)} \\ R^{CH_3}(Q,\omega) &= A_0(Qr)\delta(\omega) + [1 - A_0(Qr)]\frac{\Gamma_{rot}}{\pi(\Gamma_{rot}^2 + \omega^2)} \end{aligned}$$
$$\tag{8.3}$$

where Γ_{tr} and Γ_{rot} are the translational and rotational broadenings (half width half maxima, HWHM); $A_0(Qr) = \frac{1}{3}[1 + 2j_0(Qr)]$ with $j_0(Qr)$ the zeroth-order spherical Bessel function, $j_0(Qr) = \frac{sin(Qr)}{Qr}$; r is the H-H distance in the methyl group, taken as 1.8 Å. Combining equations 8.2 and 8.3, we obtain

$$S_{inc}(Q,\omega) = \frac{[C + BA_0(Qr)]\Gamma_{tr}}{\pi(\Gamma_{tr}^2 + \omega^2)} + \frac{B[1 - A_0(Qr)]\Gamma}{\pi(\Gamma^2 + \omega^2)} \tag{8.4}$$

where $\Gamma=\Gamma_{tr}+\Gamma_{rot}$. The final model contains therefore a purely translational and a trans-rotational component (in addition to the elastic component of

an imposed intensity accounting for the quartz cell), with respective intensities of $C + BA_0(Qr)$ and $B[1 - A_0(Qr)]$. Even this simplified model has three adjustable parameters (overall intensity $C + B$, Γ_{tr} and Γ_{rot}). Γ_{tr} (in meV) is related to the translational diffusion coefficient, D_{tr} (in Å^{2}ps^{-1}), via $\lim_{Q\to 0}(\Gamma_{tr}) = \hbar D_{tr}Q^2$ and Γ_{rot} (in meV) determines the characteristic methyl group rotational time, τ_{rot} (in ps), via $\Gamma_{rot} = \frac{3\hbar}{2\tau_{rot}}$.

In the actual fitting we impose the broadening of the methyl rotation (at $\sim$5ps [Cabral 2000]) with certain flexibility, the ratio of the translational and trans-rotational intensity predicted by the model and search for the translational-type broadening (i.e. should be Q-dependent/ dispersive). Except at high Q values (>1.6 Å^{-1}) the model fits well the TOF data (refer to figure 8.4). Figure 8.5 features the translational broadening extracted. It increases linearly with Q^2 and corresponds to a translational diffusion coefficient of $(0.24\pm0.03)\times10^{-9}$m^{2}s^{-1}, as extracted from the slope of a linear fit of the translational broadening passing through the origin.

8.3.1.2   Spin Echo Study

For $Q>0.6$ Å^{-1}, we have also carried out test dynamic measurements on NSE. We see from figure 8.1, that in this region NSE polarisation analysis predicts a rather unfavourable mix of coherent and incoherent contributions. However, looking at the total scattered intensity in the insert, between 0.8 and 1.2 Å^{-1}, we arrive at a flat background, typical of incoherent scattering. The residual coherent intensity in this region could be simply the background noise of the polarisation analysis and in the modelling we consider the signal as purely incoherent. We fit the NSE data (obtained at Q=0.8, 1.1 and 1.3 Å^{-1}) with both a translational and a trans-rotational contribution. Note that the equivalent of a Lorentzian broadening in the (Q,ω) domain is an exponential decay in the (Q,t) domain, and a convolution of the translational and rotational contributions becomes a simple product. The Fourier transform of equation 8.4 is therefore

$$I_{inc}(Q,t) = \frac{C + BA_0(Qr)}{B + C}e^{-\frac{t}{\tau_{tr}}} + \frac{B[1 - A_0(Qr)]}{B + C}e^{-t(\frac{1}{\tau_{tr}} + \frac{3}{2\tau_{rot}})} \qquad (8.5)$$

where τ_{rot} is as defined previously and τ_{tr} is the translational relaxation time, for which $\Gamma_{tr} = \frac{\hbar}{\tau_{tr}}$ is true. The intensities of the two terms in equation 8.5 are normalised such that the overall $I_{inc}(Q,t)$ departs from 1 at t=0. In our fitting, imposing the value of τ_{rot} as in the TOF analysis, we arrive at τ_{tr} (or Γ_{tr}). The three values are plotted in figure 8.5 alongside those from TOF. The agreement is good. We note that the polarisation on NSE for $Q>0.6$
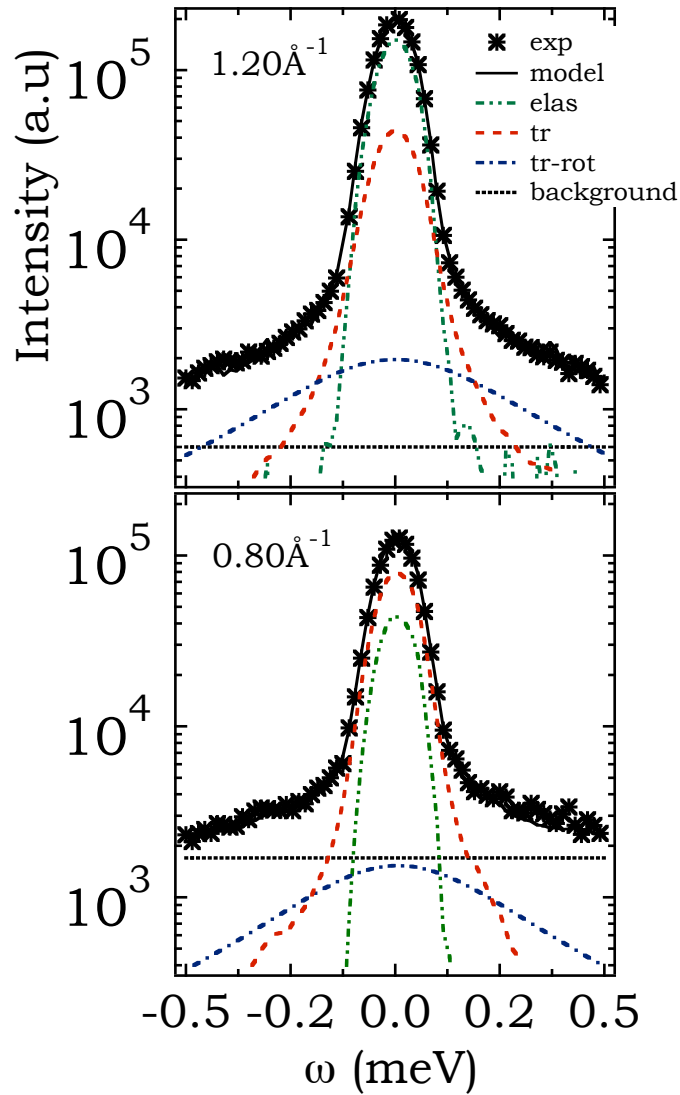
Figure 8.4: Incoherent scattering functions, $S_{inc}(Q,\omega)$, versus energy transfer for Q=1.20 Å^{-1} (top) and Q=0.80 Å^{-1} (bottom) measured by TOF. Different components of the model function are shown: background (dashed black), elastic (green), translational (red), trans-rotational (blue) and total (full black).
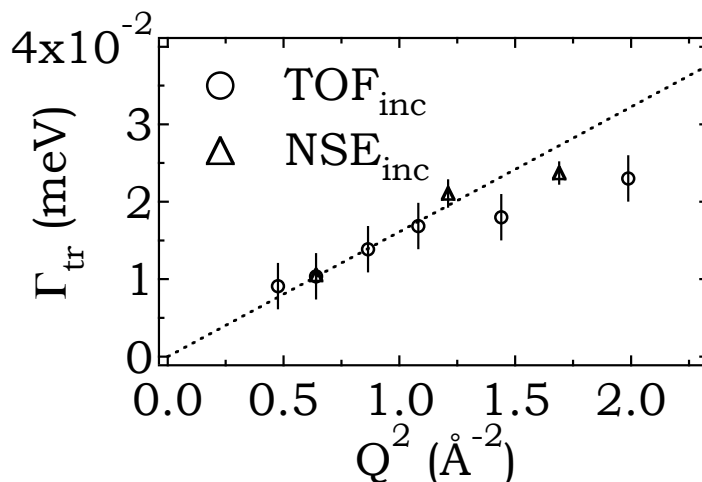
Figure 8.5: Translational broadening, Γ_{tr}, versus Q^2 extracted from the incoherent signal in the middle Q region by as measured by TOF and NSE.

Å^{-1} is rather low (5% approximately) and thus large error bars in the NSE data are present (data not shown). As a result, we did not attempt to draw any conclusions regarding the incoherent dynamics on the basis of NSE, but turned to TOF instead. The fact that the two techniques are in agreement is nevertheless a proof of consistency between them.

8.3.1.3   Simulation Study

We start by presenting the result of MSD (Mean Square Displacement). If we want to compare it with the values extracted from neutron TOF experiment, we must consider two things. First, the MSD of all the hydrogen atoms in TBA$^+$ should be calculated together. This is because the region we have exploited in our TOF experiment, is principally incoherent in nature i.e. it basically highlights average TBA$^+$ hydrogen atom dynamics (solvent is deuterated). From the plotting of TBA$^+$ hydrogen MSD (black circle) as a function of time [insert of figure 8.6 (top)], we distinguish three regions in the curve for H atoms which are time t - i) less than $\sim$5ps, ii) from $\sim$5ps to $\sim$400ps and iii) beyond 400ps. The MSD curves show a non-diffusive (non-linear) behaviour in the first time region (t less than $\sim$5ps). Using equation 6.26, translational diffusion coefficients for H atoms in the other two regions

(below and above 400ps) are calculated as $(0.34\pm0.01)\times10^{-9}$m^{2}s^{-1} ($D_{MSD_H}^{short}$) and $(0.19\pm0.01)\times10^{-9}$m^{2}s^{-1} ($D_{MSD_H}^{long}$) respectively [figure 8.6 (top)]. We also try to extract D_{tr} from incoherent I(Q, t) curves [figure 8.6 (top)] with the TBA$^+$ hydrogen atoms using the same model as defined in equation 8.5. By these I(Q,t) data analysis we deduce $D_{tr} = (0.27\pm0.01)\times10^{-9}$m^{2}s^{-1}. The value of the diffusion coefficient noted here, extracted by $I(Q,t)_{inc}^H$ signal, is intermediate between the two values determined from MSD$_H$ in the regions below and above 400ps. While the MSD representation is more direct and allows to identify clearly distinct temporal regions, in the $I(Q,t)_{inc}^H$ representation the mixing of the different H motions leads to a certain departure from a pure mono-exponential decay (which is indeed seen in the fitting region 1-800ps). The exponential fitting of $I(Q,t)_{inc}^H$ thus results in an intermediate diffusion coefficient for the H atoms.

Secondly, to compare the MSD with our TOF neutron experiment, the time-window we consider in our MSD analysis (in simulation), must be similar to the energy-window of TOF experiment. Because we have mentioned before that the HWHM of our TOF experiment is 50 μeV that corresponds to $\sim$14ps $\left(\tau(ps) = \frac{0.673}{\Gamma(meV)}\right)$, we only need to concentrate up to t=14ps in MSD data. We show that considering all the hydrogens in the ions up to 14ps, D_{tr} equals to $(0.32\pm0.03)\times10^{-9}$m^{2}s^{-1} (black dashed line of figure 8.6 (top)). Before $\sim$5ps, we see a fast dynamics. Please note that all the values mentioned here are corrected by the difference in viscosity between D$_2$O and H$_2$O [Cho 1999] (this is because all the simulation studies are carried out with light water).

8.3.2 Centre of Mass Motion

8.3.2.1 Spin Echo Study

Referring back to Figure 8.1, we see that probing the dynamics of the coherent signal at low Q (<0.6 Å^{-1}) allows us to study the cation Centre of Mass (CoM) motion. The discussion on the interpretation of low Q SANS coherent intensity (see section 7.3.2 and 7.3.3) establishes the fact that the low Q coherent signal comes from the individual cation. The choice of NSE to study the coherent signal is effective because the decreased intensity of the incoherent signal highlights the coherent signal.

The time-dependent intermediate scattering function, obtained from the NSE polarization measurements can be written according to [Mezei 1980] [Bée 1988]

$$I^{NSE}(Q,t) = \frac{P(Q,t)}{P(Q,0)} = \frac{A_{coh}(Q)I'_{coh}(Q,t) - \frac{1}{3}A_{inc}I'_{inc}(Q,t)}{A_{coh}(Q) - \frac{1}{3}A_{inc}} \qquad (8.6)$$
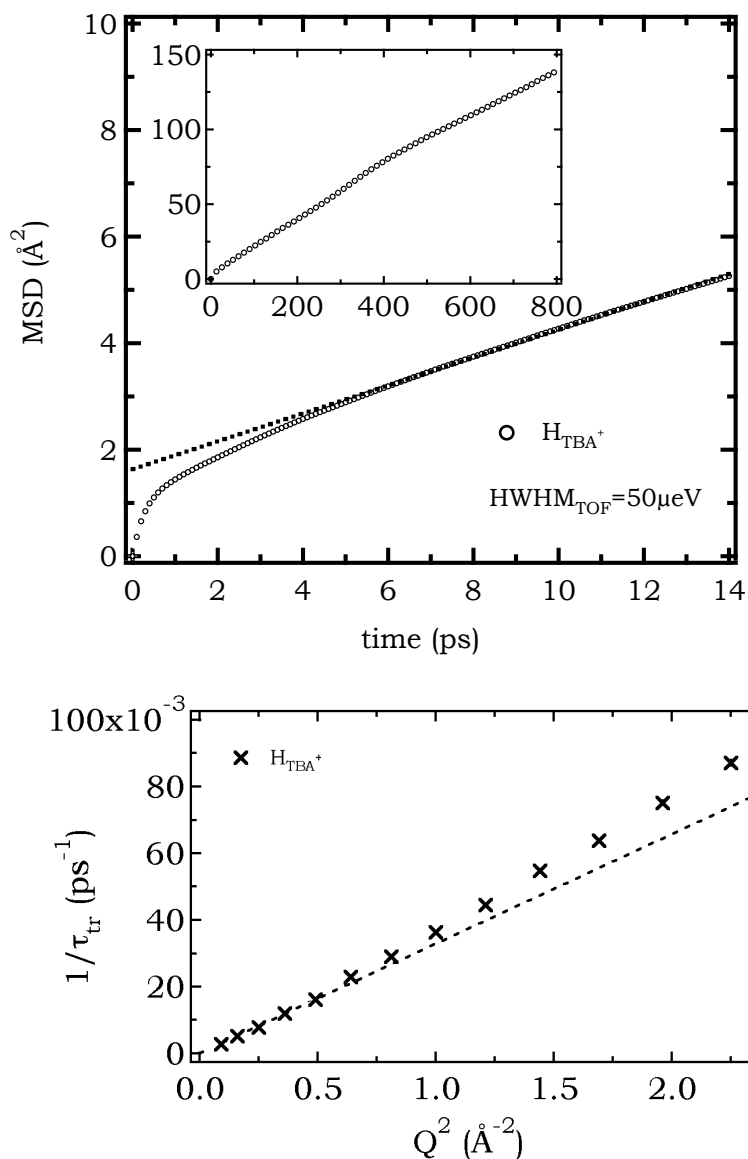
Figure 8.6: (top) D_{tr} extracted from MSD analysis of hydrogen atoms present in aqueous TBABr solutions with x_m=1:56. Note the hydrogen MSD changes its slope after $\sim$400ps which indicates the global rotation time. (bottom) inverse translational relaxation time as a function of Q^2. $I_{inc}(Q,t)$ of average hydrogen predicts an intermediate D_{tr} as in MSD analysis.
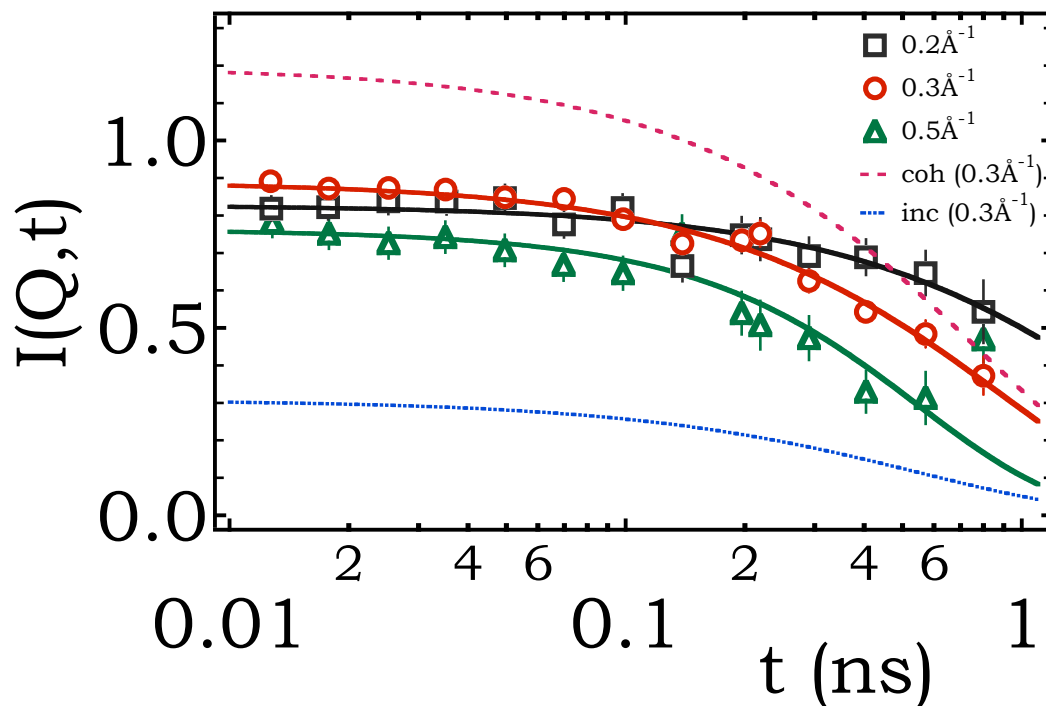
Figure 8.7: Intermediate scattering functions $I^{NSE}(Q,t)$, measured by NSE, for 3 different wave-vectors in the low-Q region (Reseda spectrometer). The signal for Q=0.3 Å^{-1} is decoupled into the coherent and incoherent contribution.

where $I^{NSE}(Q,t)$ is a normalised function (by definition) in time domain. We have measured NSE $I(Q,t)$ curves at three different Q values (at 298K), which are featured in figure 8.7. The polarisation analysis (figure 8.1) indicates that we cannot completely neglect the incoherent contribution in the low Q region. Thus, we fit the NSE data with equation 8.6, in which both $I'_{inc}(Q,t)$ and $I'_{coh}(Q,t)$ are simple exponential functions $[(I'_{inc}(\text{Q,t}) = \text{e}^{-\frac{t}{\tau_{inc}}})$ and $(I'_{coh}(\text{Q,t})$ $= \text{e}^{-\frac{t}{\tau_{coh}}})]$. A single exponential term for the incoherent signal is justified in the low-Q region on the grounds of intensity (the intensity of the second term in the full expression, equation 8.5, is very low at small Q). The use of a single exponential term for the coherent signal (which contains the cation CoM dynamics), at this stage, is a choice of simplicity.

In the fitting of the NSE data sets, the ratio of coherent and incoherent intensity is imposed from the polarisation analysis. The incoherent relaxation time, τ_{inc}, is fixed to the one determined from the incoherent diffusion coefficient obtained by TOF. The two free parameters are therefore τ_{coh} and an overall intensity pre-factor (<1), as we observe that the experimental data do not depart from 1. The inverse of the extracted τ_{coh} behaves linearly with Q^2. It is plotted alongside the Γ_{tr} from the incoherent signal in figure 8.8. The motion contained in the coherent signal shows a diffusive behavior but with a diffusion coefficient of $D_{coh}=(0.12\pm0.01)\times10^{-9}\text{m}^2\text{s}^{-1}$, i.e. about a factor of two lower than the incoherent translational diffusion coefficient determined by TOF. Note that if we model the NSE coherent data with a single exponential (i.e. ignoring the minor incoherent contribution we arrive at $D_{coh}=(0.09\pm0.01)\times10^{-9}\text{m}^2\text{s}^{-1}$, so the error made is not substantial).

8.3.2.2   Simulation Study

The Centre of Mass (CoM) motion is also studied by MD simulation. The analysis can be done in two ways stated as before. It is clear that central nitrogen atom is the CoM of the TBA$^+$ with arms fully stretched (from our earlier SANS experiment we have calculated arms flexibility $\sim$7%). So any diffusive motion of this nitrogen atom will denote the true CoM translational diffusive motion of the ion itself. The MSD analysis of central nitrogen predicts diffusion coefficient as $^{MSD}D_{tr}^N = (0.17\pm0.01)\times10^{-9}\text{m}^2\text{s}^{-1}$ (figure 8.9). The short time fast motion (less than $\sim$1ps) can be due to bond vibration (but this needs to be verified). We can also study the CoM motion by coherent intermediate scattering function $[I_{coh}(\text{Q,t})]$ as a function of time where the position correlations (R_{j_α}, R_{j_β}) are among different and similar kinds of atoms at two distinct times (t=0 and t=t') [Mezei 1980] [Bée 1988] [Squires 1988]. As explained before in section 8.3.2.1, a single exponent is sufficient to extract D_{tr} i.e. $I_{coh}(\text{Q,t}) = \text{e}^{-\frac{t}{\tau_{coh}}}$ with τ_{coh} is the translational relaxation time extracted
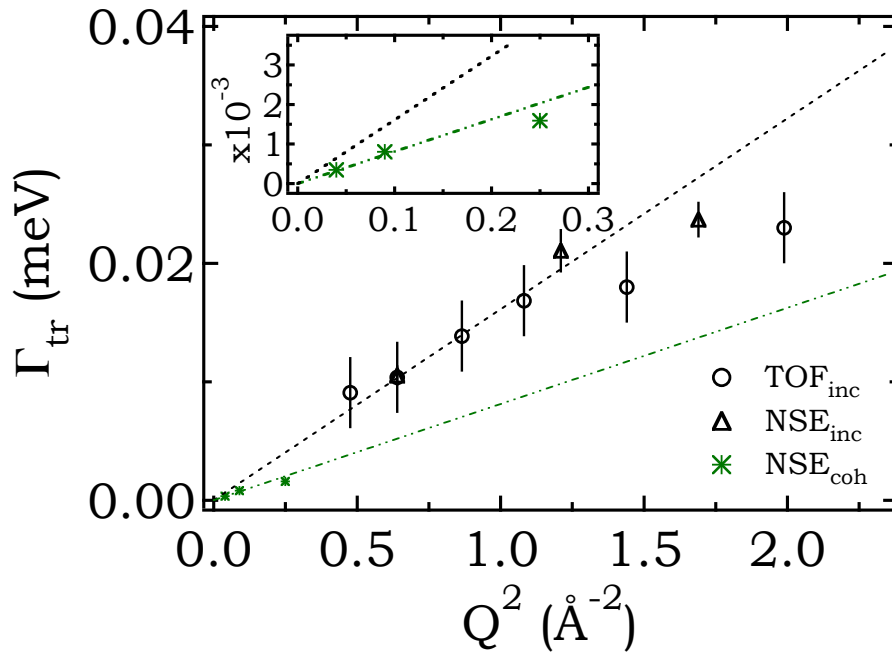
Figure 8.8: Translational broadening, Γ_{tr}, extracted from the incoherent and coherent signal is plotted as a function of Q^2. The broadening Γ_{tr} corresponds to the translational relaxation time, $\Gamma_{tr} = \frac{\hbar}{\tau_{tr}}$. The straight lines correspond to linear fits of the incoherent and coherent broadening from which the corresponding diffusion coefficients were determined. Insert: A zoom of the low Q region.

by coherent analysis. The $I_{coh}(Q,t)$ curves are analyzed for long time and only at low Q (up to $\sim 0.65 \text{Å}^{-1}$) because anything above this Q range will probe inside the ions and at very low Q rotational contribution is negligible (figure 8.10). From $I_{coh}(Q,t)$ analysis, D_{tr} is estimated as $(0.16\pm0.01)\times10^{-9}\text{m}^2\text{s}^{-1}$ [figure 8.11 (b)]. Like before, all the values mentioned here are corrected by the difference in viscosity between D_2O and H_2O [Cho 1999].
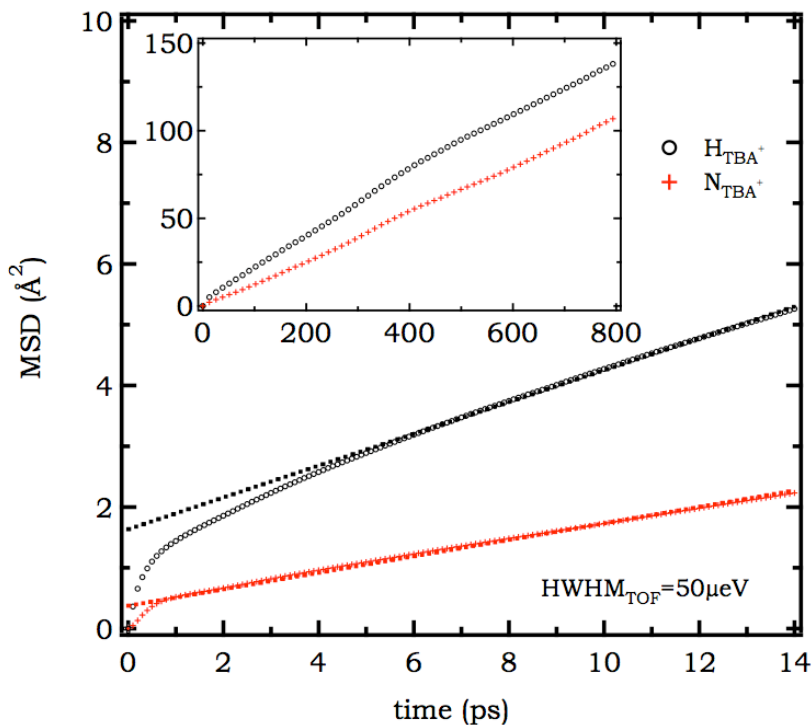
Figure 8.9: (a) D_{tr} extracted from MSD analysis of aqueous TBABr solutions with x_m=1:56. Difference between nitrogen (CoM) motion (red cross) and average hydrogen movement (black circle) in TOF time-window (14ps) is shown. insert: MSD of the same two quantities i.e. nitrogen (CoM) and hydrogen atoms but for a much longer time scale. Note the hydrogen MSD changes its slope after $\sim$400ps.

8.3.3   Comparing Experiment and Simulation

It is important to note that while comparing the experimental and simulation data values, our goal is not to achieve quantitative agreement but we emphasize more on qualitative comparison. Experimentally we have carried
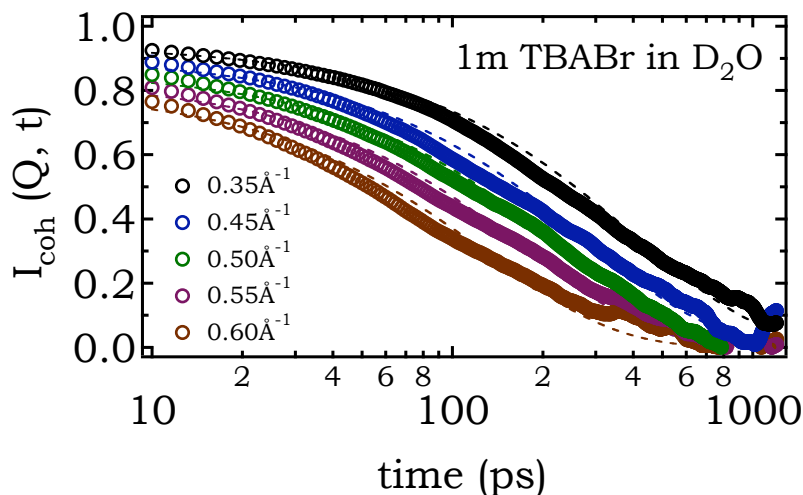
Figure 8.10: Simulated coherent I(Q,t) curves are fitted with single exponential to extract translational relaxation time. The analysis is restricted in low Q region.

the $I_{coh}(Q,t)$ analysis on NSE spectrometer at low Q values (<0.65 Å^{-1}) (as the coherent contribution is predominant in this region, figure 8.1). Using the similar method we have also studied the $I_{coh}(Q,t)$ in simulation to characterize the overall cation translation (by a single exponential fit), figure 8.10. In figure 8.11 (a), we have compared the simulated and experimentally derived I(Q,t) curves for two Q values, Q=0.2 and 0.3 Å^{-1}. These curves are the sum of incoherent and coherent contribution with their respective weightage by equation 8.6. Note while comparing simulated and experimental I(Q,t) curves, viscosity effect must be taken care of i.e the simulation extracted D_{tr} must be divided by 1.24 (difference between water and heavy water [Cho 1999]), in other words the unit timescale of simulated I(Q,t) should be increased by a factor of 1.24. A brief result of the obtained TBA$^+$ cation translational diffusion coefficient D_{tr} is summarized in table 8.1.

Thus we show the estimated D_{tr} extracted from two different approaches - by studying i) individual atom dynamics and ii) CoM motion. In MD simulation, the individual atom dynamics are analyzed by MSD or I(Q,t) of hydrogen atoms and experimentally the same is achieved by QENS incoherent techniques - TOF (and NSE); while CoM motion is probed by MSD (simulation) of nitrogen atoms or by coherent I(Q,t) analysis (simulation or experiment). Interestingly we see that the estimated D_{tr} by coherent dynamic signal is
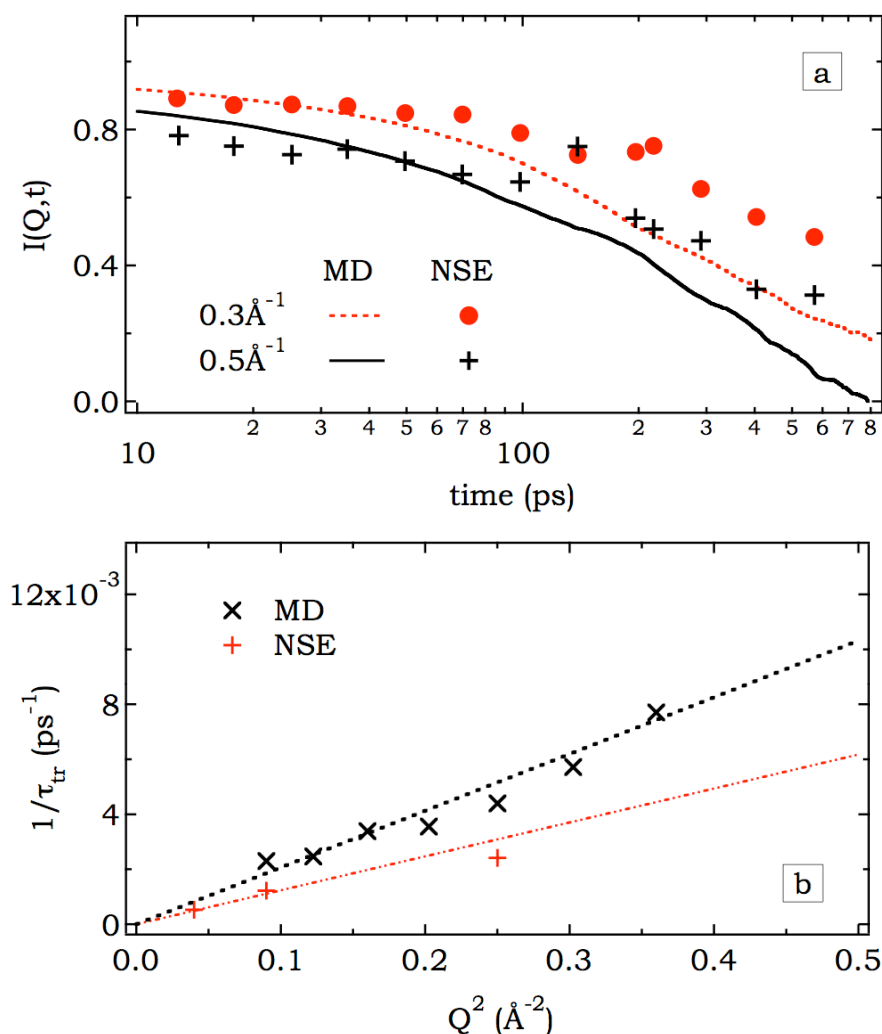
Figure 8.11: (a) The simulated and experimentally extracted I(Q,t) curves. The simulated I(Q,t) is a combination of coherent and incoherent contribution with proportionate weightage. While comparison with NSE experiment, the simulated D_{tr} should be divided by a factor of 1.24 because of the higher viscosity of heavy water (b) inverse of translational relaxation time (extracted from coherent analysis of both MD simulation and NSE experiment) is plotted against Q^2. D_{tr} is estimated from the respective slope passing through origin. The analysis is restricted at low Q region. This allows to track the TBA$^+$ as a whole and ignores the rotational contribution.

			D_{tr} in (10^{-9} m^{2}s^{-1})	
conc.	technique		incoherent	coherent
			(individual H atom)	(CoM)
x_m=1:56	exp	I(Q,t) / S(Q, ω)	(0.24±0.03)	(0.12±0.01)
	sim	I(Q,t)	(0.27±0.01)	(0.16±0.01)
		MSD		
		(short time $<\sim$ 14ps)	(0.34±0.01)	(0.17±0.01)
		(long time $>\sim$ 400ps)	(0.19±0.01)	(0.17±0.01)

Table 8.1: The extracted translational diffusion coefficient D_{tr} for TBA$^+$ cation by different techniques (the simulated D_{tr} is divided by a factor of 1.24 because of the higher viscosity of heavy water)

smaller to incoherent analysis by almost a factor of 2 both in the case of simulation [figure 8.12 (top)] and experiment [figure 8.12 (bottom)].

Note that the MD simulation result overestimates the experimentally observed dynamics by a factor of approximately 1.4 for both individual H atom and CoM motion. But this kind of disagreement is not uncommon and often observed. The reason is the field potentials which are derived for the MD simulations, are tuned for structural data. The disagreements of this order in the dynamics can be considered as very satisfactory [Malikova 2006] [Malikova 2010] [Marry 2011]. Our principal motivation was to use the MD simulation technique to decouple the cation CoM motion from that of individual H atoms motion and to study the dynamics that is on the timescale of ps to ns, to verify if the H atom motion can appear as a faster motion than the cation CoM diffusion as seen in QENS experiment. This was successfully achieved and the relative difference between the coherent and incoherent neutron scattering data is observed in MD simulation.

8.3.4   Why Difference Between Incoherent and Coherent Study?

In this segment we try to answer the discrepancy of the two different kinds of results from two different approaches (from coherent and incoherent analysis). We explain it as follows - TBA$^+$ is itself a big cation and has four long hydrocarbon chains which also move internally. When we analyze TBA$^+$ hydrogen (all) atoms dynamics by a model consisting of translational and a methyl group rotation, we inevitably add the internal motion of those hydro-
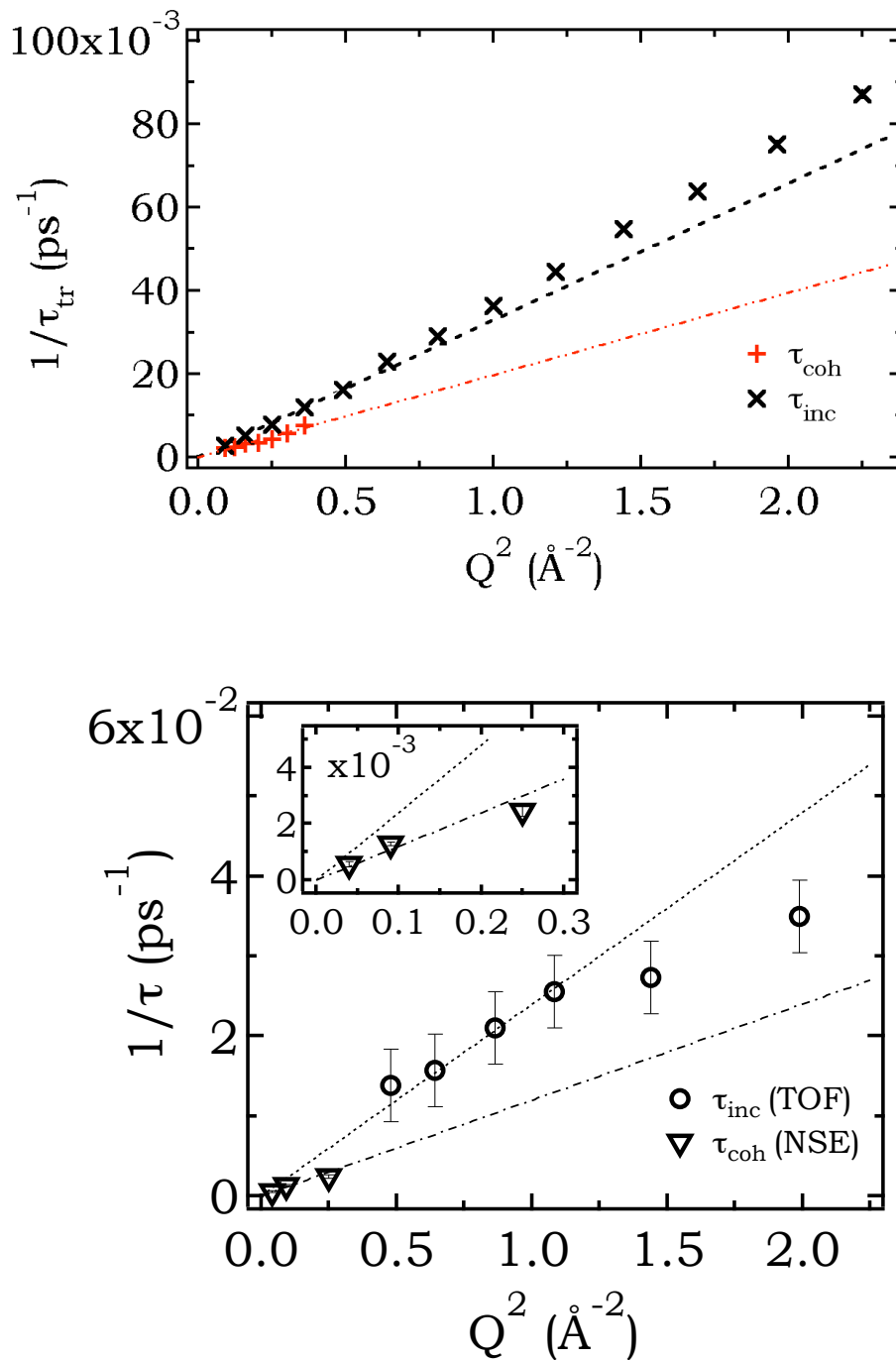
Figure 8.12: (top) MD simulation, (bottom) Neutron experiment. Inverse translational relaxation time plotted as a function of Q^2. The inverse relaxation times (τ_{inc} and τ_{coh}) are extracted from exponential modelling of simulated/ experimental intermediate scattering functions corresponding to the incoherent signal and the total coherent signal.
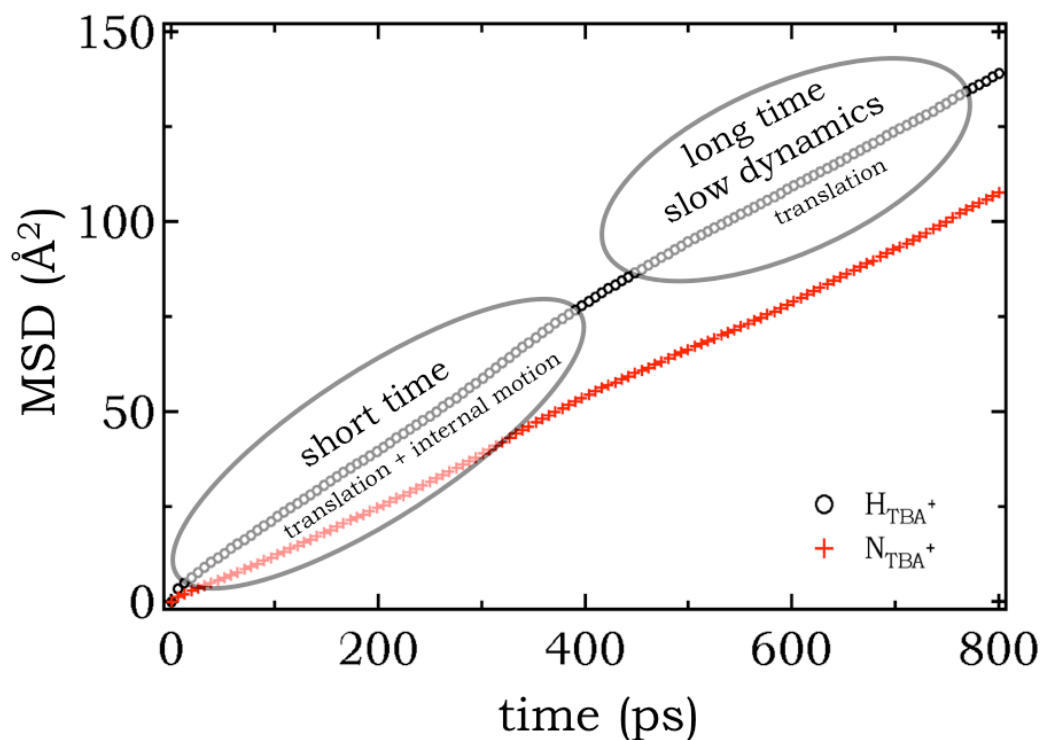
Figure 8.13: MSD of the TBA$^+$ hydrogen atoms as a function of time. Note that the hydrogen MSD changes its slope after ~400ps. The short time (less than ~400ps) can be originated from global cation rotation, individual hydrogen rotation or alkyl chain internal motion.

carbon chains into the translational part and thus the D_{tr} deduced by the incoherent technique predicts a value which is higher than real translational diffusion coefficient. In coherent analysis we do not have this problem because it probes a motion where the correlations among all (same and different) atoms are counted and at very low Q any effect of rotational dynamics is negligible. With the help of coarse-grained description [Kunz 1992b] [Kunz 1992a], it can be calculated that at low Q, most of the coherent intensity [S(Q) at less than <0.65 Å^{-1}] originates from cation-cation correlation (in the limit of Q=0, 92%). Also from SANS data analysis it can be inferred that up to a concentration of x_m=1:14, there is no aggregation and S(Q) at low Q, is mostly characterized by individual cation form factor. Thus it is a way to look at the individual TBA$^+$ cation as a whole to predict the overall cationic translational diffusive motion. In other words the $I_{coh}(Q,t)$ predicts the cation CoM motion because it probes the long time regime while the short time (<∼400ps) H atom motion contains different internal movements apart from the cation translational movement (figure 8.13).

To verify if there is any correlation among TBA$^+$ central N atoms (self + distinct), the resulting inverse relaxation time ($\tau_{N,coh}$) is extracted according to $I_{coh}(\text{Q,t}) = \text{e}^{-\frac{t}{\tau_{N,coh}}}$ and are plotted against Q^2 in figure 8.14. In addition to that (1) a data set labelled $\tau_{all,coh}$ (already explained in section 8.3.2.2 where it is denoted by simply τ_{coh}), which is extracted from the strict equivalent of the experimental $I_{coh}(Q,t)$ signal (all atoms of the cations, anions and solvent contribute to the correlations, weighted by their respective coherent scattering lengths) are plotted against Q^2 along with (2) the inverse relaxation times extracted only from self-correlations of the central N atoms, which is equivalent to tracing the motion of the individual N atoms, as in the case of MSD of central Nitrogen atoms of TBA$^+$ (data set $\tau_{N,inc}$), and (3) inverse relaxation times extracted only from self-correlations of the H atoms of the cations, as in the case of MSD of average hydrogen atoms of TBA$^+$ (data set $\tau_{H,inc}$, (already explained in section 8.3.1.3).

The associated diffusion coefficients for data sets in figure 8.14 are determined from the slope of linear fits passing through origin. Comparing the first two data sets, $\tau_{N,coh}$ and $\tau_{all,coh}$, it is evident that the characteristic relaxation time for the correlations involving all atoms is well described by that corresponding to correlations of only the central N atoms, i.e. cation CoM correlations dominate the overall coherent signal and its time-dependence. Further, these two data sets are themselves almost identical to the $\tau_{N,inc}$ data set, which shows that the correlations between the CoMs of distinct cations are negligible and the coherent signal contains therefore the time-correlations of the CoM of the individual cations, as was our conclusion on the basis of

neutron scattering data. All these data sets lead to the same diffusion coefficient in agreement with the value extracted from MSD of Nitrogen atoms of TBA$^+$ which is different from the average individual H atom motion of TBA$^+$.
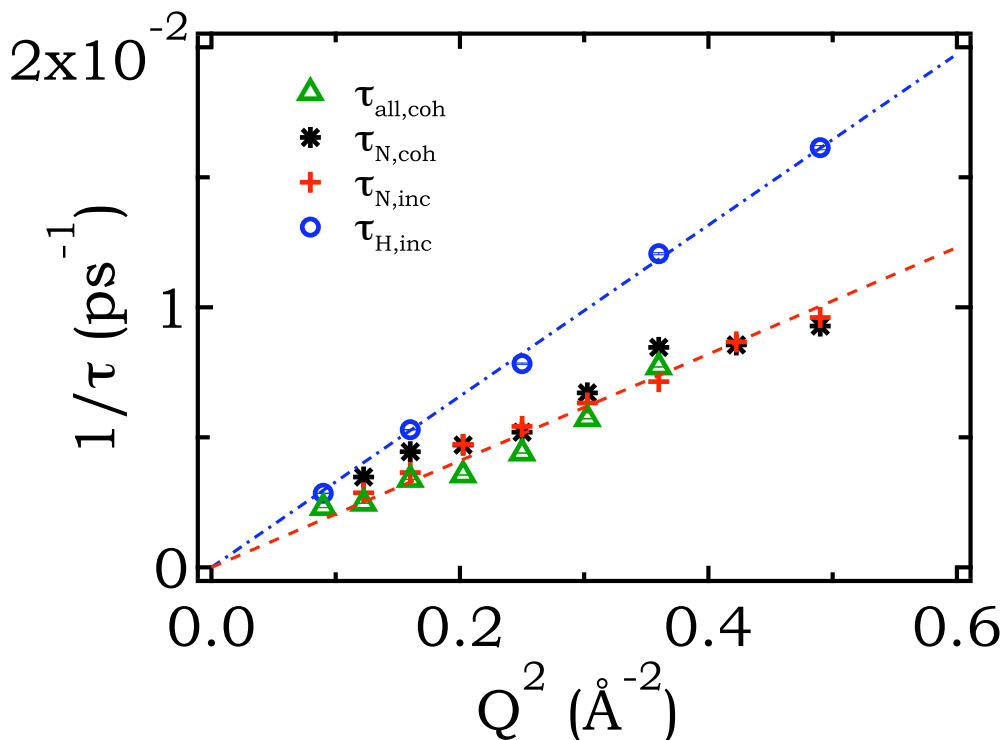
Figure 8.14: **Inverse relaxation times, plotted versus Q^2, extracted from exponential modelling of simulated intermediate scattering functions corresponding to (a) the total coherent signal (τ_{coh}^{all}), (b) correlations (self and distinct) between central N atoms of the cations (τ_{coh}^{N}), (c) *self*-correlations of the central N atoms of the cations (τ_{inc}^{N}) and (d) *self*-correlations of the H atoms of the cations (τ_{inc}^{H}).**

8.4   Dynamics of TBA$^+$: Global Rotation

After studying the translational dynamics of aqueous TBABr solution with x_m=1:56, we move to estimate the global rotational time for the cation. From

the MSD of average hydrogen atoms of TBA$^+$ [figure 8.6 (top)], we have seen that less $\sim$400ps, the hydrogens atom shows a faster dynamics compared to the long time regime (above $\sim$400ps). One possible reasoning for this fast dynamics could be the effect of global rotation which can be estimated by different ways.

8.4.1   Theoretical Study

An estimation of the overall TBA$^+$ rotational time from Debye rotational time [$\tau_{rot}^{glob} = (4\pi\eta R^3)/(3k_bT)$ [Paluch 2003]] predicts approximately 350ps (taking cation radius as $\sim$5 Å with D$_2$O corrected viscosity for aqueous TBABr solution with x_m=1:56 [Buchner 2002] [Eagland 1972]). Now our TOF resolution allows 14ps time window for measurement and the global rotation (of the whole cation) is almost impossible to be detected by our TOF experiment. But the MD simulation can access. For calculating the global rotation time by our MD simulation, we have used two different approaches. The first one is by using MSD and second one is by using the incoherent I(Q, t) analysis for H atoms of TBA$^+$.

8.4.2   Simulation Study

MSD   From the structure of TBA$^+$, we can safely assume that the carbon atoms which are directly attached to central nitrogen, have no other motion except translational motion, global rotation of the cation itself and vibration. Therefore if we calculate the difference of the MSD of these carbon atoms and the central nitrogens, the translational part for carbon atoms can be eliminated and we can extract only the global rotation term. It is then fitted with $2b^2(1 - e^{-\frac{t}{\tau_{rot}^{glob}}})$, where τ_{rot}^{glob} is the global rotational time and b is $\sim$1.5Å as nitrogen-carbon bond length (C.1). We estimate the $\tau_{rot}^{glob} \sim$341ps (figure 8.15). The effect of this global rotation can be also observed in the MSD of TBA$^+$ hydrogens. The change of slope can be clearly observable around 350ps (insert of figure 8.9).

I(Q,t)   In the second method, we consider the incoherent I(Q, t) curves by picking only the hydrogens atoms of the cation. To extract τ_{rot}^{glob} we use a model that consists of i) translational motion of cation (T) ii) terminal methyl group rotation (R$_{rot}^{met}$) iii) global rotation (R$_{rot}^{glob}$) i.e. every hydrogen experiences a translational motion; a rotational motion around the CoM and in addition to that for the terminal methyl hydrogens, there is an additional rotation around the last methyl carbon atom. Thus the complete expression can be written as
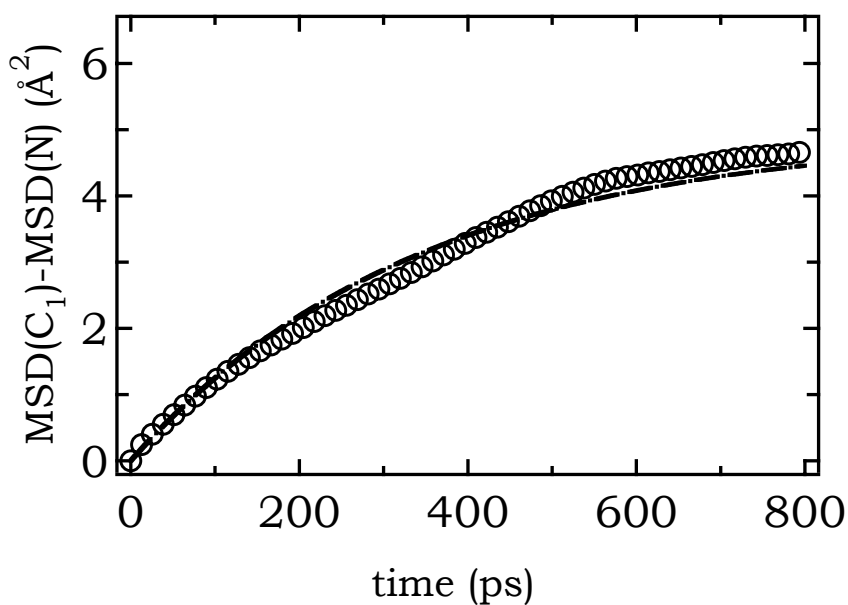
Figure 8.15: **Estimation of global rotation time of TBA$^+$ by MSD analysis. The difference of MSD between carbon (attached directly to central nitrogen) and nitrogen (CoM) atoms are calculated which provides the global rotation time. The fitting equation is $2b^2(1 - e^{-\frac{t}{\tau_{rot}^{glob}}})$, where τ_{rot}^{glob} is the global rotational time and b is the nitrogen-carbon bond length.**

$$I^H(Q,t) = \frac{T(Q,t)}{36}[8R^{glob}_{rot,1}(Q,t) + 8R^{glob}_{rot,2}(Q,t) + 8R^{glob}_{rot,3}(Q,t) +$$
$$12R^{glob}_{rot,4}(Q,t)R^{met}_{rot}(Q,t)] \quad (8.7)$$

where first three terms in equation 8.7, denote the hydrogens in three CH_2 group of TBA$^+$ cation and the last term denotes the methyl group hydrogen motion. We denote different types of motions as follows

$$
\begin{aligned}
T(Q,t) &= e^{-D_{tr}Q^2 t} \\
R^{glob}_{rot,i}(Q,t) &= \sum_{l=1}^{\infty}(2l+1)j_l^2(Q,b)F_{rot}(t), with F_{rot}(t) = e^{-l(l+1)D_r t} \\
R^{met}_{rot}(Q,t) &= \frac{1}{3}[1 + 2j_0(Q,c)] + \frac{2}{3}[1 - j_0(Q,c)]e^{-\frac{t}{3\tau}}
\end{aligned}
\quad (8.8)
$$

where $j_l(Q, b)$ is spherical Bessel function with b refers to the distance between each hydrogen and nitrogen and c is the H-H distance in methyl group [Jones 1988] [Sears 1966b] [Liu 2002]. The fitting is done with all the 18 $I^\alpha_{inc}(Q,t)$ curves at once (spaced equidistantly from 0.2 Å^{-1} to 1.8 Å^{-1}) and calculating l up to 5. This also estimates $\tau \sim$330ps. It is obvious that this global rotation time is out of the TOF time window. Thus incorporating the global rotation term in TOF analysis would not change our conclusion.

8.5 Dynamics of TBA$^+$: Hydrogen Atom Rotation

8.5.1 Methyl Hydrogen Rotation

Our all atom explicit model for TAA cation also permits us to calculate the terminal (or methyl) hydrogen rotation time. In the trajectory file (extracted from the MD simulation), we modify the individual methyl hydrogen atom (of each cation) coordinates relative to its central carbon atoms. This way, the modified methyl hydrogen atoms contain only the rotational motion about respective methyl carbon. Next we calculate the MSD using those hydrogen (with modified coordinates) which is then fitted with $2b^2(1 - e^{-\frac{3t}{\tau^{CH_3}_{rot}}})$, where $\tau^{CH_3}_{rot}$ is the methyl rotational time and b is the carbon-hydrogen bond length $\sim$1.09 Å (C.2). We estimate $\tau^{CH_3}_{rot}$ as $\sim$11ps (figure 8.16). It is important to note that our TOF analysis predicts $\sim$5ps. The difference in experimentally (TOF) extracted and simulated $\tau^{CH_3}_{rot}$ can be explained as follows - in TOF data

analysis, the analyzed $\tau_{rot}^{CH_3}$ is a mixture of alkyl-chain flexibility, cation global rotation and the methyl hydrogen rotation itself. It is difficult to decouple these effects from TOF extracted $\tau_{rot}^{CH_3}$ and thus TOF analyzed $\tau_{rot}^{CH_3}$ is smaller than simulated $\tau_{rot}^{CH_3}$. It is also interesting to know when we apply the same method to estimate $\tau_{rot}^{CH_3}$ for TMA$^+$ for the same concentration, the $\tau_{rot}^{CH_3}$ is $\sim$3.3ps.
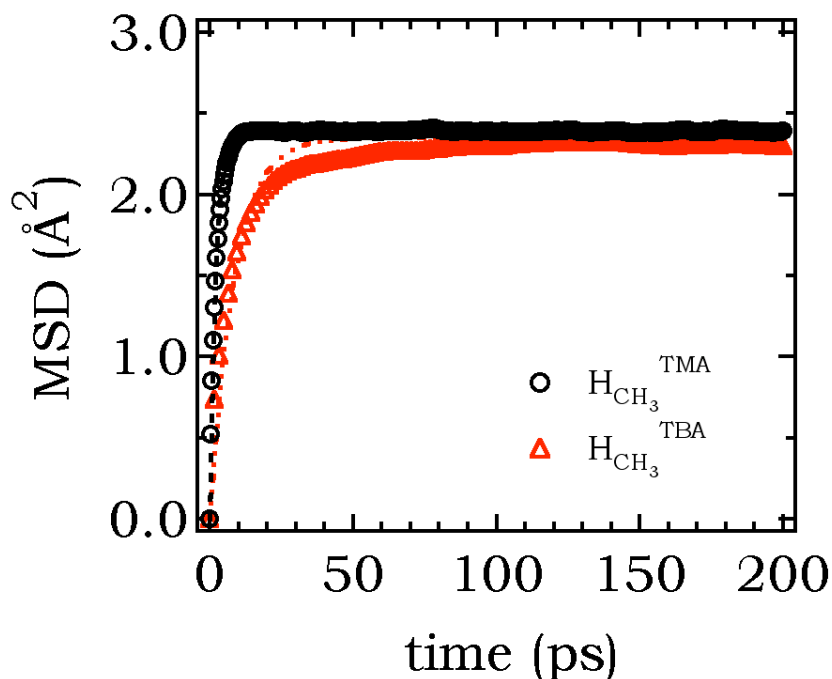
Figure 8.16: MSD of terminal methyl hydrogen atoms (with modified coordinates relative to its central carbon) as a function of time to extract methyl hydrogen rotation time ($\tau_{rot}^{CH_3}$). Black circle (TMA$^+$ methyl hydrogen) and red square (TBA$^+$ methyl hydrogen).

Elastic Incoherent Structure Factor   From the Elastic Incoherent Structure Factor (EISF), it is possible to determine the geometry of the methyl hydrogen rotational motion. From Simulation we derive the EISF by two different methods and both of them produce similar result (figure 8.17). We can calculate the I(Q,t) with the methyl hydrogen atoms with modified coordinates and then plot the I(Q,t) value for long time, as a function of Q. The EISF can also be calculated from the following way [Smith 2007]

$$EISF(\mathbf{Q}) = \frac{1}{N} \sum_\alpha b^2_{\alpha,inc} |\langle \exp[i\mathbf{Q} \cdot \mathbf{R}_\alpha]\rangle|^2. \tag{8.9}$$

where $b_{\alpha,inc}$ $\mathbf{R}_\alpha$ are the incoherent scattering length and the position of the atom α respectively. Note that the MD trajectory length should be long enough so that sampling average over conformational space is carried out well.
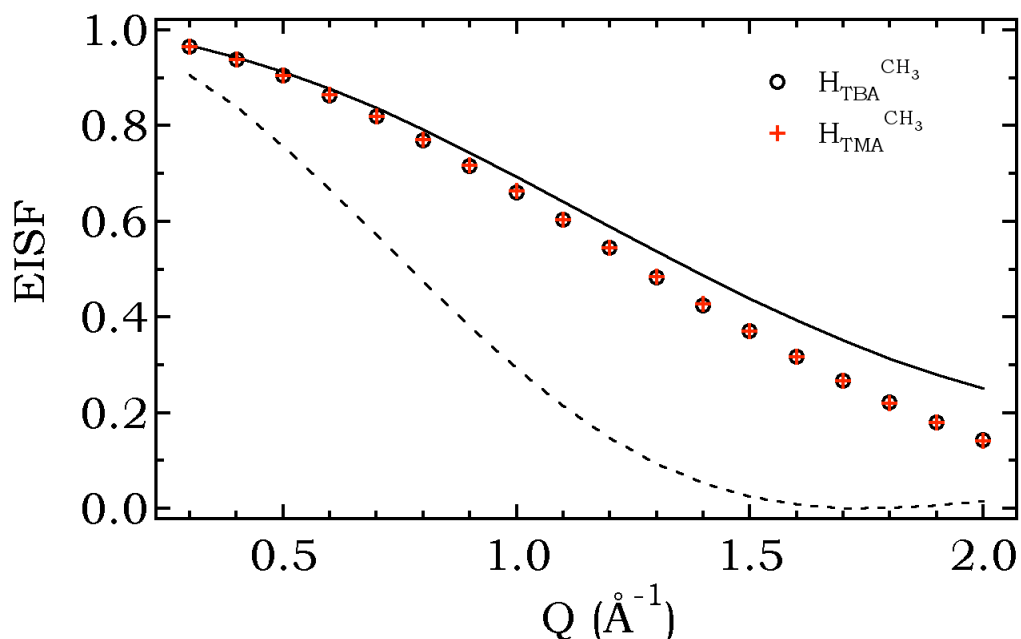
Figure 8.17: Elastic Incoherent Structure Factor (EISF) as a function of Q for methyl hydrogen of TMA$^+$ and TBA$^+$. The solid line is A$_0$(Q) with r =1.8 Å and dashed line is with r free.

In figure 8.17, we plot the EISF of methyl hydrogen of TMA$^+$ and TBA$^+$. In the same figure (figure 8.17) we also plot values calculated by $A_0(Qr) = \frac{1}{3}[1 + 2j_0(Qr)]$ (this is the static part of methyl rotation, see equation 8.4) with r equals to H-H distance as 1.8 Å (solid line in figure 8.17). It represents the methyl hydrogen rotation on a circle (denoted by solid black line in figure 8.17. Comparing with the rotation on a sphere (denoted by dashed line in figure 8.17), we conclude that the model of methyl hydrogen atoms rotating on a circle is much closer to the MD data compared to the model of rotation on a sphere.

8.5.2   Individual Hydrogen Atom Rotation
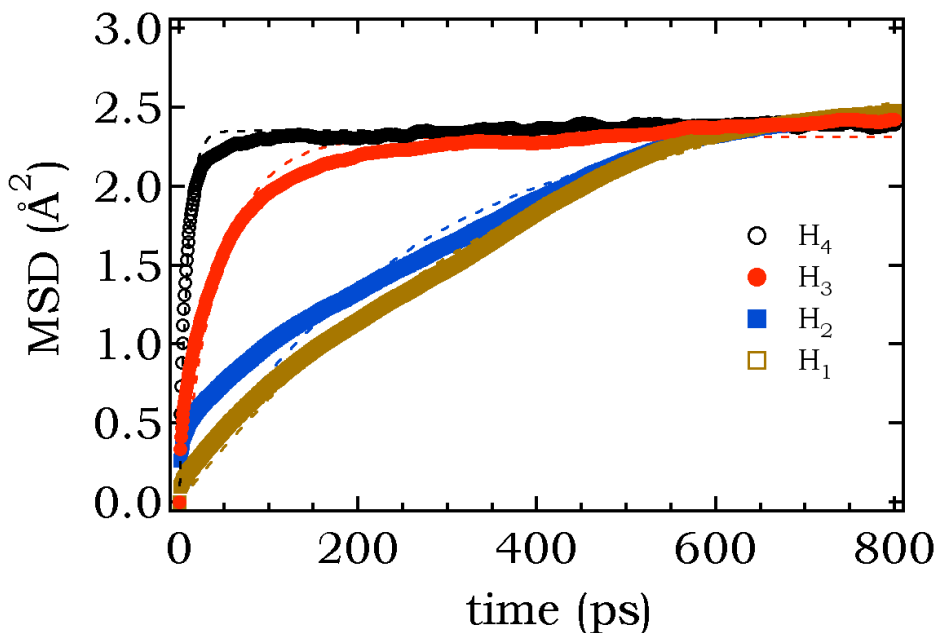
Figure 8.18: MSD of different hydrogen atoms (with modified co-ordinates relative to its central carbon) of TBA$^+$ as a function of time. The suffix of different hydrogens are named after each carbon atom in alkyl-chain.

We also plot the rotational movement for different TBA$^+$ hydrogen atoms about their adjacent carbon atoms (figure 8.18). We see that the last two types of hydrogen atoms (attached to last two carbons of each alkyl-chain) rotational times is faster than the the other two types of hydrogens (attached to first two carbons of each alkyl-chain). using again $2b^2(1 - e^{-\frac{3t}{\tau_{rot}}})$, we find the rotational times for H_4, H_3, H_2 and H_1 are $\sim$11ps, $\sim$67ps, $\sim$384ps and $\sim$586ps. Note that the simple model $2b^2(1 - e^{-\frac{3t}{\tau_{rot}}})$ does not apply well to the hydrogens close to the central nitrogen as the hindrance of the carbon chain attached to C_1 and C_2 is increasingly important and departure from a rotation on a circle for the H atoms is expected.
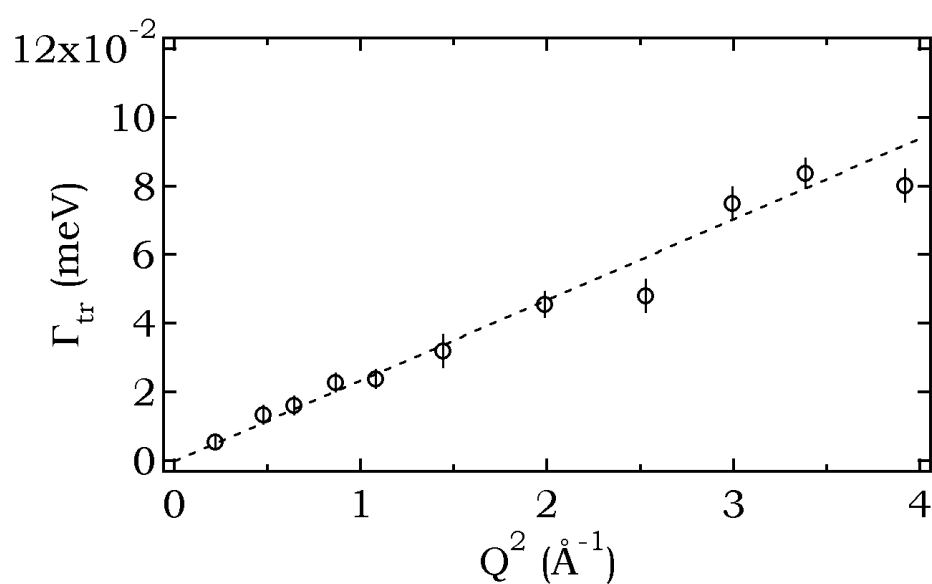
Figure 8.19: Γ_{tr} from TOF measurement for aqueous TBABr solution with x_m=1:112 is plotted as a function Q^2. The translational diffusion coefficient D_{tr} is calculated from a linear fit passing through origin (continuous diffusion).

8.6   Dynamics of TBA$^+$ at Different Concentrations

We have also applied the model with TBA$^+$ translation with its methyl group rotating (equation 8.4) at a lower concentration with x_m=1:112. The model predicts $D_{tr} = (0.35\pm0.03)\times10^{-9}$m^{2}s^{-1} from the TOF experimental data (figure 8.19). To see whether individual TBA$^+$ hydrogen atom and centre of mass motion is different, we have compared the MSD result of TBA$^+$ hydrogen and central nitrogen (figure 8.20) from our MD simulation. Again we see a difference in translation diffusion coefficient extracted by the two methods with a time window (14ps) comparable to our TOF experiment resolution. While $D_{tr}^H = (0.43\pm0.02)\times10^{-9}$m^{2}s^{-1}, we find $D_{tr}^N = (0.24\pm0.02)\times10^{-9}$m^{2}s^{-1}. The factor is close to 2. We have also verified that by the coherent study of the ion (by MD) in low Q domain (Figure 8.21), by which extracted D_{tr}^{coh} [$(0.26\pm0.03)\times10^{-9}$m^{2}s^{-1}] is closer to D_{tr}^N. An estimation of global rotational time for TBA$^+$ cation (see section 8.4.2) at this concentration gives $\sim$670ps. The MSD of average hydrogen atoms above $\sim$650ps predicts D_{tr}^{coh} $(0.26\pm0.03)\times10^{-9}$m^{2}s^{-1} (figure 8.20) which is comparable to low Q coherent or MSD analysis of Nitrogen atom. These results nonetheless validate our point that by coherent analysis (at low Q, where rotational dynamics is negligible) one can extract the centre of mass dynamics (which can also be predicted by MSD of central nitrogen) and these two approaches agree with the individual H-atom motion if there is no other internal motion. Table 8.2 summarizes the data of aqueous TBABr solution for 2 different concentrations analyzed with x_m=1:56 and x_m=1:112.

8.7   Dynamics of Other Systems

In this section, a brief comparative study will be presented for translational dynamics in aqueous TMABr and CholineBr solution with x_m=1:22 and x_m=1:56. We have carried out the NSE measurement at low Q ($<$0.6 Å^{-1}) for aqueous solution of TMABr with x_m=1:22. In figure 8.22 we have plotted the inverse relaxation time as a function of Q^2 extracted from the I(Q,t) coherent analysis. This estimates D_{tr}=$(0.72\pm0.10)\times10^{-9}$m^{2}s^{-1}. But due to very low polarization the uncertainty in the result is very high. Regarding this experimental difficulty in NSE coherent analysis for ions like (TMA$^+$ or Choline$^+$) we move to TOF noting the fact that the TOF could overestimates the true cation CoM translational motion. But at the same time, we know that it can be verified by MD simulation as we did for TBA$^+$. For the TOF data fitting
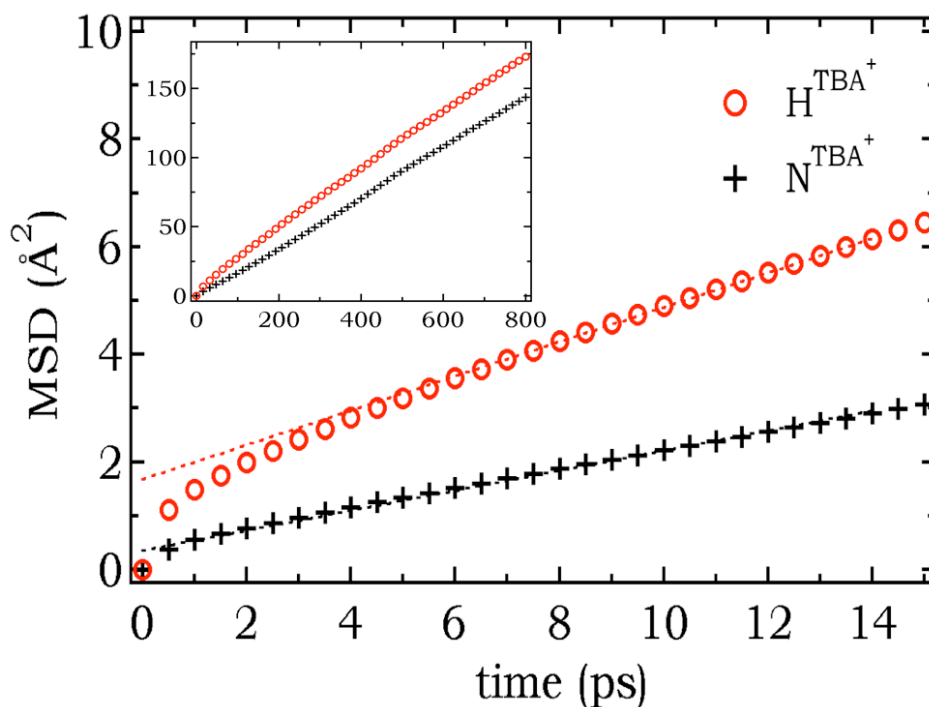
Figure 8.20: The MSD of central nitrogen and average hydrogen atoms of aqueous TBABr solution with x_m=1:112.
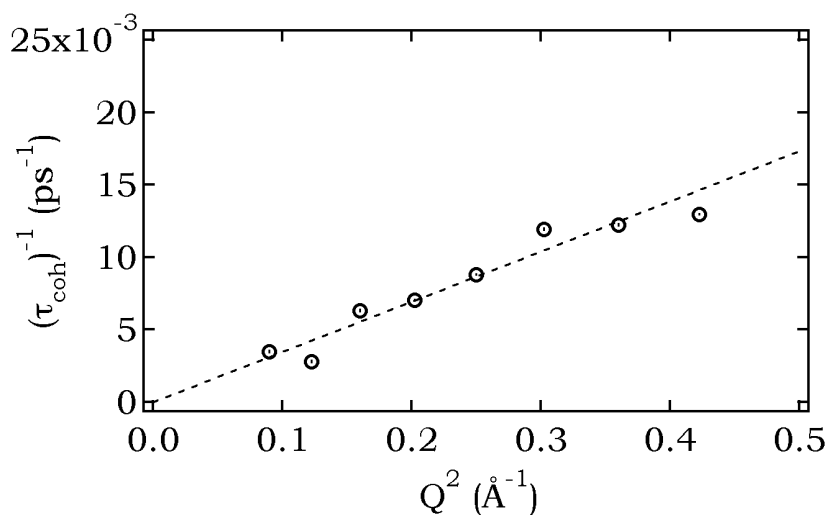
Figure 8.21: Inverse of translational relaxation time (extracted from simulated coherent I(Q,t) curves are plotted as a function of Q^2 for aqueous TBABr solution with x_m=1:112. The D_{tr} from a linear fit passing through origin (continuous diffusion).

| conc. | technique | | D_{tr} in $(10^{-9}$ m^{2}s$^{-1})$ | |
			incoherent (individual H atom)	coherent (CoM)
x_m=1:56	exp	I(Q,t) / S(Q, ω)	(0.24±0.03)	(0.12±0.01)
	sim	I(Q,t)	(0.27±0.01)	(0.16±0.01)
		MSD		
		(short time $<\sim$ 14ps)	(0.34±0.01)	(0.17±0.01)
		(long time $>\sim$ 400ps)	(0.19±0.01)	(0.17±0.01)
x_m=1:112	exp	S(Q, ω)	(0.35±0.03)	
	sim	I(Q,t)	(0.33±0.01)	(0.26±0.03)
		MSD		
		(short time $<\sim$ 14ps)	(0.43±0.01)	(0.24±0.01)
		(long time $>\sim$ 670ps)	(0.26±0.01)	(0.25±0.01)

Table 8.2: **Translational diffusion coefficient of TBA$^+$ is calculated via coherent and incoherent analysis combing both experimental and simulation techniques.**
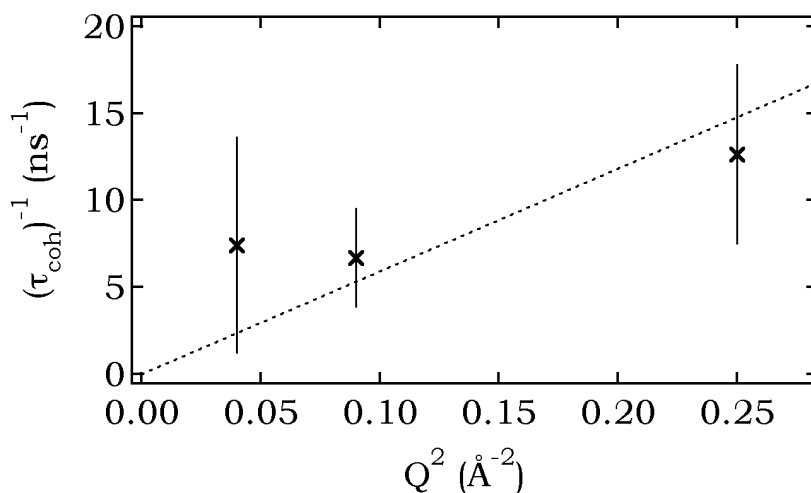
Figure 8.22: **Inverse of translational relaxation time extracted from NSE coherent I(Q,t) curves is plotted as a function of Q^2 for aqueous TMABr solution with x_m=1:22. The D_{tr} is extracted from a linear fit passing through origin (continuous diffusion).**

conc.		D_{tr} in (10^{-9} m^{2}s^{-1})	
		individual H atom	central Nitrogen
x_m=1:56	TOF	(0.98±0.10)	
	MSD	(0.91±0.01)	(0.75±0.01)
x_m=1:22	TOF	(0.81±0.07)	
	MSD	(0.69±0.01)	(0.56±0.01)

Table 8.3: Translational diffusion coefficient for TMA$^+$ calculated via coherent and incoherent analysis combing both experimental and simulation technique

conc.		D_{tr} in (10^{-9} m^{2}s^{-1})	
		individual H atom	central Nitrogen
x_m=1:56	TOF	(1.08±0.03)	
	MSD	(0.94±0.01)	(0.67±0.01)
x_m=1:22	TOF	(0.72±0.10)	
	MSD	(0.77±0.01)	(0.44±0.01)

Table 8.4: Translational diffusion coefficient for Choline$^+$ calculated via coherent and incoherent analysis combing both experimental and simulation technique

we have used the same model as in aqueous TBABr TOF data analysis (equation 8.4). In figure 8.23, we have shown the inverse translational relaxation time extracted by TOF experiment for the above mentioned systems. We have found a decrease in cationic translational diffusion coefficient with increase of concentration (as expected) and this decrease in more pronounced in case of cholineBr than TMABr. The results show that at a solution concentration with x_m=1:56 D_{tr} for TMA and choline cation are (0.98±0.10)×10^{-9}m^{2}s^{-1} and (1.08±0.07)×10^{-9}m^{2}s^{-1} while at solution concentration with x_m=1:22 the values are (0.81±0.03)×10^{-9}m^{2}s^{-1} and (0.72±0.10)×10^{-9}m^{2}s^{-1} respectively.

Although comparing the TOF with NSE coherent result for aqueous TMABr solution (with x_m=1:56), we see the NSE coherent data are close to TOF value. This is because the TMA$^+$ does not have long hydro-carbon chains and as a result the internal movement is also lesser than TBA$^+$. Thus both NSE coherent and TOF incoherent data do not differ much for TMA$^+$. But this is not the case for CholineBr (see table 8.3 and 8.4). One alkyl arm of Choline cation is much longer than TMA$^+$ and due to its internal movement, the difference in estimated D$_{tr}$ from incoherent and coherent analysis for Choline$^+$ is higher than for TMA$^+$. This can also be seen from the MSD analysis of the average hydrogen atoms of TMA$^+$, Choline$^+$ and TBA$^+$
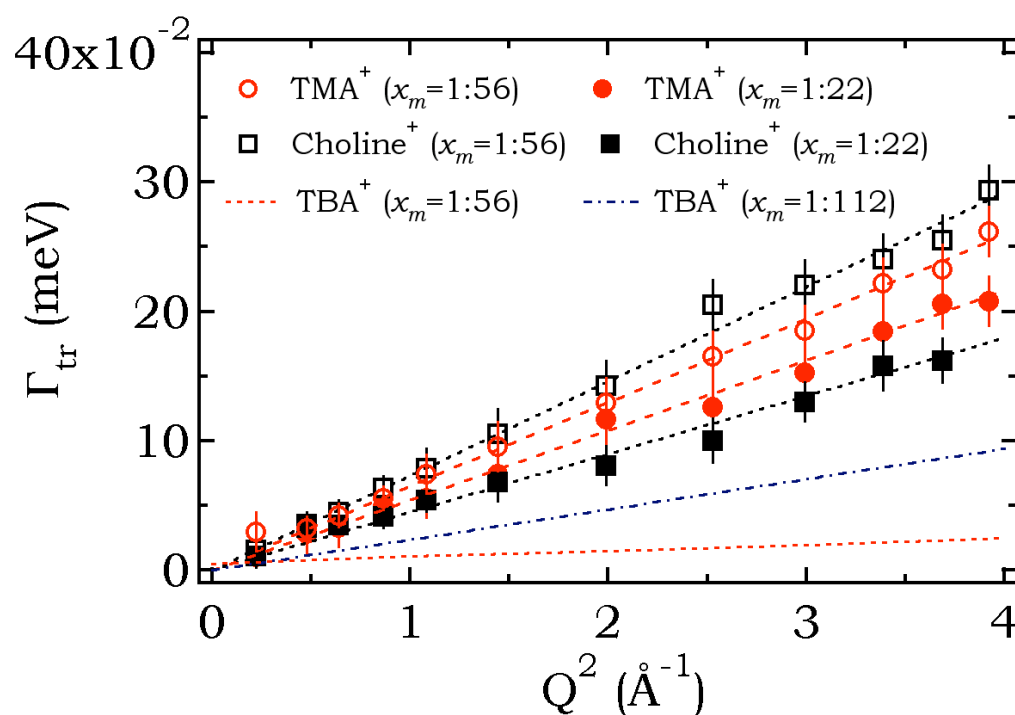
Figure 8.23: Γ_{tr} **extracted from TOF measurement for different cations at different concentrations, are plotted as a function** Q^2**. The translational diffusion coefficient** D_{tr} **is calculated from a linear fit passing through origin (continuous diffusion).**

cation (figure 8.24) where it is evident that the hydrogen atoms in TBA$^+$ and Choline$^+$ have faster motion below ~400ps due to various internal motion while this is not the case for TMA$^+$.
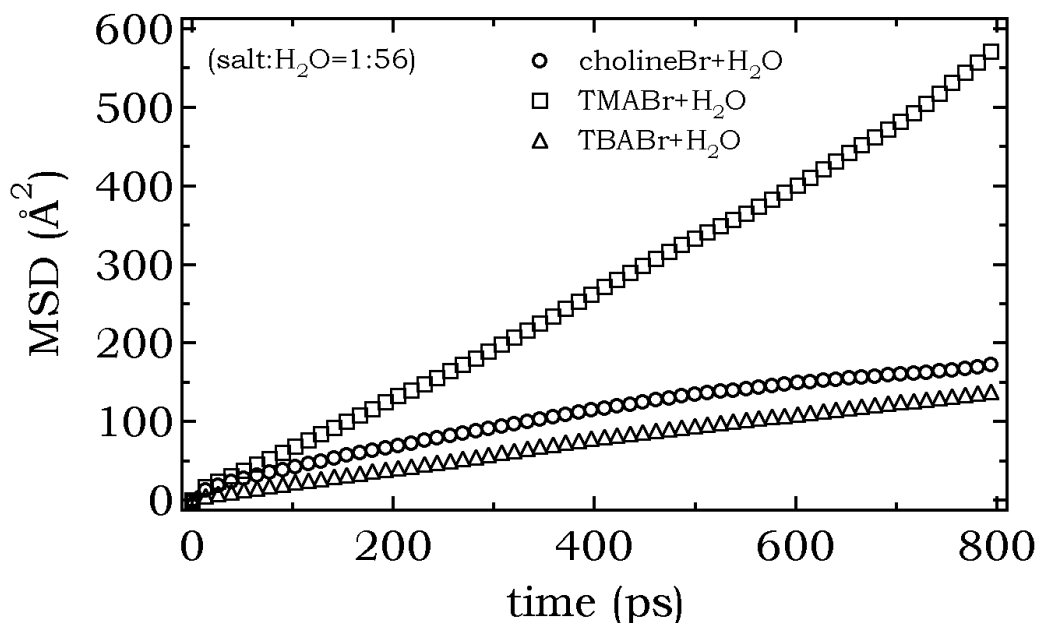
Figure 8.24: The MSD of average hydrogen atoms of TMA$^+$, Choline$^+$ and TBA$^+$ cations are plotted as a function of time for aqueous solution with x_m=1:56.

8.8 Dynamics of Bromide Ions in Solution

In this section we briefly present the result (by MD simulation) of Bromide ion (Br$^-$) dynamics for the different systems which are studied so far.

We see that for aqueous TBABr solution with x_m=1:112, the translational diffusion coefficient (D_{tr}) of Br$^-$ is estimated as $(0.92\pm0.01)\times10^{-9}$m^{2}s^{-1} (figure 8.25). In case of concentration with x_m=1:56, the diffusion rate is slowing down with time (table 8.5 and figure 8.25). The Deviations from linearity towards a lower slope (at higher concentration when x_m=1:56) at longer time may be understood by the concept of jump diffusion i.e. at large times, the mean free path available for the Br$^-$ decreases. In such cases, a possible value of the largest free space available for the motion of the Br$^-$ counter ion is the typical distance separating the two neighboring cations which are ~13 Å
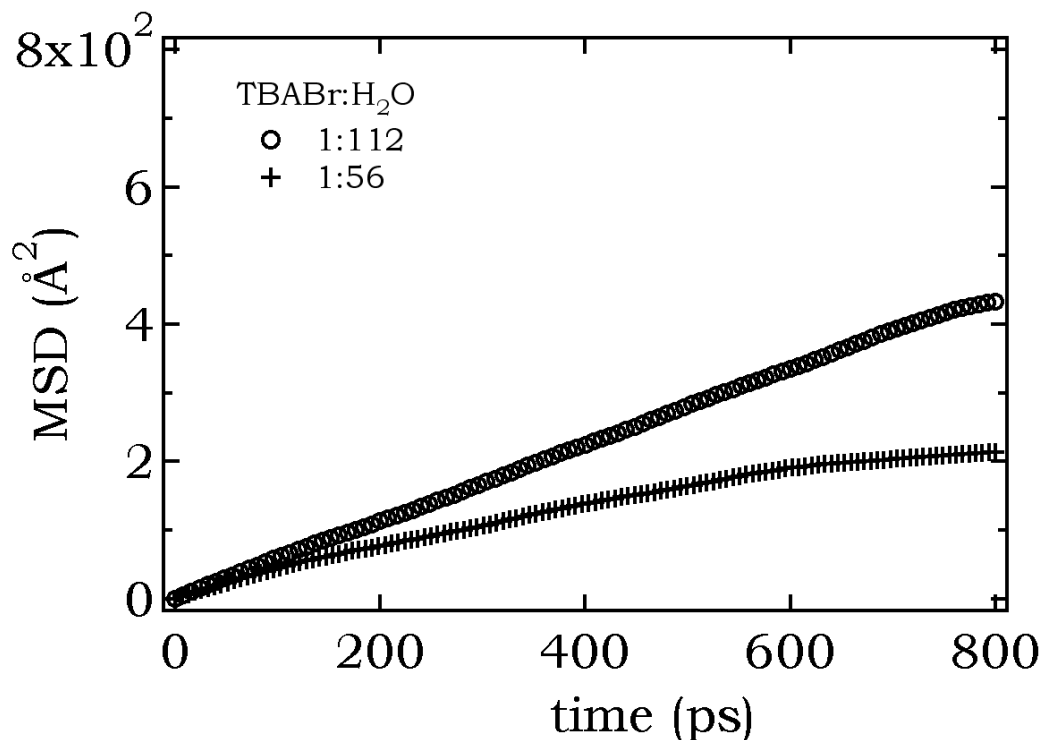
Figure 8.25: **The MSD of bromide ions are plotted as a function of time for aqueous solution of TBABr with x_m=1:56 and x_m=1:112.**

Concentration	Solution	D_{tr} of Br$^-$	in (10^{-9} m^{2}s^{-1})	
(salt:H$_2$O)		Time Scale	Time Scale	Time Scale
		(0ps to 150ps)	(150ps to 600ps)	(600ps to 800ps)
x_m=1:56	TBABr+H$_2$O	(0.56±0.01)	(0.39±0.01)	(0.15±0.01)
x_m=1:112	TBABr+H$_2$O	(0.74±0.01)	(0.74±0.01)	(0.74±0.01)

Table 8.5: **Extracted translational diffusion coefficient for Br$^-$ extracted by MSD calculation of MD simulation at two different concentration (x_m=1:56 and x_m=1:112) of aqueous TBABr solution. All the values are corrected by the difference in viscosity between H$_2$O and D$_2$O.**

Concentration (salt:H_2O)	Solution	D_{tr} of Br^- in (10^{-9} m^2s^{-1})	
		Time Scale (0ps to 400ps)	Time Scale (400ps to 800ps)
x_m=1:56	NaBr+H_2O	(0.91±0.01)	(1.57±0.01)
x_m=1:56	TMABr+H_2O	(0.91±0.01)	(1.21±0.01)
x_m=1:56	CholineBr+H_2O	(1.01±0.01)	(0.98±0.01)
		Time Scale (0ps to 450ps)	Time Scale (450ps to 800ps)
x_m=1:22	NaBr+H_2O	(0.77±0.01)	(0.87±0.01)
x_m=1:22	TMABr+H_2O	(0.77±0.01)	(0.92±0.01)
x_m=1:22	CholineBr+H_2O	(0.66±0.01)	(0.66±0.01)

Table 8.6: Extracted translational diffusion coefficient for Br^- ion in aqueous solution of TMABr, CholineBr and NaBr at two different concentration (x_m=1:56 and x_m=1:22) extracted by MSD calculation of MD simulation. All the values are corrected by the difference in viscosity between H_2O and D_2O.

apart. This distance plays a role for the change in slope in the MSD and in a way the anion is restricted in a confinement. But when there is more solvent water molecules (in case of solution concentration with x_m=1:112); the mean free path available for the Br^- increases and also because of more water molecules in the space between ions, the Br^- counter ion does not suffer from a slower dynamics as much as seen in more concentrated solution (x_m=1:56).

For other solutions where the cations (like Na^+, TMA^+ and $Choline^+$) are smaller than TBA^+, the situation is more interesting. The results are summarized in table 8.6. We observe that for aqueous solution of x_m=1:56, the bromide ion dynamics increases with time for NaBr solution (the effect is less significant for TMABr solution) [figure 8.26 (top)]. Interestingly this effect is less observed for higher concentration (x_m=1:22) [figure 8.26 (bottom)]. A tentative explanation can be the effect of a medium range order relatively well established when both anion and cation are small and spherical (like Na^+, Br^- or even considering TMA^+). Then in case of aqueous solution of NaBr or TMABr with x_m=1:56, the bromide ion can show an 'excess' of diffusion due to the coulombic forces of ions regularly separated i.e. as the bromide escapes from the electrostatic effects due to the other ions and moves into the inter-ionic space (filled by normal water) its diffusion increases. But as the concentration increases (x_m=1:22), the number of normal water molecules in the inter-ionic space decreases and the effect of this excess diffusion is not seen. This kind of behavior is not seen for aqueous CholineBr solution. Because of its longer chain, the bromide ions do not get much free inter-ionic space to

show the effect of excess diffusion.
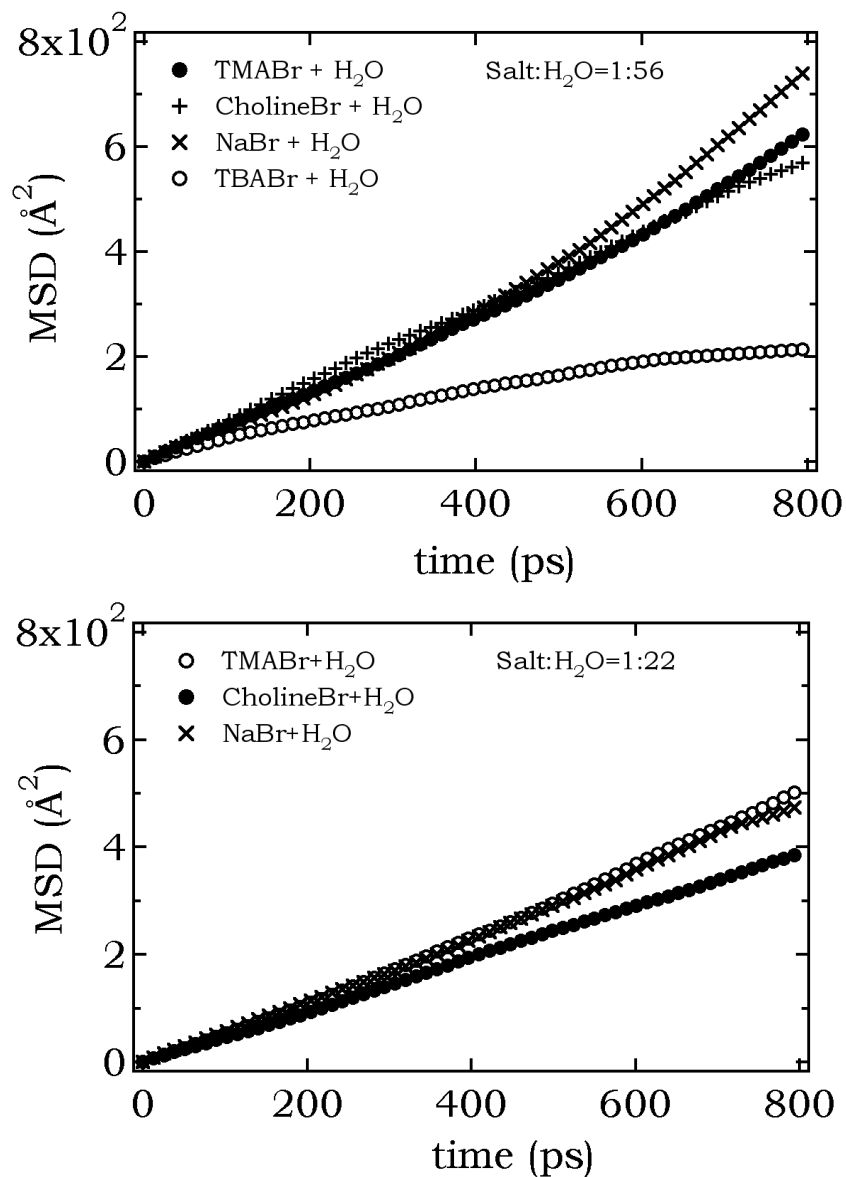
Figure 8.26: The MSD of bromide ions are plotted as a function of time for aqueous solution of NaBr, TMABr and CholineBr with x_m=1:56 (top) and x_m=1:22 (bottom).

8.9 Temperature Effect

Using the same model (equation 8.4), the TOF data on aqueous solution of TBABr with x_m=1:56 at 316K (figure 8.27) and 348K (figure 8.28) are analyzed. All the fitting conditions and symbols are same as before. We see the translational broadening (Γ_{tr}) is Q dependent (figure 8.29 and figure 8.30) and Γ_{tr} increases linearly with Q^2. The translational diffusion coefficient D_{tr} is extracted from the slope of a linear fit which passes through the origin. The results show that the D_{tr} at 316K and 348K are $(0.29\pm0.03)\times10^{-9}\mathrm{m}^2\mathrm{s}^{-1}$ and $(0.70\pm0.03)\times10^{-9}\mathrm{m}^2\mathrm{s}^{-1}$ respectively. The methyl group rotation time though does not change much ($\sim$ 4ps) from before. The rather similar rotational time for methyl group with increase in temperature, was also observed before [Cabral 2000].

The other relevant finding from the change in temperature is the number of hydrogen atoms that are seen as rotating (methyl group hydrogen rotation in model 8.4). In figure 8.31 the ratio of trans-rotational and translational intensity (equation 8.4) is plotted as a function of Q. It is evident that with increase in temperature, the intensity of the trans-rotational contribution also increases. This is only possible if some of the inner hydrogens of each hydrocarbon chain of TBABr also starts to rotate. Based on this idea, the theoretical predicted intensities (trans-rot and trans) are calculated with considering more hydrogens atoms are rotating as temperature increases. It is estimated that at 316K, the first two CH_2 group (next to central nitrogen) hydrogens are un-rotatable and at 348K, only the first CH_2 hydrogens remain un-rotatable. Here one should note that the TOF analysis (with the simplified model, equation 8.4) predicts that as the temperature increases the rotational time for internal hydrogens atoms (hydrogens other than terminal methyl group) is similar to the terminal methyl group hydrogen atoms. This result does not mean that all the hydrogens internal hydrogens are rotating similar to the terminal methyl hydrogens. It only extract the average rotational time for all the rotating hydrogens where the relatively slowly rotating internal hydrogens are biased by the faster terminal methyl hydrogen. An estimate of the rotational time for individual hydrogens can be made by the MD simulation as shown for the ambient temperature in section 8.5.2.

Activation Energy We further investigated the NSE signal (predominantly coherent) as a function of temperature for a single Q (0.3Å^{-1}) between 298K and 348K (figure 8.32). Fitting the curves with a single exponential we arrive at an activation energy (E_a) of 25.3 ± 1.5 kJ/mol. Note that the E_a from incoherent analysis is estimated around 20.6 ± 1.9 kJ/mol.
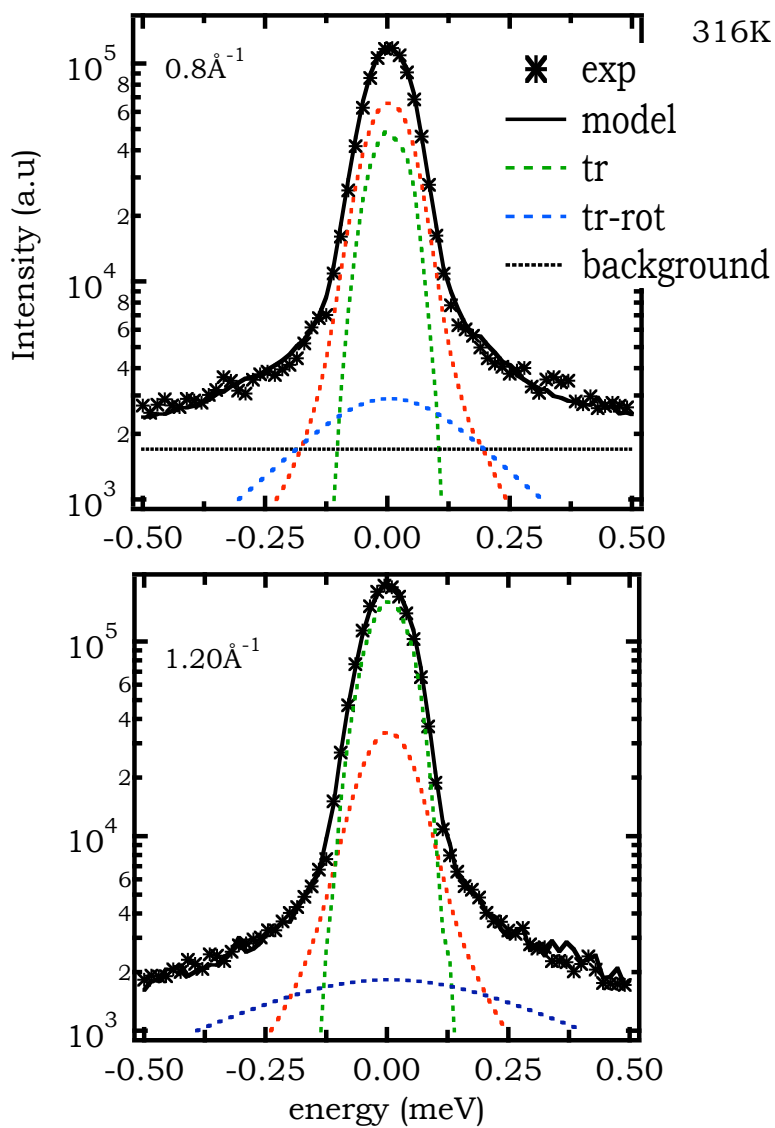
Figure 8.27: Incoherent scattering functions, $S_{inc}(Q,\omega)$, versus energy transfer for Q=1.20 Å^{-1} (top) and Q=0.80 Å^{-1} (bottom) measured by TOF at 316K on aqueous solution of TBABr with x_m=1:56. Different components of the model function are shown: background (dashed black), elastic (green), translational (red), trans-rotational (blue) and total (full black).
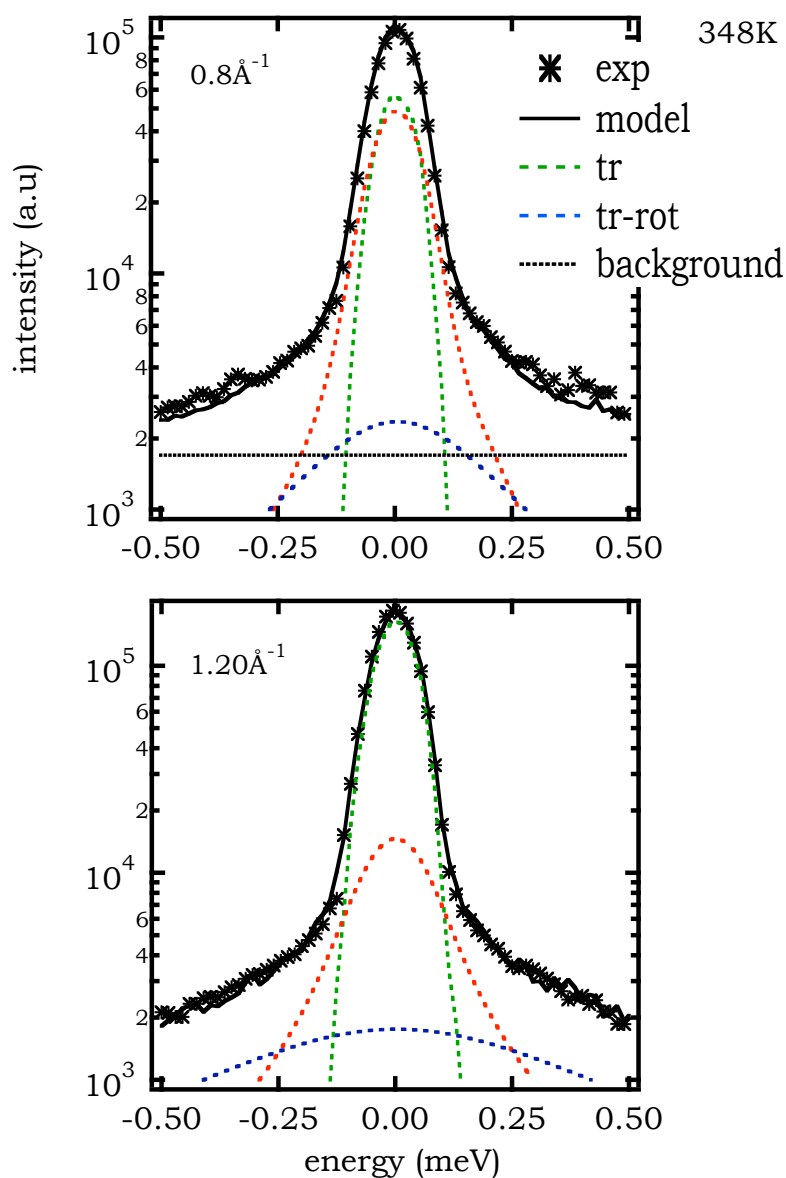
Figure 8.28: Incoherent scattering functions, $S_{inc}(Q,\omega)$, versus energy transfer for Q=1.20 Å^{-1} (top) and Q=0.80 Å^{-1} (bottom) measured by TOF at 348K on aqueous solution of TBABr with x_m=1:56. Different components of the model function are shown: background (dashed black), elastic (green), translational (red), trans-rotational (blue) and total (full black).
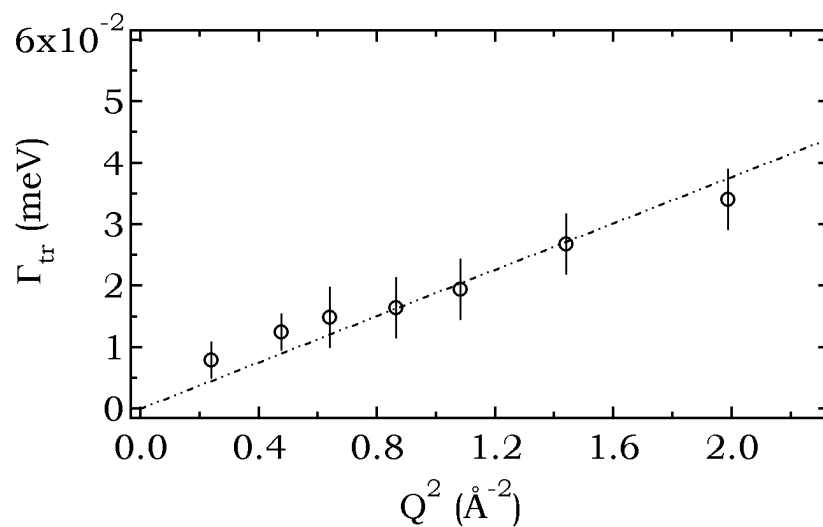
Figure 8.29: Γ_{tr} **from TOF measurement plotted as a function of** Q^2 **at 316K to extract** D_{tr} **from a linear fit passing through origin (continuous diffusion).**
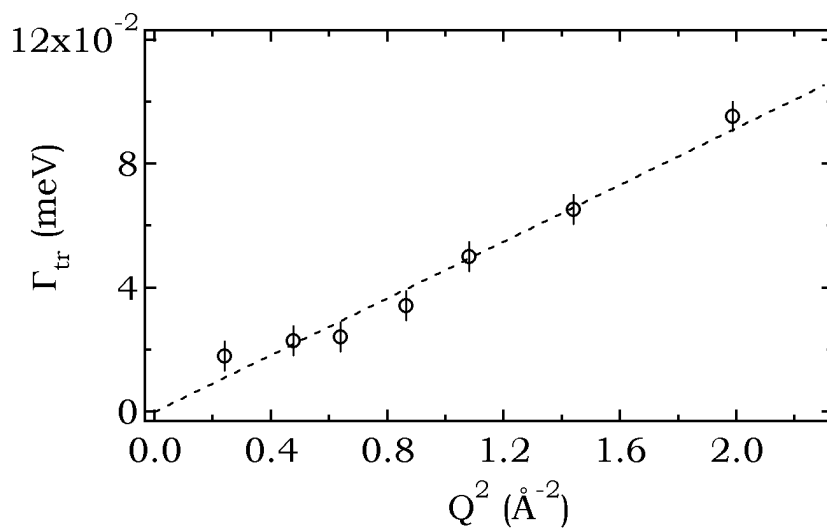
Figure 8.30: Γ_{tr} **from TOF measurement plotted as a function of** Q^2 **at 348K to extract** D_{tr} **from a linear fit passing through origin (continuous diffusion).**
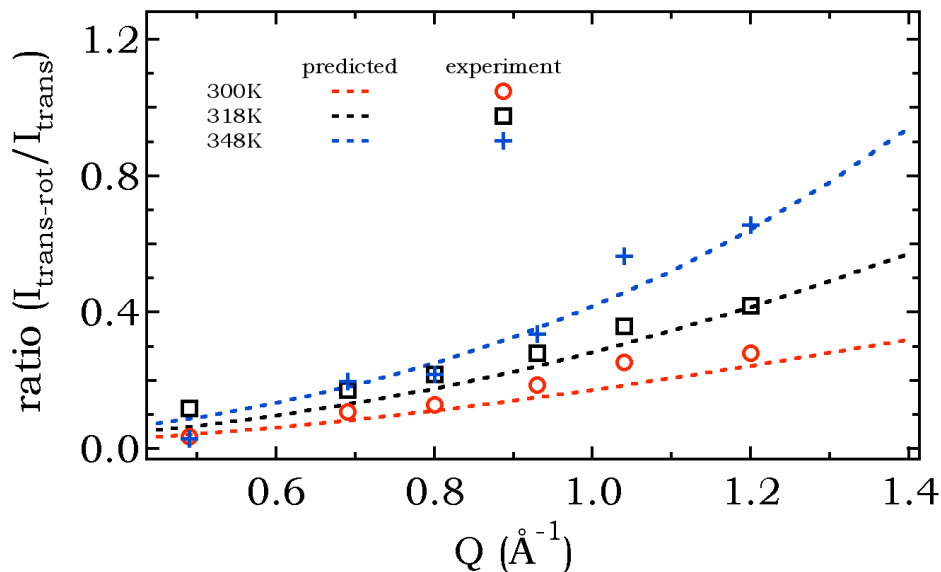
Figure 8.31: The change in trans-rotational and translational intensity with temperature as a function of Q.

Regarding the temperature activation of the coherent signal, the extracted activation energy of 25±1.5 kJ/mol from NSE coherent signal is of the same order by conductivity measurement (~ 23kJ mol^{-1}). But this is significantly higher than the activation energy of bulk water diffusion (18kJ/mol, in the range around room temperature) and about three times as high as the average energy of a hydrogen bond between two neighboring water molecules (8kJ/mol) [Teixeira 2006].

8.10   Conclusion

In this Chapter we have discussed the dynamics of ions in aqueous solutions of TAABr and CholineBr at different concentrations. Concentrating on aqueous TBABr solution with x_m =1:56, we have carefully decoupled, with the help of NSE polarization analysis, the total neutron scattering intensity into its coherent and incoherent contributions (the result is in agreement with SANS, ND and MD simulation) and studied the dynamics contained in each of these in turn. It is shown that the TBA$^+$ translational diffusion coefficient (D_{tr}) extracted from the incoherent part of the neutron scattering signal due to hydrogen atoms could be misleading. We have extensively shown that the internal motion of individual H-atoms within TBA$^+$ is a source of bias in the
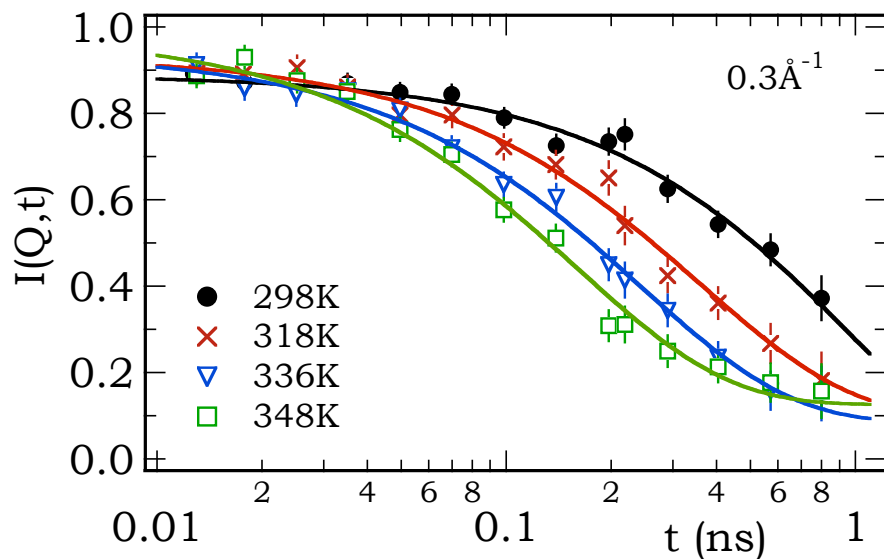
Figure 8.32: The temperature dependence of the intermediate scattering function measured by NSE, $I^{NSE}(Q,t)$, for Q=0.3Å^{-1} on aqueous solution of TBABr with x_m=1:56 (Reseda spectrometer).

determination of D_{tr} from the incoherent neutron signal. The true cation CoM diffusion on the scale of the neutron measurements is $(0.12\pm0.01)\times10^{-9}\mathrm{m}^2\mathrm{s}^{-1}$ as determined from the coherent signal at low Q, where by the nature of the coherent signal the atomic motions internal to the cation do not come into play. The fact is verified also by MD simulation and applied at different TBABr concentrations. This finding is of wider consequence for the many dynamic neutron scattering studies of polyatomic molecules (in bulk or confined geometries), the motion of which is traditionally studied via the signal of their constituent H-atoms, which dominate the incoherent scattering intensity. Based on the size and structure of such molecules, the bias in the thus extracted diffusion coefficient can be more or less severe (here, in the case of TBA$^+$, the bias leads to an overestimation by a factor of 2), depending on the characteristic time scales of the H motions internal to the molecule.

Within the context of other studies determining ionic diffusion coefficients, we note that for 0.89m (x_m =1:56) TBABr solution in D$_2$O, both NMR [Ancian] (time scale of microseconds) and Tracer measurements (carried out in H2O in ref [Woolf 1982] and corrected here by the D$_2$O/H$_2$O viscosity ratio) yield values of $0.19\times10^{-9}\mathrm{m}^2\mathrm{s}^{-1}$ for the translational diffusion coefficient of TBA$^+$ which seems close to the incoherent signal value and higher than the value extracted from the low-Q coherent signal. The NMR results of Hertz et al [Hertz 1969] on a series of TAACl in D$_2$O (for several concentrations) is also reported to be very close to incoherent neutron scattering measurements (1m TBACl in D$_2$O) [Novikov 1999]. However, there are also instances where neutron scattering predicts lower values than those of NMR (on 8.2m TMACl in D$_2$O, incoherent signal analysed [Brown 1988]). Thus for the moment, the available data from the literature do not provide a clear conclusion regarding the diffusion of TBA$^+$ (or other TAA cations) in aqueous solution when experiments carried out at different time and length scales are considered together. We provided here a reliable and detailed description at a given length and time scale (Å to nm, ps to ns) by a careful decoupling of the dynamics contained in the coherent and incoherent components of the neutron scattering signal and with the help from MD simulations. The rationalisation of the difference between our measurements and those of NMR is presented shortly in a separate section.

Contrary to previous results [Novikov 1996a] [Novikov 1999], we find that the large TBA$^+$ cation translational motion is accompanied by a global rotation of the cation and the methyl group hydrogen orientation. We have also estimated the D$_{tr}$ for smaller TAA Cations like TMA and choline for different concentrations. The MD results predict that the Choline cation Centre of Mass (CoM) motion is lower than TMA by a factor of ~1.1 to ~1.3. The difference between D$_{tr}$ extracted from individual hydrogen atom movement

and CoM motion (within time window comparable to our TOF measurement) is higher for Choline than for TMA. This is again because of the presence of a longer alkyl chain in the Choline molecule. Lastly we have showed the change in dynamics for TBA cation with temperature and estimated the activation energy (25.3 ± 1.5 kJ/mol from coherent signal) associated with it, which is 1.5 times higher than activation energy of bulk water and 3 times higher than the average energy of a H-bond of neighbouring water molecules. Higher temperature translational and trans-rotational intensities suggest that as the temperature increases the internal hydrogen atoms (other than in the terminal methyl groups) also start to rotate locally.

Ionic Translational Diffusion Coefficient as Seen by NMR/Tracer and QENS Here we outline a possible explanation for the difference in the diffusion coefficient extracted by NMR/Tracer and QENS techniques for aqueous TBABr solution with x_m =1:56. According to the consideration of [Hynes 1979] [Bagchi 1998], in a solution, the motion of a particle is inßuenced mainly by two kinds of effects: 1) by its close neighbours that give rise to Brownian motion of the particle and 2) by the flow of the solvent liquid (i.e. the viscosity). These two processes occur at different length scales. The former is controlled by molecular dynamics while the latter via Navier-Stokes hydrodynamics. For the first effect, the friction (microscopic Enskog friction [Hynes 1979]) is due to (a) the collisions between the solute and the solvent molecules and (b) the solvent number density (n) fluctuations. The second effect (viscosity term) is controlled by the hydrodynamic friction [Hynes 1979] [Bagchi 1998]. Now, (A) When n tends to 0 the particle diffusion is controlled only by the collisions with the solvent molecules (and there are no hydrodynamic effects from the solvent); (B) When n is such that solution density tends to infinity (at infinite dilution of liquid, the dominating term is hydrodynamics due to the solvent and the collisions are negligible). These are the two limiting conditions. (C) When the solute and solvent particles are of a comparable size and n has a finite value (which is our case), the collisions and hydrodynamics both act together. Based on this argument, the total translational diffusion coefficient (D_{tot}) can be decomposed into two parts

$$D_{tot} = D_{mic} + D_{hyd}$$

where D_{mic} is the microscopic diffusion coefficient and D_{hyd} is due to the hydrodynamic effect [Hynes 1979] [Bagchi 1998].

In NMR the measurement is over a distance of 10-100 μm (Q$\sim$$10^{-6}$ to 10^{-5} Å^{-1}) while our QENS experiments are typically in the Q range of 0.2

to 1.8Å^{-1}. So QENS measures on a significantly more local scale than NMR. In that respect QENS measures the 'micro-dynamics' (molecular dynamics) while for NMR (and tracer) measurement contains both the 'micro-dynamics' and the 'hydrodynamic effect'.

Based on the above discussion and the diffusion coefficient extracted by NMR/Tracer and QENS techniques for aqueous TBABr solution with x_m =1:56, we can say that D_{mic} = 0.09×10^{-9}m^{2}s^{-1} (single exponential fit) or 0.12×10^{-9}m^{2}s^{-1} (double exponential fit) for the cations, as measured by NSE coherent analysis at low Q. The D_{tot} is measured by NMR. D_{tot} = 0.19×10^{-9}m^{2}s^{-1}. In that case the D_{hyd} is ∼(0.07-0.10)×10^{-9}m^{2}s^{-1}. The hydrodynamic contribution can however be estimated independently as follows: At infinite dilution D_{mic} tends to zero (discussed before) and thus, at infinite dilution, D_{tot} ∼ D_{hyd}. Now we know for TBABr in D$_2$O, at infinite dilution D_{hyd} (∼D_{tot}) is 0.39×10^{-9}m^{2}s^{-1} (by NMR [Hertz 1969]). If we extrapolate this to 1m TBABr in D$_2$O, by Stokes-Einstein relation, it becomes 0.14×10^{-9}m^{2}s^{-1} (considering the difference in viscosity for 1m TBABr in D$_2$O and pure D$_2$O [Buchner 2002]). Further, introducing the 'distance correction' (closest approach distance of solute and solvent), we can arrive at a better result. The correction factor is ($\frac{\mu}{\mu+1}$), where μ= (R/r), R and r are the solute and solvent radii [Hynes 1979]. For our case R=5.12Å (density measurement) and (R+r) = 7.8Å (first prominent hydration shell for TBABr from MD). So multiplying the obtained D_{hyd} by the correction factor, the modified D_{hyd} becomes ∼0.9×10^{-9}m^{2}s^{-1}. This value of D_{hyd} is close to D_{hyd} calculated by direct subtraction of D_{mic} (by NSE$_{coh}$) from D_{tot} (by NMR value), discussed earlier. This would therefore be consistent with the picture of NMR (Tracer) measurements containing the two contributions D_{mic} and D_{hyd} (D_{tot} = D_{mic} +D_{hyd}), while in NSE$_{coh}$ only D_{mic} is measured. Note in [Bagchi 1998], the author has also explicitly predicted (in the conclusion section) that for Tetraalkylammonium (TAA) systems both D_{mic} and D_{hyd} are of importance. This is because these ions are neither very small nor very large compared with the solvent water molecules. They have an intermediate size and thus both contributions are observed at different length scales.

Now the question may come why we see a similar diffusion coefficient in incoherent component of neutron scattering and in NMR/ Tracer? This for us is a mere coincidence. Especially in view of the previous neutron scattering studies, which sometimes apparently agree with NMR, other times not. The incoherent neutron scattering analysis yields a higher diffusion coefficient because it is difficult to take into account properly all the different types of H motion internal to the cation (global rotation, inner hydrogen dynamics, internal motion of chains). We are in the short time regime where all these

effects are visible. If we were able to incorporate these effects into the incoherent analysis, the extracted overall translational diffusion coefficient of the cation must go down and come closer to the result obtained by NSE_{coh}.

9

Study of Solvent Behavior

Contents

9.1   Introduction

After studying the structures and dynamics of ions in aqueous solution of TBABr, TMABr and CholineBr in detail, here we discuss the solvent structure and dynamics. Like before we concentrate on aqueous TBABr solution along with TMABr and NaBr with x_m=1:56. And at the end, the results for higher concentration (with x_m=1:22) for NaBr, KBr, CsBr and TMABr solutions will be discussed. We will start by simulation results and then the experimental results will be presented.

9.2   Structure

9.2.1   Ion Water Correlation

Figure 9.1: Cation-water Radial Distribution Function of aqueous TBABr, TMABr and NaBr solutions with x_m=1:56, to show how the hydration water is structured differently as we move from simple (such as NaBr) to hydrophobic salts (TMABr, TBABr)

As it is already evident that for the structural study, the radial distribution functions g (r) by MD simulations is fruitful. A comparison to simple salts (NaBr for example) or smallest TAA cation (TMABr) is useful to see how the solvent structure is affected in case of TBABr. Here all the results are with x_m=1:56. The most straight forward way to study the structure is to look into the RDF (Radial Distribution Function). In figure 9.1, we present the RDF between cation (N^+ of TBABr and TMABr or Na^+ of NaBr) and oxygen/ hydrogens of water. From figure 9.1, we have mainly two types of information - (a) the structure of water-shell around the cation and (b) indication of water penetration between hydrocarbon arms of TAA cations.

In case of simple salts (NaBr for example) the hydration shell is distinct, well structured and the orientation of oxygen and hydrogens of water molecules are as expected i.e. oxygen atoms are closer than hydrogens with more probability because of the positive cationic nature of Na^+ (Na-O_W ∼2.4 Å and Na-H_W ∼3.1 Å). This situation is not the same for aqueous solution of TMA$^+$ ions. Here the oxygen and hydrogen atoms are at almost similar distance from cation (N^+-O_W ∼4.4 Å and N^+-H_W ∼4.5 Å) with almost equal probability (and the RDF peak is less intense than aqueous NaBr solution). It indicates that the hydration water orientation is tangential. This conclusion is in agreement with earlier diffraction measurement [Soper 1992] [Turner 1995]. For TBA$^+$, the hydration shell is farther away (N^+-O_W ∼7.8 Å) (as expected due to a larger size) than TMA$^+$(N^+-O_W ∼4.4 Å) which is same as the second hydration sphere for NaBr (Na$^+$-O_W ∼4.5 Å) and RDF peak-height is also diminished. Note that the last hydrogen of TBA$^+$ is around 6.2 Å and TMA$^+$ is ∼ 2.2 Å. The same figure also tells that for TBA$^+$, the water can penetrate up to the same distance (∼3.4 Å) as TMA$^+$ (as predicted in [Buchner 2002]) though the first prominent hydration shell is farther away (∼7.8Å). Before this distance, the water orientation has no preferential direction [this can be inferred from the fact that the g($N_{TBA}O_W$) or g($N_{TBA}H_W$] has non-zero almost constant value <∼6.5 Å). This is because of several effects such as electrostatic interaction of atoms in cation and the movement of the cation hydrocarbon arms which influence the water molecules orientation in between them.

In case of TBA$^+$, the water molecules can penetrate upto the third carbon of each arm [the last hydrogen of the TBA$^+$ is at ∼6.2 Å from the centre of mass (CoM)]. Using this RDF and integrating up to appropriate distance, it is estimated that up to the last hydrogen of respective TAA cation, there are ∼16 water molecules for TBA$^+$ and none for TMA$^+$ (size of TMA$^+$ is ∼3.4 Å). Note that the first hydration shell of TMA$^+$ and TBA$^+$ consists of ∼25 and ∼50 H_2O molecules respectively.

The Choline hydration structure is similar to TMA$^+$ except where we observe that the first peak of cation-water (oxygen) of choline$^+$ is less intense

than TMA$^+$ and the g(N$_{choline}$O$_W$) and g(N$_{choline}$H$_W$) are closer to each other than for TMA$^+$ (figure 9.2).

Figure 9.2: Cation-water Radial Distribution Function for aqueous TMABr and CholineBr solutions with x_m=1:56.

9.3   Dynamics

9.3.1   Aqueous TBABr Solution

For aqueous TBABr solution, we have studied the average solvent dynamics or mainly its translational dynamics by MD simulation. We start by aqueous TBABr solution with x_m=1:56. The average solvent D$_{tr}$ is calculated by two different methods - i) MSD and ii) I(Q,t) analysis. First we consider the central oxygen atoms of solvent water molecules and plot their position as a function of time, the slope estimates the D_{tr}=(1.29±0.03) ×10^{-9}m^{2}s^{-1} [figure 9.3 (a)]. In an H$_2$O molecule the oxygen atom is close to its CoM, so by tracing this oxygen atom, one can study the average water dynamics without rotational contribution. The same result can be obtained by the intermediate scattering function with an exponential decay [figure 9.3 (b)]. We observe

Figure 9.3: **Dynamics of average solvent water of TBABr solutions with x_m=1:56 from (a) MSD analysis and (b) $I_{inc}(Q,t)$ analysis of oxygen atom of water molecule by MD simulation.**

that the average solvent translational diffusion coefficient is $\sim$2 times smaller than that of bulk water [Jorgensen 1986].

Next the solvent D_{tr} is estimated from the hydrogen of water molecules [figure 9.4 (a)]. To analyze the data, in analogy to the QENS measurement, we use the model consists of a translational $T(Q,t)$ and rotational term $R(Q,t)$ [Teixeira 1985]. The rotational term is considered up to the second Bessel term. Thus the translational $T(Q,t)$ and rotational term $R(Q,t)$ can be written as

$$
\begin{aligned}
T(Q,t) &= e^{\frac{-t}{\tau_{tr}}} \\
R(Q,t) &= j_0^2(Qa) + (1 - j_0^2)e^{\frac{-t}{3\tau_{rot}}}
\end{aligned}
\tag{9.1}
$$
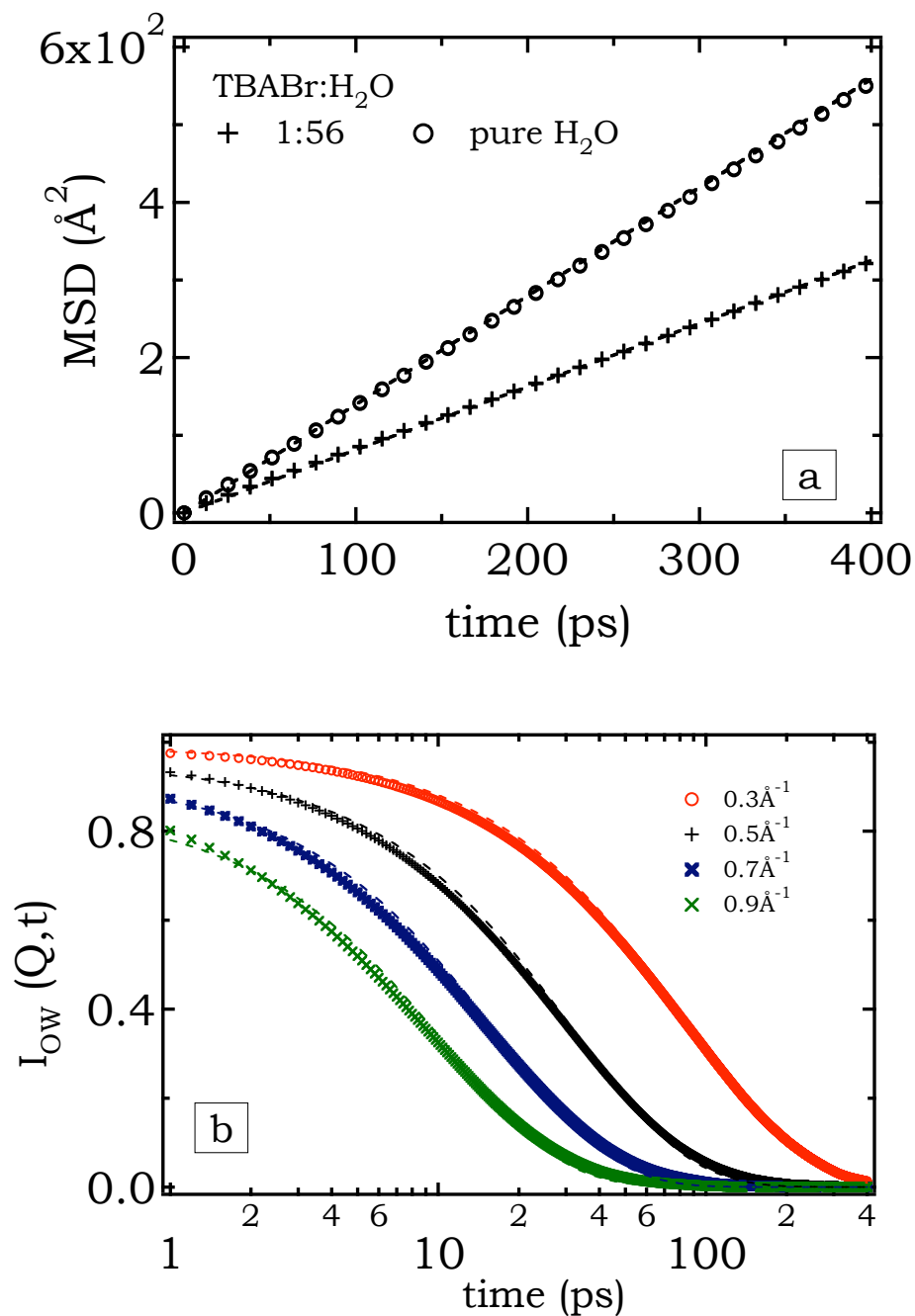
This predicts average solvent D_{tr} $(1.26\pm0.03)\times10^{-9}$m^{2}s^{-1} with $\sim$1ps [Teixeira 1985] for rotational time (figure 9.4). The estimated average solvent water D_{tr} value $\sim$2 times smaller than bulk water and in good agreement with earlier QENS experiment [Novikov 1999].

9.3.2 Comparison at Different Concentrations

Using MD simulation, average solvent translational dynamics is compared between aqueous solution of TBABr with x_m=1:56 and with x_m=1:112. It is found that for x_m=1:112, the average water dynamics is reduced by a factor of 1.3 compared to a factor 2 in case of concentration with x_m=1:56. This can be seen from figure 9.5 where MSD of oxygen atoms of solvent water molecules is plotted as a function of time.

9.3.3 Comparison among Different Salts

By QENS TOF experiment we have also estimated the average solvent translational dynamics for TMABr aqueous solution with concentration at x_m=1:56 and at x_m=1:22. By dissolving deuterated TMABr in water, we have found that the average solvent molecule translational diffusion coefficient for aqueous TMABr solution with x_m=1:56 is $(1.83\pm0.03)\times10^{-9}$m^{2}s^{-1} and decreased 45% $[(1.31\pm0.03)\times10^{-9}$m^{2}s$^{-1}]$ when the concentration increases to x_m=1:22 compared to bulk. Note that the translational diffusion coefficient of average solvent molecule in aqueous solution of simple salts is slightly higher than for aqueous TMABr solution. This can be verified from the extracted D_{tr} of average solvent molecule at concentration of x_m=1:22 for aqueous NaBr, KBr and CsBr salts. For all the cases, to analyze the TOF data, a two Lorentzian model (equation 9.1 in energy domain [Teixeira 1985]) is used.
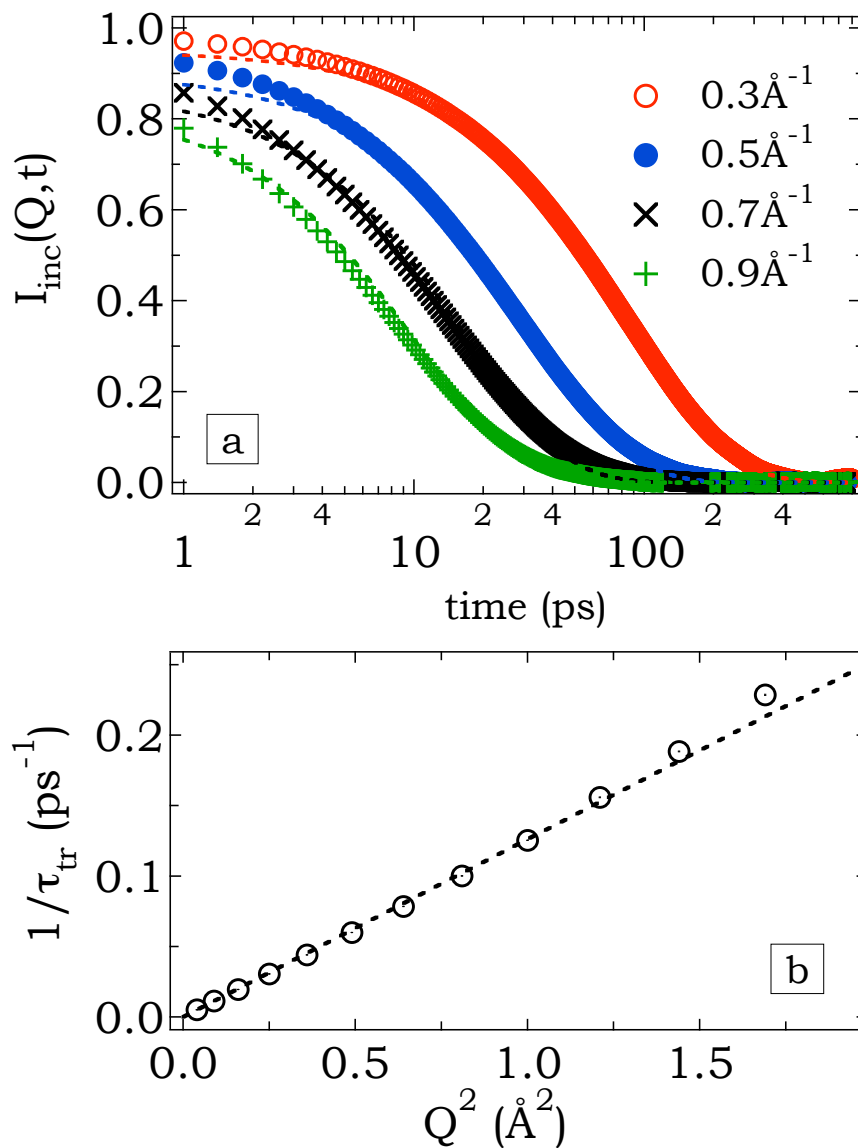
Figure 9.4: Dynamics of average solvent water molecule of TBABr solutions with x_m=1:56. (a) $I_{inc}(Q,t)$ of hydrogen atoms of water (b) Inverse translational time extracted from $I_{inc}(Q,t)$ versus Q^2. The slope corresponds to the D_{tr} of solvent water.
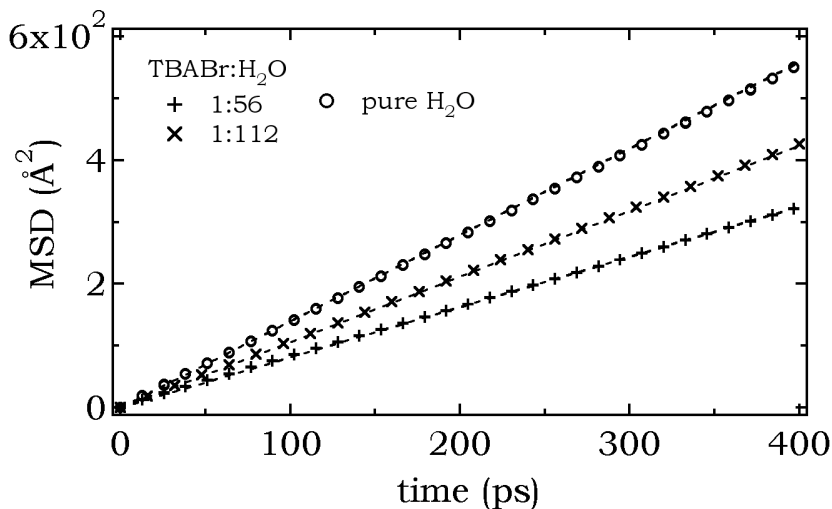
Figure 9.5: The MSD of oxygen atoms for water molecules of aqueous TBABr solution with x_m=1:56 and with x_m=1:112.

The average solvent D_{tr} is also estimated by MD simulation. If we focus on aqueous TMABr and NaBr solution with x_m=1:56, we see that the average water diffusion coefficient is 1.5 higher than for aqueous TBABr at the same concentration. At a concentration of x_m=1:22 (TMABr and NaBr) average solvent D_{tr} is further reduced. Due to unavailability of deuterated CholineBr and TBABr, experimental solvent diffusion can not not be estimated. The simulation suggests that CholineBr reduces average solvent dynamics more than TMABr or simple salts like NaBr when concentration is increased from x_m=1:56 to x_m=1:22. The result is summarized in table 9.1.

9.3.4   Rotational motion

Like in section 8.5, we have modified the individual hydrogen atom (of each H_2O molecule) coordinates relative to its central oxygen atoms in the MD simulation trajectory file. This way we can calculate the average water hydrogen atom rotational motion about respective oxygen atom. Next like before we calculate the MSD with the modified water hydrogen atom and fitted with $2b^2(1-e^{-\frac{t}{\tau_{rot}^{H_2O}}})$, where $\tau_{rot}^{H_2O}$ is the water hydrogen rotational time around oxygen and b is ~1.0Å as oxygen-hydrogen bond length (figure 9.8). We find the $\tau_{rot}^{H_2O}$ of solvent water molecules in aqueous solution NaBr, TMABr, CholineBr and TBABr solution are ~1.71ps, ~1.97ps, ~1.79ps and ~2.59ps. However, it is worth noting that rotations of water molecules must be decomposed in
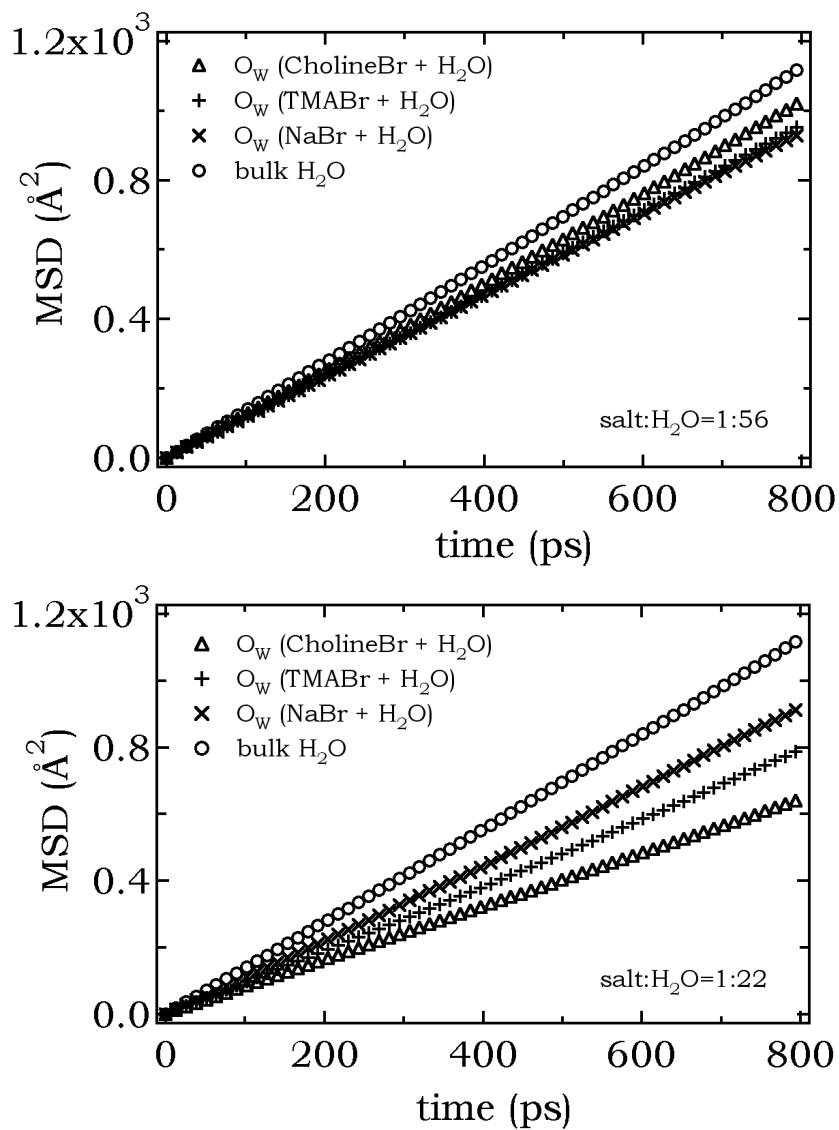
Figure 9.6: The MSD of oxygen atoms for water molecules of aqueous TMABr and NaBr solution with (top) x_m=1:56 and (bottom) x_m=1:22.
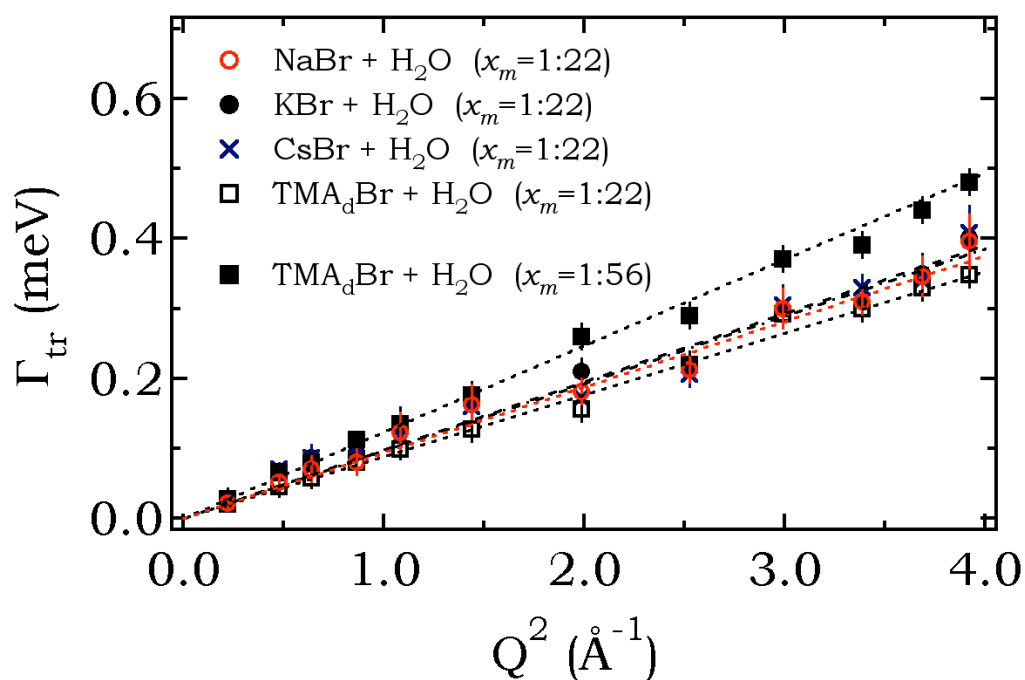
Figure 9.7: Γ_{tr} from TOF measurement is plotted as a function Q^2 to extract the D_{tr} of average solvent water molecules from a linear fit passing through origin (continuous diffusion) .

concentration	Aqueous solution of	D_{tr} of solvent water in $(10^{-9}$ $m^2s^{-1})$	
		exp	sim
x_m=1:112	TBABr		(1.78±0.01)
x_m=1:56	TBABr	(1.40±0.4)	(1.26±0.01)
	TMABr	(1.83±0.10)	(1.98±0.01)
	CholineBr		(2.10±0.01)
	NaBr		(2.00±0.01)
x_m=1:22	TMABr	(1.31±0.03)	(1.63±0.01)
	CholineBr		(1.44±0.01)
	NaBr	(1.39±0.05)	(1.82±0.01)
	KBr	(1.45±0.05)	
	CsBr	(1.43±0.05)	
	bulk H_2O	(2.2±0.1)	(2.35±0.01)

Table 9.1: **Extracted translational diffusion coefficient estimated by MD simulation and QENS experiment for average solvent water molecules of different systems [aqueous solution of simple salts (like NaBr, KBr, CsBr), TMABr, CholineBr and TBABr].**

their three components. The component that we evaluate here, around the C2 axis, corresponds to a short relaxation time but it is not easily decoupled from the others in dedicated experiments. What makes the situation more complex is the fact that water molecules are bound in average to at least 2 neighbouring molecules and all the motions are coupled at short time scales, in the time domain extending from 1 ps (characteristic lifetime of a hydrogen bond) to 10 ps (the global rotation of the molecule).

9.4   Conclusion

In this chapter we have discussed about the solvent structure and dynamics of aqueous TAABr systems and cholineBr along with normal salts like NaBr, KBr and CsBr at ambient temperature. We show that the hydration structure around TAA salts is different from normal salts. The water molecules are oriented tangentially around TAA or Choline cation while for NaBr, the oxygen atoms are closer than hydrogen because of the positive nature of the cation. For TBA cation, the water molecules penetrate up to the same distance as TMA. The presence of prominent hydration shell indicates that the cations are placed inside a cage and as the solute size increases the solvation cage becomes weaker.
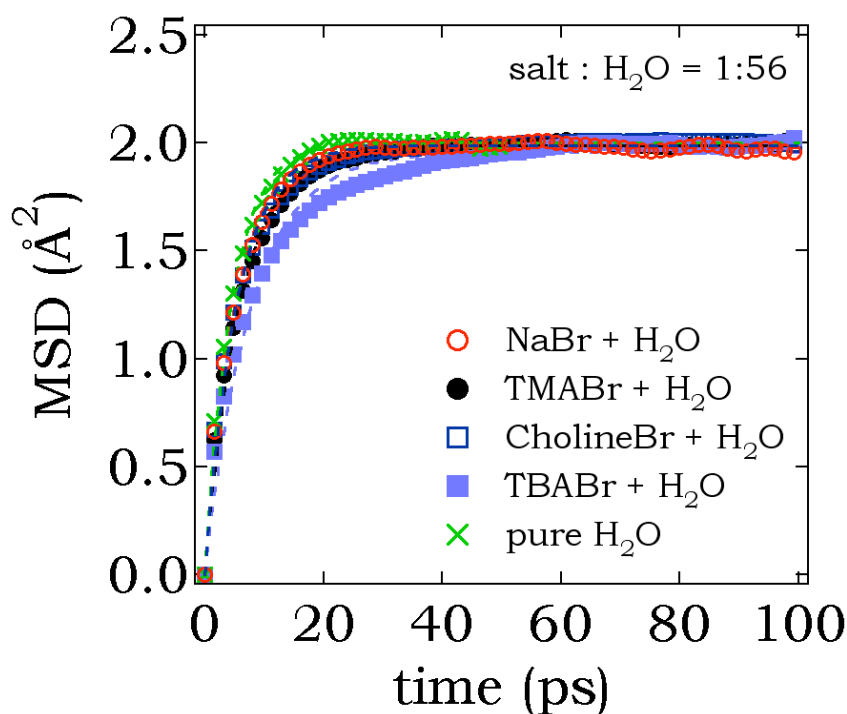
Figure 9.8: MSD of water hydrogen atoms (with modified coordinates relative to its central oxygen atom) are plotted as a function of time to extract estimate the rotation time of water hydrogen atom around central oxygen atom, $\tau_{rot}^{H_2O}$. The fitting equation is $2b^2(1 - e^{-\frac{t}{\tau_{rot}^{H_2O}}})$, where b is $\sim$1.0Å as oxygen-hydrogen bond length.

The average solvent water dynamics is measured by a combination of TOF and MD simulation. At a concentration of x_m=1:56 for aqueous TBABr solution, solvent translational dynamics is decreased by a factor of 2 (for x_m=1:112, the factor is 1.3) with respect to bulk. The D_{tr} estimated by TOF for simple salts (NaBr, KBr, CsBr) and TMA at x_m=1:22 or 2.5m (1 hydration sphere concentration of TMA cation) shows that solvent dynamics is reduced by a factor of 2 compared to bulk. This indicates that the change in the nature of solute does not significantly alter the solvent dynamics (for TMA or simple salts). But from MD results, it is observed that in case of CholineBr solution, the decrease of solvent dynamics is faster than others. Lastly at any certain concentration (x_m=1:56 or 1m for example), the decrease in solvent translational dynamics is larger for the bigger TBA cations (larger size and hydrophobic effect of longer alkyl chain) while smaller TMA cations behaves like normal salts.

It is important to understand that the dynamics of water molecules which is measured by the QENS experiment, is an average over several types of water molecules. Some of these water molecules are in the hydration shell or at the vicinity of the ion and others are bulk-like. The difference between concentrations are likely due to the amount of population of each species.

10

General Conclusion

The symmetric TAA cations are the model systems for studying the behaviour of hydrophobic ions because they can provide a combination of short range hydrophobic effect and long range electrostatic force. These salts are also advantageous because i) it is possible to selectively deuterate the solute as there is no exchangeable H-atoms in the solute (important for neutron experiments) and ii) the hydrophobicity of the TAA cations can be controlled by the cationic hydrocarbon chains. In this work, we have investigated the aqueous TAABr solutions to obtain the information on microscopic structure and dynamics by a combination of molecular dynamics (MD) simulation and neutron scattering techniques. Starting with the atomic scale structural description of the solutes, we proceed to the study of dynamics of the ions and finally show how the solvent behaviour is affected by the presence of these hydrophobic ions. The main results are be summarized as follows -

No sign of aggregation is observed up to a high concentrations of aqueous TAABr solutions [for example up to 3.56m (salt:D_2O=1:14) for TBA^+ ions]. Our result shows that the Br^- counter ions can partially penetrate into the larger TAA^+ (such as TBA^+) alkyl chains. We have also found that the water molecules can fill the space between the cationic hydrocarbon chain [$\sim$16 molecules in case of TBA^+ from the calculation of Coordination Number (CN)]. From the calculation of the radii of gyration, we estimate a low flexibility of the hydrocarbon arms ($\sim$7% for TBA^+). All these data on ion or water penetration into the cation hydrocarbon chains which are also flexible to some extent refer to the fact that TAA^+ cation can not be treated as a hard sphere.

In case of cation dynamics, we have decoupled the coherent and incoherent signal and separately analysed them, for aqueous TAABr and CholineBr solution to estimate the diffusion coefficient. We have presented a detailed study of the ion dynamics at a given length and time scale (Å to nm and ps to ns respectively) by combining Quasi-elastic Neutron Scattering (QENS) and MD simulation. We have explicitly shown that the calculation of trans-

lational diffusion of the cation CoM by studying incoherent neutron signal overestimates the true value due to the internal motion of the H atoms. For example the overall cation CoM diffusion of TBA$^+$ cation in 0.89m aqueous solution, is slower by a factor of ~ 2 compared to the value extracted from incoherent signal. This finding is of wider consequence for many of the studies on dynamics of polyatomic molecules (in bulk or confined geometry), which are often analysed by the incoherent signal of their constituent H atoms. Of course the overestimation of cation CoM by incoherent signal depends on the structure and size of the concerned molecule and the time scale of the H atoms dynamics, present in the molecule. The other important fact is the comparison among different experimental techniques, with their varying characteristic observation length and time-scales (such as NMR, tracer or QENS measurements) which becomes more difficult as the concentration increases and solute and solvent molecule sizes are of the same order (such as for TAA cations in aqueous medium). Currently, the available literature does not provide a homogeneous picture regarding the diffusion of TAA cations in aqueous solution when experiments are at different time and length scales. One possible explanation is also proposed in this manuscript to bridge this gap between these two boundaries (length and time-scales) but requiress a better treatment.

In addition to the translational dynamics, we have identified the global cation rotation and methyl group H atom rotation with a characteristic time of ~ 350ps and ~ 5ps respectively (for TBA$^+$). These are such internal motions which cause the dynamics contained in the incoherent signal to overestimate the translational diffusion coefficient. The activation energy (E_a) of the TBA$^+$ CoM diffusion extracted from our neutron scattering data is (25.3 ± 1.5) kJ/mol, which is higher than the activation energy of bulk water diffusion (18 kJ/mol, in the range around room temperature) and about three times as high as the average energy of a hydrogen bond between two neighbouring molecules (8 kJ/mol). Note that the E_a from incoherent analysis is estimated around (20.6 ± 1.9) kJ/mol.

For the solvent, we conclude that the hydration structure around TAA salts are not same as simple salts like NaBr. The orientation of the solvent water molecules are tangential around TAA or choline cation whereas for simple salts (like Na$^+$) the oxygen atoms of water molecules are closer than hydrogen atoms. The water molecules can even penetrate in to TBA cation up to the same distance of first hydration shell for TMA (~ 3.4Å). The TAA cations are usually stay inside a cage and this solvation cage becomes weaker as the cation size is increased while around simple salts (like Na$^+$) more stable hydration shells are formed. Considering the dynamics, the decrease in solvent translational dynamics is more prominent for larger TAA cations because of the size and of the hydrophobic effect of the longer alkyl chain. The change

in solvent dynamics is not very different for the smallest TAA cation (TMA$^+$) compared to the simple salts. But it is seen that Choline$^+$ decreases the solvent dynamics $\sim$2 times faster than TMA$^+$.

10.1 Perspectives

Given the results discussed in this manuscript, several further experiments or studies would be interesting to carry out on TAABr solutions. Firstly, to characterise the solvent and solute behaviour in even more concentrated aqueous solutions and to find out the reason behind the surprisingly high solubilities of TAABr salts in water. Note that beyond the TBABr member, the water solubility of larger TAABr systems is drastically reduced [Nakayama 1989]. Secondly, the very short time dynamics (less than $\sim$5ps), both of solvent and the ions might deserve more attention because they can be originated from the bond stretches, vibrations. It would be interesting to study the dynamics in this region by Infra-Red (IR) spectroscopy and then to compare it with the result from Velocity Auto Correlation Function (VACF). However, for all these detailed comparisons, investigation and development of force fields tuned to dynamic rather than only structural information is necessary, as the former show in general much more sensitivity to the force field parametrisation. Such more elaborated force fields would hopefully also lead to a better numerical agreement between the ps-ns dynamics seen by MD simulations and quasi-elastic neutron scattering, as presented here.

Lastly, the natural extension of this study on aqueous TAABr solutions is to move to the measurement of thermodynamic and transport properties of different charged hydrophobic polyelectrolytes (PEs) in aqueous solution, moving closer towards modelling biologically and environmentally important macromolecules. Ionenes are one such class of PEs. Their structure is very simple, $[-(CH_3)_2N^+-(CH_2)_x-(CH_3)_2N^+-(CH_2)_y-]$, and it is analogous to a sequence of TMA cations linked via hydrocarbon chains of variable length (x and y). The length of these links tunes in detail the hydrophobicity of the overall PE chain. Apart from their role as models, aqueous solutions of ionenes are known to be used in many applications, such as ion exchange resins, humidity detectors, anti-microbial agents, water treatment in oil industry (with clay particles) etc.

11

Conclusion Générale (version française)

Les cations symétriques TAA constituent des systèmes idéaux pour étudier le comportement d'ions hydrophobes puisqu'ils combinent les effets hydrophobes à courte portée et les forces électrostatiques à grande portée. Ces sels présentent d'autres avantages : i) il est possible de deutérer sélectivement le soluté, étant donné qu'il ne comporte pas d'atomes d'hydrogène échangeables (ce qui est essentiel pour les expériences de diffusion neutronique), et ii) le degré d'hydrophobicité des cations de TAA peut être ajusté via les longueurs des chaînes alcanes. Au cours de ce travail, nous avons étudié les solutions aqueuses de TAA pour obtenir des informations sur la structure et la dynamique microscopiques via une combinaison de simulations de dynamique moléculaire et de diffusion de neutrons. En partant de la description structurale des solutés, nous avons analysé la dynamique des ions et étudié comment le comportement du solvant est modifié par la présence des ions hydrophobes. Les résultats principaux sont résumés ci-dessous.

Nous n'avons trouvé aucun signe d'agrégation des ions TBA$^+$ jusqu'à des concentrations de 3,56 m (sel : D$_2$O = 1:14) pour les ions TBA$^+$. Nos résultats montrent que les contreions Br- pénètrent partiellement entre les longues chaînes alcanes des TAA$^+$ (cas du TBA$^+$). Nous avons aussi observé que les molécules d'eau peuvent remplir l'espace entre les chaînes (environ 16 molécules d'eau dans le cas du TBA$^+$, d'après les calculs des coordinances à partir des fonctions de distribution de paires). Du calcul des rayons de giration nous déduisons une assez faible flexibilité des chaînes, estimée à 7% dans le cas du TBA$^+$. Tous ces résultats sur les ions et la pénétration de l'eau entre des chaînes alcanes flexibles démontrent bien que les cations TAA$^+$ ne peuvent pas être traités comme des sphères dures.

En ce qui concerne la dynamique, nous avons découplé et analysé séparément les composantes cohérente et incohérente de la diffusion de neutrons par des solutions de TAABr et de CholineBr afin d'estimer les coefficients de diffusion. Nous avons procédé à une étude détaillée de la dynamique des ions à une échelle de longueur entre l'angstrëm et le nm et à l'échelle de temps entre

la ps et la ns, en combinant la diffusion quasi-élastique de neutrons (QENS) et la dynamique moléculaire. Nous avons montré explicitement que le calcul de la diffusion translationnelle du centre de masse (CoM) des cations à partir de la diffusion incohérente surestime sa vraie valeur à cause de la contribution des mouvements intramoléculaires des atomes d'hydrogène. Ainsi, la diffusion globale du CoM du cation TBA$^+$ dans une solution à 0.89 m est inférieure d'un facteur de l'ordre de 2 par rapport à celle que l'on pourrait déduire à partir d'une analyse directe du résultat issu de la diffusion incohérente. Cette conclusion a des conséquences importantes pour beaucoup d'études de la dynamique de molécules polyatomiques (sous forme massique ou sous confinement) qui sont souvent effectuées à partir de la diffusion incohérente due aux atomes d'hydrogène constitutifs. Bien sûr, la surestimation de la diffusion du CoM à partir de la diffusion incohérente dépend de la structure et de la taille de la molécule étudiée et de l'échelle de temps typique de la dynamique des atomes d'hydrogène qui la composent. L'autre fait important est la comparaison entre les diverses méthodes expérimentales, en tenant compte de leurs fenêtres d'observation spatio-temporelles respectives (cas de la NMR, des méthodes de traceur ou de la QENS), qui devient très complexe dans le cas de solutions concentrées ou quand les molécules du soluté et du solvant ont des tailles comparables (cas des cations de TAA en solution aqueuse). D'une manière générale, la littérature existante ne donne pas une image homogène de la diffusion des cations de TAA en solution aqueuse dès que les expériences abordent des échelles différentes d'espace et de temps. Une explication possible visant à combler le fossé entre ces divers cas limites d'échelles spatio-temporelles est aussi donnée dans ce travail.

En plus de la diffusion translationnelle, nous avons étudié la rotation globale du cation ainsi que celle du groupe méthyl, caractérisées par des temps d'environ 350 et 5 ps, respectivement (dans le cas du TBA$^+$). Ce sont tous ces mouvements qui contribuent à que la diffusion incohérente amène à surestimer le coefficient de diffusion translationnelle. L'énergie d'activation (Ea) de la diffusion du CoM du TBA$^+$ extraite de nos données de diffusion de neutrons est égale à (25,3±1,5) kJ/mol, ce qui est significativement au-dessus de l'énergie d'activation de l'eau pure (18 kJ/mol à la température ambiante) et environ trois fois plus élevé que l'énergie moyenne d'une liaison hydrogène établie entre deux molécules d'eau voisines (8 kJ/mol). On peut noter que la valeur de Ea obtenue à partir de la diffusion incohérente est de l'ordre de (20,6±1,0) kJ/mol.

En ce qui concerne le solvant (l'eau), nous concluons que l'hydratation des sels TAA n'est pas aussi simple que celle des sels tels que le NaBr. L'orientation des molécules d'eau est tangentielle autour des TAA ou du cation choline tandis que pour les sels simples (comme Na$^+$) les atomes

d'oxygène des molécules d'eau sont plus proches du cation que ne le sont les atomes d'hydrogène. Les molécules d'eau peuvent même pénétrer dans les cations TBA jusqu'à des distances comparables à celles de la première sphère d'hydratation du TMA, soit 3.4 Å environ. Les cations de TAA restent généralement à l'intérieur d'une cage de solvatation mais cette cage est plus lâche pour les cations de plus grande taille tandis que, dans le cas d'ions plus simples (par exemple, Na$^+$), la sphère d'hydratation est plus stable. En ce qui concerne la dynamique, la diffusion translationnelle diminue quand la taille des cations TAA augmente à cause de la longueur des chaînes alcanes et de leur effet hydrophobe. En revanche, la dynamique du solvant dans le cas du plus petit des cations (TMA$^+$) n'est pas très différente de celle observée avec les sels simples. Mais, la Choline$^+$ réduit de moitié la dynamique du solvant par rapport à ce qui se passe avec le TMA$^+$.

11.1   Perspectives

Compte tenu des résultats discutés dans ce mémoire, nous pensons qu'il serait intéressant de mener plusieurs expériences ou études sur les solutions de TAABr. Tout d'abord, il faudrait caractériser le comportement du solvant et du soluté dans les solutions aqueuses encore plus concentrées et d'éclaircir les raisons fondamentales de leur excellente solubilité. Néanmoins, il convient de noter que, au-delà du TBABr, la solubilité des TAABr est fortement réduite [Nakayama 1989]. Deuxièmement, la dynamique aux temps très courts (inférieurs à 5 ps), aussi bien des ions que du solvant, devrait attirer plus d'attention car provenant d'élongations des liaisons et autres vibrations. Il serait intéressant d'étudier la dynamique dans cette fenêtre de temps par spectroscopie d'absorption infra-rouge et de la comparer avec la fonction de self corrélation des vitesses. Cependant, de telles comparaisons détaillées impliquent la recherche et le développement de champs de force adaptés aussi bien à la dynamique qu'aux études purement structurales. En effet, la dynamique semble particulièrement sensible à la paramétrisation des champs de force. De tels champs de force plus élaborés devraient amener tout naturellement à que les résultats de la dynamique moléculaire et de la diffusion neutronique à l'échelle ps-ns concordent encore mieux entre eux que dans les résultats présentés ici.

Enfin, le prolongement naturel de cette étude sur les solutions aqueuses de TAA est le passage à la mesure des propriétés thermodynamiques et de transport des différents polyélectrolytes hydrophobes chargés (PEs) en solution aqueuse, en vue de la modélisation des macromolécules similaires si importantes en Biologie et pour les études environnementales. Les ionènes

constituent une classe de PE. Leur structure est très simple : $[-(CH_3)_2N^+-(CH_2)_x-(CH_3)_2N^+-(CH_2)_y-]$ analogue à une séquence de cations de TMA liés par des chaînes hydrocarbonées de longueur variable (x et y). La longueur de ces liaisons module en détail l'hydrophobicité de l'ensemble de la chaîne du PE. Au-delà de leur importance en tant que modèle, les solutions aqueuses d'ionomènes sont aussi intéressantes pour de nombreuses applications, tels que les résines échangeuses d'ions, les détecteurs d'humidité, les agents antimicrobiens, le traitement de l'eau dans l'industrie pétrolière (contenant des particules d'argile), etc.

A

Chemical Model, Pitzer Equation and Hypernetted Chain Theory

A.1 Chemical Model and Pitzer Equation

A. m < m$^{'}$: In the lower concentration (m in molality) range (m < $m^{'}$, where $m^{'}$ is the lower concentration limit of validity of the polynomials), the calculation of osmotic coefficients is carried out with the help of data from model calculations. In range where m < $m^{'}$, experimental data analysis is based on the chemical model for electrolyte solution. The association constant $K_A{}^{(m)}$ ($= \frac{1-\alpha}{\alpha^2 m} \frac{\gamma_0}{\gamma_{\pm}^{'2}}$) remains the only parameter which modifies the osmotic coefficients via the chemical model using

$$\phi = 1 + \frac{1}{m} \int_0^m m.d(ln(\alpha\gamma_{\pm}^{'})) \tag{A.1}$$

and the activity co-efficeint by the relation

$$\gamma_{\pm} = \alpha\gamma_{\pm}^{'}, \tag{A.2}$$

where $\ln\gamma_{\pm}^{'} = -\frac{\kappa q}{1+\kappa R} \ln\frac{\rho/\rho_0}{1+mM_E}$ and $\ln\gamma_0 = 0$, with $q = \frac{e^2}{8\pi\varepsilon\varepsilon_0 kT}$; $\kappa^2 = 16000\pi q N_A(\alpha c)$. [$\gamma_{\pm}^{'}$ is mean activity coefficient in molality scale of the dissociated part of electrolyte, γ_0 is of ion pairs, α is degree of dissociation, ε and ε_0 are relative and absolute permittivity, e is charge of electron, N_A is Avogadro number, ρ_0 is density and R is distance parameter of the chemical model used where R = a(sum of cation and anion radii) + s(length of oriented methanol molecule)]

B. m > $m^{'}$: At higher concentration (m > $m^{'}$), reproduction of osmotic coefficients (1-1 electrolytes) are done using the Pitzer equation [Pitzer 1974b] [Pitzer 1974a] [Pitzer 1973b] [Pitzer 1977] [Pitzer 1973a]

$$
\begin{aligned}
\phi - 1 &= f^{\phi} + mB^{\phi} + m^2 C^{\phi}; \\
f^{\phi} &= -A^{\phi} I^{1/2}/(1 + bI^{1/2}) \\
B^{\phi} &= \beta^{(0)} + \beta^{(1)} exp[\alpha_1 I^{1/2}] + \beta^{(2)} exp[\alpha_2 I^{1/2}] \\
A^{\phi} &= (1/3)(2\pi N_A \rho_0)^{1/2} (e^2/4\pi\varepsilon\varepsilon_0 kT)^{3/2} \\
I &= 0.5 \sum m_i z_i^2
\end{aligned}
\tag{A.3}
$$

With the help of the seven parameters described here, the osmotic pressure can be calculated (though the quality of the fit or deviation $\Delta\phi$ depends on the number of parameters fitted) and to determine mean molal activity coefficient $\gamma_{\pm}$, Gibbs-Duhem equation is used.

$$
\begin{aligned}
ln\gamma_{\pm} &= f^{\gamma} + mB^{\gamma} + m^2 C^{\gamma}; \\
f^{\gamma} &= f^{\phi} - A^{\phi}(2/b)ln(1 + bI^{1/2}) \\
B^{\gamma} &= 2\beta^{(0)} + \zeta^{(1)} + \zeta^{(2)} \\
\zeta^{(i)} &= (2\beta^{(i)}/\alpha_i^2 I)[1 - exp(-\alpha_i I^{1/2})(1 + \alpha_i I^{1/2} - 0.5\alpha_i^2 I)], i = 1, 2 \\
C^{\gamma} &= 1.5 C^{\phi}
\end{aligned}
\tag{A.4}
$$

A.2   Hypernetted Chain Theory

Hypernetted chain theory (HNC) theory creates a link between the interaction potential $u_{ij}(r)$ of two particles i and j and their radial distribution function $g_{ij}(r)$ at a temperature T

$$
g_{ij}(r) = exp[-\beta u_{ij}(r) + \xi_{ij}(r)]
\tag{A.5}
$$

where $\beta = 1/(KT)$. $\xi_{ij}(r)$ can be written as the difference between direct pair potential $u_{ij}(r)$ and overall pair potential $w_{ij}(r)$

$$
\xi_{ij}(r) = \beta[u_{ij}(r) - w_{ij}(r)]
\tag{A.6}
$$

HNC approximates this as

$$
\xi_{ij}(r)] = h_{ij}(r) - c_{ij}(r)]
\tag{A.7}
$$

where

$$
h_{ij}(r)] = g_{ij}(r) - 1
\tag{A.8}
$$

is called the total correlation function and $c_{ij}(r)$ comes from Ornstein-Zernike equation

$$h_{ij}(r) = c_{ij}(r) + \sum_{i=k} \rho_{i=k} \int c_{ij} h_{ij} dr_k \qquad (A.9)$$

($\rho_{i=k}$ is the k type particle density). Substituting (A.7) and (A.8) in (A.5), $g_{ij}(r)$ can be solved iteratively as a function of $u_{ij}(r)$. In infinite dilution the solvent averaged potential $u_{ij}(r)$ can be expressed as

$$u_{ij}(r) = u_{ij}^*(r) + \frac{z_i z_j e^2}{4\pi\varepsilon\varepsilon_0} \frac{1}{r} \qquad (A.10)$$

$u_{ij}^*(r)$ is the short range potential here which depends on the model (this can be modified by Friedman-Gurney (FG) potential) and the second part is coulomb potential. The connection between HNC and osmotic coefficients can be drawn by writing the virial equation of state

$$\phi - 1 = -\frac{\beta}{6\rho} \sum \rho_i \rho_j \int r \frac{\partial u_{ij}(r)}{\partial r} g_{ij}(r) 4\pi r^2 dr \qquad (A.11)$$

where $\rho = \sum \rho_i$ and $\phi = \frac{\Pi}{\beta\rho}$ (Π is the osmotic pressure)

B

Force Field parameter

B.1 TEA and TPA Force Field parameters

atom or part of molecule	atom charge (e)	(from bold part)	
	N	C	H
-**N**-	0.026550		
-N-**CH₂**-		0.024951	0.068434
-N-$CH_2 - $**CH₃**-		-0.069047	0.050197

Table B.1: TEA$^+$ atomic charge distribution.

atom or part of molecule	atom charge (e)	(from bold part)	
	N	C	H
-**N**-	0.002611		
-N-**CH₂**-		-0.006390	0.068726
-N-$CH_2 - $**CH₂**-		0.022797	0.031648
-N-$CH_2 - CH_2 - $**CH₃**-		-0.113046	0.048413

Table B.2: TPA$^+$ atomic charge distribution.

bond elongation harmonic parameters	energy (kcal/mol/Å^2)	length (Å)
C-H$_C$	340	1.090
C-H$_N$	240	1.090
C-C	310	1.526
C-N	367	1.471

bond bending harmonic parameters	energy (kcal/mol/rad^2)	angle (degree)
H$_C$-C-H$_C$	35	109.5
H$_N$-C-H$_N$	35	109.5
C-C-H$_C$	50	109.5
C-C-H$_N$	50	109.5
C-C-N	80	111.2
H$_N$-C-N	50	109.5
C-N-C	50	109.5

dihedral interaction	energy (kcal/mol)	angle (degree)	L-J parameters	ε kcal/mol	σ Å
H$_C$-C-C-H$_C$	0.15	0.0	H$_C$	0.0157	1.487
H$_C$-C-C-H$_N$	0.15	0.0	H$_N$	0.0157	1.100
X-C-C-X	0.15	0.0	C	0.1094	1.900
X-C-N-X	0.15	0.0	N	0.1700	1.8240

Table B.3: TEA$^+$ Force Field.

Force field parameters for TEA$^+$ atoms are shown (H$_N$ represents the hydrogens attached to the central N).

bond elongation harmonic parameters	energy (kcal/mol/Å^2)	length (Å)
C-H$_C$	340	1.090
C-H$_N$	240	1.090
C-C	310	1.526
C-N	367	1.471

bond bending harmonic parameters	energy (kcal/mol/rad^2)	angle (degree)
H$_C$-C-H$_C$	35	109.5
H$_N$-C-H$_N$	35	109.5
C-C-H$_C$	50	109.5
C-C-H$_C$	50	109.5
C-C-C	40	109.5
C-C-N	80	111.2
H$_N$-C-N	50	109.5
C-N-C	50	109.5

dihedral interaction	energy (kcal/mol)	angle (degree)
H$_C$-C-C-H$_C$	0.15	0.0
H$_C$-C-C-C	0.16	0.0
H$_C$-C-C-H$_N$	0.15	0.0
H$_N$-C-C-C	0.16	0.0
X-C-C-X	0.15	0.0
X-C-N-X	0.15	0.0

L-J parameters	ε kcal/mol	σ Å
H$_C$	0.0157	1.487
H$_N$	0.0157	1.100
C	0.1094	1.900
N	0.1700	1.8240

Table B.4: TPA$^+$ Force Field.
Force field parameters for TPA$^+$ atoms are shown (H$_N$ represents the hydrogens attached to the central N).

C
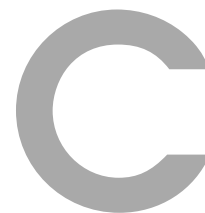
Estimation of Rotation time

C.1 Estimation of Rotation time from MSD calculation
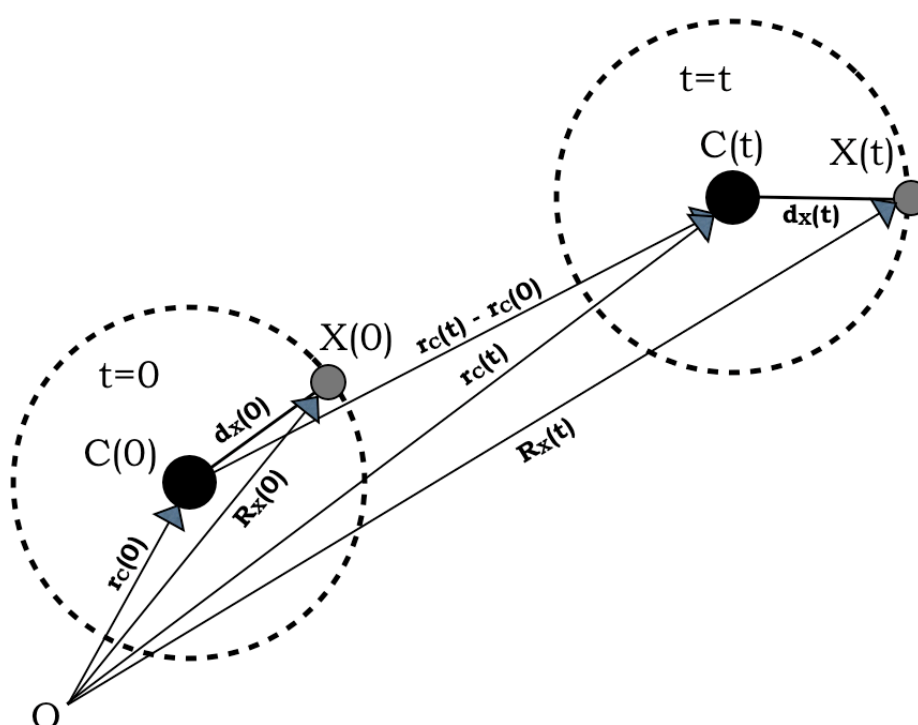
Figure C.1: Estimation of Rotation time from MSD calculation. A molecule with CoM at C with attached atom X moves with time.

We have a molecule whose Centre of Mass (CoM) is located at C with an atom associated with it is at X. Let us suppose at time t=0 and t=t, the

respective positions are C(0), X(0) and C(t), X(t). In figure C.1, the atomic distances are expressed with respect to origin O.

Now if the molecule rotates, the motion of atom X will contain the CoM translation of C plus the its own rotation around C. The Mean Square Displacement (MSD) of atom X can be written as

$$
\begin{aligned}
\left\langle [\mathbf{R_X}(t) - \mathbf{R_X}(0)]^2 \right\rangle &= \left\langle [\mathbf{r_c}(t) + \mathbf{d_X}(t) - \mathbf{r_c}(0) - \mathbf{d_X}(0)]^2 \right\rangle \\
&= \left\langle [\mathbf{r_c}(t) - \mathbf{r_c}(0) + \mathbf{d_X}(t) - \mathbf{d_X}(0)]^2 \right\rangle \\
&= \left\langle [\mathbf{r_c}(t) - \mathbf{r_c}(0)]^2 \right\rangle + \left\langle [\mathbf{d_X}(t) - \mathbf{d_X}(0)]^2 \right\rangle
\end{aligned}
$$
$$
+2(\mathbf{r_c}(t) - \mathbf{r_c}(0)) \cdot (\mathbf{d_X}(t) - \mathbf{d_X}(0)) \tag{C.1}
$$

So if we take the difference of MSD between atom X and C, the resultant will be like following

$$
\begin{aligned}
\left\langle [\mathbf{R_X}(t) - \mathbf{R_X}(0)]^2 \right\rangle - \left\langle [\mathbf{r_c}(t) - \mathbf{r_c}(0)]^2 \right\rangle &= \left\langle [\mathbf{d_X}(t) - \mathbf{d_X}(0)]^2 \right\rangle \\
&= 2b^2[1 - \frac{1}{b^2}\mathbf{d_X}(t) \cdot \mathbf{d_X}(0)]
\end{aligned}
$$
$$\tag{C.2}$$

where the last term of equation C.1 is 0 because $(\mathbf{r_c}(t) - \mathbf{r_c}(0))$ and $(\mathbf{d_X}(t) - \mathbf{d_X}(0))$ are uncorrelated and b is modulus of $\mathbf{d_X}$ i.e the distance between CoM (C) and the atom X . This can be compared with $2b^2(1 - e^{-\frac{t}{\tau_{rot}}})$ to estimate the rotational time (τ_{rot}).

C.2   Estimation of methyl Rotation time

Let us assume that $p(\mathbf{r_1}, t)$, $p(\mathbf{r_2}, t)$ and $p(\mathbf{r_3}, t)$ are the probability of finding a particle at time t, at position $\mathbf{r_1}$, $\mathbf{r_2}$ and $\mathbf{r_3}$ respectively. Then the rate equations can be written as

$$
\begin{aligned}
\frac{d}{dt}p(\mathbf{r_1}, t) &= \frac{1}{\tau}[-2p(\mathbf{r_1}, t) + p(\mathbf{r_2}, t) + p(\mathbf{r_3}, t)] \\
\frac{d}{dt}p(\mathbf{r_2}, t) &= \frac{1}{\tau}[-p(\mathbf{r_1}, t) - 2p(\mathbf{r_2}, t) + p(\mathbf{r_3}, t)] \\
\frac{d}{dt}p(\mathbf{r_3}, t) &= \frac{1}{\tau}[p(\mathbf{r_1}, t) + p(\mathbf{r_2}, t) - 2p(\mathbf{r_3}, t)] \tag{C.3}
\end{aligned}
$$

where $\frac{1}{\tau}$ is the jump-rate probability from one position to other. Now considering the whole system is at equilibrium at t=0 and t=∞ with the
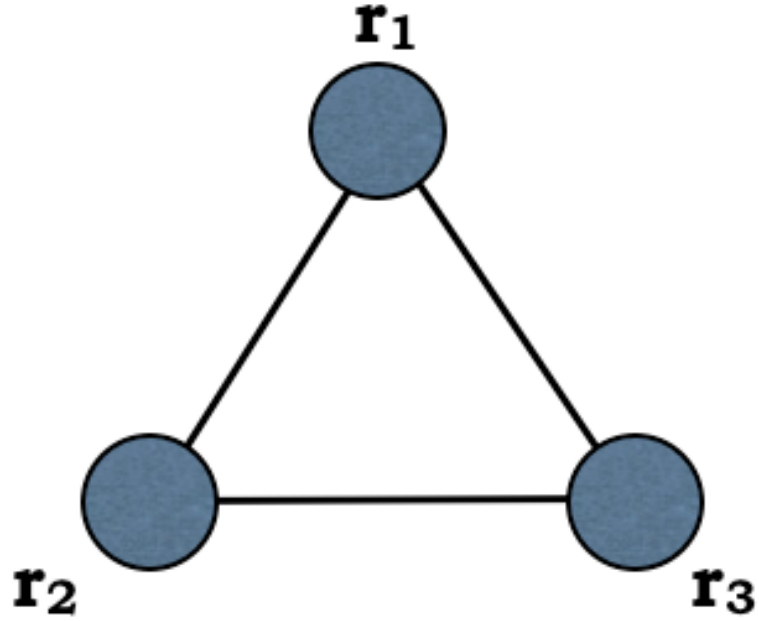
Figure C.2: Jump model for three points placed equidistantly on a circle.

particle is at position $\mathbf{r_1}$ we can write

$p(\mathbf{r_1}, 0) = 1; \; p(\mathbf{r_2}, 0) = p(\mathbf{r_3}, 0) = \frac{1}{3}$
and $p(\mathbf{r_1}, \infty) = p(\mathbf{r_2}, \infty) = p(\mathbf{r_3}, \infty) = \frac{1}{3}$

Again we know that
$p(\mathbf{r_1}, t) + p(\mathbf{r_2}, t) + p(\mathbf{r_3}, t) = 1$

With all these condition, the solution for $p(\mathbf{r_i}, t)$ can be written as

$$p(\mathbf{r_i}, t) = \alpha_i + \beta_i e^{-\frac{3t}{\tau}} \tag{C.4}$$

where

$$\sum_i \alpha_i = 1$$

$$\sum_i \beta_i = 0 \tag{C.5}$$

that means $\alpha_1 = \frac{1}{3}$, $\beta_1 = \frac{2}{3}$; $\alpha_2 = \frac{1}{3}$, $\beta_2 = -\frac{1}{3}$
and
$\alpha_3 = \frac{1}{3}$, $\beta_3 = -\frac{1}{3}$

So we have

$$p(\mathbf{r_1}, t; \mathbf{r_1}, 0) = \frac{1}{3}[1 + 2e^{-\frac{3t}{\tau}}] = p(\mathbf{r_2}, t; \mathbf{r_2}, 0) = p(\mathbf{r_3}, t; \mathbf{r_3}, 0)$$

$$p(\mathbf{r_2}, t; \mathbf{r_1}, 0) = \frac{1}{3}[1 - e^{-\frac{3t}{\tau}}] = p(\mathbf{r_1}, t; \mathbf{r_2}, 0) = p(\mathbf{r_2}, t; \mathbf{r_3}, 0)$$

$$p(\mathbf{r_3}, t; \mathbf{r_1}, 0) = \frac{1}{3}[1 - e^{-\frac{3t}{\tau}}] = p(\mathbf{r_3}, t; \mathbf{r_2}, 0) = p(\mathbf{r_1}, t; \mathbf{r_3}, 0) \qquad \text{(C.6)}$$

where $p(\mathbf{r_i}, t; \mathbf{r_j}, 0)$ is the probability of finding a particle that comes to position $\mathbf{r_i}$ at time t from $\mathbf{r_j}$ at time t=0. Therefore we can write

$$\frac{1}{b^2}\mathbf{dx}(t) \cdot \mathbf{dx}(0) \quad = \quad cos(0)p(\mathbf{r_1}, t; \mathbf{r_1}, 0) + cos\left(\frac{2\pi}{3}\right)p(\mathbf{r_2}, t; \mathbf{r_1}, 0)$$

$$+cos\left(-\frac{2\pi}{3}\right)p(\mathbf{r_1}, t; \mathbf{r_1}, 0)$$

$$= \quad 1\left(\frac{1}{3}\right)\left(1 + 2e^{-\frac{3t}{\tau}}\right) + \left(-\frac{1}{2}\right)\left(\frac{1}{3}\right)\left(1 - e^{-\frac{3t}{\tau}}\right)$$

$$+\left(-\frac{1}{2}\right)\left(\frac{1}{3}\right)\left(1 - e^{-\frac{3t}{\tau}}\right)$$

$$= \quad e^{-\frac{3t}{\tau}} \qquad\qquad\qquad\qquad\qquad \text{(C.7)}$$

Bibliography

[Ancian] B Ancian. *NMR measurements on 0.89m TBABr in D2O.* private communication, . (Cited on page 153.)

[Andreani 1991] C Andreani, V Merlo, A Ricci M and A. K Soper. Mol. Phys., vol. 73, page 407, 1991. (Cited on page 33.)

[Bagchi 1998] B Bagchi. *Microscopic derivation of the hubbard-onsager-zwanzig expression of limiting ionic conductivity.* Journal of chemical physics, vol. 109, pages 3989–3993, 1998. (Cited on pages 154 and 155.)

[Barthel 1994] J Barthel, L Klein, W Kunz, Calmettes P and P Turq. *Tetraalkylammonium bromides in methanol: small angle neutron scattering and vapor pressure measurements.* J. Solution Chem., vol. 23, pages 955–971, 1994. (Cited on page 22.)

[Ben-Naim 1980] A Ben-Naim. *Hydrophobic Interactions.* Plenum Press, New York, 1980. (Cited on pages 16 and 17.)

[Berendsen 1987] H. J. C Berendsen, J. R Grigera and T. P Straatsma. *The Missing Term in Effective Pair Potentials.* J. Phys. Chem, vol. 91, pages 6269–6271, 1987. (Cited on page 82.)

[Bradl 1993] S Bradl and E. W Lang. *Hydration water dynamics in undercooled aqueous solutions of hydrophobic ions.* J. Phys. Chem., vol. 97, pages 10463–10471, 1993. (Cited on pages 18, 34 and 35.)

[Bradl 1994] S Bradl, E. W Lang, J. Z Turner and Soper A. K. *NMR and neutron scattering investigation of undercooled aqueous solutions of apolar solutes.* J. Phys. Chem., vol. 98, pages 8161–8168, 1994. (Cited on pages 34 and 35.)

[Brodholt 1993] J Brodholt and B Wood. *Simulations of the Structure and Thermodynamic Properties of Water at High Pressures and Temperatures.* Journal of Geophysical Research, vol. 98, pages 519–536, 1993. (Cited on page 82.)

[Brown 1988] A. N Brown, M Newbery, R. K Thomas and J. W White. *Ion and Solvent Dynamics in Aqueous Tetramethylammonium Chloride Soliutions.* J. Chem. Soc., Faraday Trans. 2, vol. 84, pages 17–33, 1988. (Cited on page 153.)

[Buchner 2002] R Buchner, C Holzl, J Stauber and J Barthel. *Dielectric spectroscopy of ion-pairing and hydration in aqueous tetra-N-alkylammonium halide solutions.* Phys. Chem. Chem. Phys., vol. 4, pages 2169–2179, 2002. (Cited on pages 23, 27, 29, 84, 96, 131, 155 and 159.)

[Bée 1988] M Bée. *Quasielastic neutron scattering.* Quasielastic neutron scattering, adam hilger, bristol and philadelphia, 1988. (Cited on pages 40, 48, 49, 54, 61, 63, 113, 114, 118 and 121.)

[Cabral 2000] J. T Cabral, A Luzar, J Teixeira and M. C Bellissent-Funel. *Single-particle dynamics in dimethyl-sulfoxide/water eutectic mixture by neutron scattering.* J. Chem. Phys., vol. 113, pages 8736–8745, 2000. (Cited on pages 113, 114, 115 and 147.)

[Calandrini 2006] V Calandrini, A Deriu, G Onori, A Paciaroni and T. F Telling. *Pressure effect on water dynamics in tetra-butyl alcohol/water solutions.* J. Phys.: Condens. Matter, vol. 18, pages 2363–2371, 2006. (Cited on page 34.)

[Calmettes 1992] P Calmettes, W Kunz and P Turq. *Distribution of small organic cations in aqueous solutions.* Physica B, vol. 180, pages 868–870, 1992. (Cited on pages 19 and 22.)

[Cartailler 1991] T Cartailler, W Kunz, P Turq and M-C Bellisent-Funel. *Lithium bromide in acetonitrile and water: a neutron scattering study.* J. Phys.: Condens. Matter, vol. 3, pages 9511–9520, 1991. (Cited on page 35.)

[Case 2008] D.A Case, T. A Darden, T. E Cheatham, III, C. L Simmerling, J Wang, R. E Duke, R Luo, M Crowley, R. C Walker, W Zhang, K; M Merz, B Wang, S Hayik, A Roitberg, G Seabra, I Kolossváry, K. F Wong, F Paesani, J Vanicek, X Wu, S. R Brozell, T Steinbrecher, H Gohlke, L Yang, C Tan, J Mongan, V Hornak, G Cui, D. H Mathews, M. G Seetin, C Sagui, V Babin and P. A Kollman. *AMBER 10.* AMBER 10, University of California, San Francisco, 2008. (Cited on page 82.)

[Chahid 1994] A Chahid, A Alegria and J Colmenero. *Methyl group dynamics in poly(vinyl methyl ether). a rotation rate distribution model.* Macromolecules, vol. 27, pages 3282–3288, 1994. (Cited on page 114.)

[Chandler 2005] D Chandler. *Interfaces and the driving force of hydrophobic assembly.* Nature, vol. 437, pages 640–647, 2005. (Cited on pages 11, 13 and 16.)

[Cho 1999] C. H Cho, J Urquidi, S Singh and G. W Robinson. *Thermal Offset Viscosities of Liquid H2O, D2O, and T2O.* J. Phys. Chem. B, vol. 103, pages 1991–1994, 1999. (Cited on pages 118, 123 and 124.)

[Diamond 1963] R. M Diamond. *Aqueous solution behavior of large univalent ions. a new type of ion-pairing.* J. Phys. Chem., vol. 67, pages 2513–2517, 1963. (Cited on page 21.)

[Dianoux 2003] A-J Dianoux and G Lander. *Neutron data booklet.* Neutron data booklet, institut laue-langevin, vol. 2, 2003. (Cited on pages 95 and 113.)

[Eagland 1972] D Eagland and G Pilling. *On the Viscosity of Concentrated Aqueous Solutions of Tetraalkylammonium Bromides.* J. Phys. Chem., vol. 76, pages 1902–1906, 1972. (Cited on pages 23, 27, 29, 84 and 131.)

[Enderby 1979] J. E Enderby and G. W Neilson. *Water: A comprehensive Treatise.* (Plenum) Chap.5, vol. 6, 1979. (Cited on page 30.)

[Evans 1966] D. F Evans and R. L Kay. *The conductance bahavior of the symmetrical tetraalkylammonium haides in aqueous at 25 and 10°C.* J. Phys. Chem., vol. 70, pages 367–374, 1966. (Cited on page 21.)

[Evans 1990] D Evans and G Morriss. *Statistical Mechanics of Nonequilibrium liquids.* Academic Press, 1990. (Cited on page 70.)

[Feakins 1989] D Feakins, F. M Canning, J. J Mullally and W. E Waghorne. *The thermodynamics of solutions.* Pure Appl. Chem., vol. 61, pages 133–142, 1989. (Cited on page 33.)

[Frank 1957] H. S Frank and W. Y Wen. . Discussions Faraday SOC., vol. 24, 1957. (Cited on page 29.)

[Franks 1975] F Franks. Water: A comprehensive Treatise, vol. 4, 1975. (Cited on pages 11, 13 and 16.)

[Frenkel 2002] D Frenkel and B Smit. *Understanding Molecular Simulations, From Algorithms to Applications.* Academic Press, 2002. (Cited on pages 71, 73, 74 and 80.)

[Friedman 1988] H. L Friedman. Faraday Discussion, vol. 85, page 1, 1988. (Cited on page 22.)

[Green 1987] J. L Green, M. G Sceats and A. R Lacey. *Hydrophobic effects in the water network structure of aqueous solutions of a semiclathrate molecule.* J. Chem. Phys., vol. 87, pages 3603–3610, 1987. (Cited on page 91.)

[Grillo 2008] I Grillo. *Small-Angle Neutron scattering and Applications in Soft Condensed Matter.* Springer-Verlag Berlin Heidelberg, 2008. (Cited on page 59.)

[Guillot 2002] B Guillot. *A Reappraisal of what we have learnt during three decades of computer simulations on water.* J. Mol. Liq., vol. 101, pages 219–260, 2002. (Cited on page 82.)

[Hansen 1986] J. P Hansen, D and I. R McDonald. *Theory of simple liquids.* Academic Press, 1986. (Cited on pages 19, 70, 71 and 80.)

[Hertz 1969] H. G Hertz, B Lindman and V Siepe. *Translational motion and hydration of the symmetrical tetraalkylammonium ions in aqueous solution.* Berichte der Bunsengesellschaft, vol. 73, pages 542–549, 1969. (Cited on pages 27, 28, 30, 153 and 155.)

[Hewish 1983] N. A Hewish, J. E Enderby and W. S Howels. *The dynamics of water molecules in ionic solutions.* J. Phys. C: Solid State Phys., vol. 16, pages 1777–1791, 1983. (Cited on page 29.)

[Heyda 2010] J Heyda, M Lund, M Oncak, P Slavicek and P Jungwirth. *Tetraalkylammonium ions in aqueous and non-aqueous solutions.* J. Phys. Chem., vol. 114, pages 10843–10852, 2010. (Cited on pages 22, 32, 82 and 96.)

[Horinek 2009] D Horinek, S Mamatkulov and R Netz. *Rational design of ion force fields based on thermodynamic solvation properties.* J. Chem. Phys., vol. 130, page 124507, 2009. (Cited on page 82.)

[Hummer 2000] G Hummer, S Garde, A. E Garcia and L. R Pratt. *New Perspective on hydrophobic effects.* Chem. Phys, vol. 258, pages 349–370, 2000. (Cited on page 36.)

[Hynes 1979] J. T Hynes, R Kapral and M Weinberg. *Molecular theory of translational diffusion: microscopic generalization of the normal velocity boundary condition.* J. Chem. Phys., vol. 70, pages 1456–1466, 1979. (Cited on pages 154 and 155.)

[James 2000] E. M et al James. *Topics in Polymer Science.* Clarenson press, Oxford, 2000. (Cited on page 41.)

[Jones 1988] R. B Jones. *Rotational Diffusion of a tracer colloid particle.* Physica A, vol. 150, pages 339–356, 1988. (Cited on page 133.)

[Jorgensen 1986] W. L Jorgensen and J Gao. *Monte carlo simulations of the hydration of ammonium and carboxylate ions.* J. Phys. Chem., vol. 90, pages 2174–2182, 1986. (Cited on page 162.)

[Joung 2008] I. S Joung and T. E Cheatham. *Determination of Alkali and Halide Monovalent Ion Parameters for Use in Explicitly Solvated Biomolecular Simulations.* J. Phys. Chem., vol. 112, pages 9020–9041, 2008. (Cited on page 82.)

[Kauzmann 1959] W Kauzmann. *Some factors in the interpretation of protein denaturation.* Adv. Prot. Chem., vol. 14, pages 1–63, 1959. (Cited on page 16.)

[Kay 1965] R. L Kay and D. F Evans. *The conductance of the tetraalkylammonium halides in deuterium oxide solutions at 25° C.* J. Phys. Chem., vol. 69, pages 4216–4221, 1965. (Cited on pages 27 and 29.)

[Kay 1966a] R. L Kay and D. F Evans. *The effect of solvent structure on the mobility of symmetrical ions in aqueous solution.* J. Phys. Chem., vol. 70, pages 2325–2335, 1966. (Cited on pages 18, 24 and 25.)

[Kay 1966b] R. L Kay, T Vituccio, Zawoyski and D. F Evans. *Viscosity B coeffients for the tetraalkylammonium halides.* J. Phys. Chem., vol. 70, pages 2336–2341, 1966. (Cited on pages 18 and 26.)

[Kim 1973] H Kim, A Revzin and Gosting L. J. *Diffusion coefficients of tetrabutylammonium halides in water at 25° C.* J. Phys. Chem., vol. 77, pages 2567–2570, 1973. (Cited on pages 28, 30 and 95.)

[Kneller 1996] G. R Kneller, V Keiner, M Kneller and M Schiler. *nMOLDYN. nMOLDYN: A Program Package for a Neutron Scattering Oriented Analysis of Molecular Dynamics Simulations00 8,* 1996. (Cited on pages 81, 82 and 83.)

[Koneshan 1998] S Koneshan, J. C Rasaiah, R. M Lynden-Bell and S. H Lee. *Solvent Structure, Dynamics, and Ion Mobility in Aqueous Solutions at 25° C.* J. Phys. Chem. B, vol. 102, pages 4193–4204, 1998. (Cited on page 82.)

[Kunz 1990] W Kunz, P Calmettes and P Turq. *Structure of nonaqueous electrolyte solutions by small-angle neutron scattering, hypernetted chain,*

and brownian dynamics. J. Chem. Phys., vol. 92, pages 2367–2372, 1990. (Cited on page 22.)

[Kunz 1991] W Kunz, P Turq, M-C Bellissent-Funel and P Calmettes. *Dynamics and spatial correlations of tetrapentylammonium ions in acetonitrile.* J. Chem. Phys., vol. 95, pages 6902–6910, 1991. (Cited on pages 22 and 97.)

[Kunz 1992a] W Kunz, P Calmettes, G Jannink, T Cartailler and P Turq. *The charge structure factor of 1:1 electrolyte in solution.* J. Phys. Chem., vol. 96, pages 7034–7038, 1992. (Cited on pages 20, 21, 95 and 129.)

[Kunz 1992b] W Kunz, P Turq, P Calmettes, J Barthel and L Klein. *n-tetrapentylammonium bromide in 2-propanol: vapor pressure and small-angle neutron scattering measurements.* J. Phys. Chem., vol. 96, pages 2743–2749, 1992. (Cited on pages 22, 95, 97, 101 and 129.)

[Lang 1990] E. W Lang, S Bradl, W Fink, H Radkowitsch and D Girlich. *Nuclear magnetic resonance studies of supercooled aqueous electrolyte solution.* J. Phys.: Condens. Matter, vol. 2, pages SA195–SA200, 1990. (Cited on page 34.)

[Lang 1991] E. W Lang, S Bradl, W Kunz and P Turq. *NMR relaxation study of tetrapentylammonium ions in acetonitrile solutions.* J. Phys. Chem., vol. 95, pages 10576–10582, 1991. (Cited on page 34.)

[Lechner 2006] R Lechner and S Longville. *Neutron scattering in biology techniques and applications.* , 2006. (Cited on pages 54, 57 and 58.)

[Lee 1988] J. J Lee and M. D Lee. *Conductance of tetraalkylammonium halides in ethanol-water mixtures.* Korean J. Chem. Eng., vol. 5, pages 5–13, 1988. (Cited on pages 18 and 21.)

[Lee 1996] S. H Lee and J. C Rasaiah. *Molecular Dynamics Simulation of Ion Mobility. 2. Alkali Metal and Halide Ions Using the SPC/E Model for Water at 25° C.* Biophys. Chem., vol. 100, pages 1420–1425, 1996. (Cited on page 82.)

[Lindenbaum 1964] S Lindenbaum and G. E Boyd. *Osmotic and activity coefficients for the symmetrical tetraalkylammonium halides in aqueous solution at 25° C.* J. Phys. Chem., vol. 68, pages 911–917, 1964. (Cited on page 21.)

[Liu 2002] Li Liu, A Faraone and S-H Chen. *Model for the rotational contribution to quasielastic neutron scattering spectra from supercooled water.* Phys. Rev. E, vol. 65, pages 041506–1–041506–8, 2002. (Cited on page 133.)

[Lopez 1998] M. M Lopez and G. I Makhataze. *Solvent isotope effect on thermodynamics of hydration.* Biophys. Chem., vol. 74, pages 117–125, 1998. (Cited on page 36.)

[Lovesey 1984] S. W Lovesey. *Theory of Neutron Scattering from Condensed Matter.* Clarenson press, Oxford, vol. 1, 1984. (Cited on page 40.)

[Malikova 2006] N Malikova, A Cadène, V Marry, E Dubois and P Turq. *Diffusion of water in clays on the microscopic scale : modeling and experiment.* J. Phys. Chem. B, vol. 110, pages 3206–3214, 2006. (Cited on page 126.)

[Malikova 2010] N Malikova, E Dubois, V Marry, B Rotenberg and P Turq. *Dynamics in Clays - Combining Neutron Scattering and Microscopic Simulation.* Zeitschrift Phys. Chem., vol. 224, no. 1-2, pages 153–181, 2010. (Cited on page 126.)

[Marcus 2008] Y Marcus. *Tetraalkylammonium ions in aqueous and non-aqueous solutions.* J. Solution Chem., vol. 37, pages 1071–1098, 2008. (Cited on pages 23 and 25.)

[Markovich 1996] G Markovich, L Perera, M. L Berkowitz and O Cheshnovsky. *The solvation of Cl2, Br2, and I2 in acetonitrile clusters: Photoelectron spectroscopy and molecular dynamics simulations.* J. Chem. Phys., vol. 7, pages 2675–2685, 1996. (Cited on page 82.)

[Marry 2011] V Marry, E Dubois, N Malikova, S Durand-Vidal, S Longeville and J Breu. *Water dynamics in hectorite clays: influence of temperature studied by coupling Neutron Spin Echo and Molecular Dynamics.* Envir. Sci. and Technol., vol. 45, pages 2850–2855, 2011. (Cited on page 126.)

[Masakatsu 1996] U Masakatsu, T Noriaki, Y Koji and I Kazuyasu. *Pressure and solvent isotope effects on the mobility of monovalent cations in water.* J. Chem. Phys., vol. 105, pages 3662–3670, 1996. (Cited on page 36.)

[Mezei 1980] F Mezei. *Lecture notes in physics.* Lecture notes in physics, springer-verlag berlin heidelberg new yok, 1980. (Cited on pages 40, 54, 58, 118 and 121.)

[Mukherjee 1985] L.M Mukherjee and R. G Bates. *Osmotic and Activity Coefficients at 25°C for Tetraalkylammonium Bromides in Deuterium Oxide.* J. Sol. Chem., vol. 14, pages 255–262, 1985. (Cited on page 102.)

[Nakayama 1989] H Nakayama, H Kuwata, N Yamamoto, Y Akagi and H Matsui. *Solubilities and dissolution states of a series of symmetrical tetraalkylammonium salts in water.* B. Chem. Soc. JPN., vol. 62, pages 985–982, 1989. (Cited on pages 173 and 177.)

[Nallet 1983] F Nallet, G Jannink, J. B Hayter, R Oberthur and C Picot. *Observation of the dynamics of polyelectrolyte strong solutions by quasielastic neutron scattering.* J. Physique, vol. 44, pages 87–99, 1983. (Cited on page 19.)

[Novikov 1996a] A Novikov, M Rodnikova, V. V Savostin and Sobolev. Russ. J. Phys. Chem., vol. 70, page 1011, 1996. (Cited on pages 28 and 153.)

[Novikov 1996b] A. G Novikov, M. N Rodnikova, V. V Savostin and O. V Sobolev. *The vibration-rotation motions of water molecules in a 2m aqueous CsCl solution.* Chem. Phys. Lett., vol. 259, pages 391–396, 1996. (Cited on page 34.)

[Novikov 1997] A. G Novikov, M. N Rodnikova, V. V Savostin and O. V Sobolev. *Study of Li+ ion hydration by inelastic neutron scattering.* Physica B, vol. 234–236, pages 340–342, 1997. (Cited on page 34.)

[Novikov 1999] A Novikov, M Rodnikova, J Barthel and O Sobolev. *Quasielastic neutron scattering of aqueous tetrabutylammonium chloride.* J. Mol. Liq., vol. 79, pages 203–212, 1999. (Cited on pages 28, 153 and 162.)

[Novikov 2001] A. G Novikov, M. N Rodnikova and O. V Sobolev. *Comparative analysis of ionic and hydrophobic hydration effects.* J. Mol. Liq., vol. 91, pages 91–97, 2001. (Cited on page 34.)

[Paluch 2003] M Paluch, M Sekula, S Pawlus, S. J Rzoska, J Ziolo and C. M Roland. *Test of the Einstein-Debye Relation in Supercooled Dibut ylphthalate at Pressures upto 1.4 GPa.* Phys. Rev. Lett., vol. 90, pages 175702–1–175702–4, 2003. (Cited on page 131.)

[Pitzer 1973a] K. S Pitzer. *Thermodynamics of electrolytes. I. Theoretical basis and general equations.* J. Phys. Chem., vol. 77, pages 268–277, 1973. (Cited on pages 19 and 179.)

[Pitzer 1973b] K. S Pitzer and G Mayorga. *Thermodynamics of electrolytes. III. activity and osmotic coefficients for strong electrolytes with one or ions univalent.* J. Phys. Chem., vol. 77, pages 2300–2308, 1973. (Cited on pages 19 and 179.)

[Pitzer 1974a] K. S Pitzer and J. J Kim. *Thermodynamics of electrolytes. iv. activity and osmotic coefficients for mixed electrolytes.* J. Am. Chem. Soc., vol. 96, pages 5701–5707, 1974. (Cited on pages 19 and 179.)

[Pitzer 1974b] K. S Pitzer and G Mayorga. *Thermodynamics of electrolytes. iii. activity and osmotic coefficients for 2-2 electrolytes.* J. Solution Chem., vol. 3, pages 539–546, 1974. (Cited on pages 19 and 179.)

[Pitzer 1977] K. S Pitzer, R. N Roy and F Silvester L. *Thermodynamics of electrolytes. 7. sulfuric acid.* JACS, vol. 99, pages 4930–4936, 1977. (Cited on pages 19 and 179.)

[Ramanathan 1972] P. S Ramanathan, C. V Krishnan and H. I Friedman. *Models Having the Thermodynamic Properties of Aqueous Solutions of Tetraaikylammonium Halides.* J. Sol. Chem., vol. 1, pages 237–262, 1972. (Cited on page 19.)

[Rasaiah 1968] J. C Rasaiah and H. L Friedman. *Charged square-well model for ionic solutions.* J. Chem. Phys., vol. 72, pages 3352–3353, 1968. (Cited on page 19.)

[Rasaiah 1969] J. C Rasaiah and H. L Friedman. *Integral equation computations for aqueous 1-1 electrolytes. accuracy of the method.* J. Chem. Phys., vol. 50, pages 3965–3976, 1969. (Cited on page 19.)

[Robinson 2002] R. A Robinson and R. H Stokes. *Electrolyte solutions.* Electrolyte solutions, Dover publication, inc., new york, vol. 2, 2002. (Cited on page 27.)

[Sears 1966a] V. F Sears. *Theory of Cold Neutron Scattering by Homonuclear Diatomic Liquids I. Free Rotation.* Canad. J. Phys., vol. 44, pages 1279–1297, 1966. (Cited on page 63.)

[Sears 1966b] V. F Sears. *Theory of Cold Neutron Scattering by Homonuclear Diatomic Liquids II. Hindered Rotation.* Canad. J. Phys., vol. 44, pages 1299–1311, 1966. (Cited on pages 63 and 133.)

[Slusher 1997] J. T Slusher and P. T Cummings. *Molecular simulation study of tetraalkylammonium halides. 1. solvation structures and hydrogen*

bonding in aqueous solutions. J. Phys. Chem. B, vol. 101, pages 3818–3826, 1997. (Cited on pages 29 and 34.)

[Smith 2007] W Smith, T. R Forester and I. T Todorov. *THE DL POLY 2 USER MANUAL*. THE DL POLY 2 USER MANUAL, Version 2.18, STFC Daresbury Laboratory, Daresbury, Warrington WA4 4AD Cheshire, UK, 2007. (Cited on pages 73, 74, 77, 82 and 134.)

[Soper 1992] A. K Soper, J Turner and J. L Finney. *Solute-solute correlations in aqueous solutions of tetramethylammonium chloride*. Mol. Phys., vol. 77, pages 431–437, 1992. (Cited on pages 30, 33 and 159.)

[Squires 1988] G. L Squires. *Introduction to the thermal neutron scattering*. Introduction to the thermal neutron scattering, cambridge university press, 1988. (Cited on pages 40, 48, 61, 63, 109 and 121.)

[Surdo 1979] A. L Surdo and H. E Wirth. *Transport Properties of Aqueous Electrolyte Solutions. Temperature and Concentration Dependence of the Conductance and Viscosity of Concentrated Solutions of Tetraalkylammonium Bromides, NH,Br, and LiBr* . J. Phys. Chem., vol. 83, pages 879–888, 1979. (Cited on pages 23, 24, 25, 27 and 29.)

[Tanford 1979] C Tanford. *The Hydrophobic Effect, Formation of Micelles and Biological Membranes, 2ED*. John Wiley and Sons, Inc, 1979. (Cited on page 17.)

[Teixeira 1985] T Teixeira, M. C Bellissent-Funel, S.H Chen and A. J Dianoux. *Experimental determination of the nature of diffusive motions of water molecules at low temperatures*. Physical Review A, vol. 31, pages 1913–1917, 1985. (Cited on page 162.)

[Teixeira 2006] J Teixeira, A Luzar and S Longeville. *Dynamics of hydrogen bonds: how to probe their role in the unusual properties of liquid water*. J. Phys.: Condens. Matter, vol. 18, pages S2353–S2362, 2006. (Cited on page 151.)

[Turner 1990] J Turner, A. K Soper and J. L Finney. *A neutron-diffraction study of tetramethylammonium chloride in aqueous solution*. Mol. Phys., vol. 70, pages 679–700, 1990. (Cited on pages 30, 31, 32 and 33.)

[Turner 1992] J Turner, A. K Soper and J. L Finney. *Water structure in aqueous solutions of tetramethylammonium chloride*. Mol. Phys., vol. 77, pages 411–429, 1992. (Cited on pages 30 and 32.)

[Turner 1994] J Turner and A. K Soper. *The effect of apolar solutes on water structure: alcohols and tetraalkylammonium ions.* J. Chem. Phys., vol. 101, pages 6116–6125, 1994. (Cited on pages 30, 32, 33 and 91.)

[Turner 1995] J. Z Turner, A. K Soper and J. L Finney. *Ionic versus apolar behavior of the tetramethylammonium ion in water.* J. Chem. Phys., vol. 102, pages 5438–5443, 1995. (Cited on pages 30, 32 and 159.)

[Wen 1964] S Wen W. Y; Satio. *Apparent and partial molal volumes of five symmetrical tetraalkylammonium bromides in aqueous solutions.* J. Phys. Chem., vol. 68, pages 2639–2644, 1964. (Cited on pages 21, 22, 27, 95 and 96.)

[Woolf 1982] L. A Woolf and H Weingartner. *Isothermal transport properties in solutions of symmetrical tetra-alkylammonium bromides.* Faraday Symp. Chem. Soc., vol. 17, pages 41–53, 1982. (Cited on pages 30 and 153.)

THE EUROPEAN
PHYSICAL JOURNAL
SPECIAL TOPICS

Regular Article

Study of tetrabutylammonium bromide in aqueous solution by neutron scattering

D. Bhowmik[1,2,a], N. Malikova[1], J. Teixeira[1], G. Mériguet[3], O. Bernard[3], P. Turq[3], and W. Häussler[4,5]

[1] Laboratoire Léon Brillouin, UMR CEA-CNRS 12, CEA Saclay, 91191 Gif-sur-Yvette, France
[2] Donostia International Physics Center, Paseo Manuel de Lardizabal 4, 20018 San Sebastián, Spain
[3] Université Pierre et Marie Curie - Paris 6, UMR-UPMC-CNRS-ESPCI 7195, Laboratoire PECSA, Case 51, 4 place Jussieu, 75005 Paris, France
[4] Technische Universität München, Forschungsneutronenquelle Heinz Maier-Leibnitz (FRM II), 85747 Garching, Germany
[5] Physics Department E21, Technische Universität München, 85747 Garching, Germany

Abstract. The study of electrolyte solutions by neutron scattering is an example of the large range of possibilities of the technique. Structure and dynamics at different time and length scales, discrimination of global from local motions, separation of coherent from incoherent contributions are necessary to embrace the complexity of a subject where charge and hydrophobicity play important and competitive roles. The behaviour of aqueous solutions of tetrabutylammonium bromide is studied here by several neutron scattering techniques: Small Angle Neutron Scattering, Neutron Diffraction, Time-of-Flight and Neutron Spin Echo. We concentrate on the conformation and dynamics of the hydrophobic cations. In particular, the center-of-mass (CoM) motion of the cation at the microscopic scale is best described via the low Q coherent signal, as measured by Neutron Spin Echo. Due to a possible cage formation effect in the TBABr solution, at the scale of the distance between cations, the cationic CoM relaxation time is larger than that predicted by a simple extrapolation of results issued from the hydrodynamic regime and those obtained from the incoherent signal analysis.

1 Introduction

Electrolyte solutions remain an active field of research, with a goal of developing their description valid over a wide concentration range and to encompass phenomena occurring at different time-scales. Aqueous solutions of hydrophobic ions present an

---

[a] e-mail: debsindhu_bhowmik@ehu.es

added complexity due to the combined effect of hydrophobic and electrostatic interactions. Their study is fully justified in view of their abundance in nature and their importance for the many biological, environmental and technological applications. Symmetric tetraalkylammonium (TAA) cations, $N^+(C_nH_{2n+1})_4$, have attracted attention for several decades as the archetypal hydrophobic ions. This is due to their simple structure: four linear hydrocarbon chains attached to a central quaternary nitrogen atom, bearing a positive charge. From the side of applications, TAA ions are used as phase transfer catalysts [1] and choline, their close derivative, is an integral part of phospholipid-based biological membranes [2] and of acetylcholine, a common neurotransmitter.

TAA cations have been mostly studied in solution in the presence of halide counterions and comparison has been made to alkali halide solutions, considered as their purely electrostatic analogues. The first feature that catches attention is the high solubility of TAA halides, comparable to alkali halides [3]. A wealth of information exists regarding the possible formation of either cation–anion or cation–cation pairs in these solutions, the overall picture is however not clear. Cation–anion pair formation is suggested by measurements of osmotic and activity coefficients, as well as dielectric spectroscopy and microscopic simulations [4–8]. Formation of cation–cation pairs driven by the hydrophobic effect is proposed on the basis of neutron diffraction measurements [9] and recent small angle X-ray scattering (SAXS) measurements [10], however previous small angle neutron scattering (SANS) data do not support the formation of such pairs [11].

In this study we present a combination of several neutron scattering techniques to give us information on the arrangement, conformation as well as microscopic dynamics of TAA cations in aqueous solution. Neutron scattering is uniquely suited for such a study, due to the possibility of deuterating the solvent and thus highlighting the signal from the hydrogenated cations. The originality of our approach is in the combination of SANS (and neutron diffraction, ND) with two quasi-elastic neutron scattering techniques (time-of-flight, TOF, and neutron spin echo, NSE), which allows us to decouple dynamic information concerning the cation, contained in the coherently and incoherently scattered signal. We apply this approach to a tetrabutylammonium bromide (TBABr, TBA is the n = 4 member of the TAA series) solution in D_2O at a molar ratio $TBABr:D_2O = 1:56$ (this corresponds to a 0.75M solution, a water content just sufficient to form a single independent hydration sphere around each TBA cation [12,13]).

2 Experimental

Crystals of (hydrogenated) tetrabutylammonium bromide (TBABr, Fluka, purity >99%) were dried under vacuum for several hours prior to being dissolved in liquid D_2O (Euriso-top, 99.9%D). Experimental details of the neutron scattering techniques used are summarized in Table 1.

Using and interpreting several neutron scattering techniques together is seldom reported. Merging the terminology of these techniques into a consistent set is not straight-forward and we present our choice here: Measurements of SANS and ND give access to the total scattered intensity as a function of the wave-vector Q, which we denote $I(Q)$. $I(Q)$ is a sum of a coherent (Q-dependent) and an incoherent intensity (Q-independent). We denote these intensities $I_{coh}(Q)$ and I_{inc} respectively. For structural studies only the coherent intensity provides useful information, from the position of peaks at specific Q values. For dynamic studies, the time (or energy) dispersion of both the coherent and incoherent part of $I(Q)$ is of value. The

Table 1. Experimental details of neutron scattering techniques used. λ stands for incident neutron wavelength, l_{SD} for sample to detector distance. Apart from NSE measurements, all other data was collected at room temperature.

Technique	Q range (Å^{-1})	Time/energy range	Details	Measured Quantity	Spectrometer
SANS	0.03–0.3	–	$\lambda = 4.5$ Å, $l_{SD} = 1.5$ m	$I(Q)$	PAXE (LLB)
ND	0.2–3.3	–	$\lambda = 2.425$ Å	$I(Q)$	G4.1(LLB)
TOF	0.5–2.0	HWHM(res) $= 50\mu eV$	$\lambda = 6.0$ Å, non-polarized incident beam, 0.2mm flat quartz cell	$S(Q,\omega)$	MIBEMOL (LLB)
NSE	0.2–1.9	1–1100 ps	$\lambda = 5.0$ Å, polarised incident beam, 1mm flat quartz cell, T $= 298$K 348K	$I_{coh}(Q)$, I_{inc}, $I(Q,t)$	MUSES (LLB), RESEDA (FRM-II)
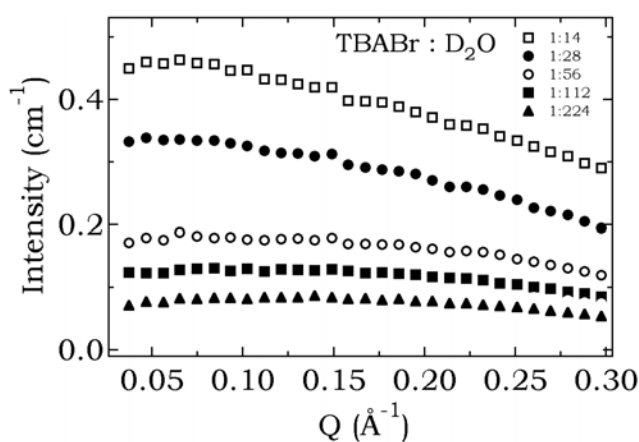
Fig. 1. Coherent intensity (in cm^{-1}) versus the wave-vector, Q, for a series of TBABr solutions in D_2O (molar ratio of solute and solvent = 1:224 to 1:14).

energy dispersion of $I(Q)$ is the full scattering function, $S(Q,\omega)$, where ω is the energy transfer. $S(Q,\omega)$ is directly measurable by TOF [14]. NSE gives direct access to the temporal Fourier transform of this quantity, the intermediate scattering function, $I(Q,t)$, where t is the correlation time [15–17].

3 Results

3.1 Structure

SANS measurements were carried out on a series of TBABr solutions in D_2O for molar ratios TBABr:D_2O from 1:224 to 1:14 (corresponding to concentrations from 0.22M to 1.82M). Figure 1 shows the resulting coherent intensity as a function of Q (obtained from the total measured intensity by subtracting the empty cell signal, incoherent scattering and the solvent, or compressibility, contribution). All the curves feature a flat or a slightly sloping signal, which indicates the absence of macroscopic aggregates in the solution across this concentration range (in case of aggregation, a steep increase of scattered intensity as Q tends to zero would be observed).

As already done for this and neighbouring systems [11,18,19], it is possible to interpret such low Q data within the contrast approximation, which describes the solution as a three component system (solvent, cation, anion), with cations and anions as spheres of a given radius (r) and scattering length density (ρ): $r_+ = 5$ Å, $\rho_+ = -4.17 \times 10^9$ cm^{-2}, $r_- = 1.96$ Å, $\rho_- = 2.15 \times 10^{10}$ cm^{-2} [11]. Note that the basis of the contrast approximation is the smearing of the atomic detail of both the ions and the solvent, i.e. at this large spatial scale (low Q region) the atomic detail is not resolved. This is of great importance for our discussion of dynamic data later on.

On the grounds of intensity, we can estimate that the coherent intensity in Figure 1 is dominated by the form factor of the cations. This is due to the relatively large size of the cations as compared to anions and to solvent molecules. Nevertheless, dividing all the curves by their respective concentrations does not collapse the data exactly onto a single curve, therefore some contribution of the structure factor (distinct cation-cation correlation) exists, though it is featureless in the given Q-range. The cation form factor depends on the average cation shape but can be approximated by an exponential term (Guinier approximation, $I(Q) \propto e^{-\frac{R_g^2 Q^2}{3}}$) dependent solely on the radius of gyration, R_g [20]. From the plot of $ln(I(Q))$ versus Q^2 we extract the radius of gyration of a single TBA cation as 3.8Å, all concentrations giving a very similar value. From an atomic model, a calculation based on bond lengths corresponding to fully stretched arms of TBA arrives at $R_g = 4.1$ Å. We can thus calculate a rough estimate of the hydrocarbon arm flexibility as only 7%, i.e. $(4.1 - 3.8)/4.1$. This represents the fluctuation of the distance between the CoM of the cation and the extremity of the chains.

We concentrate from now on the 0.75M TBABr solution, for which the subsequent dynamic data is presented. On the basis of concentration, the estimated average distance between neighbouring TBA cations is 13 Å (which leaves only a few Å between the outer methyl groups of two neighbouring TBA cations) and a corresponding cation-cation correlation peak would be at approximately $Q = 2\pi/13 = 0.5$ Å^{-1}. The insert of Fig. 2 shows the scattered intensity from this solution in an extended Q range. We note that no such peak is found, which points to the absence of position correlations between the cations. This is a suggestion that the electrostatic repulsion between the cations is largely neutralised, by a close approach of the anions. (Note that the well-known broad peak centred on 1.8 Å^{-1} arises due to the structure of the D$_2$O solvent itself and will not be discussed here.) This weak correlation between cations as well as the absence of aggregation have been confirmed by our molecular dynamics simulations, which will be detailed in a forthcoming paper [21,22].

3.2 Dynamics

Prior to dynamic measurements on the 0.75M TBABr solution in D$_2$O, we decouple quantitatively the total scattered intensity into the coherent and the incoherent signal as a function of Q, using polarization analysis on an NSE spectrometer (MUSES) [15,23]. This decoupling is shown in Fig. 2. The incoherent intensity is presented at its full value, as well as with a pre-factor of 1/3. In the TOF dynamic measurements (using non-polarized neutron beam), both contributions appear at their full intensity. In the NSE dynamic measurements (using polarized neutron beam), the incoherent contribution is detected with a pre-factor of 1/3 due to an inherent neutron spin flip (with a probability of 2/3) during a spin-incoherent scattering event [24]. Taking this into account, we distinguish the following regions of interest in Fig. 2: i) low Q region, $0.2 - 0.65$ Å^{-1}, where coherent signal dominates in case of NSE, ii) middle Q region, $0.65 - 1.4$ Å^{-1}, where incoherent signal dominates in case of TOF. The third region, beyond 1.4 Å^{-1}, will not be discussed here.
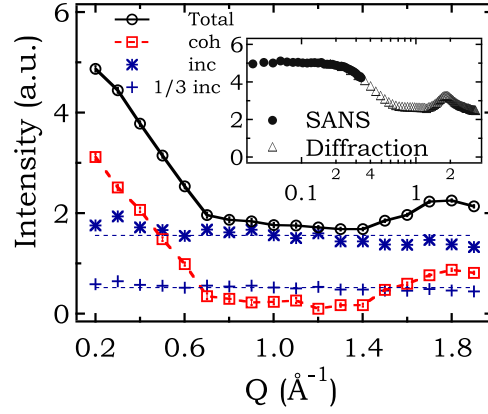
Fig. 2. Aqueous solution of TBABr in D_2O (0.75M): total scattered intensity and the decomposition into the coherent and incoherent contribution versus wave-vector Q as measured by NSE (MUSES spectrometer). The diminished incoherent intensity (1/3 inc) reflects the intensity of the incoherent signal contained in the time-dependent NSE measurements. The signal from the quartz sample holder has been subtracted. Insert: For comparison, the total scattered intensity measured by SANS and a neutron diffractometer (significantly higher Q-resolution than for NSE).

3.2.1 Incoherent dynamic signal

On the basis of Fig. 2, the TOF technique in the middle Q range $(0.6 - 1.4\,\text{Å}^{-1})$ measures an almost purely incoherent signal, i.e. it measures a full incoherent scattering function $S_{inc}(Q,\omega)$. Hydrogen atoms present in the sample have by far the highest incoherent scattering cross-section [25], and thus $S_{inc}(Q,\omega)$ is interpreted in terms of motion of individual H atoms of the TBA cation, the only hydrogenated species present. From previous treatment of TOF spectra on these solutions, work by Novikov et al [26], the spectra was modelled by a single Lorentzian contribution, interpreted as the overall diffusion of the cation. Our TOF data could not however be modelled satisfactorily using a single Lorentzian contribution (be it with a Q-dependent or Q-independent broadening). Thus we proceeded onto modelling the signal with a translational motion of the overall cation, convoluted by a three-fold rotation of the terminal methyl groups [14]. For the overall $S_{inc}(Q,\omega)$, this leads to a purely translational and a trans-rotational component with well defined intensities (a_{tr} and a_{tr-rot}) and Lorentzian broadenings (HWHM, Γ_{tr} and Γ_{tr-rot}) [22]:

$$S_{inc}(Q,\omega) = a_{tr}\frac{\Gamma_{tr}}{\pi(\Gamma_{tr}^2 + \omega^2)} + a_{tr-rot}\frac{\Gamma_{tr-rot}}{\pi(\Gamma_{tr-rot}^2 + \omega^2)} \qquad (1)$$

where $\Gamma_{tr-rot} = \Gamma_{tr} + \Gamma_{rot}$. The TOF data were fitted with this model between -0.5 and $0.5\,\text{meV}$ to obtain Γ_{tr} and Γ_{rot}. Γ_{tr} is related to the translational relaxation time, τ_{tr}, via $\frac{\Gamma_{tr}}{\hbar} = \frac{1}{\tau_{tr}}$ and further to the translational diffusion coefficient, D_{tr} (in m^2s^{-1}), via $\lim_{Q\to 0}(\frac{1}{\tau_{tr}}) = D_{tr}Q^2$. Γ_{rot} determines the characteristic methyl group rotational time, τ_{rot}, via $\frac{\Gamma_{rot}}{\hbar} = \frac{3}{2\tau_{rot}}$ [14]. Figure 3 features the TOF data at two Q values together with the fitting. The methyl group rotational time extracted from the Q-independent rotational broadening was determined as 4ps, in accordance with previously reported values [27]. The translational broadening extracted increases linearly with Q^2, see Fig. 4, and corresponds to a translational diffusion coefficient $D_{inc} = (0.24 \pm 0.03) \times 10^{-9}\,\text{m}^2\,\text{s}^{-1}$, as extracted from the slope of a linear fit of the translational broadening passing through the origin. This value is surprisingly close to
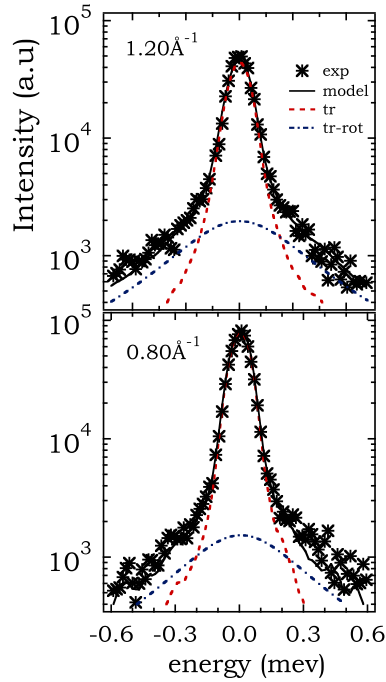
Fig. 3. Incoherent scattering functions, $S_{inc}(Q,\omega)$, versus energy transfer for $Q = 1.20\,\text{Å}^{-1}$ (top) and $Q = 0.80\,\text{Å}^{-1}$ (bottom) measured by TOF for TBABr solution in D_2O at $0.75\,\text{M}$. Different components of the model function are shown: translational (red), trans-rotational (blue) and total (full black).

the value obtained by Novikov, $(0.26\pm0.02)\times10^{-9}\,\text{m}^2\,\text{s}^{-1}$, who neglected the terminal methyl group rotation. At the same time, our molecular dynamics simulations, suggest that even our model of H atom motion within the TBA cation is far too simplified, as there are not only the fast methyl group rotations, but also much slower modes, such as the overall cation rotation and hindered motion of the individual hydrocarbon arms [21]. These slower motions are likely to have much more influence on the correct determination of the overall cation translation as the time-scales match more closely than with the methyl group rotation. We shall return to this point later on.

3.2.2 Coherent dynamic signal

Returning to Fig. 2, we concluded that the NSE technique measures a primarily coherent signal in the low Q region $(0.2 - 0.65\,\text{Å}^{-1})$. We have measured the $I(Q,t)$ curves at three different Q values below $0.6\,\text{Å}^{-1}$, the result can be seen in Fig. 5.

In the low Q region measured by NSE, the coherent intensity is due to the form factor of the cations, as discussed in Sect. 3.1. The associated relaxation therefore corresponds to the dynamics of the cation center-of-mass (CoM). This is a very important point. As explained earlier, at low Q, the system is seen in a coarse-grained manner and the atomic detail of the poly-atomic cation is irrelevant. The individual atom-atom correlations are important only at much larger Q values. Therefore the internal modes of the cation, which render the analysis of the incoherent signal very complex, do not contribute or pollute the dynamic signal in the low Q region. The low-Q NSE signal was therefore modelled as an exponential decay in the time-domain
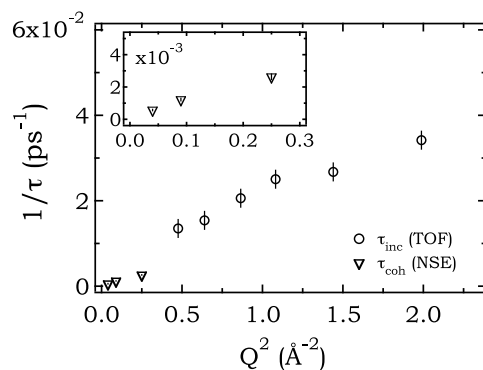
Fig. 4. Inverse of the translational relaxation time $\frac{1}{\tau}$, extracted from the incoherent signal ($\Gamma_{inc} = \frac{\hbar}{\tau_{inc}}$) in the middle Q region and also from the coherent analysis ($\Gamma_{coh} = \frac{\hbar}{\tau_{coh}}$), extracted from NSE in the low Q region (NSE$_{coh}$ error bars are the size of the symbols or smaller). Insert: A zoom of the low Q region.
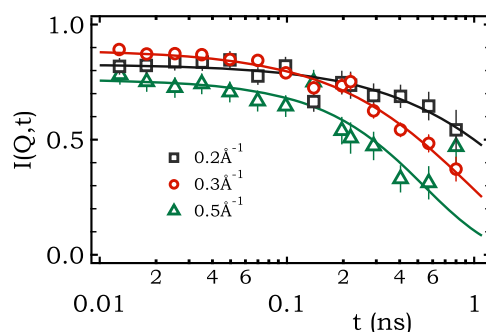
Fig. 5. Intermediate scattering functions measured by NSE, $I_{coh}(Q,t)$, for 3 different wavevectors in the low-Q region at 296 K (Reseda spectrometer).

(the equivalent of a Lorentzian broadening in the ω domain) according to:

$$I_{coh}(Q,t) = Ae^{-t/\tau_{coh}} + B \qquad (2)$$

where A is an overall free intensity pre-factor and B is a background term, as the curves do not decay exactly from 1 to 0 in the time-range probed. A less than 1 is often seen, it could be due to faster relaxation processes or more simply a technical artefact. Non-zero B is attributed to the elastic scattering from the quartz sample holder. At room temperature, the extracted relaxation time (τ_{coh}) is Q-dependent and is featured in Fig. 4 along with the TOF data. The temperature variation (Fig. 6, $T = 298–348$ K) of the $I(Q,t)$ curves at $Q = 0.3$ Å^{-1} leads to an activation energy of 25.3 ± 1.5 kJ mol^{-1}.

4 Discussion

Cation dynamics in the 0.75M TBABr solution was studied using two quasielastic techniques, TOF and NSE. Each of these was applied in a specific Q range, to probe the cation dynamics either through the incoherent or the coherent signal. We emphasize that this is made possible due to the two techniques measuring the dynamic signal with a different ratio of coherent and (spin) incoherent intensity.
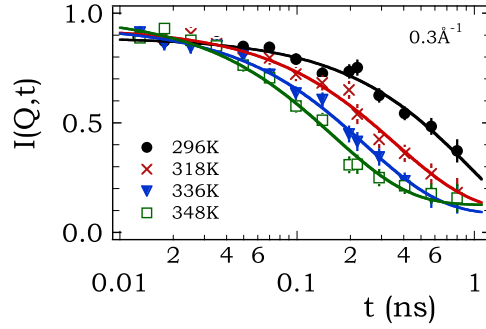
Fig. 6. The temperature dependence of the intermediate scattering function measured by NSE, $I_{coh}(Q,t)$, for $Q = 0.3\,\text{Å}^{-1}$ (Reseda spectrometer).

We conclude that the incoherent dynamic signal is very cumbersome to treat even for a relatively small polyatomic species such as TBA. This is due to the complexity of motions of hydrogen atoms in the cation. Apart from the methyl group rotation and overall CoM motion, the internal hydrogen atoms are necessarily involved in slower complex movements of the hydrocarbon arms and the cation carries out a global rotational motion. Evidence for these is indeed clear from our molecular dynamics simulations. Terms corresponding to all these motions are not trivial to include in a model of the TOF data. Even if it was possible, from the point of an experimentalist, the rapidly increasing number of parameters that the fitting function would contain makes such a fitting procedure highly unrealistic. As a result, we treat any CoM diffusion coefficient calculated from the extracted linewidths of the TOF data fitting only as a gross estimate at this corresponding length scale.

The CoM motion at this scale is for us much more faithfully represented by the dynamics originating from the coherent signal at low Q, measured by NSE, as it is not influenced by the variety of internal modes of the cation, as we explained earlier with the help of SANS data. Given the size of the cations and the Q range covered in NSE, the measurements are performed far from the hydrodynamic limit, meaning that the relaxation time τ_{coh} is not directly related to self-diffusion D by Fick's law, $\tau_{\text{Fick}}^{-1} = DQ^2$. As shown in the insert of Fig. 2, at $Q = 0.5\,\text{Å}^{-1}$ the inverse relaxation time does not follow the linear dependence suggested by the two lower Q values, a flattening is observed. By NSE at this Q we obtain a relaxation time of the order of 330 ps. We can compare this experimental result with extrapolation of Fick's law from the measurement of macroscopic diffusion coefficients obtained by tracer methods in H_2O [28] (after scaling of the ratio of viscosities between H_2O and D_2O [7]) or field gradient NMR [29,30]. These give $D = 0.19 \times 10^{-9}\,\text{m}^2\,\text{s}^{-1}$ and thus a relaxation time equal to 210 ps at $Q = 0.5\,\text{Å}^{-1}$, in other words an underevaluation of about 36%, in view of our microscopic NSE data point. Despite the small number of NSE data points, we can assume a jump model for the cation diffusion at the microscopic scale. From the equations,

$$\tau^{-1} = \frac{DQ^2}{1 + DQ^2\tau_0} \quad \text{and} \quad D = \frac{\langle \ell^2 \rangle}{6\tau_0} \tag{3}$$

we can evaluate a residence time τ_0 of the order of 120 ps and a mean square jump length, $\sqrt{\langle \ell^2 \rangle}$, of the order of 4 Å, i.e. comparable to the radius of the cation, what is the expected order of magnitude as far as the jump model can represent conveniently the translational diffusion of the cations. Note that a value of the linewidth measured by quasielastic neutron scattering smaller than the one predicted by the extrapolation of Fick's law and NMR data for self-diffusion [29] has already been observed in 1:6.13

(solute:solvent) solutions of TMACl (tetramethylammonium chloride) in D_2O [31]. The presence of a cage effect that justifies the jump model for the cation diffusion is reinforced by previous neutron diffraction experiments [32] or measurement of partial molar volumes [33] on aqueous TAA systems.

Lastly we note that the activation energy of the TBA CoM motion deduced from neutron scattering correlation functions measured at different temperatures (Fig. 6) is $25.3 \pm 1.5\,\mathrm{kJ\,mol^{-1}}$ which is significantly higher than the activation energy for bulk water diffusion at the same temperature ($18\,\mathrm{kJ\,mol^{-1}}$) and around three times higher than the average energy of the hydrogen bonds formed between two neighbouring water molecules [34]).

5 Conclusion

With a combination of SANS, ND, TOF and NSE, we have extracted several pieces of information regarding the structure and the dynamics of the hydrophobic cation TBA in aqueous TBABr solutions at the microscopic scale. Up to a concentration of 1.82M, no sign of cation aggregation is observed (the absence of aggregation was also reported previously for lower concentrations [11]). Detailed measurements were carried out for the 0.75M TBABr solution. At this concentration, though the terminal methyl groups of adjacent TBA cations are very close to each other, no appreciable correlation between cations is found. The electrostatic repulsion between the cations is largely nullified by the close presence of the negative counterions (here Br^-). The estimation of the radius of gyration of TBA cations indicates a flexibility of the constituent hydrocarbon chains of 7%. Further, we have measured the cation motion via both the incoherent and the coherent neutron scattering signal. The cation CoM motion is best reflected in the dynamic signal from the low Q coherent signal, as measured by NSE. Our results show that, due to a possible cage formation effect in the TBABr solution, at the scale of the distance between cations, the cationic CoM relaxation time is larger than that predicted by a simple extrapolation of results issued from the hydrodynamic regime and those obtained from the incoherent signal analysis.

References

1. M. Fedorynski, M. Jezierska-Zieba, B. Kakol, Acta Pol. Pharm. **65**, 647 (2008)
2. J. Klein, D. Touraud, W. Kunz, Green Chem. **10**, 433 (2008)

3. H. Nakayama, H. Kuwata, N. Yamamoto, Y. Akagi, H. Matsui, B. Chem. Soc. Jpn. **62**, 985 (1989)
4. S. Lindenbaum, G.E. Boyd, J. Phys. Chem. **68**, 911 (1964)
5. D.F. Evans, C. Zawoyski, R.L. Kay, J. Phys. Chem. **69**, 3878 (1965)
6. A.L Surdo, H.E Wirth, J. Phys. Chem. **83**, 879 (1979)
7. R. Buchner, C. Holzl, J. Stauber, J. Barthel, Phys. Chem. Chem. Phys. **4**, 2169 (2002)
8. J. Heyda, M. Lund, M. Oncak, P. Slavicek, P. Jungwirth, J. Phys. Chem. **114**, 10843 (2010)
9. N.G. Polydorou, J.D. Wicks, J.Z. Turner, J. Chem. Phys. **107**, 197 (1997)
10. N. Huang, D. Schlesinger, D. Nordlund, C. Huang, T. Tyliszczak, T.M. Weiss, Y. Acremann, L.G.M. Pettersson, A. Nilsson, J. Chem. Phys. **136**, 074507-1 (2012)
11. P. Calmettes, W. Kunz, P. Turq, Physica B **180**, 868 (1992)
12. J. Turner, A.K Soper, J. Chem. Phys. **101**, 6116 (1994)
13. J.L. Green, M.G. Sceats, A.R. Lacey, J. Chem. Phys. **87**, 3603 (1987)
14. M. Bée, *Quasielastic neutron scattering* (Adam Hilger, Bristol and Philadelphia 1988)
15. F. Mezei, *Fundamentals of Neutron Spin Echo Spectroscopy in Neutron Spin Echo Spectroscopy, Lecture Notes in Physics*, edited by F. Mezei, **128** (Springer Verlag, Berlin, 1980)
16. R. Gähler, R. Golub, Z. Phys. B - Cond. Mat. **65**, 269 (1987)
17. R. Golub, R. Gähler, Phys. Lett. A **123**, 43 (1987)
18. W. Kunz, P. Turq, P. Calmettes, J. Barthel, L. Klein, J. Phys. Chem. **96**, 2743 (1992)
19. W. Kunz, P. Calmettes, G. Jannink, T. Cartailler, P. Turq, J. Phys. Chem. **96**, 7034 (1992)
20. I. Grillo, *Soft Matter Characterization*, Ch. 13: Small-Angle Neutron Scattering and Applications in Soft Condensed Matter 128 (Springer Verlag, Berlin 2008), p. 723
21. D. Bhowmik, N. Malikova, J. Teixeira, G. Mériguet, O. Bernard, P. Turq (to be published)
22. D. Bhowmik, Ph.D. thesis, Université Pierre et Marie Curie - Paris 6 and Laboratoire Lon Brillouin, 2011 [`http://www-llb.cea.fr/theses/Bhowmik_2011.pdf`]
23. F. Nallet, G. Jannink, J.B. Hayter, R. Oberthür, C. Picot, J. Physique **44**, 87 (1983)
24. G.L. Squires, *Introduction to thermal neutron scattering* (Cambridge University Press, 1988)
25. A-J. Dianoux, G. Lander, Neutron data booklet, Institut Laue-Langevin **2** (2003)
26. A. Novikov, M. Rodnikova, J. Barthel, O. Sobolev, J. Mol. Liq. **79**, 203 (1999)
27. J.T. Cabral, A. Luzar, J. Teixeira, M.C. Bellissent-Funel, J. Chem. Phys. **113**, 8736 (2000)
28. L.A. Woolf, H. Weingartner, Faraday Symp. Chem. Soc. **17**, 1982 (1982)
29. H.G. Hertz , B. Lindman, V. Siepe, Ber. Bunsenges. Phys. Chem. **73**, 542 (1969)
30. B. Ancian (private communication)
31. A.N. Brown, M. Newbery, R.K. Thomas, J.W. White, J. Chem. Soc., Faraday Trans. 2 **84**, 17 (1988)
32. J.Z. Turner, A.K. Soper, J.L. Finney, J. Chem. Phys. **102**, 5438 (1995)
33. W.Y. Wen, S. Satio, J. Phys. Chem. **68**, 2639 (1964)
34. J. Teixeira, A. Luzar, S. Longeville, J. Phys.: Condens. Matter **18**, S2353 (2006)

Aqueous solutions of ionenes: interactions and counterion specific effects as seen by neutron scattering

Natalie Malikova,[*a] **Sašo Čebašek,**[b] **Vincent Glenisson,**[†a] **Debsindhu Bhowmik,**[‡a] **Geraldine Carrot**[§a] **and Vojko Vlachy**[b]

Aqueous solutions of ionenes with bromide and fluoride counterions have been investigated using small angle neutron scattering for the first time. Ionenes are a class of cationic polyelectrolytes based on quaternary ammonium atoms and, considering the very low solubility of their uncharged part (hydrocarbon chain), would be formally classified as hydrophobic. Ionenes present important structural differences over previously studied polyelectrolytes: (a) charge is located on the polyelectrolyte backbone, (b) the distance between charges is regular and tunable by synthesis, (c) hydrophobicity comes from methylene groups of the backbone and not from bulky side groups. Results for Br ionenes feature a disappearance of the well-known polyelectrolyte peak beyond a given monomer concentration. Below this concentration, the position of the peak depends on the chain charge density, f_{chem}, and scales as $f_{chem}^{0.30\pm0.04}$. This is an indication of a hydrophilic character of the ionene backbone. In addition, osmotic coefficients of ionene solutions resemble again other hydrophilic polyelectrolytes, featuring no unusual increase in the water activity (or a significant counterion condensation). We conclude that despite the hydrophobicity of the hydrocarbon chain separating charged centers on ionenes, these chains behave as hydrophilic. In contrast to Br ionenes, the polyelectrolyte peak remains at all concentrations studied for the single F ionene investigated. This strong counterion effect is rationalized in terms of the different hydrating properties and ion pairing in the case of bromide and fluoride ions.

1 Introduction

Despite the interest coming from science and industry, the properties of aqueous polyelectrolyte solutions are still not understood sufficiently well. The reason for this is a relatively complicated interplay of the intra- and intermolecular interactions taking place in such systems.[1–10] The average conformation of charged macromolecules (polyions) in water depends on the chemical structure of the monomer unit carrying charged group, pH of the solution, possible presence of the low-molecular electrolyte or other co-solvent, and polyelectrolyte concentration. The charge of some polyelectrolytes (PEs), for example poly-carboxylates, can be altered by pH variations. Poly(acrylic acid) or poly(methacrylic acid) can dramatically change their conformation in water; the polyion chain opens from a coiled to an extended configuration as the chain is neutralized by a suitable base (see, for example, ref. 9 and 11 and the references therein).

Another class of PEs, which can be prepared with a different degree of charge density by synthesis and may undergo conformational transition are partially sulfonated polystyrenesulfonates (psPSS), studied experimentally[12–17] and theoretically[8,18–21] by several groups of researchers. These PEs exhibit a transition between the extended and the collapsed state (the so-called pearl-necklace conformation) in agreement with predictions of the scaling theory. Theoretical results are additionally supported by molecular simulations. The psPSS system has been used to represent a class of hydrophobic PEs and its behaviour has been contrasted to hydrophilic PEs represented by sodium-2-acryl-amide-2-methyl propane sulfonate (AMAMPS).[13–16]

The subject of the present work is yet another group of PEs, the so called ionenes.[22–27] The generic name *ionene* is used for a group of cationic polymers having quarternized nitrogen atoms in their backbone. Values x and y represent the number of $-CH_2-$ (methylene) units between adjacent nitrogen atoms. The numbers x and y can be varied by synthesis, and this way we can vary the charge density of the macromolecule.

[a] *Laboratoire Léon Brillouin, UMR CEA-CNRS 12, CEA Saclay, 91191 Gif-sur-Yvette, France. E-mail: natalie.malikova@cea.fr; Tel: +33 169 08 79 25*
[b] *Faculty of Chemistry and Chemical Technology, University of Ljubljana, Slovenia*
† Present address: Institut Laue-Langevin, Avenue des Martyrs-BP 156, 38042 Grenoble Cedex 9, France.
‡ Present address: Donostia International Physics Center, Paseo Manuel de Lardizabal 4, 20018 San Sebastian, Spain.
§ Present address: Laboratory of Chemistry of Surfaces and Interfaces, CEA Saclay, Gif-sur-Yvette, France.

This makes ionenes ideally suited for studies of Coulomb and hydrophobic effects in water, in the presence of various counterions. In view of the previous classification of PEs into hydrophilic and hydrophobic, ionenes should fall *a priori* into the class of hydrophobic PEs, due to the very low solubility of hydrocarbon chains in water. As other PEs, ionenes have a potential to be used in many practical applications (see for example ref. 28 and 29).

Aqueous ionene solutions have been characterized experimentally by several groups of researchers. Minakata and co-workers[30,31] studied the electrical conductance and activity coefficients of 3,3-, 4,5-, 6,6-, and 6,9-ionene solutions in mixtures with alkali halides, while enthalpies of dilution and osmotic coefficients for pure ionene halides were determined by Pohar and coworkers.[32,33] More recently, Lukšič *et al.*[34,35] examined the dielectric relaxation of counterions in aqueous solutions of Br ionenes and F ionenes as well as the transport numbers of ions in these systems.[36] The measurements indicate strong deviations from theoretical predictions based on the continuum solvent models of PE solution. The deviations depend on the ionene charge density (x, y values) and on the nature of the counterion. The ion specific effects are most strongly revealed by thermal properties, such as heats of dilution[32,37] and heats of mixing.[38] Models of the 3,3- and 6,6-ionene oligoions with alkali halide counterions were studied by computer simulations: the explicit water molecular dynamics simulation results[39,40] were consistent with experimental data and helpful in explaining significant deviations between implicit solvent theories[41–44] and experiments.

While the transport and thermodynamic properties of ionene solutions seem to be rather well investigated, there is surprisingly little information about the structure of these macromolecules in solution. First characterization of ionenes in water was performed by Casson and Rembaum.[22] Much later Zhuomei and coworkers[45] examined viscosity of the 2,10-, 6,10-, and 6,6-Br ionene in water. The authors concluded that in the absence of added electrolytes the polymer molecules behaved as "stiff rods", while in the presence of 0.4 M KBr they assumed more coiled conformations; the 2,10-ionene coiled up more than the other ionenes. The results mentioned in ref. 45 are consistent with the osmotic pressure data for the 3,3-, 4,5-, 6,6-, and 6,9-ionenes with Br and Cl counterions[32] in salt-free aqueous solutions. A remarkably constant osmotic coefficient of these ionene aqueous solution over several orders of magnitude of monomer concentration is suggestive of a locally extended conformation of the polyion. However, so-far we have no direct measurements on the local structure and conformation of ionenes in aqueous solution, under conditions of different charge densities and concentrations.

In order to fill the gap and provide the missing information we performed a small angle neutron scattering (SANS) study of aqueous ionene solutions. Our work was motivated by differences in chemical structure between ionenes and some other PEs studied recently. These differences are: (i) charge (quaternary ammonium group) is a part of the backbone, (ii) the distance between the charges is regular and tunable by synthesis, (iii) the hydrophobicity comes from the methylene groups and not from benzene side groups, present for example in psPSS, which are prone to π–π interaction, *e.g.* ref. 46.

The 3,3-, 4,5-, 6,9-, and 6,12-Br ionenes were studied here by SANS at several PE concentrations. In this first study only salt-free (no additional salt present) aqueous solutions were examined. To obtain some preliminary information on how the nature of counterions (the ion-specific effect) is reflected in the structure of the polyion we also studied the 6,9-ionene solutions with fluoride counterions.

2 Ionenes: nomenclature and structural parameters

The most important parameter for PE chains is their charge density. We may express it simply *via* the distance between charges on the PE backbone, a. Alternatively, within the notation used previously for other PEs,[13,47] we may describe the PE chain as a sequence of charged and uncharged monomers of size b, in which case the charge density is reflected in the fraction of charged monomers. This quantity is usually referred to as the chemical charge and is denoted f_{chem}. The distance between charges on the PE backbone is then b/f_{chem}.

The latter notation, which we shall adopt throughout the rest of this article, requires the definition of a neutral and a charged monomer for the case of ionenes. These two entities are schematically shown in Fig. 1. Rather conveniently, the size of these monomers projected onto the ionene backbone is identical to that of PSS, *i.e.* 2.5 Å. The corresponding molar volume for the neutral monomer is 32.2 cm³ mol⁻¹, for the charged monomer (cation part only) it is 65.9 cm³ mol⁻¹.[48] For completeness, the molar volumes of Br⁻ and F⁻ anions are 18.99 cm³ mol⁻¹ and 5.93 cm³ mol⁻¹ respectively.

The series of Br ionenes used allowed us to access both ionenes with charge densities above and below the Manning condensation limit, defined *via* the charge density parameter ξ, as reported in ref. 41 and 42

$$\xi = \frac{L_B}{a} = 1 \tag{1}$$

where L_B is the Bjerrum length (7.14 Å in water at room temperature) and a is the distance between charges. Alternatively ξ can be expressed as

$$\xi = \frac{L_B f_{chem}}{b} \tag{2}$$
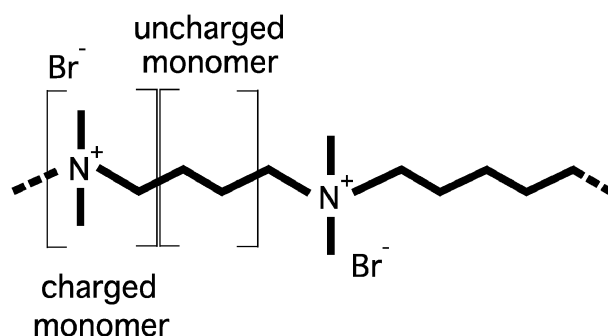

Fig. 1 Schematic view of the repeat unit of a 4,5-Br ionene chain, showing the definition of a charged and an uncharged ionene monomer. The charged monomer contains the quaternary ammonium atom, its adjacent two methyl groups (CH₃) and another methylene group (CH₂) along the ionene backbone. The uncharged monomer contains two methylene groups along the ionene backbone.

Table 1 Structural parameters for ionenes, a is the charge separation on the backbone, f_{chem} is the fraction of charged monomers and ξ is the Manning charge density parameter

Ionene	a [Å]	f_{chem}	ξ
3,3-	5.00	0.50	1.43
4,5-	6.88	0.36	1.04
6,6-	8.75	0.29	0.82
6,9-	10.63	0.24	0.67
6,12-	12.50	0.20	0.57

where f_{chem} is the fraction of charged monomers (chemical charge) and b is the size of the monomer projected onto the backbone (2.5 Å). Table 1 summarizes a, f_{chem} and ξ parameters for the series of ionenes presented here.

As we see from Table 1, according to the Manning theory, condensation of counterions should occur only for the 3,3-ionene, the only system with $\xi > 1$. For the 4,5-ionene ξ is actually at the condensation limit and for all other ionenes $\xi < 1$.

Unless stated otherwise, all concentrations of Br ionenes or F ionenes reported in this article are given in terms of the number of moles of all monomers (neutral and charged) per dm^3 (M), denoted c_p. These concentrations can be converted to moles of monovalent counterions per dm^3, c_m, according to $c_m = c_p f_{chem}$.

3 Experimental

3.1 Materials

Br ionenes were synthesized from the corresponding equimolar amounts of N,N,N',N'-tetramethyl-1,x-alkane and 1,y-dibromoalkane (Aldrich) by a polyaddition reaction in dimethylformamide (methanol in the case of 6,12-ionene) at room temperature and under an argon atmosphere for a duration of 7 days.[23,27] The crude product was washed with a large amount of acetone and dried under vacuum for 48 hours at 40 °C. The polydispersity index of ionenes thus synthesized is 1.8–2.0, as determined by size exclusion chromatography. Br ionenes were further dialyzed against water (2 weeks) to ensure the purity of the sample. Dialysis tubes from Sigma (MWCO = 12 000 g mol^{-1}) were used. This procedure results in molecular masses of the obtained ionenes between 12 000 g mol^{-1} and 100 000 g mol^{-1}.[34] Such ionene chains contain approximately 100 charged monomers per chain and their length is thus of the order of 100 to 1000 Å.

Ionenes with fluoride counterions were prepared from bromide salts by ion exchange during dialysis. Dialysis tubes were filled with 0.02 M (c_m) solutions of the Br ionene and first dialyzed against 0.05 M solution of NaF (3 weeks) to exchange anions and then dialyzed against water (2 weeks) to remove sodium ions. Ion conversion was checked potentiometrically using the bromide selective electrode and the saturated mercury sulfate electrode as the reference and the standardized solutions of AgNO$_3$ as the titrant reagent. The concentration of bromide ions was under the detection limit. Successfulness of the sodium removal was verified with a flame test.

All ionene solutions for neutron scattering measurements were prepared gravimetrically with deuterated water (Euriso-top, 99.9%D). The exact counterion concentrations were determined potentiometrically using bromide or fluoride selective electrodes and a saturated mercury sulfate electrode as the reference. Samples were titrated with standardized solutions of AgNO$_3$ or LaCl$_3$.

3.2 Small angle neutron scattering

Small angle neutron scattering (SANS) measurements were carried out on the PAXE spectrometer at LLB-Orphée, Saclay, France. Using a combination of two configurations (configuration 1: incident neutron wavelength, $\lambda = 6$ Å, and sample to detector distance, $l_{SD} = 5$ m, configuration 2: $\lambda = 6$ Å and $l_{SD} = 1.2$ m), a wave-vector (Q) range of 0.01 to 0.35 Å^{-1} was covered ($Q = 4\pi \sin(\theta/2)/\lambda$). All samples were measured inside quartz cells of path length of 1 or 2 mm. PAXE is equipped with an XY BF$_3$ multidetector (area of 64×64 cm^2 with 4000 cells, each 1 cm^2). Due to the isotropic nature of our samples, data were grouped in concentric rings, each corresponding to a given Q value. The detector efficiency was taken into account by normalisation of data with the flat (incoherent) signal from bulk light water.

The coherently scattered signal from our samples arises from the contrast (= difference in neutron scattering length densities) between the hydrogenated ionene chains and the deuterated solvent. The scattering length density (SLD) for the ionenes used varies between -1.42×10^9 cm^{-2} and -2.28×10^9 cm^{-2}, for 3,3- and 6,12-ionene respectively. The scattering length density for bulk D$_2$O is $+6.34 \times 10^{10}$ cm^{-2}. Note that the ionene backbone contains no exchangeable hydrogen atoms to smear out this contrast. For completeness, the scattering length densities of Br$^-$ and F$^-$ ions are $+2.15 \times 10^{10}$ cm^{-2} and $+5.74 \times 10^{10}$ cm^{-2} respectively. Considering both the anion volume and SLD, the signal from F$^-$ ions can be easily neglected in comparison to that of the hydrogenated ionene chain. The situation is not as clear-cut in the case of Br$^-$ ions, for now we neglect their contribution in the overall signal.

The measured scattered intensities for ionenes were corrected for transmission, sample thickness, incoherent and solvent background. They were converted to absolute units of cm^{-1}, using direct beam measurements.[49] They are presented here either in these absolute units or after a further division by the monomer concentration, c_p.

4 Results and discussion

Fig. 2 features the coherently scattered neutron intensity normalised by the monomer concentration (c_p) for a series of 6,9- and 6,12-Br ionenes. The familiar polyelectrolyte peak (PE peak) is seen without ambiguity for $c_p < 1$ M. However, beyond this concentration the peak dissapears. The same applies for all the other Br ionenes studied here. (From the molar volumes of the ionene monomers defined previously, $c_p = 1$ M corresponds to a volume fraction of ionenes in the solution between 4 and 6%.) Note that the commonly observed increase in scattered intensity as Q tends to zero, usually interpreted as the presence of large scale aggregates, e.g. ref. 17, is not noticeable in the case of Br ionenes.

Fig. 3 traces the dependence of the position of the PE peak (q^*) as a function of ionene monomer concentration (c_p) for all

12900 | *Phys. Chem. Chem. Phys.*, 2012, **14**, 12898–12904

This journal is © the Owner Societies 2012

Fig. 2 Coherent neutron scattering intensity normalised by monomer concentration (I_{coh}/c_p) *versus* scattering wave-vector (Q) for aqueous solutions of 6,9- and 6,12-Br ionenes (in D_2O). Monomer concentrations as indicated in the legends.

ionenes studied. Curves of $c_p^{1/3}$ and $c_p^{1/2}$ are also included for guidance. These dependencies reflect the theoretical behaviour for q^* of hydrophilic PEs in the dilute and semi-dilute concentration range respectively.[47] For hydrophobic PEs, theory predicts the same two dependencies for the so-called string-controlled and a bead-controlled regime of the pearl-necklace conformation.[50]

We can estimate the cross-over concentration between the dilute and semi-dilute regimes, for the two limits of ionene
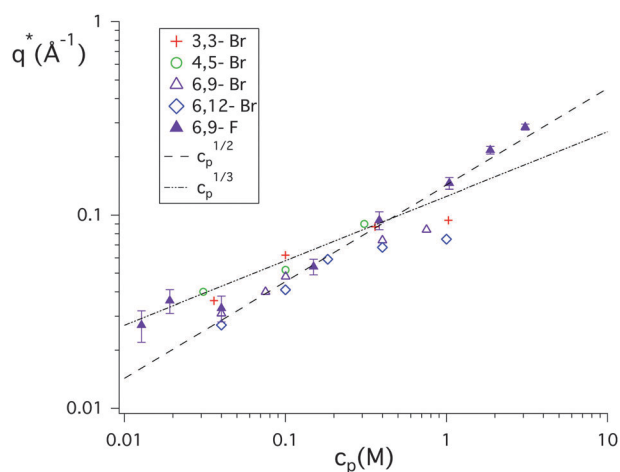
Fig. 3 Position of the PE peak (q^*) for all ionene aqueous solutions studied *versus* monomer concentration (c_p). Lines indicate a $c_p^{1/3}$ and $c_p^{1/2}$ dependence of q^*, as predicted by theory for dilute and semi-dilute regimes respectively. Error bars represented on the 6,9-F ionene data.

chain lengths mentioned previously, 100 Å and 1000 Å, according to

$$c_p^* = \frac{10^{27}}{N_A L^2 a} = \frac{10^4}{6.022 L^2 a} \qquad (3)$$

where c_p^* is the cross-over concentration (in molar units), N_A is the Avogadro constant, L is the chain length (in Å) and a is the size of the ionene monomer along the backbone ($a = 2.5$ Å). Eqn (3) yields c_p^* of 7×10^{-2} M and 7×10^{-4} M for the lower and upper limit of the ionene chain size. Therefore beyond approximately $c_p = 7 \times 10^{-2}$ M, even the shortest ionene chains should find themselves in the semi-dilute regime. From Fig. 3 we observe that for c_p between 4×10^{-2} M and 2×10^{-1} M, q^* for 6,12-Br and 6,9-Br ionenes seems to follow a $c_p^{1/2}$, however the number of points is rather limited. For 3,3- and 4,5-Br ionenes the data are inconclusive in this regime. Beyond $c_p = 2 \times 10^{-1}$ M, we observe a weaker power dependence, however the cause is most probably the gradual disappearance of the PE peak itself and thus a rather imprecise determination of its position. We shall return to the data for 6,9-F ionene in Fig. 3 later on.

The available data allow us to trace the evolution of q^* for Br ionenes at a given c_p but for differing chain charge densities or f_{chem}. As shown in Fig. 4, a weak dependence of q^* on the chain charge density is observed, and that at all three monomer concentrations considered (0.04 M, 0.1 M and 0.4 M). Fitting the available data with a power law, we arrive at an exponent of 0.30 ± 0.04. For f_{chem} below the onset of counterion condensation, theory predicts a scaling of q^* as $f_{chem}^{2/7}$ for hydrophilic PEs in water (*i.e.* the case of a good solvent) and as $f_{chem}^{1/3}$ in the case
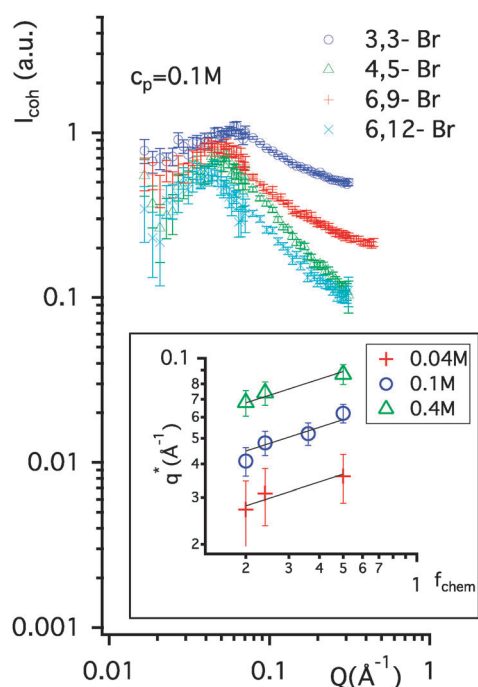
Fig. 4 Coherent neutron scattering intensity (I_{coh}) *versus* Q for a sequence of four ionenes of decreasing charge density at a monomer concentration of 0.1 M. Inset: position of the observed PE peak (q^*) *versus* charge density (f_{chem}) for three chosen monomer concentrations as indicated. Full lines are fits of the data points with a power law, $A f_{chem}^{\gamma}$, yielding $\gamma = 0.30 \pm 0.04$.

of a theta solvent.[51] Experimentally, these laws have indeed been observed, for AMAMPS[52] and for a sodium salt of poly(vinyl alcohol) partially esterificated with sulfuric acid.[53] On the other hand, hydrophobic PEs in water (the case of a bad solvent) are to show a scaling of $f_{chem}^{2/3}$.[50] In view of this information, the current data show that water acts as either a good or theta solvent for ionenes (the precision of our data does not allow us to distinguish between the 1/3 and 2/7 exponent). Strictly speaking, the data points for $f_{chem} = 0.5$ (3,3-ionene) are already beyond the formal onset of counterion condensation (refer back to Section 2), so these data points should show a departure from the theoretical scaling law, however this is not observed here.

Alongside the data from SANS measurements, it is instructive to recall measurements of osmotic coefficients, which lead, albeit indirectly, to the determination of effective charge on the PE chain and thus the degree of counterion condensation. In the case of the hydrophobic psPSS, the surprisingly low osmotic coefficients, reported by Essafi *et al.*, have been explained as an "anomalous" condensation of counterions onto the psPSS chain, brought on by the formation of "pearls" on the chain.[15] Essafi *et al.* have converted the measured osmotic coefficients into an effective chain charge according to ref. 14, 15, and 41

$$f_{eff} = 2\varphi f_{chem} \qquad (4)$$

where φ is the osmotic coefficient. Thermodynamically, a low osmotic coefficient (leading to a low effective chain charge according to the above equation) reflects a high solvent activity (or vapour pressure), see for example ref. 54. In the
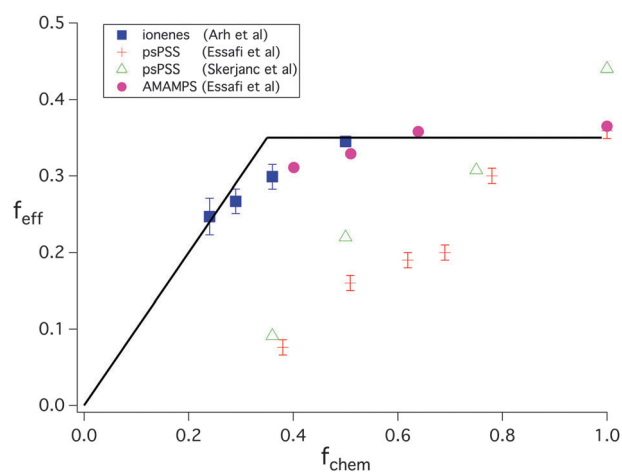
Fig. 5 Effective charge *versus* chemical charge for psPSS, AMAMPS and ionenes (3,3-, 4,5-, 6,6- and 6,9-).[15,33,55] Effective charge is determined from measurements of osmotic coefficients (see text). The available error bars are shown. Theoretical predictions of the Manning theory are shown as straight lines, distinguishing clearly the regime below and above the Manning condensation limit at $f_{chem} = 0.35$.

case of formation of "pearls", or simply regions of significant hydrophobicity, the increase in water vapour pressure above the solution is indeed to be expected.

Fig. 5 features a compilation of the effective chain charge (f_{eff}), determined from osmotic coefficients according to eqn (4), for a series of ionenes, psPSS, and AMAMPS, as available from literature.[14,15,33,55] Also, the predictions of the Manning theory are indicated by lines in Fig. 5 and distinguish clearly the region $\xi < 1$, where the effective charge is equal to the chemical charge and region $\xi > 1$ where the effective charge reaches saturation due to counterion condensation. Formally, the condition of $\xi = 1$ occurs at the same chemical charge for all three systems presented ($f_{chem} = 0.35$), as the size of the monomers, as projected onto the PE backbone, is the same (2.5 Å). This simplifies the comparison. We note firstly that two independent sources (ref. 15 and 55) indeed confirm the "anomalously" low osmotic coefficients for psPSS. Secondly, we observe that ionenes feature f_{eff} much closer to the predictions of the Manning theory and also the experimental data for hydrophilic PE AMAMPS. In other words, the osmotic coefficients of ionenes point towards the absence of hydrophobic regions in their aqueous solution, in contrast to psPSS aqueous solutions. Note that the available osmotic coefficients for ionenes are those for Br ionenes and Cl ionenes, which show the same trends, though slight numerical differences;[33] we used the average of the two osmotic coefficients for each ionene to calculate f_{eff}.

Putting together the information available from osmotic coefficients and the behaviour of the position of the PE peak, ionenes seem to present a hydrophilic character, contrary to what is expected considering the hydrophobicity of the hydrocarbon chain separating charged centers on ionenes.

Within the purely electrostatic picture, we consider the chain charge density as the most important parameter governing the behaviour of ionenes and other PEs in solutions. Beyond this parameter, we wish to highlight the counterion specific effects
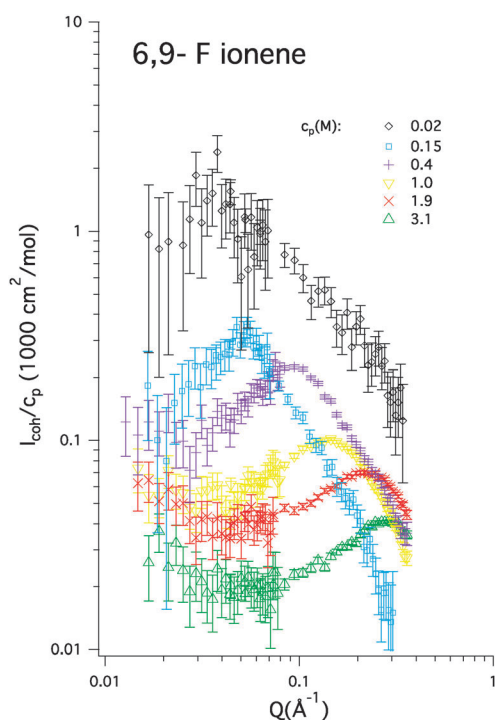
12902 | *Phys. Chem. Chem. Phys.*, 2012, **14**, 12898–12904
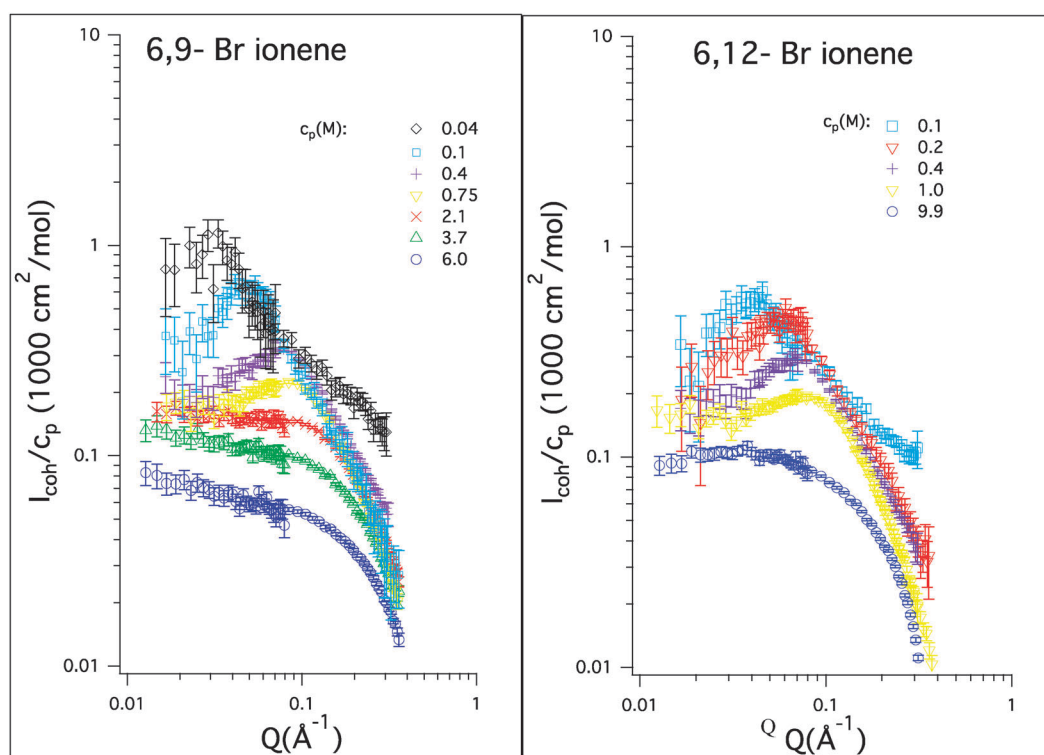
This journal is © the Owner Societies 2012

Fig. 6 Coherent neutron scattering intensity normalised by monomer concentration (I_{coh}/c_p) *versus* scattering wave-vector (Q) for aqueous solutions of 6,9-F ionene (in D_2O). Monomer concentrations as indicated in the legend.

that may and indeed do appear for ionenes, as we change the nature of the counterion along the halide series. Fig. 6 features the coherently scattered intensity normalised by the monomer concentration for a series of 6,9-F ionene, to be compared with Fig. 2 (left), where the same charge density Br ionene is presented. The difference is striking, unlike for the Br ionenes, the PE peak for 6,9-F ionene remains clearly present for concentrations beyond 1 M, as is seen for other PEs.[47] As seen from Fig. 3, the position of q^* for 6,9-F ionene follows convincingly a $c_p^{1/2}$ dependence in a range much beyond that for 6,9-Br ionene (0.04 M to 3 M). This is again an indication of the hydrophilic character of the ionene backbone. Note that the semi-dilute regime for psPSS is characterised by a somewhat weaker power law (exponent <0.4), seen as a transition between the string-controlled and a bead-controlled regime of the pearl-necklace conformation.[13]

The disappearance of the peak for Br ionenes beyond $c_p = 1$ M signifies a loss of correlations between the ionene chains, while this correlation persists for F ionenes. Such loss of correlations arises due to sufficient screening of ionene chains by the more weakly hydrating Br^- counterions such that the radial extent of the counterion atmospheres of two neighbouring ionene chains is smaller than the interchain distance. These differences between Br^- and F^- ionenes agree with our interpretations of measured osmotic coefficients,[33] enthalpies of dilution and mixing,[37,38] and also with counterion distributions seen directly by molecular dynamics (MD) simulations.[39,40]

The differences seen in PE solutions due to counterion specific effects are usually considered second order to the purely electrostatic effects, but as we observe here, in some

measurements, these effects give rise to spectacular differences. One other example is the enthalpy of dilution of ionenes (or mixing with various salts), which, on the change of the counterion from F^- to Br^-, is accompanied by a change in sign.[32,37,38] This is completely at odds with the purely electrostatic picture of the systems. Note that we are dealing with cationic PE chains and halide counterions, in comparison to the majority of PEs which are anionic and counterion effects are usually studied on the series of alkali and/or alkaline Earth cations.[17] Ion specific effects are likely to be more pronounced in the case of anionic counterions, which have stronger effects on water.

Within this context, note that the changing of the nature of the positive counterion in fully charged PSS, between Na^+ and a more weakly hydrating cation, tetramethylammonium (TMA^+), causes no disappearance of the PE peak.[47] It would be interesting to see if this persists for PSS with lower charge densities, but we are not aware of any such data existing at present.

5 Conclusion

Aqueous solutions of ionenes have been investigated here for the first time using neutron scattering. Small angle neutron scattering has allowed us to investigate the interactions between individual ionene chains, as a function of ionene concentration for a series of Br ionenes with differing chain charge density, as well as make comparison, for the case of 6,9-ionene, between the effects of Br^- and F^- counterions. Throughout, we have made comparison with the existing data for psPSS and AMAMPS, representing the reference systems for hydrophobic and hydrophilic PEs respectively.

Among the 6,9-Br ionene and 6,9-F ionene, it is the latter, with its strongly hydrating F^- counterion, that resembles the behaviour of a typical PE as seen by small angle neutron scattering: a clear PE peak is present over almost three decades of ionene concentration, showing a scaling law of $c_p^{1/2}$, typical of a hydrophilic PE. In contrast to 6,9-F ionene, all Br ionenes studied feature a PE peak that disappears beyond a certain monomer concentration (1 M). We interpret this as the constriction of the counterion atmosphere around the ionene backbone to an extent that adjacent ionene chains are completely screened. The effect is consistent with the ideas of the matching water affinities.[56,57] According to this concept, oppositely charged ions (ionic groups) with widely different sizes pair weakly, while those of similar size pair strongly. In our case this means a more compact double layer around the ionene backbone when Br^- ions are present, in comparison to F^- counterions. Up to now only very few studies have been concerned with PE solutions in the concentrated regime, we note the work of Nishida *et al.*,[58] in which PSS is considered. The disappearance of the PE peak is seen at higher concentration than in the case of ionenes (around 5 M) and is followed by the appearance of another peak as the system is concentrated even further. Other electrostatic effects come into play at these high concentration regimes.

Below the 1 M monomer concentration, the position of the PE peak in Br ionenes scales as $f_{chem}^{0.30\pm0.04}$, which is again an indication of a hydrophilic character of the ionene backbone. In addition, osmotic coefficients of ionene solutions resemble

also the hydrophilic reference, featuring no unusual increase in the water activity (or a significant counterion condensation).

Overall, ionenes should be formally examples of hydrophobic PEs due to the very low solubility of the hydrocarbon chain separating the charged centers. However, on the basis of our findings, we arrive at the opposite conclusion: ionenes show hydrophilic character. As an extension, direct evidence for the expected absence of the "pearl-necklace" configuration in the case of ionenes in aqueous solution may be provided in the form of measuring the single ionene chain conformation using the zero-average contrast method in neutron scattering.[13]

These initial neutron scattering results on ionenes are very promising and, with the versatility and flexibility of ionene structures, they open a wide field of possible investigations within the field of PE solutions.

Acknowledgements

References

1 H. Dautzenberg, W. Jaeger, J. Kötz, B. Philipp, C. Seidel and D. Stscherbina, *Polyelectrolytes. Formation, Characterization and Application*, Hanser, Munich, 1994.
2 K. S. Schmitz, *Macroions in Solution and Colloidal Suspension*, VCH, New York, 1993.
3 S. Forster and M. Schmidt, *Adv. Polym. Sci.*, 1995, **120**, 51–133.
4 J. Blaul, M. Wittemann, M. Ballauff and M. Rehahn, *J. Phys. Chem. B*, 2000, **104**, 7077–7081.
5 C. E. Williams, *NATO Science Series*, Kluwer Academic Publishers, Dordrecht, 2001, vol. 46, p. 487.
6 V. Vlachy, B. H. Lee, J. Reščič and Y. Kalyuzhnyi, *NATO Science Series II: Mathematics, Physics and Chemistry*, Springer, 2005, vol. 206.
7 C. Holm, M. Rehahn, W. Opperman and M. Ballauff, *Adv. Polym. Sci.*, 2004, **166**, 1–27.
8 A. V. Dobrynin, *Curr. Opin. Colloid Interface Sci.*, 2008, **13**, 376–388.
9 M. Borkovec, G. J. Koper and C. Piguet, *Curr. Opin. Colloid Interface Sci.*, 2006, **11**, 280–289.
10 A. Yethiraj, *J. Phys. Chem. B*, 2009, **113**, 1539–1551.
11 B. Jerman, M. Breznik, K. Kogej and S. Paoletti, *J. Phys. Chem. B*, 2007, **111**, 8435–8443.
12 V. O. Aseyev, S. I. Klenin, H. Tenhu, I. Grillo and E. Geissler, *Macromolecules*, 2001, **34**, 3706–3709.
13 M. N. Spiteri, C. E. Williams and F. Boué, *Macromolecules*, 2007, **40**, 6679–6691.
14 W. Essafi, *PhD Thesis*, Université Orsay, Paris-Sud, France, 1996.
15 W. Essafi, F. Lafuma, D. Baigl and C. E. Williams, *Europhys. Lett.*, 2005, **71**, 938–944.
16 W. Essafi, M.-N. Spiteri, C. Williams and F. Boué, *Macromolecules*, 2009, **42**, 9568–9580.
17 E. Dubois and F. Boué, *Macromolecules*, 2001, **34**, 3684–3697.
18 R. Chang and A. Yethiraj, *Macromolecules*, 2006, **39**, 821–828.
19 A. Chepelianskii, F. Mohammad-Rafiee, E. Trizac and E. R. el, *J. Phys. Chem. B*, 2009, **113**, 3743–3749.
20 J.-M. Y. Carrillo and A. Dobrynin, *J. Phys. Chem. B*, 2010, **114**, 9391–9399.
21 J.-M. Y. Carrillo and A. Dobrynin, *Macromolecules*, 2011, **44**, 5798–5816.
22 D. Casson and A. Rembaum, *Macromolecules*, 1972, **5**, 75–81.
23 A. Rembaum and H. Naguchi, *Macromolecules*, 1972, **5**, 261–269.
24 A. N. Zelikin, N. I. Akritskaya and V. A. Izumrudov, *Macromol. Chem. Phys.*, 2001, **202**, 3018–3026.
25 A. N. Zelikin, O. V. Davydova, N. I. Akritskaya, S. I. Kargov and V. A. Izumrudov, *J. Phys. Chem. B*, 2004, **108**, 490–495.
26 J. M. Layman, E. M. Borgerding, S. R. Williams, W. H. Heath and T. E. Long, *Macromolecules*, 2008, **41**, 4635–4641.
27 S. R. Williams and T. E. Long, *Prog. Polym. Sci.*, 2009, **34**, 762–782.
28 E. S. Trukhanova, V. A. Izumrudov, A. A. Litmanovich and A. N. Zelikin, *Biomacromolecules*, 2005, **6**, 3198–3201.
29 S. A. Sukhishvili, E. Kharlampieva and V. Izumrudov, *Macromolecules*, 2006, **39**, 8873–8881.
30 J. Nagaya, A. Minakata and A. Tanioka, *Langmuir*, 1999, **15**, 4129–4134.
31 J. Nagaya, A. Minakata and A. Tanioka, *Colloids Surf., A*, 1999, **148**, 163–169.
32 K. Arh and C. Pohar, *Acta Chim. Slov.*, 2001, **48**, 385–394.
33 K. Arh, C. Pohar and V. Vlachy, *J. Phys. Chem. B*, 2002, **106**, 9967–9973.
34 M. Lukšič, R. Buchner, B. Hribar-Lee and V. Vlachy, *Macromolecules*, 2009, **42**, 4337–4342.
35 M. Lukšič, R. Buchner, B. Hribar-Lee and V. Vlachy, *Phys. Chem. Chem. Phys.*, 2009, **11**, 10053–10058.
36 M. Lukšič, B. Hribar-Lee and V. Vlachy, *J. Phys. Chem. B*, 2010, **114**, 10401–10408.
37 S. Čebašek, M. Lukšič, C. Pohar and V. Vlachy, *J. Chem. Eng. Data*, 2011, **56**, 1282–1292.
38 M. Seručnik, M. Bončina, M. Lukšič and V. Vlachy, *Phys. Chem. Chem. Phys.*, 2012, **14**, 6805–6811.
39 M. Druchok, B. H. Lee, H. Krienke and V. Vlachy, *Chem. Phys. Lett.*, 2008, **450**, 281–285.
40 M. Druchok, V. Vlachy and K. A. Dill, *J. Phys. Chem. B*, 2009, **113**, 14270–14276.
41 G. S. Manning, *J. Chem. Phys.*, 1969, **51**, 924–933.
42 G. S. Manning, *J. Chem. Phys.*, 1969, **51**, 934–938.
43 A. Katchalsky, *Pure Appl. Chem.*, 1971, **26**, 327–373.
44 D. Dolar, *Polyelectrolytes*, D. Reidel Publ. Co., Dordrecht-Holland, 1974, pp. 97–113.
45 L. Zhuomei, Z. Xuexin, C. Yuanpei and Z. Yuanzhen, *Macromolecules*, 1992, **25**, 450–453.
46 G. B. McGaughey, M. Gagne and A. K. Rappe, *J. Biol. Chem.*, 1998, **273**, 15458–15463.
47 J. Combet, Collection SFN, http://www.neutron-sciences.org/, 2010, **11**, 153–176.
48 C. Klofutar, D. Rudan-Tasic and V. Mancic-Klofutar, *J. Solution Chem.*, 1997, **26**, 1037–1047.
49 J. P. Cotton, *Comment faire une calibration absolue des mesures de DNPA*, LLB Web site, www-llb.cea.fr.
50 A. V. Dobrynin and M. Rubinstein, *Macromolecules*, 1999, **32**, 915–922.
51 A. V. Dobrynin, R. H. Colby and M. Rubinstein, *Macromolecules*, 1995, **28**, 1859–1871.
52 D. Qu, J. S. Pedersen, S. Garnier, A. Laschewsky, H. Möhwald and R. von Klitzing, *Macromolecules*, 2006, **39**, 7364–7371.
53 K. Nishida, K. Kaji and T. Kanaya, *Macromolecules*, 1995, **28**, 2472–2475.
54 Y. V. Kalyuzhnyi, V. Vlachy and K. A. Dill, *Phys. Chem. Chem. Phys.*, 2010, **12**, 6260–6266.
55 J. Skerjanc and K. Kogej, *J. Phys. Chem.*, 1989, **93**, 7913–7915.
56 K. D. Collins, *Biophys. J.*, 1997, **72**, 65–76.
57 W. Kunz and R. Neueder, *Specific Ion Effects*, World Scientific, New Jersey, 2009, pp. 3–54.
58 K. Nishida, K. Kaji and T. Kanaya, *J. Chem. Phys.*, 2001, **114**, 8671–8677.

Aqueous solutions of tetraalkylammonium halides: ion hydration, dynamics and ion–ion interactions in light of steric effects†

Debsindhu Bhowmik,‡[a] Natalie Malikova,§*[a] Guillaume Mériguet,[b] Olivier Bernard,[b] José Teixeira[a] and Pierre Turq[b]

Molecular simulations have allowed us to probe the atomic details of aqueous solutions of tetramethyl-ammonium (TMA) and tetrabutylammonium (TBA) bromide, across a wide range of concentrations (0.5 to 3–4 molal). We highlight the space-filling (TMA$^+$) *versus* penetrable (TBA$^+$) nature of these polyatomic cations and its consequence for ion hydration, ion dynamics and ion–ion interactions. A well-established hydration is seen for both TMA$^+$ and TBA$^+$ throughout the concentration range studied. A clear penetration of water molecules, as well as counterions, between the hydrocarbon arms of TBA$^+$, which remain in an extended configuration, is seen. Global rotation of individual TBA$^+$ points towards isolated rather than aggregated ions (from dilute up to 1 m concentration). Only for highly concentrated solutions, in which inter-penetration of adjacent TBA$^+$s cannot be avoided, does the rotational time increase dramatically. From both structural and dynamic data we conclude that there is absence of hydrophobicity-driven cation–cation aggregation in both TMABr and TBABr solutions studied. The link between these real systems and the theoretical predictions for spherical hydrophobic solutes of varying size does not seem straightforward.

1 Introduction

In the field of ionic solutions, those containing tetraalkylammonium (TAA, $N(C_nH_{2n+1})_4{}^+$) cations occupy a very specific position. These cations, considered to be the archetypal hydrophobic cations, bring into play both charge and hydrophobicity, a combination of great importance in many environmental and biological processes. As such they are also widely used in phase transfer catalysis, involving an aqueous and an organic phase. The series of small symmetric TAA cations, most often with halide counterions, has been at the core of numerous studies to investigate the effect of hydrophobicity on ion hydration and ion–ion interactions in aqueous solutions, for reviews, see ref. 1–3. The hydrophobic character of TAAs is considered to be tuneable *via* the length of the four alkyl chains attached to the central nitrogen atom. The first four members of

the TAA series (referred to from now onwards as TMA$^+$, TEA$^+$, TPA$^+$ and TBA$^+$, from the smallest to the largest cation) have been studied most extensively. They show high solubility limits, comparable to alkali halides, considered to be their purely electrostatic analogues.[4]

Despite the wealth of past studies, as of today we are unable to link the thermodynamic and structural data for TAA ions in solution into a coherent picture. Thermodynamic data show clearly that the transfer of TAA cations from aqueous to non-aqueous solutions is accompanied by an increasingly negative Gibbs free energy as the cation size increases (TMA$^+$ features, however, a positive value), which put forward the idea of larger TAAs being "hydrophobic ions". Moreover, this Gibbs free energy is dominated by an increasingly positive entropy term.[3] To explain these findings, several structural studies have focused on providing evidence for (a) increased structuring of water in the vicinity of TAA ions, perhaps leading all the way to clathrate formation, and (b) formation of cation–cation pairs, as the cation size increases. Unfortunately, the evidence for either one of them is not clearly established. Neutron diffraction,[5–7] microscopic simulation[8,9] as well as dynamic studies by NMR and neutron scattering,[10–15] conclude against increased water structuring and see no clathrate formation, with the possible exception of TBA$^+$ in the low temperature regime only.[12] At the same time, neutron diffraction and microscopic simulation

[a] *Laboratoire Léon Brillouin, UMR CEA-CNRS 12, CEA Saclay, 91191 Gif-sur-Yvette, France*

[b] *Sorbonne Universités, UPMC Univ Paris 06, CNRS, UMR 8234, PHENIX, F-75005, Paris, France*

† Electronic supplementary information (ESI) available. See DOI: 10.1039/c4cp01164c

‡ Present address: Department of Physics and Astronomy, Wayne State University, 666 W Hancock Street, Detroit, MI 48201, USA.

§ Present address: Sorbonne Universités, UPMC Univ Paris 06, CNRS, UMR 8234, PHENIX, F-75005, Paris, France. E-mail: natalie.malikova@upmc.fr

agree on the unusual tangential orientation of water molecules around individual TAA ions, in stark contrast to alkali cations.[8,9,16] Defining θ as the angle between the vector joining the cation (central N atom in the case of TAA) to the oxygen atom of a water molecule and the dipole moment vector of the same water molecule, tangential orientation refers to cases when these two vectors are at or close to 90 degrees. This is the case for TAA ions and in contrast to θ close to zero in the case of alkali ions. Within the microscopic picture, this tangential orientation of water molecules has since been referred to as "hydrophobic hydration". However, a direct correspondence of this feature and the thermodynamic classification is not easy, as even the TMA$^+$ (thermodynamically hydrophilic) features this type of unusual hydration. Regarding cation–cation aggregation, small angle neutron scattering (SANS) and neutron diffraction do not support it in TAA halide solutions, though they give evidence for instances where adjacent TAA cations are not separated by water.[17–19] Any inferred TAA–TAA association is clearly very weak in comparison to that seen for larger phenyl containing phosphonium based cations in aqueous solution, where phenyl–phenyl specific interaction is likely to play a non-negligible role.[20] In contrast, some recent results obtained by small angle X-ray scattering and simulation[21] as well as femtosecond infrared spectroscopy[22] are interpreted as giving evidence for TAA–TAA aggregation or cluster formation.

It is clear that TAA halide solutions have some distinct features when compared to solutions of alkali halides. However, which of these features can truly be assigned to their hydrophobicity? Whereas theoretical studies concerned with hydrophobic solutes have the power to tune a single parameter, such as the solute size,[23] clearly, when it comes to real systems, the transition from an alkali cation towards a TAA cation is far from an addition of a single parameter. This is obvious from the polyatomic nature of TAA cations, their size and the finite distribution of charge among the atoms. Without resorting to hydrophobicity, these steric and geometrical aspects play a significant role by themselves. As has been highlighted recently,

for example, it is the substantial excluded volume fraction occupied by TAA-resembling ions in moderate to concentrated solutions that is the reason behind the slowing down of water dynamics observed, rather than any intrinsic hydrophobicity effect of the ions present.[24] This reasoning revives the obstruction effect mentioned already in the past.[11]

Motivated by highlighting the steric/geometrical aspects of TAA ions in aqueous solutions, we have resorted to microscopic simulations using a fully-atomic model of the ions (explicit H atoms). We study a range of concentrations, 0.5 to 3–4 on the molality scale, which includes the moderate to concentrated systems studied experimentally in the past. The exact concentrations chosen for a given system were guided by the concentration of a single hydration shell per TAA cation, which has been used as a reference point extensively.[7,8,11,25] Importantly, we report upon both structural *and* dynamic properties of the ions, we highlight their space-filling (TMA$^+$) *versus* penetrable (TBA$^+$) nature and its consequence for ion hydration, ion dynamics and ion–ion interactions.

2 Simulation techniques

Classical molecular dynamics (MD) simulations (using the code DL POLY 2.18[26]) were performed on a series of aqueous solutions of TMABr, TBABr and NaBr, spanning a range of concentrations. The overview of simulated systems is given in Table 1. An all-atom (explicit N, C and H atoms), flexible (bond stretching, bond bending, dihedral interaction), non-polarizable model was taken for the TMA$^+$ and TBA$^+$ ions. The non-bonding interactions in the system were described *via* the Coulombic and Lennard-Jones (LJ) potentials, with the use of Lorentz–Berthelot mixing rules for the LJ parameters.[27] Individual atomic charges within the TMA$^+$ and TBA$^+$ ions were determined by the restrained electrostatic potential (RESP) fitting of Hartree–Fock results included in the Antechamber library of the AMBER code.[28–32] Other interaction parameters of these ions were taken directly from the Generalized

Table 1 Overview of simulated systems. "Composition" indicates the total contents of the simulation box, in terms of the numbers of cations, anions and water molecules. "Box size" stands for the length of the side of the cubic box, it is determined by MD simulations in an NPT ensemble (T = 298 K, p = 1 bar). [L] indicates large box simulations for a chosen set of concentrations. "MD length" is the length of the collected simulated trajectory in the NVE ensemble used for further analysis. Asterisk (*) indicates the concentration formally considered to be just sufficient for the formation of a single hydration shell per cation

System	Composition cat–ani–H$_2$O	Box size [Å]	MD length [ns]	Molar ratio ions : H$_2$O	Molality (m) [mol kg^{-1}]	Molarity (M) [mol dm^{-3}]
TMABr	8–8–176	18.92	3.4	1 : 22	2.52 (*)	2.01
	8–8–352	22.93	3.4	1 : 44	1.26	1.12
	8–8–448	24.65	3.4	1 : 56	0.99	0.90
	8–8–528	25.87	3.4	1 : 66	0.84	0.77
	8–8–704	28.27	3.4	1 : 88	0.63	0.59
TBABr	8–8–112	19.42	3.4	1 : 14	3.96	1.83
	24–24–336	28.17 [L]	16.4	1 : 14	3.96	1.83
	8–8–224	21.97	3.4	1 : 28	1.98	1.25
	8–8–448	25.90	3.4	1 : 56	0.99 (*)	0.77
	16–16–896	32.54	16.4	1 : 56	0.99 (*)	0.77
	24–24–1344	37.35 [L]	3.4	1 : 56	0.99 (*)	0.77
	8–8–896	31.39	3.4	1 : 112	0.50	0.43
	1–1–896	30.14	8.2	1 : 896	Isolated (0.06)	Isolated (0.06)
NaBr	8–8–448	24.07	3.4	1 : 56	0.99	0.97

Amber Force Field (GAFF).[28–32] Bromide and sodium ion parameters were taken from the literature[33–37] and a rigid SPC/E model was used for water.[38] A compilation of parameters used in our simulations is provided in the ESI.†

For any given system, a cubic simulation box was filled initially with regularly spaced ions and water molecules (at random orientations). Three dimensional periodic boundary conditions were used, a cutoff radius for short-range interactions was half of the box-size, long-range part of the electrostatic interaction was evaluated using the 3D Ewald sum,[39] SHAKE algorithm[27,40] was used for rigid SPC/E water molecules. The initial configuration was equilibrated in NpT (p = 1 atm, T = 298 K) and then NVT ensembles. As an initial check of the interaction potentials, the simulated density obtained from the NpT equilibration was compared to the available experimental data. The comparison is given in the ESI,† the difference in simulated and experimental values is <0.2%. A production run was further carried out in the NVE ensemble, with a total length of at least 3.4 ns and a timestep of 1 fs. Individual atomic trajectories were saved every 0.1 ps, producing at least 34×10^3 frames in total. The trajectories were then analysed using nMoldyn[41,42] to obtain both static and dynamic properties of ions and water molecules.

3 Results

3.1 Ion hydration

We consider at first the hydration of ions in TMABr, TBABr and NaBr aqueous solutions and its concentration dependence. Fig. 1 shows the radial distribution functions between central nitrogen atoms of the cation and oxygen atoms of water molecules, g_{NOw}, for TMABr and TBABr solutions. We observe that g_{NOw} for TMABr solutions is very much concentration

independent in the range shown. The first prominent peak is centered on 4.4 Å, with the corresponding coordination number of 25 water molecules. Thus we see a well-defined first hydration shell for TMA$^+$, which has been suggested previously by MD simulation for a very dilute solution using a 5-site TMA model (no explicit H atoms),[9] and also reported by neutron diffraction at a higher concentration.[16] We see that this hydration sphere survives with almost no modification across a wide concentration range, up to and including the one hydration sphere limit. A weaker secondary shell is also seen here, centered at a distance of 7.5 Å. The g_{NOw} functions for TBABr show, between 4 and 9 Å, a rather complicated structure, but the notable features are at comparable distances to those for TMABr. The first part, up to 6.2 Å, corresponds now to water molecules which are closer than the outermost H atoms of TBA$^+$ (their position is indicated by the vertical dashed line). In the $g(r)$ representation, the intensity of this peak is highly concentration dependent, but should not be interpreted automatically as a significant change in the number of these "inner" water molecules: their number varies slightly from 20 H$_2$O at 0.06 m down to 17 at 1.98 m (and then fast to 13 at 3.96 m). The strong intensity variation in the first $g(r)$ peak is a consequence of the significant volume fraction occupied by the TBA$^+$ ions in these solutions (from 2% at 0.06 m to 50% at 3.96 m), which leads to strong variation in the number density of water molecules, $i.e.$ the $g(r)$ normalisation factor. The well-defined peak between 6.2 and 10 Å in the $g(r)$ shows in contrast more constant intensity, thus the relative density of water molecules in this region is permanently in excess of the average density (the corresponding coordination number is 100 water molecules at 0.06 m and 50 at 3.96 m).

Comparing the details of water orientation between TMABr, TBABr and NaBr (at 1 m concentration), we confirm the close to tangential orientation in the case of TMA$^+$ and TBA$^+$ (see ESI† for the relevant graphs). In addition, we observe that this orientation
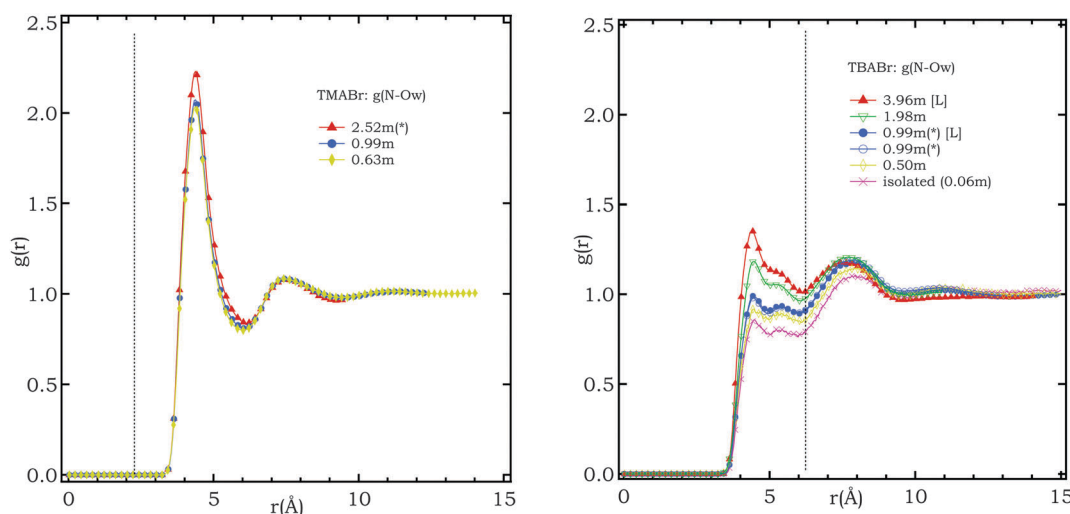
Fig. 1 Radial distribution function between the nitrogen atoms of cations and the oxygen atoms of water molecules, g_{NOw}, for TMABr solutions (left) and TBABr solutions (right) for a series of concentrations as indicated. Vertical dotted lines indicate the position of the outermost hydrogen atoms of the cation. Symbol [L] indicates the use of large simulation boxes for certain concentrations, refer to Table 1. Asterisk (*) indicates the concentration formally considered to be just sufficient for the formation of a single hydration shell per cation.

is lost in the second hydration shell of TMA$^+$. It is retained in the case of the second hydration shell of TBA$^+$, though this is most probably the effect of an adjacent TBA$^+$. Hydration of Br$^-$ in the TMABr and TBABr solutions is similar to that of NaBr (data not shown). The coordination number found for alkali halide solutions (= 7.5) is also found for TMABr and TBABr solutions, it remains almost constant up to concentrations corresponding to the respective one hydration sphere limits, beyond which the anion is losing its usual coordination.

3.2 Ion–ion interactions

Ion–ion correlation functions were inevitably poorer in statistics than ion–water correlation functions, due to the finite number of ions in the simulation box. In the following we thus had to omit data for some of the lower concentrations. Fig. 2 shows the radial distribution functions between the nitrogen atom of the cation and Br$^-$ (g_{NBr}) for the series of TMABr and TBABr solutions as a function of concentration. The main feature in the g_{NBr} for TMABr is a well-defined intense peak centered at 5 Å, the position of which is concentration independent and is 2.8 Å away from the hydrogen atoms of the TMA$^+$ (position of these H atoms is indicated by a vertical dashed line in the figure). Interestingly, the g_{NBr} for TBABr solutions features its first peak at the same distance as for TMABr solutions, *i.e.* at 5 Å. Br$^-$ ions corresponding to this first peak are closer to the nitrogen atom than the outermost H atoms, though farther than the next inner layer of H atoms. The penetration of Br$^-$ in between the last quarter of the hydrocarbon arms of the TBA$^+$ is thus made clear, a similar observation was reported in the previous section for water molecules themselves. The coordination number of these inner Br$^-$ ions is about 1/3 and note that this increases dramatically as we move above the one hydration sphere concentration, we shall discuss this point later. Further out, the g_{NBr} features a broader double peak.

Fig. 3 features the radial distribution functions between the nitrogen atoms of cations for TMABr and TBABr solutions, with dotted and dashed-dotted vertical lines indicating, respectively, the position of the outermost hydrogen atoms of the cation and the first layer of water oxygen atoms (first peak position in g_{NOw}). A distinct TMA–TMA correlation peak centered at 8.4 Å is visible at the one hydration sphere concentration. It persists as the system is diluted, with no change in position, though decreasing in intensity. This peak lies farther than the first correlation peak both in g_{NOw} and g_{NBr}. Considering the position of the hydrogen atoms on a single TMA$^+$, the first TMA–TMA correlation peak does not correspond to two adjacent TMA$^+$s in contact, rather two TMA$^+$s sharing a hydration shell, but possibly also a Br$^-$ counterion. In contrast to TMA$^+$, a broad TBA–TBA correlation peak is visible only at the highest concentration considered (3.96 m, significantly above the one hydration sphere limit). At the one hydration sphere limit (1 m), the $g(r)$ shows very little correlation. Considering again the position of the outermost hydrogen atoms on a single TBA$^+$ (6.2 Å), the peak observed at 3.96 m has to correspond to interpenetration of the arms of the adjacent TBA$^+$s. Note that the hydrocarbon arms are rather rigid and do not show any bending as the concentration is increased. This is made obvious from our MD simulations from the radial distribution functions of the terminal carbon atoms around the central N atom (data not shown). Moreover, we have also observed this experimentally *via* small angle neutron scattering.[43] In the case of such extended arms, the interpenetration of adjacent TBA$^+$s seems to be sterically very much feasible as they are far from space filling objects, as was made obvious already from the corresponding g_{NOw} and g_{NBr}. In the space between adjacent TBA$^+$s there is again non-zero density of water molecules and possibly also Br$^-$ counterions, as in the case of two adjacent TMA$^+$s. This applies for all concentrations studied.

3.3 Diffusion

The translational diffusion coefficients of TAA ions and water in our solutions have been calculated from the mean square

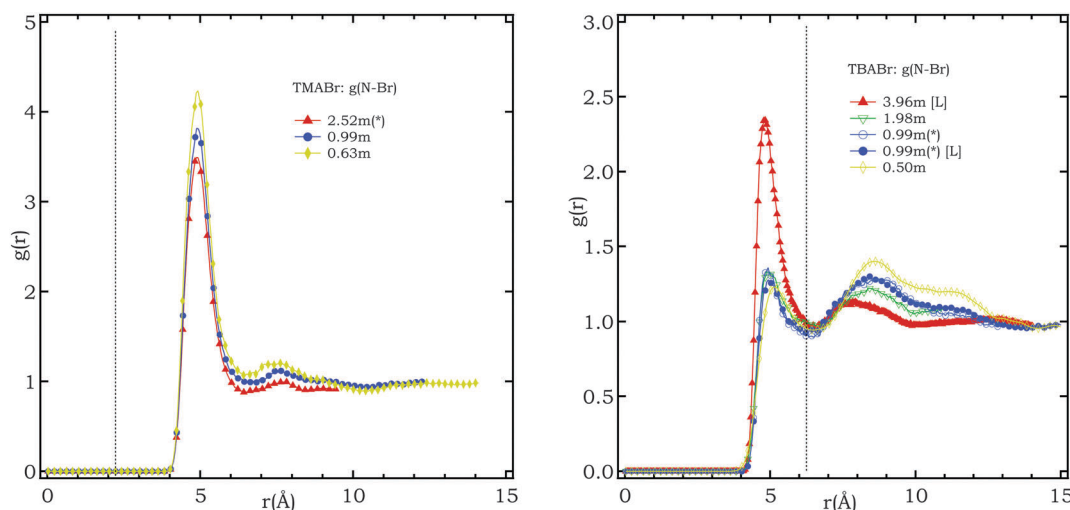**Fig. 2** Radial distribution function between the nitrogen atom of the cation and the bromide anion, g_{NBr}, for TMABr solutions (left) and TBABr solutions (right) for a series of concentrations as indicated. Vertical dotted lines indicate the position of the outermost hydrogen atoms of the cation. Symbol [L] for the TBABr systems indicates the use of large simulation boxes.
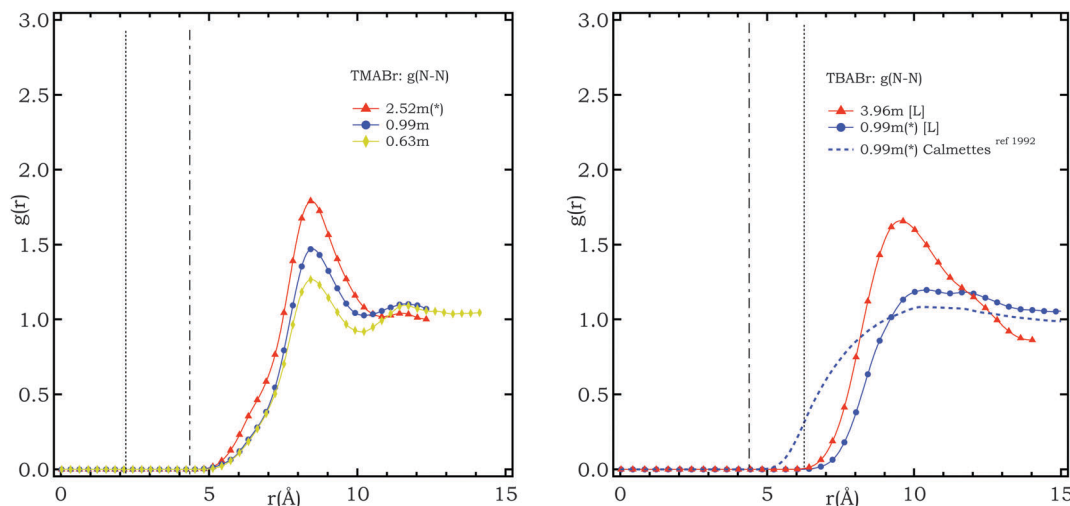
Fig. 3 Radial distribution function between the nitrogen atoms of cations, g_{NN}, for TMABr solutions (left) and TBABr solutions (right) for a series of concentrations as indicated. Symbol [L] indicates the use of large simulation boxes. Dotted and dashed-dotted vertical lines indicate, respectively, the position of the outermost hydrogen atoms of the cation and the position of the first peak in g_{NOw}. Dashed blue series in the right figure corresponds to data from a TBA–TBA potential derived from hypernetted chain (HNC) calculations in ref. 18.

displacements (MSD) of the central N atoms for the ions and O atoms for water, according to:

$$\mathrm{MSD}(t) = \langle |\mathbf{r}_i(t) - \mathbf{r}_i(0)|^2 \rangle = 6Dt \qquad (1)$$

Fig. 4 shows our simulated translational diffusion coefficients of cations and water molecules in a series of TMABr and TBABr solutions, together with a compilation of other experimental and simulated data available from the literature. Note that in MD, the size of the system has an a priori measurable effect on the measured diffusion coefficients.[44,45] We have, however, tested this for the 1 m concentration of TBABr with three box sizes and no dependence has been observed, certainly because of the high viscosity of the system. For comparison between data from different techniques, note that deuterated water is often necessary to measure experimentally the diffusion coefficient of the hydrogen containing cations (in NMR and neutron scattering in particular), while tracer experiments (and simulations) are carried out in light water. Solvent deuteration leads to a difference in the solvent viscosity (D_2O/H_2O viscosity ratio is 1.23 at 298 K), which marks its effect only at low TAABr concentrations: tracer data consistently above NMR data at low concentration in Fig. 4(a) and (b). Already at 1 m concentration, this effect seems however insignificant.

3.4 Local and internal motion of TAA cations

We have chosen to concentrate on two types of local/internal motions of the TAA ions: (1) global cation rotation, also referred to in the literature as the tumbling motion and (2) rotation of the terminal methyl groups, since they are both well documented in the literature, mostly using experimental techniques. Global cation rotation was probed using the mean square displacement (MSD) of the α C atoms (directly bonded to the central N atom) relative to the central N atom. We considered this to be the most accurate estimate, as the effects of arm bending on this MSD play

a minimal role. Methyl group rotation was treated in a similar manner, from the mean square displacement of H atoms relative to adjacent C atoms, *while* correcting for any possible global cation rotation. This correction is especially important when the characteristic time of global rotation is similar to that of the methyl group rotation. We shall see that this is the case for TMA$^+$, contrary to TBA$^+$.

For rigid molecules, rotational dynamics is evaluated from the orientational correlation function $C_\ell(t) = \langle P_\ell(\mathbf{u}(0)\cdot\mathbf{u}(t)) \rangle$, where $\mathbf{u}$ is a unit vector indicating the orientation of the molecule and P_ℓ the ℓ-rank Legendre polynomial.[46,47] For a pure global rotational diffusion, we obtain $C_\ell(t) = e^{(-\ell(\ell+1)D_{rot}t)}$, where D_{rot} is the rotational diffusion coefficient. The relative MSD displacement is related to $C_1(t)$ as follows:

$$\begin{aligned}
\mathrm{MSD}(t) &= 2b_{N-C}{}^2(1 - C_1(t)) \\
&= 2b_{N-C}{}^2\left(1 - e^{-2D_{rot}t}\right) \qquad (2) \\
&= 2b_{N-C}{}^2\left(1 - e^{-2t/\tau_{rot}}\right)
\end{aligned}$$

where b_{N-C} is the length of the N–C bond. Since it has been derived for rigid molecules, the above equation does not apply to short correlation times ($t < 1$ ps), where the fast vibration and distortion of the bonds play a significant role. Fig. 5 summarizes the relative MSD obtained for the case of global cation rotation for both TMA$^+$ and TBA$^+$ and it is well modelled by eqn (2). For TBA$^+$, global rotation is seen to be strongly concentration dependent, but only beyond the one-hydration sphere limit (0.99 m). The characteristic time is $\tau_{rot} = 0.54$ ns for infinite dilution up to 1 m and then reaches $\tau_{rot} = 3.1$ ns at 3.96 m. The orientational dynamics of every carbon and hydrogen atom inside TBA$^+$ was investigated for selected TBABr systems (data not shown). For any atom in the two most inner methylene (CH$_2$) groups, the characteristic times were close to
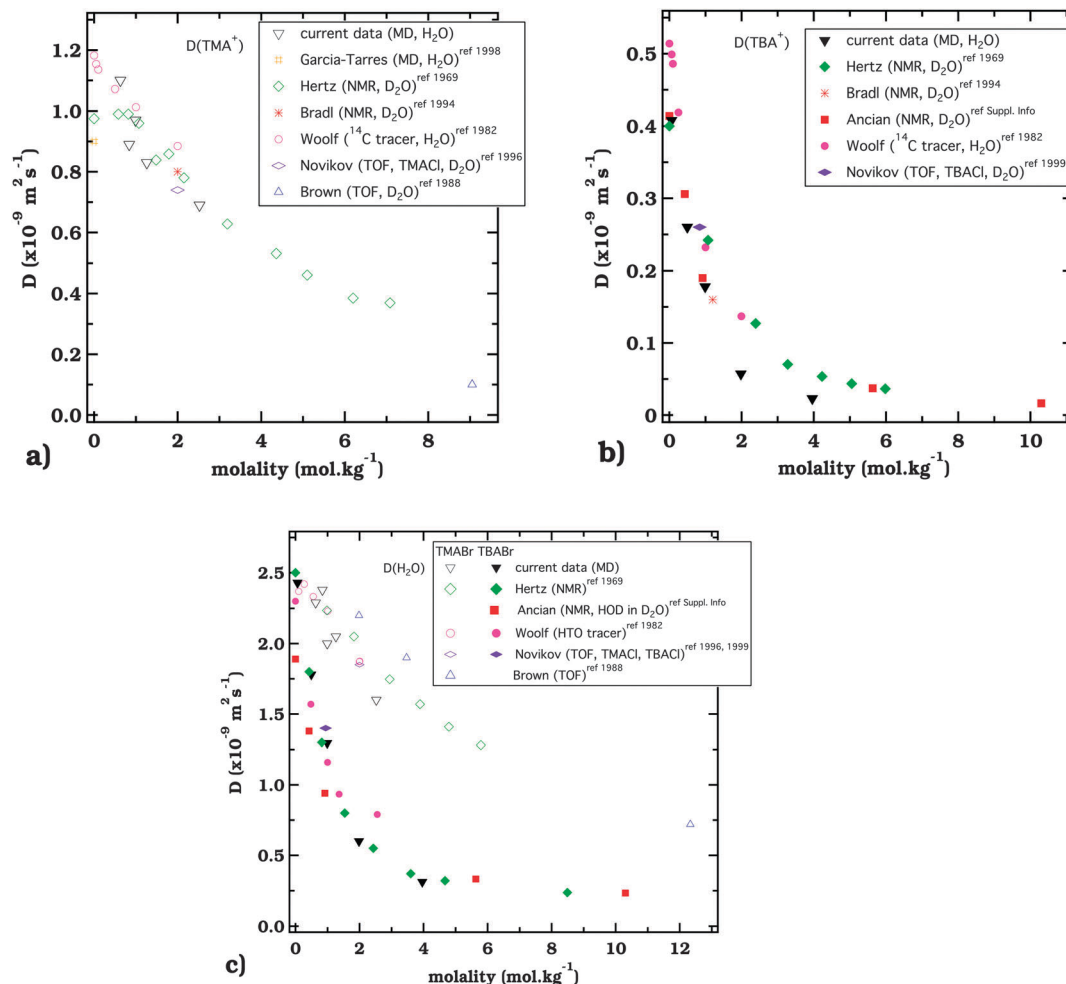
Fig. 4 Compilation of experimental and simulated translational diffusion coefficients for (a) TMA$^+$, (b) TBA$^+$ and (c) H$_2$O in a series of aqueous solutions of TMABr and TBABr. Solvent deuteration was used in some experimental set-ups (as indicated) to measure the diffusion coefficients of the cations. To compare the data whatever the isotopic nature of the solvent, the concentration scale for measurements in D$_2$O is in aquamolality (molality of the solution, if D$_2$O had the same mass as H$_2$O). Estimated error bars for current MD data are 0.05 × 10^{-9} m^2 s^{-1} for TMA$^+$ and 0.02 × 10^{-9} m^2 s^{-1} for TBA$^+$ and H$_2$O. Note: MD = molecular dynamics, TOF = time-of-flight neutron scattering, other symbols have their usual meaning.

the global rotation time, as determined above. This indicates the significant stiffness of the TBA$^+$ core. The global rotation for TMA$^+$ in the range studied (up to and including its one-hydration sphere limit) is found to be concentration independent, but with a much smaller characteristic time, $\tau_{rot} = 5 \pm 1.5$ ps.

As for methyl dynamics, two main classical descriptions exist: a continuous diffusion on a circle and a threefold jump process.[47–49] The corresponding relative MSD, once corrected for the global rotation, can be expressed in a similar manner to eqn (2):

$$\mathrm{MSD}(t) = 2b_{C-H}^2 \sin^2 \phi (1 - e^{-D_{rot}t}) = 2b_{C-H}^2 \sin^2 \phi (1 - e^{-t/\tau_{rot}}) \tag{3}$$

where b_{C-H} is the length of the C–H bond and $\phi = 109.5°$ is the angle between the C–H bonds. For a jump process, the characteristic time between jumps is $\tau_j = \frac{3}{2}\tau_{rot}$.[48,50] MSD behaviour cannot distinguish between the two types of methyl dynamics, but it is still possible to compare TMA$^+$ and TBA$^+$. Relative MSD for terminal methyl group rotation shows minimal concentration

dependence for both TBA$^+$ and TMA$^+$ (see ESI†), with somewhat different mean characteristic times τ_{rot} of 6 ps and 2 ps respectively.

4 Discussion

We shall now summarize our results regarding ion-hydration, ion–ion interactions and ion dynamics in TAABr solutions, putting them into context with previous literature.

Our MD results show TMA$^+$ hydration as a distinct layering of hydration shells (first shell containing approximately 25 water molecules), as in the case of simple monoatomic cations. We confirm the tangential orientation observed experimentally and in previous simulations.[8,9,12,16] We see that this orientation is lost in the second hydration shell of TMA$^+$. The well-defined first hydration shell of TMA$^+$ exists over a wide concentration range, up to and including the single hydration layer reference, with very little variation in the coordination number. Hydration of TBA$^+$ is dominated by the fact that it is not an impenetrable

Fig. 5 Investigation of global cation rotation for TBA$^+$ and TMA$^+$: mean square displacement (MSD) of α C atoms with respect to the central N atom, *versus* time, for TBA$^+$ in selected TBABr solutions; in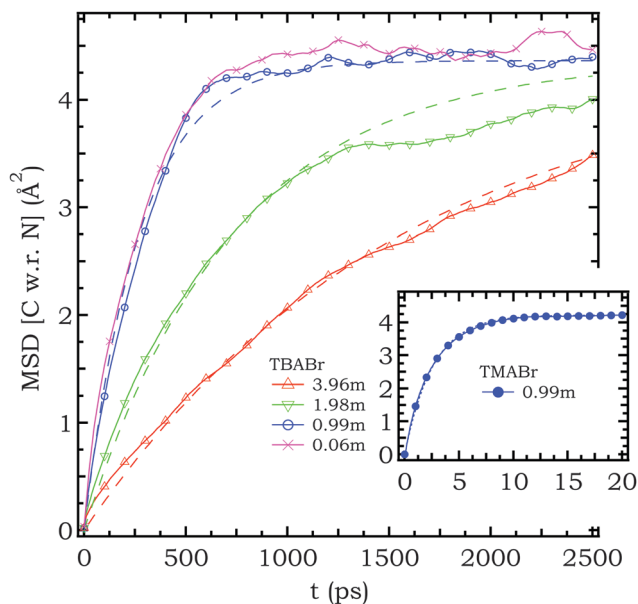set features the same type of data for TMA$^+$ in 0.99 m TMABr solution. Dashed lines represent the fit of data with eqn (2).

species and that its hydrocarbon arms remain in an extended configuration across a wide concentration range. A rather constant number of water molecules (approximately 20) fill the space between the arms, the density of these "inner" water molecules is naturally the result of the space available and the interactions with the arms of TBA$^+$. Interestingly these molecules also possess a close to tangential orientation with respect to the central N atom.

The charge on any given TAA cation is crucial for hydration to occur and for the stability of the solution (removal of charges on TAA results, as expected, in demixing[21]). Where available in the literature, we see that charge distribution in the microscopic models of TAA cations has been (a) +1 charge distributed equally over the four α C atoms irrespective of the length of the hydrocarbon arms[8,9] or (b) charge more spread out along the hydrocarbon arms as in our model.[28,51] The difference between these charge distributions does not affect the water orientation observed, tangential is seen in all. For coarser models, the entire TAA cation considered to be a single pseudoatom, this type of information is blurred and no preferential orientation is concluded.[52] Spatially extended and non-spherically distributed charge density on the cation seems then an important condition for the tangential configuration of water molecules. Apart from water molecules, the space between the arms of TBA$^+$ is also occupied by Br$^-$ counterions (with a coordination number of 1/3 up to the 1.98 m concentration). These counterions possess their full hydration shell of 7.5 water molecules up to the 1 m concentration. Beyond this point it begins to be lost, certainly due to steric effects. Penetration of Br$^-$ was previously seen in the case of TPA by simulation[28] and is consistent with the notion of penetration cation–anion pairs referred to earlier on the basis of dielectric spectroscopy measurements.[53]

The extent of cation–cation aggregation in TAA halide solutions remains a widely-discussed topic, let us view the ion–ion correlation functions we have obtained by MD in light of this aspect. We may start by considering that cation–cation effective pair potentials in our solutions possess (a) a short-range repulsive part due to steric effects, (b) cation–cation electrostatic repulsion and (c) a short-range attractive (hydrophobicity-driven) part. Regarding electrostatic repulsion, we note that in the highly concentrated solutions studied, it is screened over a few Å (the Debye screening length for 1 molar aqueous solution at 298 K is only 3 Å). If cation–cation electrostatic repulsion was dominating we would expect to see the position of the first peak in g_{NN} to be concentration dependent. Further, assuming a simple model of the cations on a grid, the equilibrium cation–cation distance would be varying between 9.5 Å and 14 Å for 2.52 m and 0.63 m TMABr solutions (9.7 Å and 30.1 Å for 3.96 m and 0.50 m TBABr solutions). However, we observe no shift in the first peak of g_{NN} for both TMABr and TBABr solutions. Apart from the 3.96 m TBABr system, the peak position is at smaller distances than what is predicted by the simple grid model. Thus the observed correlation peak reflects a short-range interaction, which, without any other knowledge, could have its origin either in short-range steric repulsion or short-range hydrophobic attraction.

At this point, the information on cation hydration seems to be of utmost importance and, as mentioned above, we report a well-established hydration of both TMA$^+$ and TBA$^+$ persisting throughout the whole concentration range considered. A hydrophobicity-driven cation aggregation would be accompanied by at least a partial loss of hydration water, but this is not observed. In the case of TMA$^+$, considering the sizes of the "naked" and hydrated cation, we were brought to conclude that the clear TMA–TMA correlation peak at 8.4 Å does not correspond to two TMA$^+$s in contact but rather being separated by a hydration sphere, albeit incomplete, and possibly also a Br$^-$ counterion. Thus we trace the first peak in g_{NN} to the short-range steric repulsion between partially hydrated TMA$^+$s. Further, comparing g_{NN} of TMABr and TBABr solutions at a given concentration (consider 1 m), we observe a clear decrease in the first peak intensity as we move from TMA$^+$ to TBA$^+$. Indeed, even at 1 m, there is only a very weak peak in the g_{NN} for TBABr. If hydrophobicity was the underlying interaction, we would expect the opposite trend, an increase in the correlation peak as we move to TBA$^+$. The observed intensity trend reflects in our opinion the relative hardness/softness of the short-range cation–cation steric repulsion and is consistent with the space-filling (hard) nature of the TMA$^+$ and the penetrable (soft) nature of TBA$^+$. The transition from 0.99 m to 3.96 m for TBABr is then an interesting case. We observe finally a clear appearance of a TBA–TBA correlation, also a dramatic increase in TBA–Br correlation at 5 Å. Referring to the above simple model of TBA$^+$ ions on a regular grid, the transition 0.99 m to 3.96 m corresponds to a TBA–TBA separation decreasing from 13.0 to 9.7 Å. At 3.96 m the TBA$^+$s are effective at this predicted distance, they are closely packed, with partially inter-penetrated arms and counterions as well as water molecules locked inside the region between the arms. This interpenetration is accompanied by a

decrease in "inner" water molecules (from 17 to 13). The effective TBA–TBA potential is suddenly "harder", *i.e.* even more repulsive due to steric reasons, and a correlation peak appears in g_{NN}.

Overall, regarding cation–cation correlations, we observe some agreement but also differences from the available literature. Our results agree well with the distance of the most prominent peaks for both TMA–TMA and TBA–TBA correlations.[21] However, in terms of trends in peak intensities, the results clearly disagree. The only concentration for which we see a clear TBA–TBA correlation peak is only at 3.96 m, while a clear TMA–TMA peak is present throughout the whole concentration range studied. Simulations in ref. 21 refer to 1 m concentration and show a strong TBA–TBA correlation, stronger than the TMA–TMA peak. This is an important point, as it is interpreted by the authors as evidence for hydrophobicity-driven TBA aggregation, with which our results seem to be inconsistent. More in line with our results are the data for Krienke *et al.*, where the first two members of the TAA series were studied (TMA$^+$ and TEA$^+$).[51] A clear decrease in the intensity of cation–cation correlation peaks was seen upon transition from TMA$^+$ to TEA$^+$ (at roughly 0.6 m concentration). Moreover, hyper-netted chain (HNC) calculations made in conjunction with SANS experiments on TBABr aqueous solutions[18] result in a potential that leads to a very featureless TBA–TBA pair correlation function at 0.99 m (data included in Fig. 3 right). SANS is particularly sensitive to the signal from cation–cation correlations in TAABr solutions due to the high concentration of H atoms in TAA cations (yielding a good contrast with respect to the deuterated solvent) as well as their greater size in comparison to the anions. In order to assess whether the atomic configurations in our simulations reproduce scattering data from TBABr solutions, we compared directly the reciprocal space data obtained from neutron scattering from ref. 43 and those calculated from our simulations. This is another very pertinent test of the realistic nature of the force field used in our simulations. The comparison was made at 1 m concentration and is featured in Fig. 6. We see that our simulations reproduce very reliably the experimental neutron scattering data across a wide spatial range. Therefore, the same atomic configurations leading to a very featureless TBA–TBA $g(r)$ (Fig. 3 right) can reproduce experimentally measured neutron scattering data. As detailed in ref. 43, the neutron scattering data are dominated by the form factor of the individual TBA$^+$ ions at low Q values and by the broad solvent peak centered on $Q = 1.8$ Å. The data show no evidence of a strong TBA–TBA correlation peak and are in accord with previous literature using this technique.[17–19] Regarding other scattering techniques, ref. 21 presents SAXS measurements for TAA halide solutions[21] showing an interesting evolution as a function of increasing TAA cation size: the gradual appearance of a correlation peak, centered at 0.8 Å^{-1} for TBABr solution. In conjunction with the above-mentioned simulations from this reference, this peak is again taken as evidence for TBA–TBA aggregation. Interestingly, we were able to calculate the SAXS signal from our simulated TBABr system at 1 m and are able to reproduce the observed peak (see ESI†). The same atomic configurations that give rise to the SAXS peak show a very featureless TBA–TBA $g(r)$. In our opinion, the observed SAXS peak cannot reflect TBA–TBA aggregation. On the grounds of electronic density, it seems probable that this peak reflects
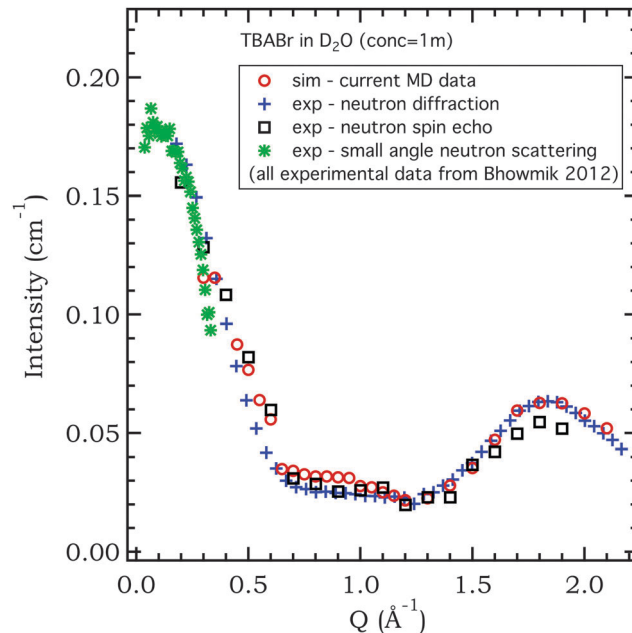

Fig. 6 Coherent neutron scattering intensity (in cm^{-1}) *versus* wave-vector, Q, for TBABr solution in D$_2$O at 1 m concentration, measured by three neutron scattering techniques and calculated from the current MD simulations (using the nMoldyn package together with the tabulated coherent scattering cross-sections of the elements present). Error bars are of the size of the symbols or smaller. All neutron scattering measurements are obtained from ref. 43.

primarily the correlations involving Br$^-$ (anion–anion or anion–cation correlation or both), but not the cation–cation correlation.

Overall, on the basis of our simulated structural data, we see no evidence for cation–cation aggregation in the TMABr and TBABr solutions studied. This is further supported by the dynamic information we were able to obtain, more precisely the individual global ion rotation. For global ion rotation the compact *versus* penetrable nature of the two TAA cations could again have a clear effect. Up to the respective one hydration sphere limits, we observe a concentration independent global rotation for both TMA$^+$ and TBA$^+$. Beyond the 1 m concentration, TBA$^+$ rotation is severely hindered and the origin is in the increasing inter-penetration of adjacent ions. This would not occur for the compact TMA$^+$ cation and we expect, beyond its one hydration sphere limit, a much weaker (if any) concentration dependence of its global rotation. Similarly, the behaviour of the terminal methyl groups is also affected by the difference in penetrability. For very similar interaction potentials, the characteristic times for methyl group rotation are indeed different (6 ps and 2 ps for TBA$^+$ and TMA$^+$ respectively). The environment for terminal methyl groups in TBA$^+$ is likely to be affected by the presence of water molecules (and counterions) penetrating between the hydrocarbon arms.

The observed evolution of TBA$^+$ global rotation from our simulations is supported by the available experimental data. The main source of experimental data regarding global rotation of TAA cations is NMR relaxation measurements, where we measure a correlation time τ_c, which is related to τ_{rot} according to $\tau_{rot} = 6\tau_c$.[49] Even if the decoupling of the different dynamics

is not straightforward in this technique, the global rotation can often be extracted using reasonable approximations, since it is the slowest dynamic mode.[49,54] For low concentrations (<0.05 mol L^{-1}) the measured correlation time for TBA$^+$ is in the range of 87–115 ps, depending on the exact concentration, counterion and nucleus probed.[55–58] A single measurement is available at high concentrations for TBACl solution (7.9 m) giving a value of $\tau_c = 0.63$ ns. Taking into account the conversion factor of 6 between τ_c and τ_{rot}, these experimental values are indeed in very good agreement with our simulations and show the changes occurring beyond the single hydration sphere limit. Regarding TMA$^+$ rotation, experimental data suggest τ_c of the order of 5 ps at low concentrations, with only a small increase up to 5 m concentrations (less than a factor of 1.5).[10,13,55,59,60] This is indeed as we expect from the compact nature of TMA$^+$. Quantitative agreement with our simulated data is however not found, our τ_{rot} of 5 ps would correspond to τ_c of 0.8 ps. In this case, we consider the experimental value to be less reliable due to the difficulty in decoupling the TMA$^+$ global rotation and methyl rotation as the characteristic times are very close, unlike for TBA$^+$. For completeness, experimental methyl rotational time ($\tau_{rot} \sim$) is 1–5 ps depending on the system studied and the technique employed.[13,50,61] A difference in terminal methyl group rotation has already been reported in a low temperature NMR study, leading to a correlation time larger by a factor of six in the case of TBA$^+$ than in the case of TMA$^+$.[62] The measurements of global as well as terminal methyl group rotation for TAA ions is a priori also available from quasi-elastic neutron scattering. However, the main and serious difficulty is, similarly to NMR, the decoupling of the different types of motion in the measured neutron signal, without the possibility to resorting to different nuclei (only H nuclei give measurable signal for these types of neutron scattering experiments). We have addressed this difficulty in detail in ref. 43. In conclusion, we were not able to extract global rotational times from our neutron scattering data.

Lastly, our MD simulations were able to reproduce well the experimental translational diffusion of TMA$^+$ and TBA$^+$, as well as water, across the concentration range studied. As our data show otherwise, the observed slowing down is not related to any cation aggregate formation, simple steric (obstruction) effects must be at the origin, as has already been suggested.[11,24] As it is a common observation that the results obtained from classical simulations are influenced by the choice of the force field, overall we have paid a close attention to assessing the quality of the employed force field. We have presented three data sets supporting its realistic nature: (a) the experimental density of TAABr solutions over a wide range is reproduced, (b) dynamical properties (translational and rotational diffusion) are in good agreement with experimental data, (c) when available neutron and X-ray scattering data are surprisingly well reproduced (in the case of 1 m TBABr solution). In our attitude, the direct agreement with several experimental data sets is a very convincing argument in favour of the chosen force field.

5 Conclusion

In conclusion, we have discussed the structural and dynamic properties of aqueous TMABr and TBABr solutions across a wide range of concentrations (0.5 to 3–4 molal). With the help of detailed all-atom molecular dynamics simulations we are able to address the aspects of ion hydration, ion dynamics and ion–ion interactions, while highlighting the steric details of the cations involved, contrasting the compact nature of TMA$^+$ and the penetrable nature of TBA$^+$. We have presented our results in light of the controversial cation–cation aggregation. Based on both structural and dynamic information regarding the TAA cations, we see no evidence for cation–cation aggregation in the systems studied. A well-established hydration is seen for both TMA$^+$ and TBA$^+$ throughout the concentration range studied. Both water molecules and counterions occupy the space between the hydrocarbon arms of TBA$^+$, which are found to remain in an extended configuration, whatever the concentration studied. At a given concentration, we observe a weaker cation–cation correlation in the case of the TBA$^+$ ions in comparison to TMA$^+$ ions. We interpret this as a "softer" interaction between the bigger penetrable ions. Up to the respective one hydration sphere limits, we observe a concentration independent global rotation for both TMA$^+$ and TBA$^+$, which again points against any cation–cation aggregation. Beyond this limit, TBA$^+$ rotation is severely hindered and the origin is in the increasing inter-penetration of adjacent ions. Overall, without resorting to hydrophobicity, steric effects of TMA$^+$ and TBA$^+$ cations seem to be sufficient to explain to a great extent the differences in the microscopic (local) behaviour of their solutions. Other types of local features in concentrated TAA halide solutions, such as slowing down of water reorientation as probed by infrared spectroscopy,[22] should also be viewed along these lines. A more appropriate description of larger TAA ions could simply be "bulky non-spherical penetrable ions". If, on top of steric features, hydrophobicity of the short hydrocarbon arms demonstrates itself, could it be masked by the effect of charge, at least for certain local properties? Looking for stark signature of hydrophobicity in local properties in order to explain the macroscopic thermodynamic data is perhaps a lost cause. Interestingly, we have observed recently that for ionene polyelectrolytes (long hydrocarbon chains with regular TAA charged centers), the effects of hydrophobicity are also suppressed to a surprising degree in their aqueous solutions, at least when certain structural features are considered.[63]

References

1 W.-Y. Wen, *Water and Aqueous Solutions. Structure, Thermodynamics, and Transport Processes*, John Wiley & Sons, New-York, 1972, ch. 15, pp. 613–661.
2 W. Wen, *J. Solution Chem.*, 1973, **2**, 253–276.
3 Y. Marcus, *J. Solution Chem.*, 2008, **37**, 1071–1098.

4 H. Nakayama, H. Kuwata, N. Yamamoto, Y. Akagi and H. Matsui, *Bull. Chem. Soc. Jpn.*, 1989, **62**, 985–992.

5 J. Turner, A. K. Soper and J. L. Finney, *Mol. Phys.*, 1990, **70**, 679–700.

6 J. Turner, A. K. Soper and J. L. Finney, *Mol. Phys.*, 1992, **77**, 411–429.

7 J. Turner and A. K. Soper, *J. Chem. Phys.*, 1994, **101**, 6116–6125.

8 J. T. Slusher and P. T. Cummings, *J. Phys. Chem. B*, 1997, **101**, 3818–3826.

9 L. Garca-Tarrés and E. Guàrdia, *J. Phys. Chem. B*, 1998, **102**, 7448–7456.

10 H. Hertz, B. Lindman and V. Siepe, *Ber. Bunsenges. Phys. Chem.*, 1969, **73**, 542–549.

11 P.-O. Eriksson, G. Lindblom, E. Elliott Burnell and G. J. T. Tiddy, *J. Chem. Soc., Faraday Trans. 1*, 1988, **84**, 3129–3139.

12 S. Bradl and E. W. Lang, *J. Phys. Chem.*, 1993, **97**, 10463–10471.

13 S. Bradl, E. W. Lang, J. Z. Turner and A. K. Soper, *J. Phys. Chem.*, 1994, **98**, 8161–8168.

14 B. Liegl, S. Bradl, T. Schätz and E. W. Lang, *J. Phys. Chem.*, 1996, **100**, 897–904.

15 A. G. Novikov, M. N. Rodnikova and O. V. Sobolev, *J. Mol. Liq.*, 2001, **91**, 91–97.

16 J. Z. Turner, A. K. Soper and J. L. Finney, *J. Chem. Phys.*, 1995, **102**, 5438–5443.

17 A. K. Soper, J. Turner and J. L. Finney, *Mol. Phys.*, 1992, **77**, 431–437.

18 P. Calmettes, W. Kunz and P. Turq, *Physica B*, 1992, **180**, 868–870.

19 N. G. Polydorou, J. D. Wicks and J. Z. Turner, *J. Chem. Phys.*, 1997, **107**, 197–204.

20 W. Kunz, P. Calmettes, T. Cartailler and P. Turq, *J. Chem. Phys.*, 1993, **99**, 2074–2078.

21 N. Huang, D. Schlesinger, D. Nordlund, C. Huang, T. Tyliszczak, T. M. Weiss, Y. Acremann, L. G. M. Pettersson and A. Nilsson, *J. Chem. Phys.*, 2012, **136**, 074507.

22 S. T. van de Post, S. Scheidelaar and H. J. Bakker, *J. Phys. Chem. B*, 2013, **117**, 15101–15110.

23 D. Chandler, *Nature*, 2005, **437**, 640–647.

24 G. Stirnemann, F. Sterpone and D. Laage, *J. Phys. Chem. B*, 2011, **115**, 3254–3262.

25 J. L. Green, M. G. Sceats and A. R. Lacey, *J. Chem. Phys.*, 1987, **87**, 3603–3610.

26 W. Smith, T. R. Forester and I. T. Todorov, *THE DL POLY 2 USER MANUAL, Version 2.18*, STFC Daresbury Laboratory, UK, 2007.

27 M. P. Allen and D. J. Tildesley, *Computer Simulations of Liquids*, Oxford University Press, 1989.

28 J. Heyda, M. Lund, M. Oncák, P. Slavcek and P. Jungwirth, *J. Phys. Chem. B*, 2010, **114**, 10843–10852.

29 T. Hrobárik, L. Vrbka and P. Jungwirth, *Biophys. Chem.*, 2006, **124**, 238–242.

30 W. D. Cornell, P. Cieplak, C. I. Bayly, I. R. Gould, K. M. Merz, D. M. Ferguson, D. C. Spellmeyer, T. Fox, J. W. Caldwell and P. A. Kollman, *J. Am. Chem. Soc.*, 1995, **117**, 5179–5197.

31 L. Vrbka and P. Jungwirth, *Aust. J. Chem.*, 2004, **57**, 1211–1217.

32 D. Case, T. A. Darden, T. E. Cheatham, III, C. L. Simmerling, J. Wang, R. E. Duke, R. Luo, M. Crowley, R. C. Walker, W. Zhang, K. M. Merz, B. Wang, S. Hayik, A. Roitberg, G. Seabra, I. Kolossváry, K. F. Wong, F. Paesani, J. Vanicek, X. Wu, S. R. Brozell, T. Steinbrecher, H. Gohlke, L. Yang, C. Tan, J. Mongan, V. Hornak, G. Cui, D. H. Mathews, M. G. Seetin, C. Sagui, V. Babin and P. A. Kollman, *AMBER 10*, University of California, San Francisco, 2008.

33 S. Koneshan, J. C. Rasaiah, R. M. Lynden-Bell and S. H. Lee, *J. Phys. Chem. B*, 1998, **102**, 4193–4204.

34 D. Horinek, S. Mamatkulov and R. Netz, *J. Chem. Phys.*, 2009, **130**, 124507.

35 S. H. Lee and J. C. Rasaiah, *Biophys. Chem.*, 1996, **100**, 1420–1425.

36 I. S. Joung and T. E. Cheatham, *J. Phys. Chem.*, 2008, **112**, 9020–9041.

37 G. Markovich, L. Perera, M. L. Berkowitz and O. Cheshnovsky, *J. Chem. Phys.*, 1996, **7**, 2675–2685.

38 H. J. C. Berendsen, J. R. Grigera and T. P. Straatsma, *J. Phys. Chem.*, 1987, **91**, 6269–6271.

39 D. Frenkel and B. Smit, *Understanding Molecular Simulation, From Algorithms to Applications*, Academic Press, 2nd edn, 2002, ch. 12, pp. 291–320.

40 J.-P. Ryckaert, G. Ciccotti and H. J. Berendsen, *J. Comput. Phys.*, 1977, **23**, 327–341.

41 G. R. Kneller, V. Keiner, M. Kneller and M. Schiller, *Comput. Phys. Commun.*, 1995, **91**, 191–214.

42 T. Róg, K. Murzyn, K. Hinsen and G. R. Kneller, *J. Comput. Chem.*, 2003, **24**, 657–667.

43 D. Bhowmik, N. Malikova, J. Teixeira, G. Mériguet, O. Bernard, P. Turq and W. Häußler, *Eur. Phys. J. Spec. Top.*, 2012, **213**, 303–312.

44 I.-C. Yeh and G. Hummer, *J. Phys. Chem. B*, 2004, **108**, 15873–15879.

45 S. Tazi, A. Botan, M. Salanne, V. Marry, P. Turq and B. Rotenberg, *J. Phys.: Condens. Matter*, 2012, **24**, 284117.

46 B. J. Berne and R. Pecora, *Dynamic light scattering: with applications to chemistry, biology, and physics*, Wiley, New York, 1975.

47 M. Bée, *Quasielastic Neutron Scattering: Principles and Applications in Solid State Chemistry, Biology and Material Science*, Adam Hilger, Bristol and Philadelphia, 1988, ch. 6, pp. 176–249.

48 D. E. Woessner, *J. Chem. Phys.*, 1962, **36**, 1–4.

49 J. Kowalewski and L. Mäler, *Nuclear Spin Relaxation in Liquids Theory, Experiments, and Applications*, Taylor & Francis, 2006, ch. 6, pp. 127–157.

50 J. T. Cabral, A. Luzar, J. Teixeira and M. C. Bellissent-Funel, *J. Chem. Phys.*, 2000, **113**, 8736–8745.

51 H. Krienke, V. Vlachy, G. Ahn-Ercan and I. Bakó, *J. Phys. Chem. B*, 2009, **113**, 4360–4371.

52 E. Hawlicka and T. Dlugoborski, *Chem. Phys. Lett.*, 1997, **268**, 325–330.

53 R. Buchner, C. Holzl, J. Stauber and J. Barthel, *Phys. Chem. Chem. Phys.*, 2002, **4**, 2169–2179.

54 J. R. Lyerla and G. C. Levy, *Topics in Carbon-13 NMR Spectroscopy*, John Wiley & Sons, 1974, ch. 3, vol. 1, pp. 79–148.

55 H. Hertz and M. Zeidler, *Ber. Bunsenges. Phys. Chem.*, 1964, **68**, 821–837.

56 T. W. McGaughy, S. Y. C. Wu and B. M. Fung, *J. Chem. Phys.*, 1978, **69**, 473–478.

57 Y. Masuda, J. Tobita and A. Muramoto, *Bull. Chem. Soc. Jpn.*, 1998, **71**, 1555–1563.

58 Y. Masuda and A. Muramoto, *J. Solution Chem.*, 2004, **33**, 811–825.

59 M. Holz and K. J. Patil, *Ber. Bunsenges. Phys. Chem.*, 1991, **95**, 107–113.

60 F. Sacher, M. Holz and H. Hertz, *J. Magn. Reson., Ser. A*, 1993, **103**, 61–71.

61 P. J. Bratt, D. G. Gilles, L. H. Sucliffe and A. J. Williams, *J. Phys. Chem.*, 1990, **94**, 2727.

62 E. W. Lang, S. Bradl, W. Fink, H. Radkowitsch and D. Girlich, *J. Phys.: Condens. Matter*, 1990, **2**, SA195–SA200.

63 N. Malikova, S. Cebasek, V. Glenisson, D. Bhowmik, G. Carrot and V. Vlachy, *Phys. Chem. Chem. Phys.*, 2012, **14**, 12898–12904.

Aqueous solutions of tetraalkylammonium halides: ion hydration, dynamics and ion-ion interactions in light of steric effects

Debsindhu Bhowmik,[†,¶] Natalie Malikova,[*,†,§] Guillaume Mériguet,[‡] Olivier Bernard,[‡] José Teixeira,[†] and Pierre Turq[‡]

Laboratoire Léon Brillouin (LLB), UMR CEA-CNRS 12, CEA Saclay, 91191 Gif-sur-Yvette, France, and Sorbonne Universités, UPMC Univ Paris 06, CNRS, UMR 8234, PHENIX, F-75005, Paris, France

E-mail: natalie.malikova@upmc.fr

---

[*]To whom correspondence should be addressed
[†]LLB
[‡]PHENIX
[¶]Current address: Department of Physics and Astronomy, Wayne State University, 666 W Hancock Street, Detroit, MI 48201
[§]Current address: Sorbonne Universités, UPMC Univ Paris 06, CNRS, UMR 8234, PHENIX, F-75005, Paris, France

Supporting Information

The Supporting Information includes:

   a) Field Parameters

   b) Simulated and experimental densities for TMABr and TBABr aqueous solutions

   c) Details of water orientation in the hydration shells of cations

   d) NMR diffusion measurements by B. Ancian and G. Mériguet

   e) Methyl group rotation for TBA^+ and TMA^+

   f) X-ray scattering intensity – comparison of experimental and simulated data

a) Field parameters

Table 1: Interaction potentials for TBA$^+$. H_N represents hydrogen atoms closest to the central nitrogen atom.

atom or group (in bold)	atomic charge (e)		
	N	C	H
-N-	0.056669		
-N-**CH$_2$**-		0.017461	0.053130
-N-$CH_2 - $**CH$_2$**-		-0.002556	0.021844
-N-$CH_2 - CH_2 - $**CH$_2$**-		0.011361	0.020886
-N-$CH_2 - CH_2 - CH_2 - $**CH$_3$**		-0.086548	0.034799

bond elongation harmonic parameters	energy term (kcal/mol/Å^2)	length (Å)
C-H$_C$	340	1.090
C-H$_N$	240	1.090
C-C	310	1.526
C-N	367	1.471

bond bending harmonic parameters	energy term (kcal/mol/rad^2)	angle (degree)
H$_C$-C-H$_C$	35	109.5
H$_N$-C-H$_N$	35	109.5
C-C-H$_C$	50	109.5
C-C-H$_C$	50	109.5
C-C-C	40	109.5
C-C-N	80	111.2
H$_N$-C-N	50	109.5
C-N-C	50	109.5

dihedral interaction	energy term (kcal/mol)	angle (degree)
H$_C$-C-C-H$_C$	0.15	0.0
H$_C$-C-C-C	0.16	0.0
H$_C$-C-C-H$_N$	0.15	0.0
H$_N$-C-C-C	0.16	180.0
C-C-C-C	0.18	0.0
X-C-C-X	0.15	0.0
X-C-N-X	0.15	0.0

LJ parameters	ϵ (kcal/mol)	σ (Å)
H$_C$	0.0157	1.487
H$_N$	0.0157	1.100
C	0.1094	1.900
N	0.1700	1.8240

Table 2: Interaction potentials for TMA$^+$.

atom or group (in bold)	atomic charge (e) N	C	H
-**N**-	0.096521		
-N-**CH₃**		-0.165381	0.130417

bond elongation harmonic parameters	energy term (kcal/mol/Å^2)	length (Å)
C-H	240	1.090
C-N	367	1.471

bond bending harmonic parameters	energy term (kcal/mol/rad^2)	angle (degree)
H-C-H	35	109.5
H-C-N	50	109.5
C-N-C	50	109.5

dihedral interaction	energy term (kcal/mol)	angle (degree)
X-C-N-X	0.15	0.0

LJ parameters	ϵ (kcal/mol)	σ (Å)
H	0.0157	1.100
C	0.1094	1.900
N	0.1700	1.8240

Table 3: Interaction parameters for monoatomic ions.

atom	LJ ϵ (kcal/mol)	LJ σ (Å)	charge (e)
Na	0.1	2.583	+1.0
Br	0.1	4.54	-1.0

b) Simulated and experimental densities for TMABr and TBABr aqueous solutions
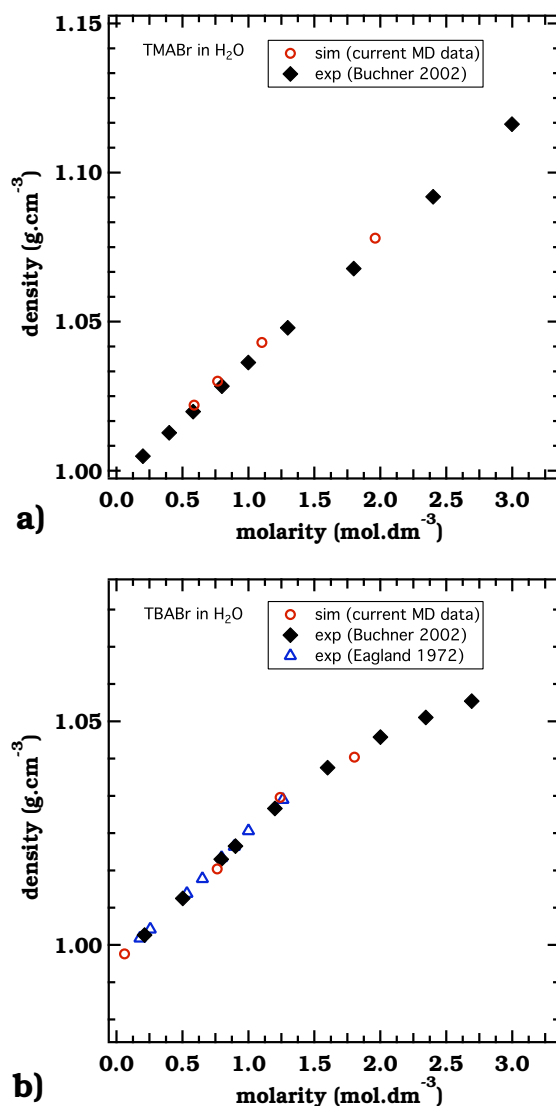

Figure 1: Simulated and experimental densities for a) TMABr aqueous solutions and b) TBABr aqueous solutions, as a function of concentration. Experimental data is taken from *R. Buchner, C. Holzl, J. Stauber and J. Barthel, Phys. Chem. Chem. Phys., 2002, 4, 2169 - 2179 and D. Eagland and G. Pilling, J. Phys. Chem., 1972, 76, 1902 - 1906.*

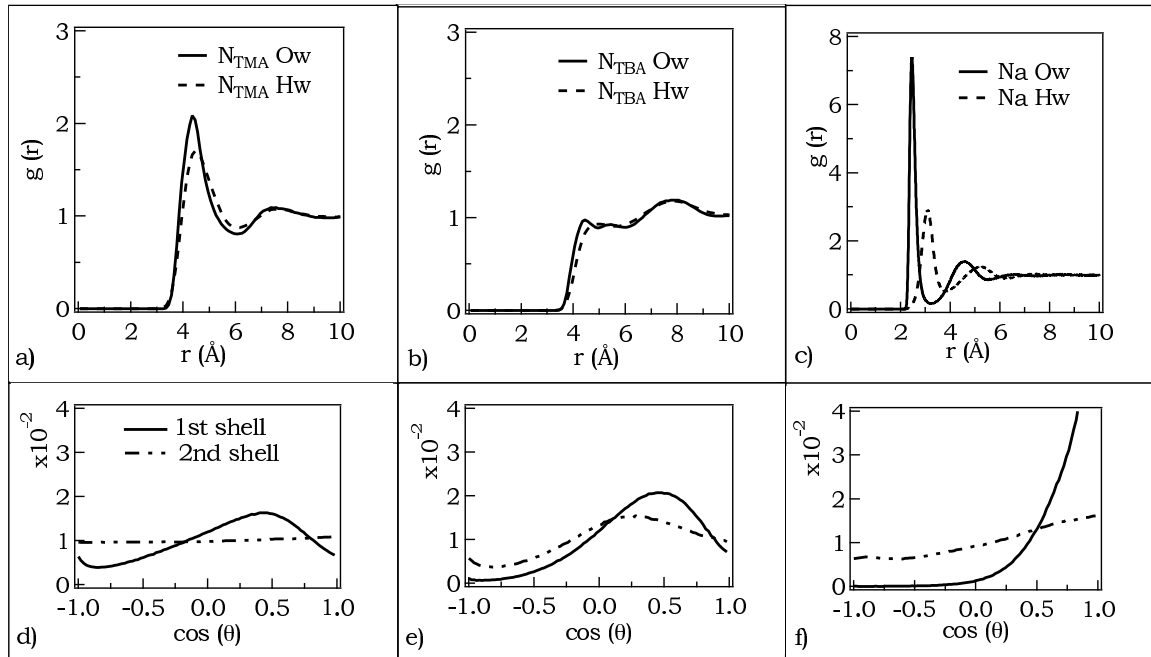# c) Details of water orientation in the hydration shells of cations

Figure 2: Details of water orientation around cations for TMABr, TBABr and NaBr solutions, all at 1m concentration: a) to c) Radial distribution functions between cations (central N atom or Na) and oxygen/hydrogen (Ow/Hw) atoms of surrounding water molecules; d) to f) Angular distribution of water molecules surrounding the cations, with θ representing the angle between the cation-Ow vector and the dipole moment vector of the water molecule. In the case of TMA$^+$ and TBA$^+$, the most probable values of θ are around 60°, which is a close to tangential orientation of the water molecules with respect to the central N atom of the cations. We see that this preferential orientation is lost in the second hydration shell of TMA$^+$, while it is retained in case of TBA$^+$. The distinction between the first and second shell in case of TBA$^+$ is taken as below or above N–O$_w$ distance of 6.2 Å

d) NMR diffusion measurements by B. Ancian and G. Mériguet

UPMC - Univ Paris 6 and CNRS (UMR 7195) , Laboratoire PECSA, Case 51, 4 place Jussieu, Paris F-75005, France

All diffusion experiments were recorded at 298 K using a ^{1}H/^{13}C/^{15}N TXI inverse probe on a Bruker Avance DRX 500 NMR spectrometer operating at 499.76 MHz for ^{1}H using the so-called bipolar pulse pair longitudinal eddy current delay sequence (BPP-LED) (*Johnson CS (1999) Diffusion ordered nuclear magnetic resonance spectroscopy: principles and applications. Prog NMR Spectrosc 34:203-256*). The ^{1}H nominal 90° pulse was around 10 μs and measured systematically on the actual sample. The maximum value of the gradient (56.5 G cm^{-1}) has been calibrated with the value of the self-diffusion coefficient of HOD in D_2O.

For each sample, a series of 32 spectra with increasing gradient value (from 0 to 56 % of the maximum value) were recorded. The data were analysed using the NMRPipe processing software package (*Delaglio F, Grzesiek S, Vuister GW, Zhu G, Pfeifer J, Bax A 736 (1995) NMRPipe: a multidimensional spectral processing system based on UNIX pipes. J Biomol NMR 6:277-293*). Rectangular gradients of constant duration (3 ms) were chosen for encoding and decoding, whereas the spoil gradient (2 ms) was sine-shaped. The LED was kept at a value of 10 ms in all the experiments. Each diffusion constant has been obtained using at least three diffusion times, Δ, from 25 to 500 ms.

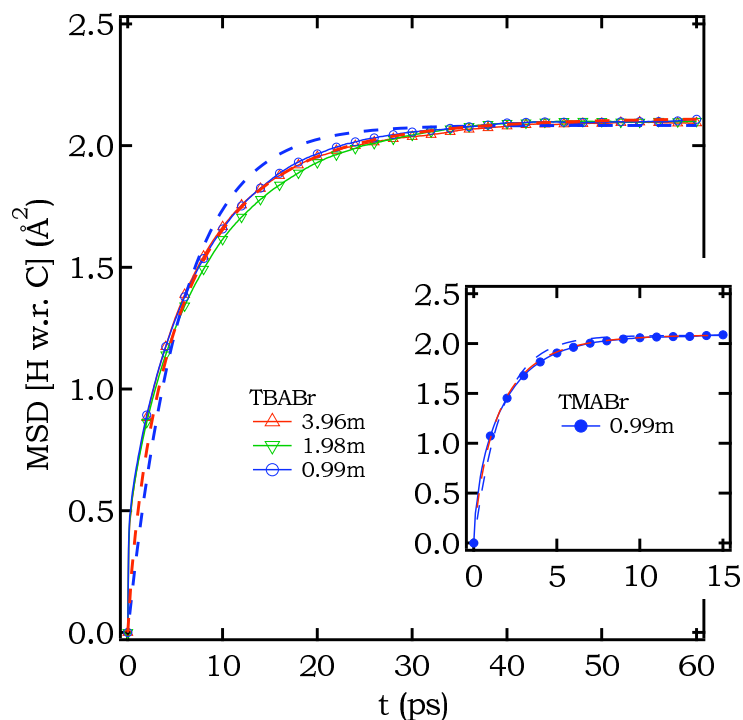## e) Methyl group rotation for TBA$^+$ and TMA$^+$

Figure 3: Investigation of methyl group rotation for TBA$^+$ and TMA$^+$: Mean square displacement (MSD) for H atoms of terminal methyl groups with respect to the adjacent C atoms, versus time, for TBA$^+$ in selected TBABr solutions; inset features the same type of data for TMA$^+$ in 0.99m TMABr solution. Dashed lines represent the fits of data with Equation 3 of the main article or its extension, which uses the same values of b_{C-H} and ϕ, but allows a range of characteristic rotational times (these are distributed according to a Gaussian function truncated at zero to avoid non-physical negative characteristic times). The obtained spread (standard deviation) of characteristic rotational times is significant, of the order of the mean value, i.e. 3-5 ps for TBA$^+$ and 2 ps for TMA$^+$.

f) X-ray scattering intensity - comparison of experimental and simulated data
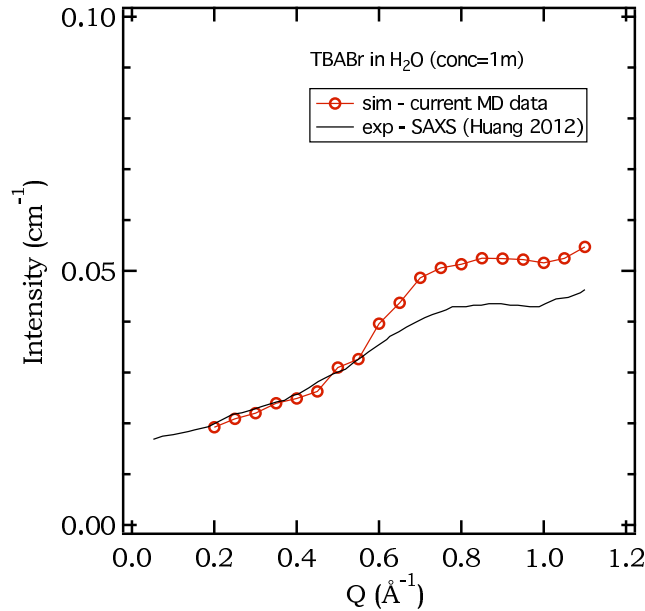

Figure 4: X-ray scattering intensity (in cm^{-1}) versus wave-vector, Q, for TBABr solution in H_2O at 1m concentration determined experimentally in ref *N. Huang, D. Schlesinger, D. Nordlund, C. Huang, T. Tyliszczak, T. M. Weiss, Y. Acremann, L. G. M. Pettersson and A. Nilsson, J. Chem. Phys., 2012, 136, 074507.* and calculated from the current MD simulations using the nMoldyn package. The principal difference between the calculation of X-ray and neutron coherent scattering signal is the use of a Q dependent X-ray scattering length for each atom in the former, instead of the Q-independent coherent neutron scattering length/cross-section for each atom in the latter. The Q-dependent X-ray scattering length was calculated using the D. Cromer and J. Mann formula from *D. Waasmaier and A. Kirfel, New Analytical Scattering-Factor Functions for Free Atoms and Ions, Acta Cryst. (1995). A51,416-43.*

Etude de la dynamique d'ions hydrophobes en solutions aqueuses par diffusion de neutrons et par simulation numérique

Abstract:

Symmetric tetraalkylammonium (TAA) cations are model systems to study the behaviour of hydrophobic ions. In this work, concentrated aqueous solutions of TAA bromides are investigated to obtain information on microscopic structure and dynamics of both the ions and solvent, by a combination of Neutron Scattering and Molecular Dynamics (MD) simulations. It is shown that TAA cations do not aggregate in aqueous solution even at high concentrations, they are penetrable for both the Br anions and solvent water molecules. The average water orientation is tangential around the cation surface, which contrasts with the simple alkali cations, such as Na^+. Using quasi-elastic neutron scattering (Neutron Spin Echo and Time of Flight techniques) and with the aid of MD simulations, the dynamics in the coherent and incoherent neutron scattering signal is decoupled. The former is identified with the center-of-mass (CoM) motion of a single TAA cation, while the latter, based on the signal of individual H atoms of the TAA cation, is a complex combination of the CoM motion and H movements internal to the cation. MD helps to identify the timescale of the global cation rotation. The slowing down of water dynamics in these solutions relative to bulk water is also made evident, though the effect is lower than might be expected.

Key Words: tetraalkylammonium bromides, neutron scattering, Neutron Spin Echo, Time of Flight, microscopic simulation, coherent and incoherent signal, dynamics, translation, water

Résumé:

Les cations de tétraalkylammonium symétrique (TAA) sont des sys-
tèmes modèles pour étudier le comportement des ions hydrophobes. Dans
ce travail, des solutions aqueuses concentrées de divers TAABr sont étudiées
pour obtenir des informations sur la structure microscopique et la dynamique
à la fois des ions et du solvant, par une combinaison de la diffusion des
neutrons et de simulations par dynamique molèculaire (MD). Il est démontré
que les TAA cations ne s'agrègent pas, même en concentration élevèe et sont
pénétrables à la fois par des anions et des molécules du solvant. L'orientation
moyenne de l'eau de solvatation est tangentielle autour de la surface des
cations, ce qui est différent de lÕorientation observée avec les cations simples,
comme Na^+. L'utilisation conjointe des expériences de diffusion de neutron
quasi-élastique (technique de l'Echo de Spin et de Temps-de-Vol) et de la
simulation MD permet de séparer la dynamique contenue dans le signal
cohérent et incohérent en diffusion de neutrons. Le premier est identifié
avec le mouvement du centre-de-masse (CoM) du cation TAA, le deuxième,
provenant des atomes individuels d'H du cation, est une combinaison
complexe de ce mouvement de CoM et les mouvements des H à l'intérieur
du cation. Le MD permet également d'identifier l'échelle caractéristique de
la rotation globale du cation TAA. Le ralentissement des molécules de l'eau
dans ces solutions est visible, mais moins important que prévu.

Mots clés: bromure de tétraalkylammonium, diffusion des neu-
trons, écho de spin de neutron, temps de vol, simulation micro-
scopique, signal cohérent et incohérent, dynamique, translation, l'eau